THE ENERGY SPECTRUM OF ULTRA HIGH ENERGY COSMIC RAYS MEASURED BY THE HIGH RESOLUTION FLY'S EYE DETECTORS

by

Kevin Reil

A dissertation submitted to the faculty of
The University of Utah
in partial fulfillment of the requirements for the degree of

Doctor of Philosophy

Department of Physics

The University of Utah

December 2002

THE UNIVERSITY OF UTAH GRADUATE SCHOOL

SUPERVISORY COMMITTEE APPROVAL

of a dissertation submitted by

Kevin Reil

This dissertation has been read by each member of the following supervisory committee and by majority vote has been found to be satisfactory.

	Chair: Wayne Springer
	Dave Kieda
	Carleton DeTar
	Kris Sikorski
	Orest Symko

THE UNIVERSITY OF UTAH GRADUATE SCHOOL

FINAL READING APPROVAL

To the Graduate Council of The University of Utah:

I have read the dissertation of Kevin Reil in its final form and have found that (1) its format, citations, and bibliographic style are consistent and acceptable; (2) its illustrative materials including figures, tables, and charts are in place; and (3) the final manuscript is satisfactory to the Supervisory Committee and is ready for submission to The Graduate School.

Date

Wayne Springer
Chair, Supervisory Committee

Approved for the Major Department

Valy Vardeny
Chair

Approved for the Graduate Council

David S. Chapman
Dean of The Graduate School

ABSTRACT

This dissertation will present the energy spectrum of Ultra High Energy Cosmic Rays (UHECR) above $10^{18}eV$ (1 EeV). The measurement is made using data from the stereo High Resolution Fly's Eye Cosmic Ray Observatory (HiRes). Data using both an average atmospheric calibration and preliminary hourly atmospheric corrections are presented. To carry out this study, a full stereo Monte Carlo with direct CORSIKA input, the Dugway atmosphere and the HiRes optics and electronics has been developed. An intrinsic energy resolution of less than 10% over all energies discussed will be shown. The measured spectrum is significantly lower than both the Fly's Eye stereo and AGASA measurements [1, 2]. However, the measurement is within error of the Fly's Eye measurement when including systematic atmospheric uncertainty. A systematic shift in energy scale of 40% is required to bring this measurement into agreement with AGASA.

In memory of my parents

C. Arland

and

Marlene J. Reil.

CONTENTS

LIST OF FIGURES

LIST OF TABLES

ACKNOWLEDGEMENTS

I wish to thank my tremendous graduate advisor, Wayne Springer. It has been his support and guidance that has allowed me to reach this point.

I would also like to acknowledge the efforts of Tareq AbuZayyad and Charlie Jui who produced the previous thesis on this subject. Their work has guided and supported the work that I present here. The thesis work of Chihwa Song and Xingzhi Zhang have also been of great help. Additionally, Zhen Cao has been a major contributor to the Monte Carlo used in this work. His work was supported by previous efforts of John Boyer and Charlie Jui.

The computationally intense analysis presented here has been supported by the Center for High Performance Computing (CHPC) at the University of Utah.

Finally, I wish to acknowledge the support of my family. I have been absent from my home for a great deal of time while taking data, preparing presentations and attending conferences. I have missed them greatly and want them to know of my love for them. I especially wish to thank Delyna. Without her support, I would not have had the strength to reach this point.

CHAPTER 1

INTRODUCTION

The term cosmic ray is a bit of a misnomer since the primary particles are predominately relativistic nuclei rather than rays. The book "Cosmic Bullets," by Roger Clay and Bruce Dawson, provides a more apt title [3]. These cosmic particles are often endowed with incredible energy. No astronomical source of the required acceleration has been found. It is the search for these highly energetic sources of acceleration that makes the study of the energy, composition and arrival direction of these particles interesting.

1.1 Motivation

I have undertaken the task of studying the energy spectrum of Ultra High Energy Cosmic Rays (UHECR). The primary measurement that I have made is the energy of cosmic ray particles hitting the earth. It has been my privilege to help in the collection of very high quality cosmic ray data above 1 EeV. The only limitation of this data set is its size, and with good fortune it should grow rapidly.

The spectrum of cosmic rays has been studied over 10 orders of magnitude, from less than 10^9 to over 10^{20} eV. Over this large energy range the spectrum falls off approximately by an E^{-3} power law. The flux ranges from $\frac{1\ particle}{m^2\ second}$ for energies of

50 GeV to $\frac{1\ particle}{km^2\ year}$ for energies of 5 EeV. Figure 1.1 shows the differential flux (dN/dE) versus energy for selected experimental measurements over this energy range[4]. Additionally, Figure 1.1 is labeled with flux rates in layman terms. At lower energies this flux is high enough for direct satellite or balloon measurement. At the highest energies, which are discussed in this paper, the flux is so low that an extremely large aperture must be used in the study of cosmic rays.

Many theories describing acceleration mechanisms capable of accelerating particles for 10^{18} eV and higher exist [5, 6, 7]. There are two main types of acceleration theory: top-down and bottom-up acceleration mechanisms. Bottom-up acceleration describes processes that take a particle, such as a proton, and accelerate it to a very high energy. For bottom-up acceleration to work, the source must provide either a very large acceleration gradient or provide acceleration over a very large distance. Figure 1.2 shows a Hillas plot of potential bottom-up sources[8]. In this Figure, sources of magnetic acceleration are shown with their relative acceleration gradients and size. A sufficient gradient or size makes the source a candidate for UHECR production.

Top-down mechanisms produce the particles locally using the decay or interaction of exotic particles such as the decay of a super heavy relic particle from the big bang or the interaction of a magnetic monopole and anti-monopole[9, 10]. While top-down models can explain the existence of UHECR, they have a more difficult time explaining the flux. Additionally, the models require the production or existence of very exotic particles. For additional information on top-down mechanisms please see the references[11, 12]. At present, no theory has yet to produce a conclusive mechanism nor has experiment been able to trace these particles to any conclusive source.

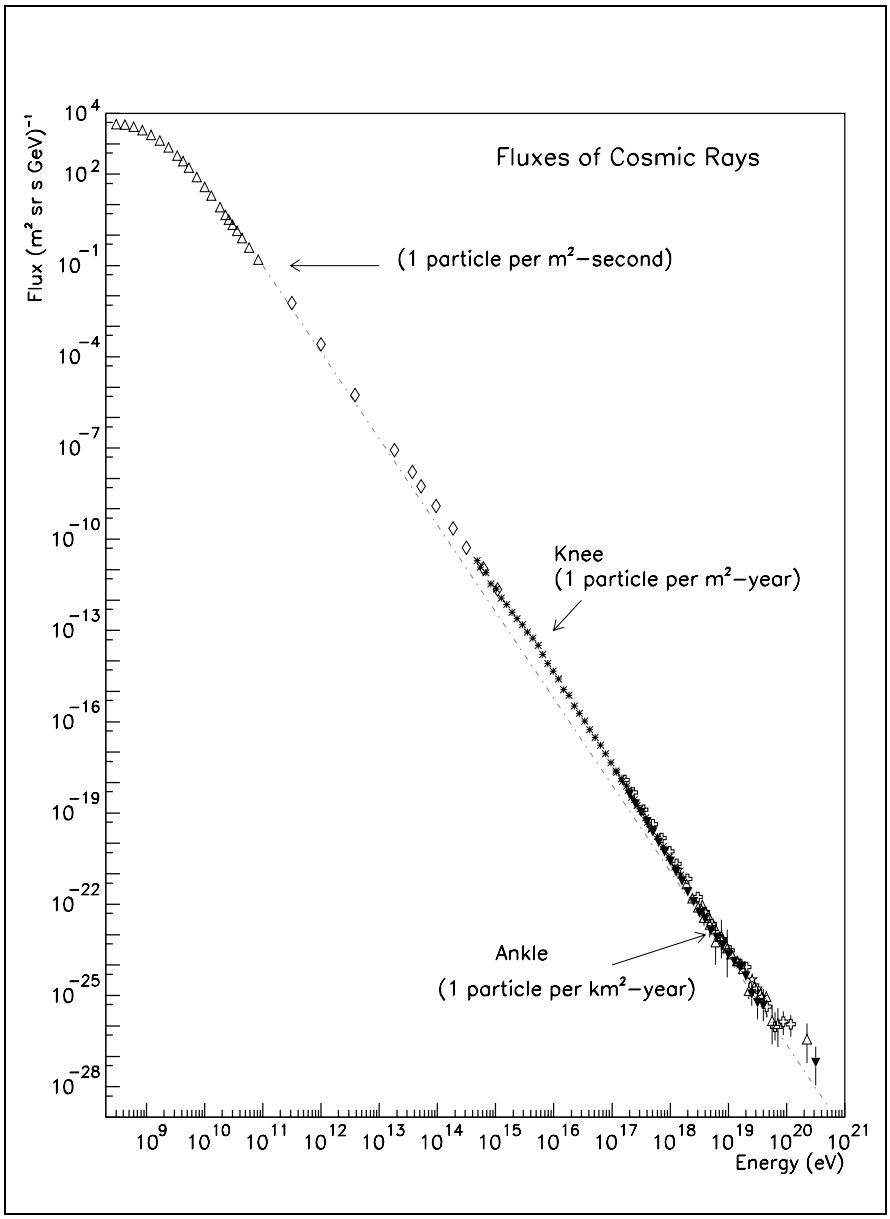

Figure 1.1. Experimental Results on the Cosmic Ray Spectrum.Adapted from [4].

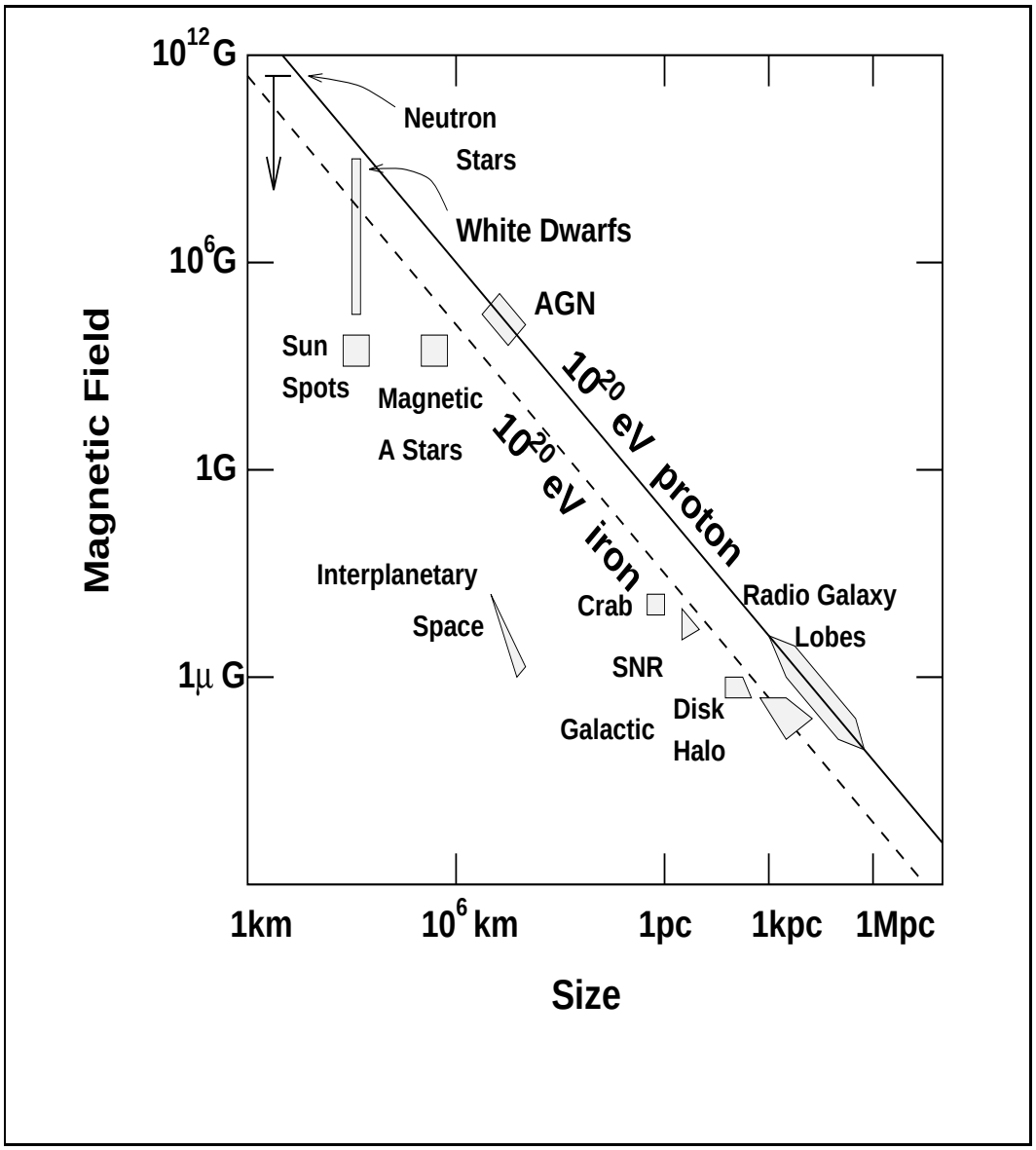

Figure 1.2. Hillas Plot of Cosmic Ray Source Candidates.Adapted from [8].

1.2 This Report

The High Resolution Fly's Eye is an air fluorescence detector. It was designed to study the spectrum, anisotropy and composition of cosmic rays above $10^{18.5}$ eV using two detectors simultaneously. The two sites are located on small mountains in the west desert of Utah on the US Army Dugway Proving Ground. The sites are separated by 12.6 km and allow stereoscopic observation of air showers. This report will focus on the spectrum of cosmic rays above 10^{18} eV. Theses describing composition and anisotropy based on this work will follow shortly[13, 14].

Stereo mode operation began at the end of 1999. However, the summer of 2000 and much of 2001 were lost due to military restrictions. Therefore, the data presented here covers almost two years of operation, but the detector was only operational for a little more than half of that time. We are, at present, prevented from data collection due to the security issues in the United States.

Several publications exist which describe the detector setup, calibration and data handling[15, 16, 17, 18, 19, 20]. I will not endeavor to present the details of this material again. Rather, I will present an overview of the manner in which our data are collected and refer the reader to more complete sources. The reader is also referred to the theses of T. Abu-Zayyad, X.Z. Zhang, and C. Song[20, 21, 22]. A few of their figures have been used with permission in the early chapters of this work.

This work is a report on new observations, new data and new methods. It is my desire to document the additional contributions that I have made in this field and not reiterate the work of others. Should my discussion of previous work, models and theory be found lacking, I would refer the reader to the Frontiers in Physics book, "Introduction to Ultrahigh Energy Cosmic Ray Physics" by P. Sokolsky as a primary reference for such items[23]. Additionally, "High Energy Astrophysics" by M.S. Longair is a standard of this field[24, 25].

1.3 Organization

The following list provides an overview of the information contained in the chapters of this work.

Chapter 2 provides a brief overview of UHECR research. The most interesting and current physics results are discussed here.

Chapter 3 describes the HiRes experimental setup. HiRes is an air fluorescence detector. Many resources exist that provide a detailed description of the detector and methods[15, 16, 17, 18, 19, 20]. Other methods of cosmic ray study will also be discussed.

Chapter 4 provides some details of our detector calibration. The calibration consists of two main parts: understanding the atmosphere and the detector's response to light.

Chapter 5 documents data collection, the HiRes software library and the details of the data processing. Additionally, the effects of preliminary data cuts are shown.

Chapter 6 details the detector Monte Carlo simulation. The physics of extensive air shower production, light production, atmospheric scattering and detector response as implemented in the Monte Carlo are discussed.

Chapter 7 provides the details of studies carried out using the Monte Carlo. Additionally, the study of detector resolution is presented. Finally, it will be shown the Monte Carlo properly predicts distributions found in the data.

Chapter 8 will show all of the details of the spectrum calculations. The study of the four variables involved, number and energy of events, and detector aperture and exposure are all presented.

Chapter 9 discusses additional information that has been learned from our data set. Studies of systematic uncertainties are shown. The final spectrum calculation and comparisons to prior and current results are shown.

CHAPTER 2

UHECR PHYSICS

Many questions persist in the study of cosmic rays. The foremost question is, "What astrophysical process could produce relativistic particles with such incredible energy?" The three main topics studied by the HiRes experiment all seek to answer this question. First, by studying the cosmic ray spectrum, we determine the energy and number of these particles. Second, if we can determine the composition of the particles it may lead us to the source(s) where such species are produced. Finally, any anisotropy in the arrival direction of these particles may point to a source for these particles from the heavens.

2.1 The Physics of Extensive Air Showers

With particle fluxes of $\frac{1particle}{km^2 year}$, building a detector that requires the cosmic ray primary to hit the detector is not feasible. Instead, detectors are built to make measurements on the products of interaction or in the case of HiRes, the light produced by the products of interaction. Upon entering the earth's atmosphere the primary cosmic ray interacts with an atmospheric nucleus. This interaction initiates a cascade of secondary particles. Measurements of the particles in this cascade can be made by the measurement of the particles that reach the ground or by the light the particles produce in the atmosphere. Various detection methods are described later in this chapter.

2.1.1 Interaction of Primary and Cascade of Particles

An extensive air shower is initiated when an UHECR interacts with an atom in the atmosphere. However, the details of the physics of the interaction of particles at UHECR energies are not well known. Rather, by extrapolating the details learned from accelerators, models exist describing the interactions. The extrapolation must be done both in energy scale and in interaction angle. Accelerators become limited as the interaction angle produces products closer and closer to the beam line. Close to the beam line, detectors cannot function due to the large amount of radiation and background in the region. The products of the initial interaction carry away the initial energy and then interact again with the atmosphere. After several interactions, the energy of the shower products is low enough to base all remaining interactions on information provided by accelerator studies.

As the shower develops in the atmosphere, the energy is divided into more and more particles. An extensive air shower is this cascade of interaction products. The location where the number of particles N ceases to increase is known as shower maximum and occurs at a depth X_{max}. From X_{max} the number of particles decreases from N_{max} since the average particle energy is not high enough to produce more particles. The remaining particles continue to deposit energy in the atmosphere until their energy is depleted or they hit the earth.

2.2 Cosmic Ray Properties

2.2.1 Energy Spectrum

The spectrum of cosmic rays is shown in Figure 1.1. As mentioned in the previous chapter, the spectrum is rapidly falling. The cosmic ray flux follows a power law according to

$$N(E)dE \propto E^{-\gamma}\, dE \tag{2.1}$$

where γ is the spectral index.

In Figure 1.1 there are two changes in the slope of the spectrum. The first change, known as the "knee", is located just above 10^{15} eV. At the knee the spectral index γ changes from 2.7 to 3.0. Over the next three orders of magnitude the spectral index remains approximately constant. Just below 10^{18} eV the index increases to 3.27 and then suddenly at $3{\times}10^{18}$ the spectrum changes to 2.7. This change is known as the "ankle."

Many possible explanations exist for the knee feature. These explanations include a change in the composition of the cosmic ray primaries, a change in propagation energy loss, or a change in the source of the acceleration[26, 27, 28]. Similar phenomena could also explain the ankle.

Multiplying by a factor of E^3 in the ankle region flattens the spectrum for closer inspection. This technique is useful for looking at the spectrum in detail, but it is very sensitive to small systematic shifts in energy scale. After multiplying a spectrum with index $\gamma = -3$ produces a flat line. $\gamma > -3$ leads to a negative slope and $\gamma < -3$ results in a positive slope. Figure 2.1 shows the spectrum measurement from the original stereo Fly's Eye experiment. This E^3 flux measurement includes the linear fits showing dramatic changes. The fit shown with dashed lines is broken into three segments: a fit showing $\gamma = -3$ up to $10^{17.4}$ eV, a fit showing $\gamma = -3.27$ from $10^{17.4}$ eV to $10^{18.3}$ eV, and a fit showing $\gamma = -2.7$ above $10^{18.3}$ eV. The dotted line shows a fit assuming a constant spectral index over the whole range.

A final region of interest is around $6{\times}10^{19}$ eV. This region contains the location of the Greisen-Zatsepin-Kuzmin (GZK) cutoff[29, 30]. At this energy, cosmic ray

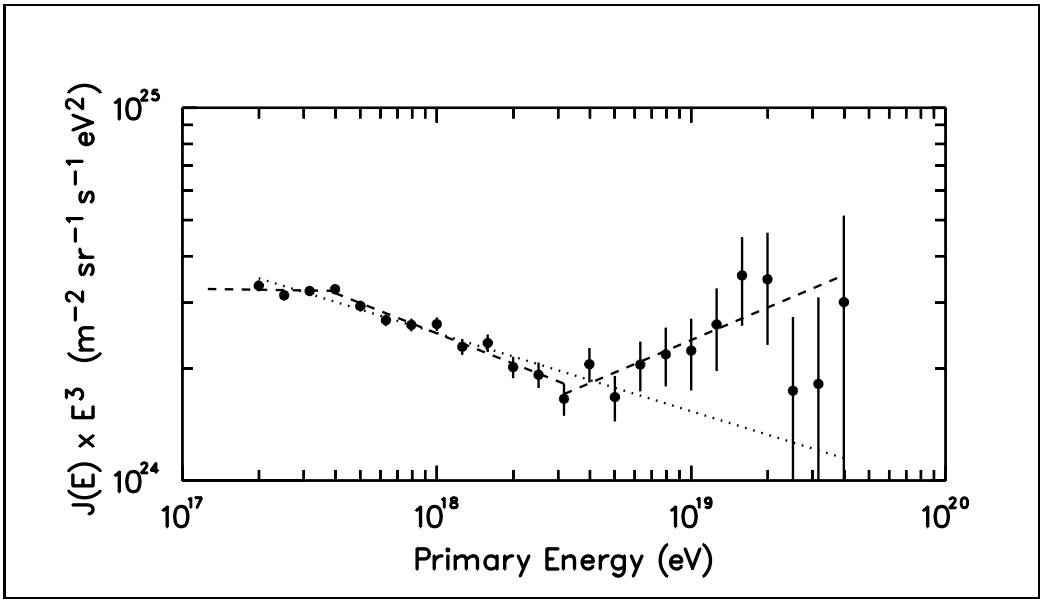

Figure 2.1. $E^3J(E)$ from the Stereo Fly's Eye Experiment (Adapted from [1])

particles are expected to interact with the cosmic microwave background (CMB). The process involved is

$$\begin{aligned} p + \gamma_{2.7K} \rightarrow \Delta^*(1232\ MeV) &\rightarrow p + \pi^0 \\ or &\rightarrow n + \pi^+. \end{aligned} \tag{2.2}$$

For heavier nuclei the propagation is limited by photospallation[31]. In this process the nucleus is broken into smaller particles when it interacts with the CMB photon. The mean free path for this process is shorter than that of protons.

The GZK interaction reduces the distance over which a super GZK event can travel and still arrive at the earth with energy above the cutoff. In searching for a source that can provide such large acceleration, the GZK cutoff limits the location of the source to be relatively close by.

As a super GZK proton travels, it loses energy by the GZK process. Repeated interactions continue to reduce the primary particles energy until it is below the threshold for equation 2.2 to occur. The more energetic the primary proton, the

quicker it will lose its energy. For example, a proton with energy of 10^{22} eV and one with energy of 10^{21} eV will each have had its energy reduced to 10^{20} eV after approximately 100 Mpc.

2.2.2 Composition

Determining the types of particles that are arriving at earth will also provide indications as to which astrophysical processes could have produced them. For example, should the primary particles be purely iron, then the astronomical source would have to have iron content such as in the final stages of the life of a star[32]. On the other hand, should all primaries be gamma rays, then a source of ultra high energy gamma rays would be required. With existing observation techniques, UHECR composition cannot be determined on an event-by-event basis. Rather, trends or changes in composition from the statistics of many events. Although these methods are inherently model dependent, all models of interaction predict that heavier nuclei will deposit their energy more quickly in the atmosphere resulting in a more shallow depth of shower maximum on average. Figure 2.2 shows the model predictions for the average X_{max} for protons and iron of different energies. The upper line is the average X_{max} value for protons for the given energy bin. The lower line is for Iron. Between the two lines is the Fly's Eye measurement for the average X_{max} versus energy. Here the trend can be interpreted as a change in composition from heavier nuclei to lighter. This measurement ends around 10^{18} eV where the data in this thesis begin.

Preliminary results from this experiment, shown later, show an almost constant composition. If prior results correctly indicate a change from heavier to lighter composition then in the energy range discussed here, we may be dominated by light nuclei. The study of composition is dependent upon X_{max} and energy determination

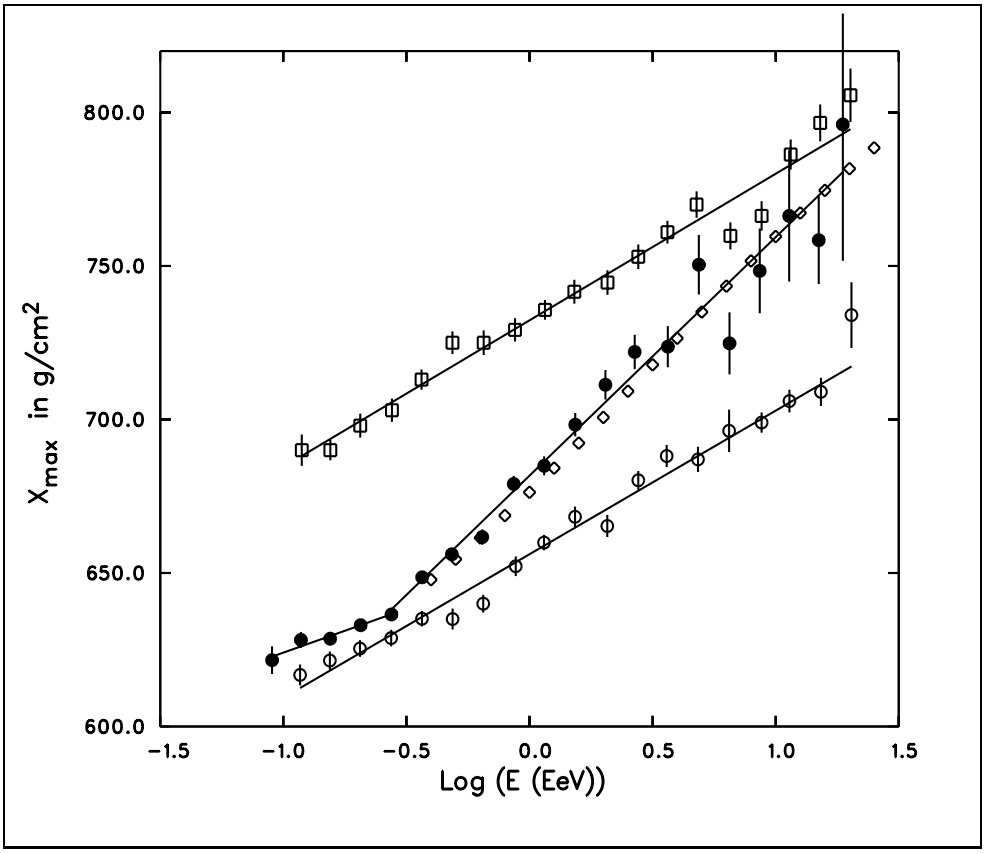

Figure 2.2. Fly's Eye Composition (adapted from [1]). Monte Carlo protons are depicted by squares and MC iron by circles. The solid circles are the Fly's Eye data with an illustration for a simple two component mixing depicted with diamonds.

and therefore upon this work. A composition study is expected to follow this work in a dissertation by Greg Archbold[13].

2.2.3 Anistropy

The primary composition of cosmic rays is assumed to be charged nuclei. In this case, the trajectory of the cosmic ray will be changed by magnetic fields. The gyro-radius of this bending is

$$R_g = \frac{\gamma m v \sin\theta}{zeB} \approx 1.1 \frac{E_{18}}{zB_\mu}(kpc), \tag{2.3}$$

where E_{18} is the energy of the cosmic ray in EeV, B_μ is the magnetic field in micro gauss and z is the charge of the particle[21].

For galactic sources ($R{\sim}10kpc$ and $B_\mu{\sim}1-10\mu G$) particles of EeV energy will have a gyro-radius of around 1kpc and all directional information will be lost. However, over 50 EeV, the deflection will be less than 1 radian and clustering will be visible. Additionally, over intergalactic space with B_μ at $10^{-3}\mu G$ clustering can still be preserved for distances up to 10Mpc[21].

The anisotropy studies from these data are expected to follow in theses by Benjamin Stokes and Jose Bellido[33, 14] and in work by John Belz and Montana State. The study of anisotropy is dependent on the predetermination of the shower energy and therefore is dependent upon the completion of this work. Anisotropy is an extremely detailed study and will require a great deal of time once this work is complete and verified.

2.2.4 Measurement of Extensive Air Showers

There are three techniques used to measure the properties of extensive air showers. These include Čerenkov light detectors, ground array particle detectors and air fluorescence light detectors. Each method has its own strengths and weaknesses in determining the properties of the initiating cosmic ray.

Čerenkov detectors determine geometry by the shape and size of the Čerenkov signal. Improvements can be made by parallax information from multiple telescopes. The radius of the Čerenkov cone and the total light contained in it also allow species identification and energy determination [34]. No Čerenkov detector exists to study the energy ranges discussed here.

Ground array detectors are comprised of many individual charged particle counters distributed over a large area. The geometry of the air shower is well determined by the relative time at which the charged particles reach each detector. The energy is determined by relating the density of charged particles as measured at a sufficient distance, known as ρ_{600} (600+ meters), from the core of the shower.

The main advantage of this method is that the array can be operated 24 hours a day. Disadvantages include the large number of detectors needed in order to obtain the required large aperture. Additionally, each air shower is measured at only one depth in the atmosphere and that depth depends upon the geometry. The more inclined the shower, the more atmospheric depth which much be penetrated before the measurement is made. The ρ_{600} method is rather model dependent as an extrapolation must be made from the highly fluctuating tail of the charge density back to the initial primary energy.

Air fluorescence detectors study the energy deposited by the cosmic ray using the atmosphere as a calorimeter. Most of the energy of the cosmic ray is deposited in the atmosphere by exciting nitrogen atoms. Light is produced as the nitrogen fluoresces. Remote telescopes then observe some of this light. By integrating the total amount of light produced and using the fluorescence spectrum a measurement of the total energy deposition is made.

The disadvantages of this method include the difficulty in the calibration of the atmospheric variations. Additionally, the detector has a 10% duty cycle since it can only be operated on clear moonless nights. Finally, the result depends upon the accuracy of models and experiments that determine the efficiency of nitrogen fluorescence. This final disadvantage is discussed in the Monte Carlo chapter. Additionally, not all energy is deposited in the atmosphere and a correction for "missing energy" must be made. The amount of missing energy is model dependant.

The main advantage of the air fluorescence technique is that it is calorimetric. A measurement of energy deposition over a larger portion of the shower can be made because of the large portion of the air shower that is viewed. Additionally, the relatively small detector size to aperture ratio makes construction easier. Rather than filling the aperture with detectors, a single fluorescence detector can observe outward into a very large aperture. Since HiRes is a fluorescence detector many additional details of this technique will follow.

CHAPTER 3

THE HIRES DETECTORS

Several sources may be referenced for more details on the HiRes detectors[15, 21, 20, 22]. I will present an overview of our experimental setup and technique.

3.1 Atmospheric Calorimeter

A calorimeter is a device in which the energy of an event or reaction is measured by the energy deposited in or removed from a measuring device. In chemistry a calorimeter is a device that determines the energy of a reaction by measuring the temperature change in a liquid surrounding a reaction vessel. At HiRes, the atmosphere becomes a calorimeter that determines energy in an air shower by measuring the amount of light produced in the atmosphere.

3.2 Sites

The observatory, located on the US Army Dugway Proving Ground, consists of two sites separated by 12.6 km. Since most aerosols are located near ground level, the sites have been built at elevated locations.

The first site, HiRes-1, is located on Little Granite mountain and consists of 22 mirrors each viewing approximately 16^o in azimuth and 14^o in elevation. This site has been operational since 1997. The second site, HiRes-2, consists of 42 mirrors divided into two rings. Each mirror still views approximately 16^o in azimuth. Ring 1 views in elevation from $3 - 17^o$ and ring 2 views from $17 - 31^o$. Figures 3.1

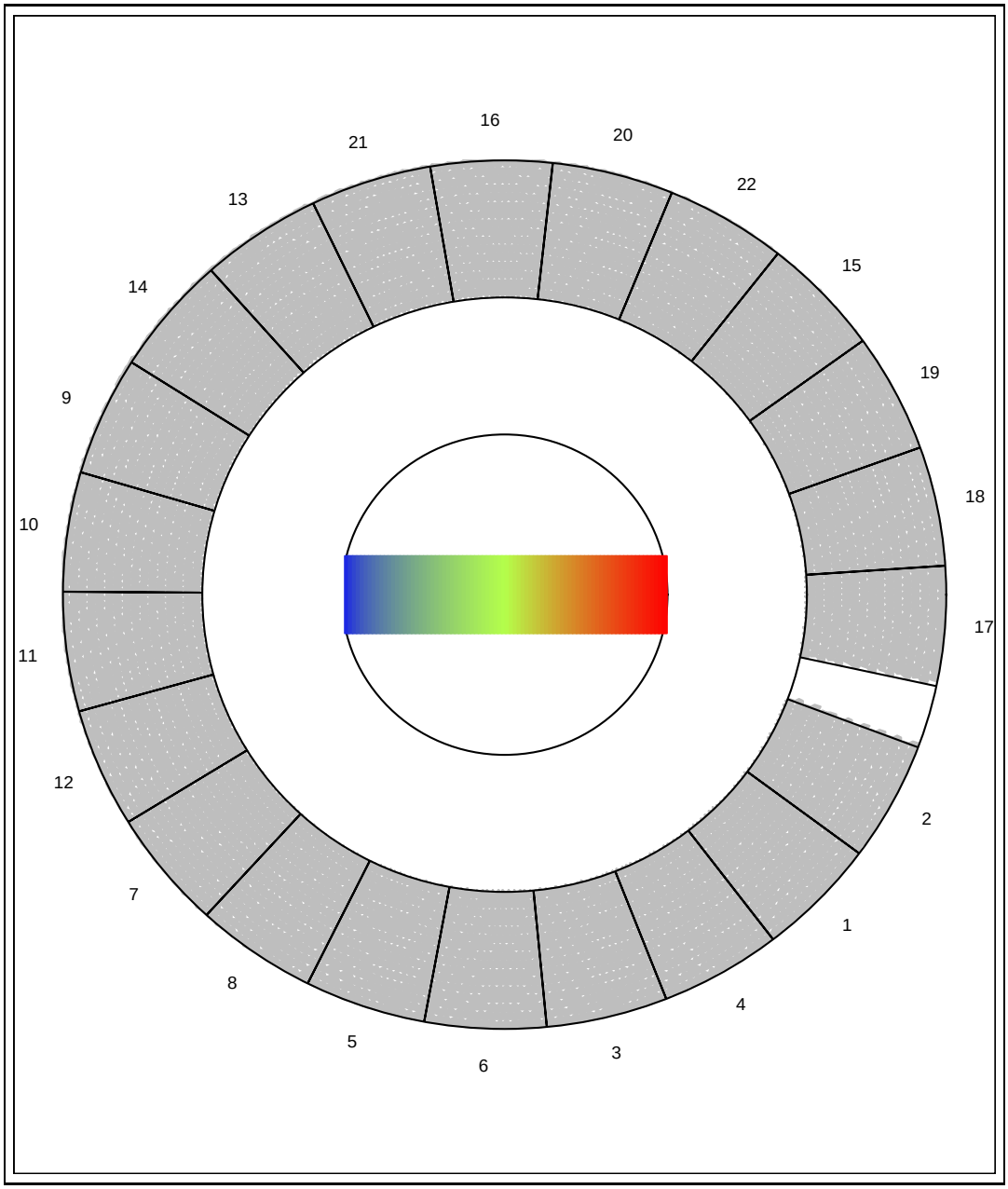

Figure 3.1. HiRes-1 Mirror Configuration:
Outer ring represents 3^o above horizon
Inner rings represent 17^o and 31^o respectively
A small gap in azimuthal coverage can be seen between mirrors 2 and 17

and 3.2, taken from an event display, show the mirror orientations. In these displays, north is upward. The elevation of 3^o is the outside of the ring and the elevations of 17^o and 33^o are the two inner rings respectively. HiRes-2 is southwest of HiRes-1. Mirror 7, at HiRes-1, looks directly at HiRes-2 and mirrors 2 and 4 at HiRes-2 look at HiRes-1.

3.3 Mirrors

The light that is produced in an air shower travels from the shower to the detector. This light is then collected by the mirrors and focused onto a cluster of photo-multiplier tubes (PMTs).

The HiRes mirrors are 2 meters in diameter. They are spherical mirrors made up of four cloverleaf segments. After accounting for losses due to obscuration of the PMT cluster, the losses due to spaces between PMTs and effects of the clover shape the effective area of the mirror is 3.8 m^2. The reflectivity of the mirrors is approximately 90% when clean with wavelength dependence as shown in Figure 3.3. In this analysis an average reflectivity of 80% is assumed as the reflectivity degrades with time as dust builds up on the mirror surface.

3.4 Photomultiplier Tubes

The HiRes mirrors focus light onto the focal plane nominally 91.5 inches from the mirrors center. Located at this focal plane is a cluster of 256 PMTs. The 256 tubes are configured into a 16x16 grid in a hexagonal close pack arrangement as show in the photograph in Figure 3.4. Each phototube is 40 mm across and views approximately 1 degree of sky.

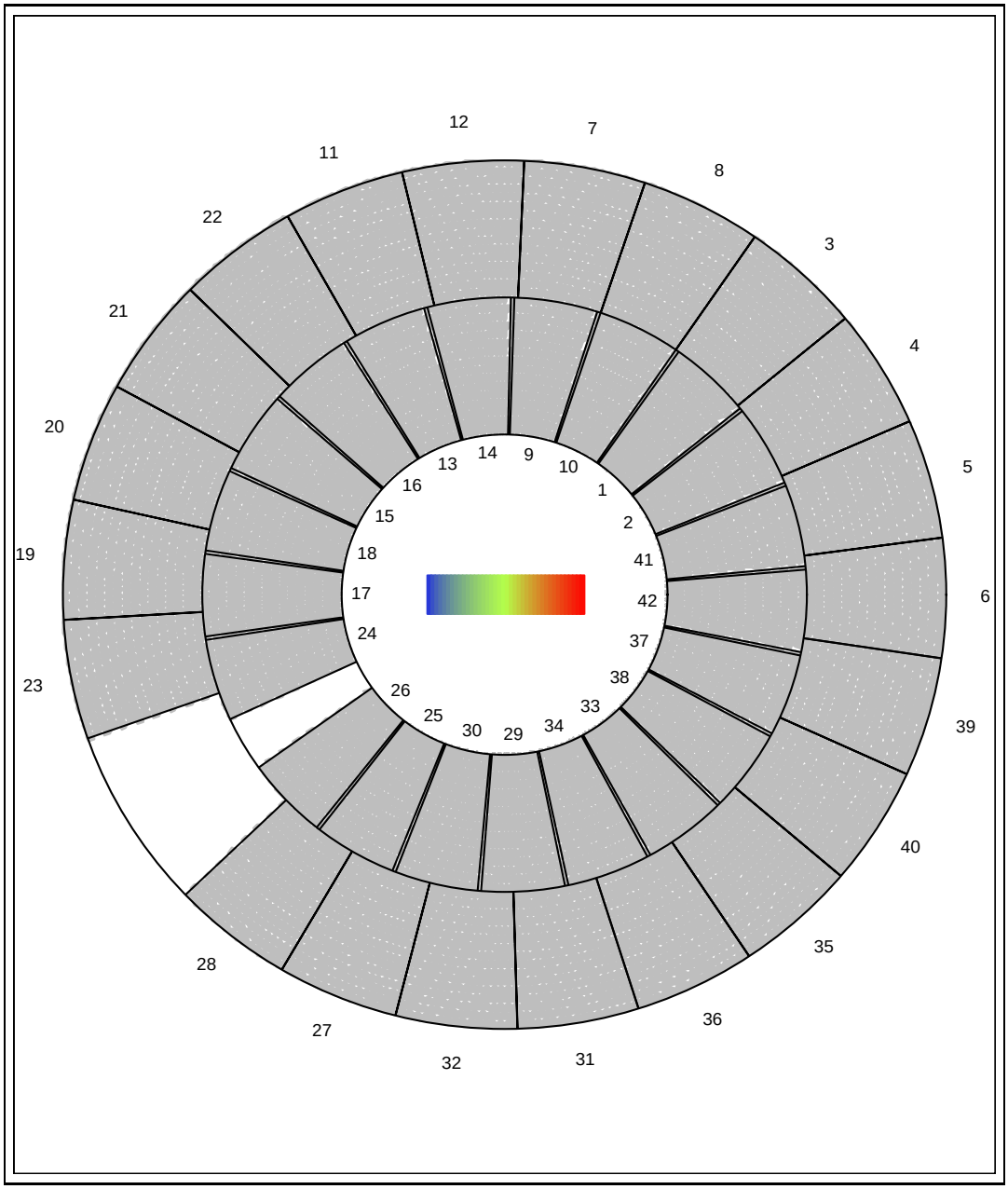

Figure 3.2. HiRes-2 Mirror Configuration:
Outer ring represents 3^o above horizon
Inner rings represent 17^o and 31^o respectively
A small gap in azimuthal coverage can be seen between mirrors 23 and 28

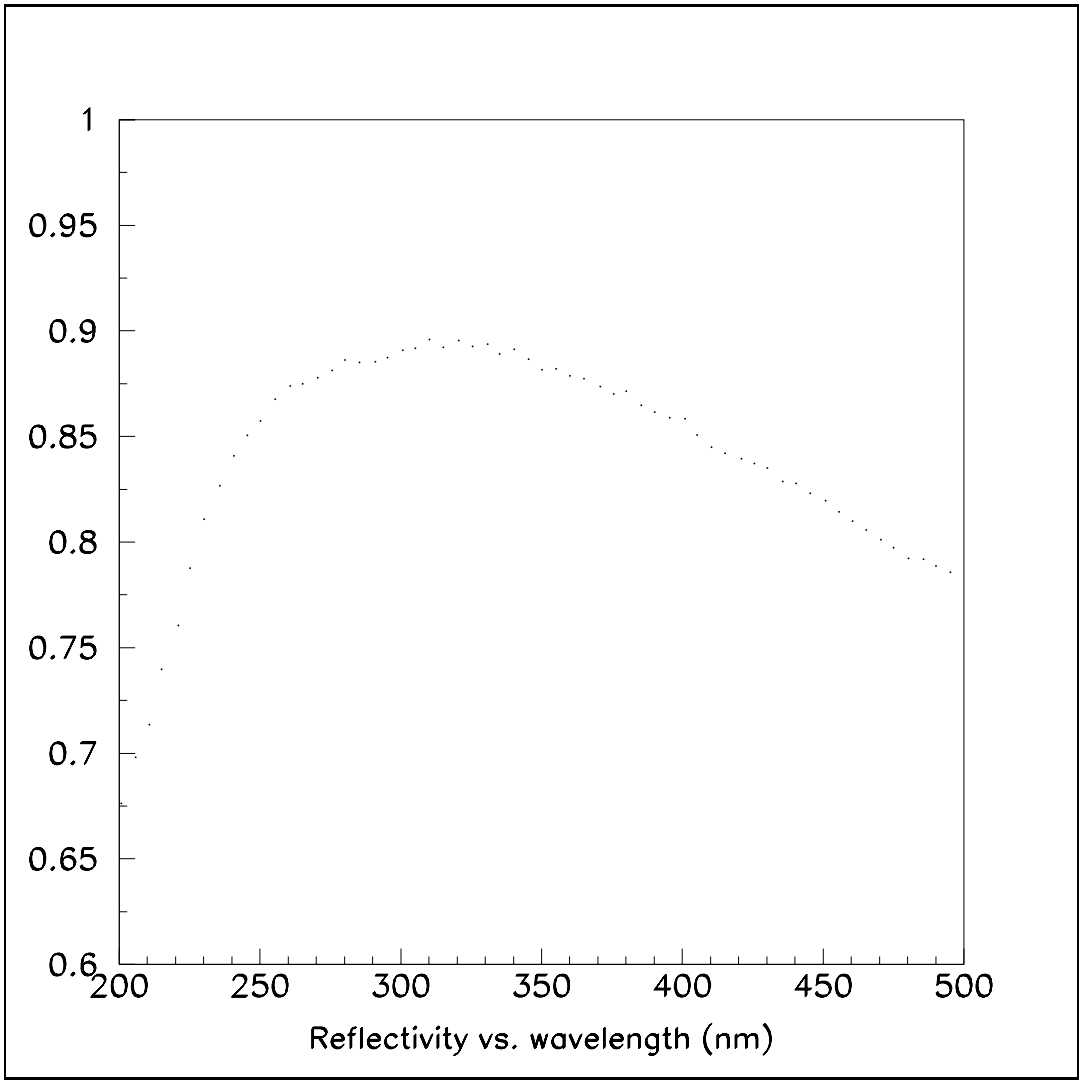

Figure 3.3. Mirror Reflectivity

Figure 3.4. Photograph of PMT Cluster with Filter Down

3.5 UV Pass Filter

In front of the phototubes, is a UV filter. This filter removes most light outside of the range of 300-400 nm, passing only the UV component through to the PMTs. The transmission spectrum is found in Figure 3.5. The filter glass shown in Figure 3.4 has been lowered to expose the phototube cluster.

3.6 HiRes Electronics

HiRes-1 and HiRes-2 have very different electronics. The reason for this is quite simple. HiRes-1 was built from recycled materials from the HiRes prototype detector[35]. Doing this allowed a full detector site to be completed and operational several years sooner than building a new site.

HiRes-1 readout consists of "sample and hold" (S&H) electronics. Using these electronics the total integrated signal from the PMTs is stored. The integration

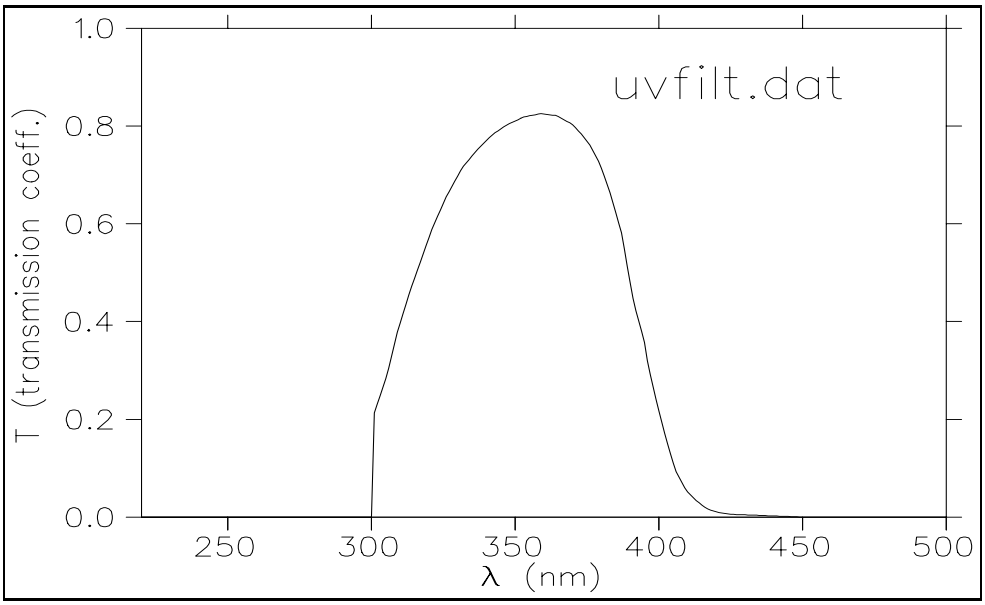

Figure 3.5. Transmission of the UV-pass Filter

time window for this system is $4.5\mu s$. Only the total number of photons arriving and the average time of arrival are stored for each tube.

HiRes-2 readout consists of "flash analog to digital" (FADC) electronics. Every 100ns the integrated number of photoelectrons is stored. This allows us to view the signal from the air shower many times with the same tube.

In this analysis, to facilitate the use the same analysis code for both sites, the FADC information is integrated and an average time is assigned. Independently, a monocular HiRes-2 analysis using the full FADC timing is being done[36]. A future analysis using only the HiRes-2 signal with geometric constraints provided by HiRes-1 would prove quite interesting.

3.7 GPS Timing

The detectors are synchronized by using the Global Positioning Satellite system[37]. Each site independently measures its time relative to the current time from a GPS module. Additionally, the steer-able calibration lasers, described in section 4.1.4, have been equipped with GPS receivers and are triggered at known offsets from the GPS second. This allows for easy identification and extraction of these known sources of light from the data stream.

3.8 HiRes Data Format

At each site, the number of photoelectrons (npe) in each triggered tube is stored. Additionally, the average arrival time of that signal is provided. The npe, time and pointing direction of each tube composes the raw data signal used in this analysis.

CHAPTER 4

CALIBRATION

HiRes determines the energy of cosmic rays by measuring the amount of light produced in the atmosphere by the extensive air shower. To accomplish this we must first understand our detectors response to light so that we can determine how much light arrived at the detector. Second, we must understand how much light was lost between our detector and the air shower.

Both the calibration of the atmosphere and the calibration of the detectors were performed by smaller dedicated groups of individuals within our collaboration. I will provide an overview of the methods and the results of their work. More detailed information can be found in other publications [16][18].

4.1 Atmospheric Calibration

Three main forms of atmospheric monitoring and calibration exist. First, the detector operators manually record hourly qualitative atmospheric observations. Second, the atmosphere is probed with many known light sources including xenon flashers and steer-able YAG lasers. Finally, newly installed cloud monitors also measure the temperature of the sky allowing us to identify warmer clouds against the cold night sky. A schematic of our atmospheric monitoring equipment is shown in Figure 4.1.

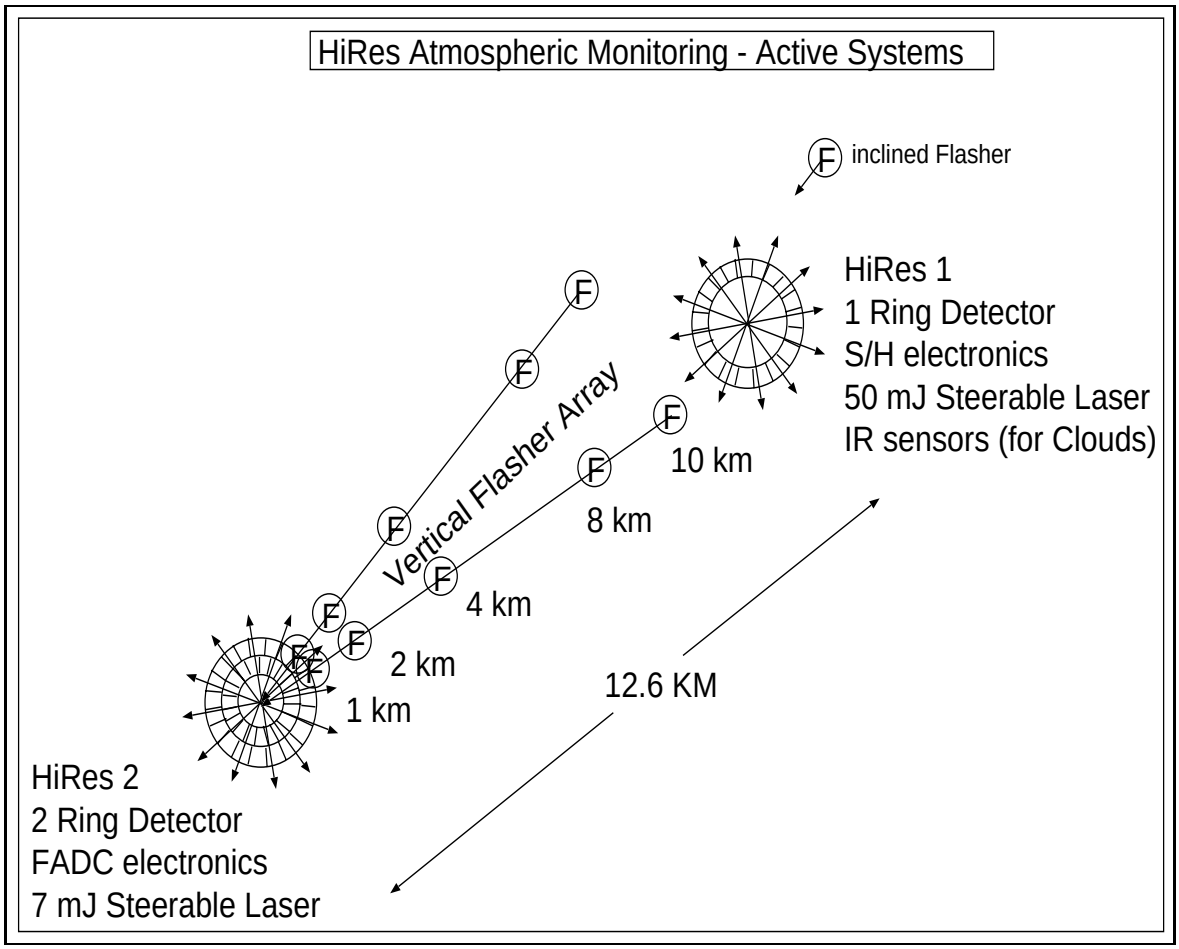

Figure 4.1. Schematic of the HiRes Atmospheric Monitoring Hardware

4.1.1 Weather Codes

Every hour, the person operating the detector is required to go outside and check the weather. Within the nightly log files a "weather code" is recorded. These weather codes are, of course, subjective and are therefore not used in this analysis.

4.1.2 Intersite and Vertical Flashers

A collection of xenon flashers is distributed within our aperture. An array of ten radio-controlled flashers is located on two rows extending from HiRes-2. These

flashers produce a vertical collimated beam of light[38]. An additional flasher fires an inclined collimated beam of light from a location NNE of HiRes-1. The path of this "intersite" flasher is approximately 4^o in elevation and 52^o south of west.

Since the flashers fire with some time variation, they provide a unique time signature that can be used to confirm time synchronization between sites. Beyond this measure the flasher system is used only qualitatively. An unusually broad signal from these sources indicates high aerosol content to the operator. Also, vertical flashers may hit a cloud and create a plume. The observation of these sources in the real time display also confirms to the operator that the detector is taking data.

4.1.3 Cloud Monitors

As part of the weather codes, the operator is required to record the amount of cloud cover in the sky. In an attempt to provide an objective quantification of this atmospheric property, a collection of cloud monitors has been installed.

Inside several of the buildings at HiRes-1 are infrared sensors. Since clouds are much warmer than a clear night sky they are clearly visible in the infrared. The cloud monitors cover $30^o \times 30^o$ of sky. Additionally, a scanning cloud monitor is located at HiRes-1. This monitor has a finer resolution (2π *ster* in 2922 bins) and provides a whole sky map of cloud cover four to five times per hour. The use of the cloud monitor data has not yet been implemented.

4.1.4 Steer-able Lasers

There are three steer-able laser systems. Yttrium Argon Gallium (YAG) lasers are used with their frequency tripled to produce $335nm$ light. The first system to be built is located at HiRes-2 and provides the only quantitative calibration of the

atmosphere. A second, almost identical system has been built at HiRes-1. The third system, a roving steer-able laser, is a portable unit which can be taken to any location within our aperture and is the only system which can be viewed by both detectors.

All of our numeric atmospheric calibration is determined using HiRes-2 steer-able laser data recorded by the HiRes-1 detector. This system has been operational during the entire stereo data taking time period. Figure 4.2 shows the range of this laser system. We are able to send a known amount of light into the atmosphere and then view the scattered signal after the beam has traveled up to 25 km out into our aperture and an equally large distance back to our detector. This range allows us to probe most of our detector aperture.

Once per hour, a set of laser shots probes the atmosphere in a pattern indicated by Figure 4.2. In this figure, the laser shots radiate out from HiRes-2 with HiRes-1 located at the origin. A set of vertical laser shots is also taken. For each laser shot, a local probe measures the amount of light sent into the sky. If the atmosphere were completely molecular the signal detected at HiRes-1 would be well predicted. However, consistently less light than expected is seen. The amount of light lost in excess of the amount predicted by a molecular atmosphere is attributed to aerosol content.

4.1.5 Atmospheric Calibration Results

Prior to the summer of 2001, the atmosphere at Dugway was assumed to have aerosol properties described by the 1976 US standard desert atmosphere[39]. However, the atmosphere at Dugway has now been measured to be significantly clearer than this model suggests. The following parameters of the standard desert atmosphere will be explained shortly: $H_S = 1.2km$, $L_M = 12km$ and $AOD = 0.1$. The effect of using this much "dirtier" atmosphere is an increased determined energy.

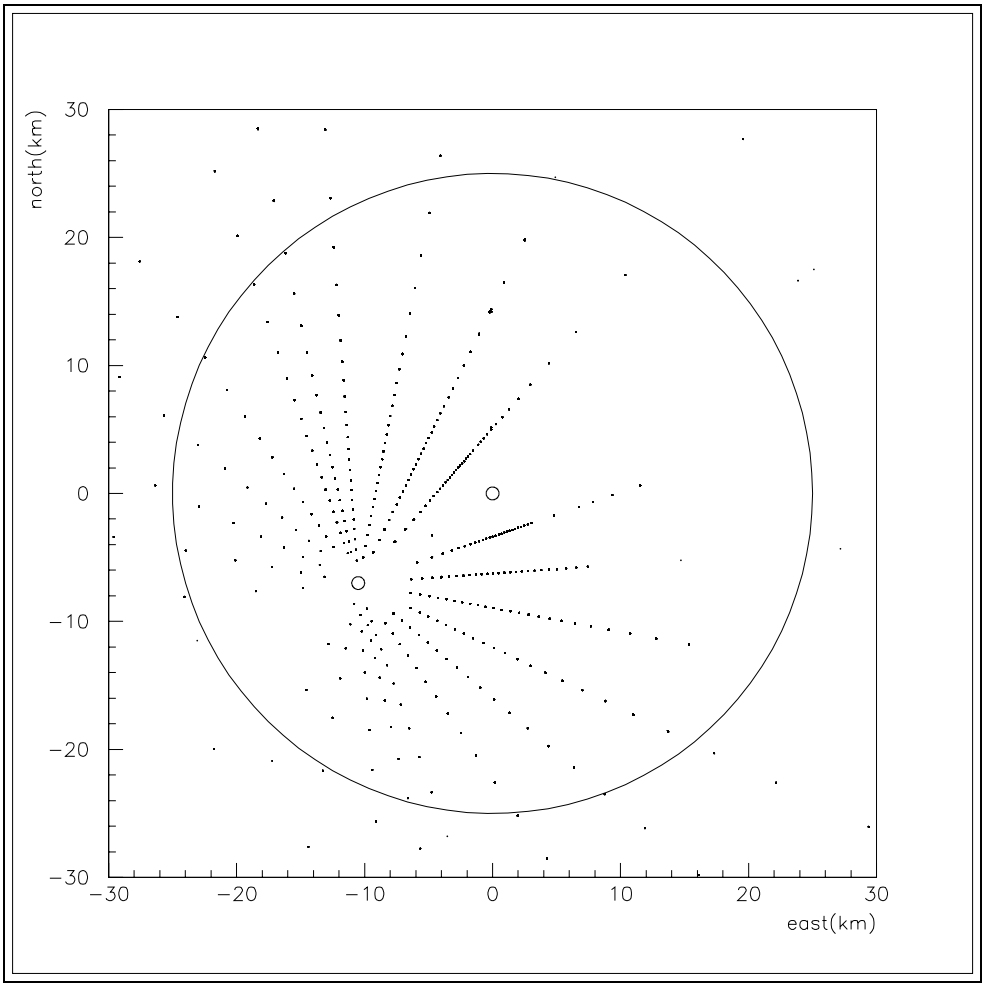

Figure 4.2. Signal of HiRes-2 Steer-able Laser as Viewed from HiRes-1

In this case more light is assumed to have been lost so a larger amount of light is assumed to have been produced in the air shower. For reference, this model will be included in several calculations. Additionally, calculations will be done using an atmosphere with no aerosol content. This purely molecular atmosphere will be shown to provide a lower bound on energy and an upper bound on aperture.

Within the atmosphere there are two main forms of scattering: Rayleigh scattering by air molecules and aerosol scattering by other particulates in the air. Rayleigh scattering is well understood and varies only with emission angle and pressure. The

"1976 US Standard Atmosphere" model is used to describe the pressure change in the atmosphere [39]. On the other hand, the aerosol content of the atmosphere produces a wide range of scattering effects.

The HiRes-2 steer-able laser system has been used to determine the aerosol content of the atmosphere at Dugway. A simplified model for aerosols is used by the HiRes collaboration[18, 19]. In this model, the density of aerosols is assumed to fall off exponentially with a vertical scale height (H_s). Additionally a simple horizontal attenuation length (L_M) is used. This allows for the "net effect" of aerosols to be used. The transmission factor due to aerosols for light leaving height h_1 and arriving at height h_2 after traveling a distance dl is given as

$$T_M = exp\Big[\frac{H_s dl}{(h2-h1)L_M}(e^{-h_1/H_s} - e^{-h2/H_s})\Big]. \tag{4.1}$$

This equation can be simplified to

$$T_M = e^{-AOD/\sin\theta} \tag{4.2}$$

where

$$AOD = \frac{H_S}{L_M} \tag{4.3}$$

where θ is the elevation angle of the observed signal[19].

AOD is determined using equation 4.2 and adjusting T_M so that the amount of "missing" light at the HiRes-1 detector can be explained. The "missing" light is the amount of light lost on the path between the laser system and the HiRes-1 detector that is in excess of the amount expected by Rayleigh (molecular) scattering. Separately, the scale height is determined from the vertical laser shots. Since the atmospheric calibration is performed using the HiRes-1 detector, HiRes-1 must be fully calibrated so that all "missing" light can be attributed to aerosol scattering.

Figures 4.3, 4.4, and 4.5 show the measured distributions of L_M, H_S and AOD.

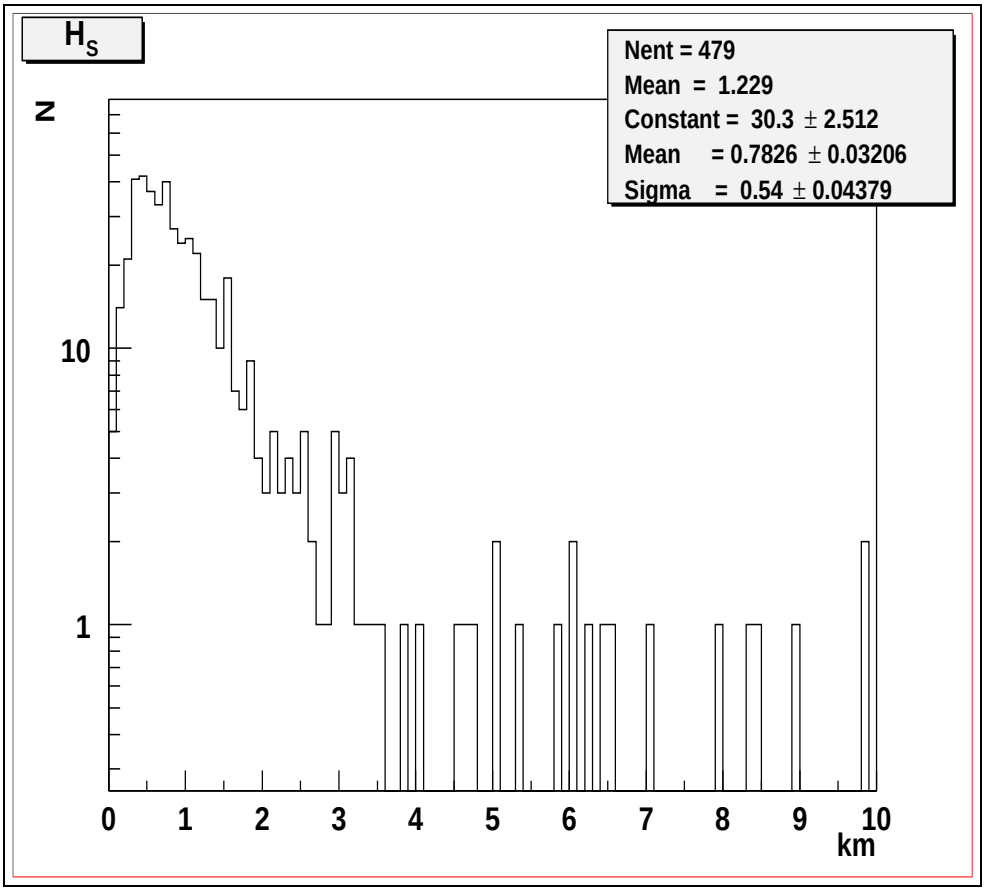

Figure 4.3. Measured Vertical Scale Height H_S of Aerosols

The accepted average value used by the collaboration is

$$AOD = 0.04 + / - 0.02stat / + / - 0.02sys. \tag{4.4}$$

This assumes an average scale height of $H_S = 1.0km$, and an average horizontal attenuation length due to aerosols of $L_M = 25.0km$. Each entry represents the measurement of one hour. These figures, therefore, represent only 479 hours of measurements. At the time of this writing approximately only 50% of the events in the data have hourly atmospheric correction available. It is expected that almost all of the data will have a correction available after the calibration data are reanalyzed.

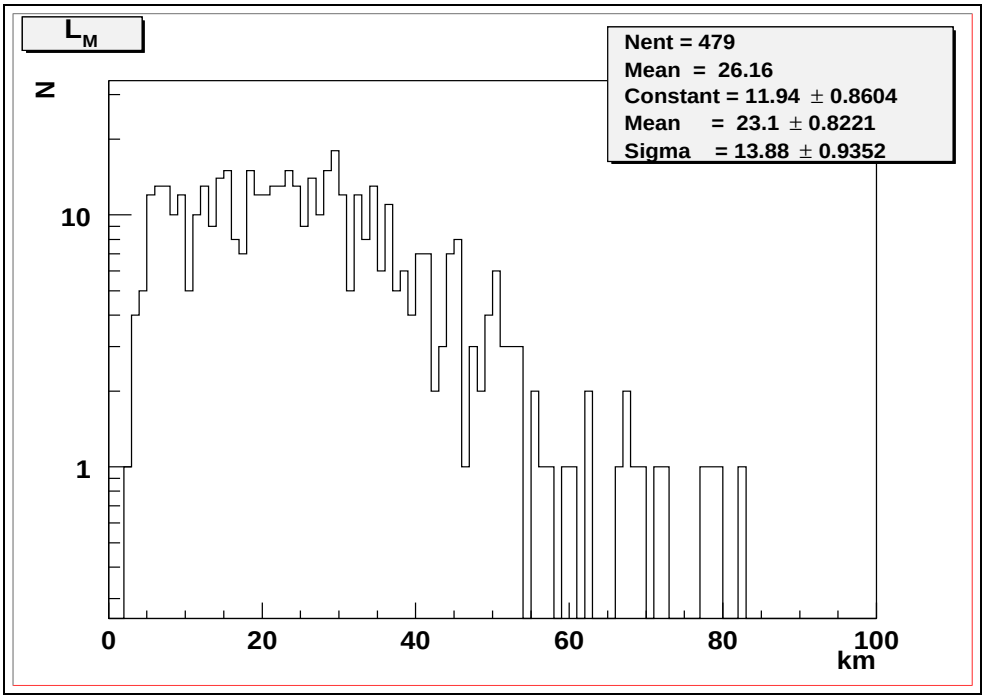

Figure 4.4. Measured Horizontal Attenuation Length L_M of Aerosols

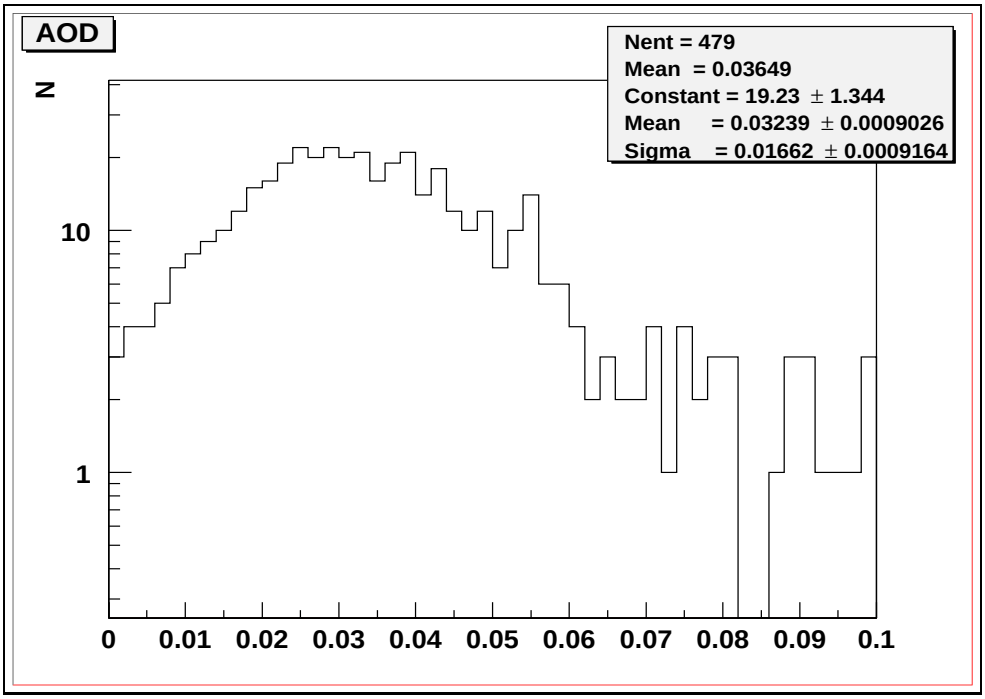

Figure 4.5. Measured Aerosol Optical Depth

4.2 Photomultiplier Calibration

4.2.1 Roving Xenon Flasher: HiRes-1

The PMT clusters have been calibrated using a standard candle provided by a xenon flasher. This flasher's portability allows it to be taken to every mirror in the detector and has provided its affectionate name of "roving xenon flasher" (RXF).

The RXF is attached to a mount in the center of each mirror. From there it illuminates the PMT cluster. Historically, this standard candle has been assumed to deliver 12,000 photons/tube. However, the use of Poisson statistics allows calibration to be made without the standard candle assumption. Instead, the number of photoelectrons (npe) is determined using

$$NPE = (1 + \alpha) \times \frac{\mu_{QDC}^2}{\sigma_{QDC}^2}. \tag{4.5}$$

The parameter α is voltage dependant but has been measured to be 0.4-0.5 for HiRes tubes at normal operating voltage[16]. The terms μ_{QDC} and σ_{QDC} are the mean and standard deviation of the charge signal in each tube after many flasher shots.

By placing filters with known transmission efficiency in front of the roving xenon flasher, several different intensities of light can be measured using this method. Figure 4.6 shows the linearity of the calibration using different filters. Additionally, a data point is shown from the YAG laser calibration system that is discussed in the next section.

4.2.2 HiRes-1 Calibration Laser

Every night, both at the start and end of the run, HiRes-1 performs a relative calibration using a YAG calibration laser system. The calibration laser is centrally located and its light is distributed to all mirrors via optical fibers. A single fiber

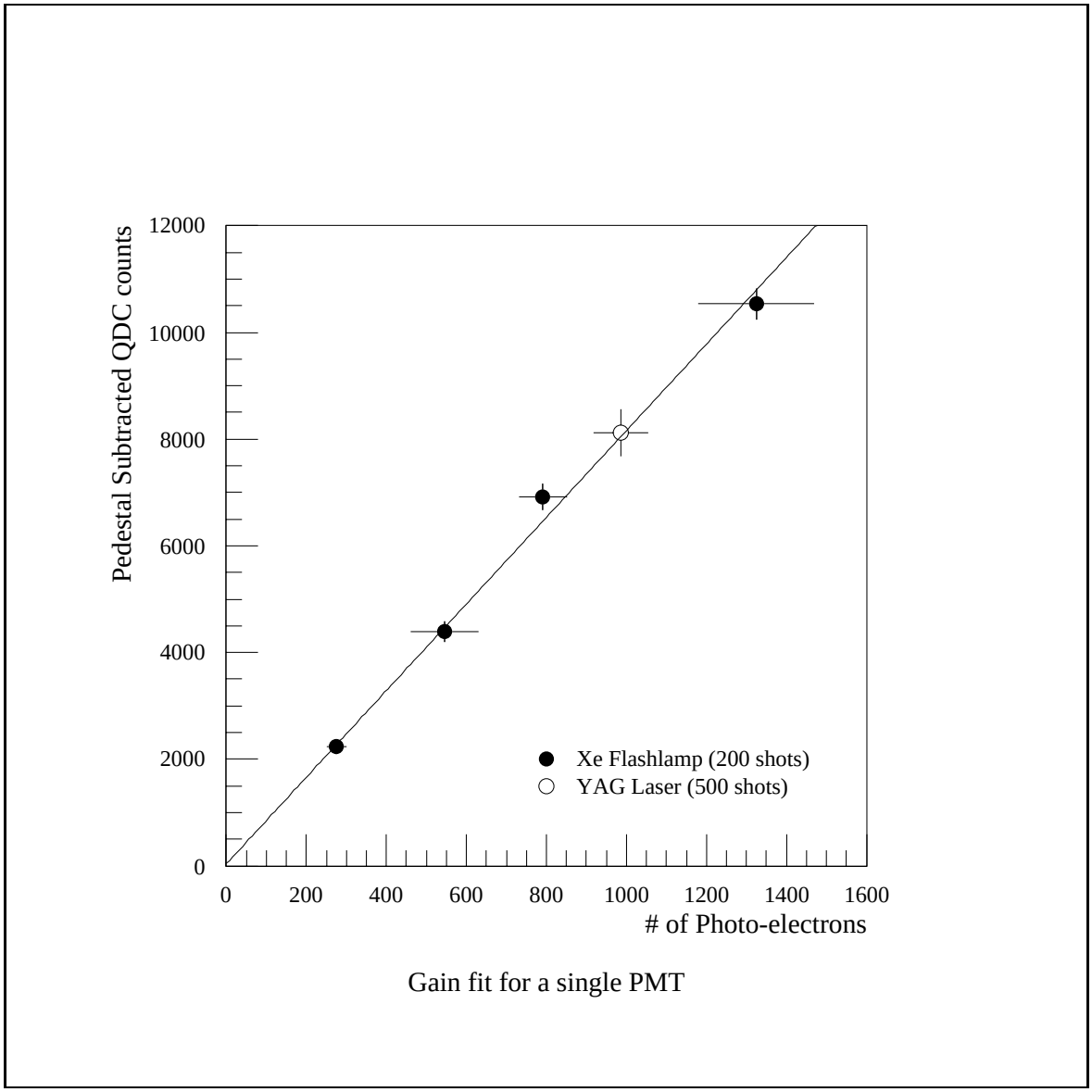

Figure 4.6. QDC Count Versus Calculated NPE

illuminates the cluster from the mirror center. Additionally, two fibers are located on the sides of the PMT cluster and illuminate the cluster by reflection from the mirror.

The mirror fiber is used to test the stability of the gains. Variations in time are tracked using data taken from this fiber. Figure 4.7 shows the relative nightly gain over more than a year. In addition to the relative gain measurements, the RXF data are also shown. RXF data are taken only between runs as it is a time consuming process.

The PMT gain is known to have some temperature dependence. Over the range of ambient outside temperatures in a year, this effect is seen to be on the order of 10%.

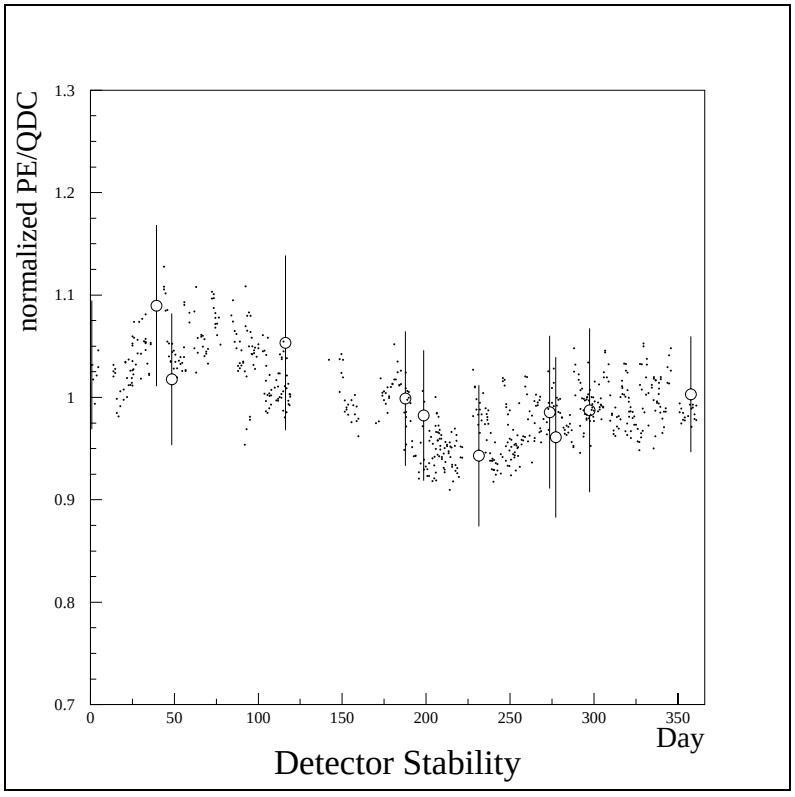

Figure 4.7. Relative Gain Over Time for HiRes-1

4.2.3 Roving Xenon Flasher: HiRes-2

At HiRes-2 the RXF is also used. The electronics at this site allow the gain of each tube to be individually adjusted. The assumptions made in the HiRes-2 calibration are a standard UV transmission through the filter, an average PMT quantum efficiency, and the 12,000 photons per tube standard candle. With these assumptions, the individual tube gains are adjusted so that on average, every tube in the cluster gives the same response of 1 FADC count per photoelectron.

4.2.4 HiRes-2 Calibration Laser

HiRes-2 has also been equipped with a YAG calibration laser[40, 41]. The light is distributed to the mirrors and clusters in the same manner as at HiRes-1. Additionally, using GPS timing, this system is now being allowed to fire at known GPS offsets throughout the nightly run. This will allow tracking of gain variations over the entire course of the night instead of a start to end variation correction. At present, this information has not been incorporated into the data calibration.

4.2.5 Hybrid Photo-Diode

To confirm the accuracy of the roving xenon flasher calibration, new efforts are being made to measure the rxf output using hybrid photo diodes. A similar technique was used by the National Institute for Standards and Testing (NIST) to provide the initial calibration of the phototubes[16].

CHAPTER 5

DATA PROCESSING

5.1 Data Collection

Both detectors produce raw data in raw network packet format. As the network packets are received from the detector they are stored immediately in their network form. Decoding of these packets in real time would reduce the bandwidth of the detector and result in dead time between events.

At HiRes-1 the data are stored with file names yYYYYmMMdDDpPP.TYPE.hal. At HiRes-2 the format is yYYYYmMMdDDpPPP.TYPE.raw. Due to the volume of HiRes-2 data, the .raw files are almost always compressed before transfer or storage. In both cases YYYY is the four digit year, MM the two digit month, DD the two digit day, PP the two (or three at HiRes-2) digit part number and TYPE the type of file. The many file types are outlined in Table 5.1.

The data are collected to a local machine at each of the two sites. From there, they are transported to the individual institutions in a variety of ways. At the University of Utah, this transport occurs most often via the network. Early each morning, a script is initiated via a *cron* job. All data are then transferred from the sites to a local machine.

All data are check-summed before and after compression/transfer. For example, the file *fname.dst* once stored on the HiRes-2 storage machine, camel1, will have a checksum created and stored in *fname.dst.cksum.camel1*. The file will then be compressed into *fname.dst.Z* and the compressed files checksum stored in

Table 5.1. Data Types

Raw Data Types		
HiRes-1		
Type	Frequency	Description
pkt	Nightly (all)	Cosmic Ray Data
cal	Nightly (s&e)	Electronic Calibration
diag	Nightly (s&e)	Electronics Diagnostics
noise-closed	Nightly (s&e)	Sky Noise: Doors Closed
noise-open	Nightly (s&e)	Sky Noise: Doors Open
yagclu-closed	Nightly (s&e)	Yag Laser from Cluster: Doors Closed
yagclu-open	Nightly (s&e)	Yag Laser from Cluster: Doors Open
yagmir-closed	Nightly (s&e)	Yag Laser from Mirror: Doors Closed
yagmir-open	Nightly (s&e)	Yag Laser from Mirror: Doors Open
rxf1	Between Runs	Roving Xenon Flasher Calibration
HiRes-2		
fpkt1	Nightly(all)	Cosmic Ray Data
test	Nightly(between fpkt1)	Pedestal Files
pulser	Nightly(s)	Electronics Diagnostics
yag12	Nightly(s&e)	Yag laser bundles1&2 (mirror fibers)
yag34	Nightly(s)	Yag laser bundle 3&4 (cluster fibers)
rxf	Between Runs	Roving Xenon Flasher Calibration
s=start of night e=end of night all=all night		

fname.dst.Z.cksum.camel1. Once the file has been transferred to the local machine (selena) a checksum file, *fname.dst.Z.cksum.selena*, is created and compared to the checksum from the remote machine. If any checksum fails to match the previous checksum, the transfer is repeated until a match can be obtained.

In order to minimize network traffic in the morning an additional script is initiated via *cron* at the start of each run night. This script continually checks the age and size of all data files taken in a given night. Once a file has stopped changing size for more than one hour, its transfer is initiated and once transferred, its checksum recorded. When the end of night script begins to transfer the night's data it will skip any previously transferred files if the checksums can be confirmed.

All files, after being transferred, are additionally transferred onto one of the local data storage farms and are also written to tape. A final checksum is taken and confirmed for the file on the local storage farm.

5.2 Data Storage

As mentioned previously, all data are transferred to one of the raw data storage machines for easy access. Additionally, a DLT library is available with all raw data.

5.3 Processing Software

5.3.1 DST2K

The HiRes collaboration has a repository for all standard software for use by group members. The name comes from dst, which the data format used by the collaboration and the year 2000, when the library was reorganized by this author. On most machines, this software is located in */hires_soft/dst2k*. The software is compiled and linked by a small collection of scripts known as "build2k". These scripts will be discussed shortly.

5.3.2 UVM2K

In order to track changes in the dst2k library, all source code is controlled by revision control management software. All changes are tracked and users may revert to older versions of code should an error be introduced.

5.3.3 BUILD2K

The purpose of the *build2k* scripts is twofold. First, it is designed to take care of mundane tasks such as finding the proper libraries for linking, locating needed include files and organizing source code.

Second, and more important, is its role in standardization. Once a student or faculty member uses these scripts, his or her work is automatically organized in identical fashion to the dst2k software library. Should the persons software prove useful to the group at large, it will have already been tested to compile and link properly in the dst2k system. Often hours and days have been wasted trying to get software to work properly when the build2k scripts would have solved the problem in a single use.

5.4 Data Processing through Calibration

The full description of how to process raw detector data through calibration (pass1) can be found in Appendix A. Additionally, the Utah method of transferring, storing and processing raw data can be found there.

5.4.1 Pass0

The raw data files, after being transferred back to the University of Utah, are first converted from raw network format to our standard dst format. Conversion of raw network packet data to dst format packet data is accomplished by separate programs for HiRes-1 and HiRes-2.

5.4.2 Pass1

Once the raw network data have been converted to dst format, the next step is calibration of the light signal. From the recorded electronic signals, the number of

photoelectrons is calculated.

The calibration method at the two sites is similar only in that a roving xenon flasher is used as a standard candle to which the detector response is tuned. Section 4.2 contains the details of the two calibration methods.

At HiRes-1, the relative gain and quantum efficiency of each tube are determined relative to the mirror average response. Additionally, the mirror-to-mirror relative transmission of the UV pass filter is determined. With these numbers determined, the final flux of light in a tube can be found as described in the Chapter 4.

At HiRes-2, all phototubes in a given PMT cluster are gain balanced by use of a digital to analog converter amplifier (DAC). The gain is also adjusted so that each photoelectron detected produces one FADC count. The total flux of light arriving in the tube is then found by integrating the number of photoelectrons in time and using the average quantum efficiency.

During some periods of time at HiRes-2 the GPS timing information has been incorrectly synchronized. A great deal of work has been one by John Boyer and Michal Seman of Columbia University to find and correct this problem. This correction is made at the pass 1 level. However, at the time of this writing the GPS corrections have not been used and it is essential that a confirmation of inter-site synchronization be performed. This is accomplished by requiring that both sites see a minimum number of vertical flashers within a data part. This requirement is further discussed in section 5.7.1.

5.4.3 Multiple Mirror Event Matching

Each mirror in our detectors has its trigger information read out independently. Events that trigger multiple mirrors are collected into single events based on their trigger time. This allows the storage of each unique event as a single dst package.

5.4.4 Stereo Event Matching

The final step of the pass1 calibration is the matching of data in time between the two detectors. Synchronization between the two sites is maintained by use of Global Positioning Satellite signals similar to the methods described in the Ph.D thesis of Chris Wilkinson[37]. One method of confirming synchronization is observing the millisecond offset produced by GPS driven laser shots. Additionally, the array of vertical flashers also provides a unique time signature to which any drift in synchronization can be determined as discussed in section 4.1.2.

5.5 Postcalibration Processing

Once the data are calibrated and matched it undergoes several more filters. All processing from this step is carried out using a single program, hr_process, which is described in Appendix B. The steps carried out are the removal of known light sources, noise filtering, track finding/plane fitting, and event reconstruction. I will first discuss the details of each processing step. The effects of the cuts made are presented in the following section.

5.5.1 Known Source Extraction: HiRes-2 Steer-able Laser

The HiRes2 steer-able laser system is essential in our atmospheric calibration. Since the autumn of 2000, this laser system has fired exclusively at 111, 361, 511, and 761 ms after the GPS second. Starting in September 2000, all events that fall within +1.0/-0.2 ms of these offsets are removed without further checking. This results in a minimal amount of dead time.

For data acquired prior to the date of GPS triggering, log files created by the laser system are used to remove events from this known source. By using the location of the laser system and the zenith and azimuth at which the laser was

fired, the expected detector signal can be predicted. Any event that falls within a very large (2.5 ms) window of the recorded laser firing time is compared to this predicted signal. This large time window is used due to a drift in the system clock of the laser control computer. If an event is within the time window and matches the predicted geometry and time development, it is removed from the data stream.

Since this laser system is co-located with the HiRes-2 detector, it generates a large amount of noise at the HiRes-2 site. If a laser shot is not identified it will be removed later by the pass2 noise filter. Since GPS triggering was enabled, the noise is vetoed at HiRes-2.

In the end, the most practical method of removing this laser is to allow the noise filter to remove most of these events. After the processing is complete the laser removal described above is run to catch any laser shots that evaded the noise cuts.

5.5.2 Known Source Extraction: HiRes-1 Steer-able Laser

The HiRes-1 steer-able laser is extracted from the data based solely on its GPS timestamp. This laser system fires at 222, 472, 722, and 972 ms after the GPS second. All events that fall within +1.0/-0.2 ms of these millisecond offsets are removed without further checking.

Since the HiRes-1 steer-able laser system is co-located with the HiRes-1 detector, these laser shots are vetoed by HiRes-1 and are not viewed in stereo.

5.5.3 Known Source Extraction: Roving Steer-able Laser

The roving steer-able laser system can be taken to any location within our aperture, allowing systematic checks of alignment and detector response. This laser system fires at 000, 250, 500, and 750 ms after the GPS second. All events that fall within +1.0/-0.2 ms of these offsets are removed without further checking.

5.5.4 Known Source Extraction: Flashers

The removal of events associated with the intersite and vertical flasher light sources is accomplished by using the constant geometry of these systems. Each of the ten vertical flashers and the intersite flasher has a unique geometric and time development. Any event that develops in space and time along the known path of one of these flashers is flagged and removed from the data set. Synchronization of the GPS clocks at the two sites is confirmed when these flashers are seen in stereo.

5.5.5 Pass2 - Noise Filter

The noise filter used in this analysis is the Rayleigh filter used in previous theses[22, 21, 20]. This filter compares the signal in the detector to a signal that could be created by a two-dimensional random walk. For each triggered tube that has an adjacent triggered tube, a unit step is taken. This unit step is in the direction of tube triggering order. The sum of the n unit steps creates our Rayleigh vector $\vec{r}$. The probability that a net displacement of $|\vec{r}| > R$ could be produced by a random walk is given by

$$P(r > R) = e^{-R^2/n} \tag{5.1}$$

The pass2 cut requires that the probability that a random walk could have produced the event in question be less than 0.01 (1%) at both sites or the event is removed as noise. Additionally, if no adjacent tube pairs can be found, events are rejected by this cut. Additionally the orientation of vector $\vec{r}$ determines if the track is upward or downward going. If the vector is within 20^o of horizontal the event is categorized as horizontal. Any events created by the known sources of light that were not removed in preceding steps, especially the vertical and intersite flashers, are removed here. All events that are not determined to be downward going at both sites are removed from the processing stream.

An excellent and complete description of the Rayleigh filter can be found in the PhD thesis of Chihwa Song (his section 5.1.3)[22]. Figure 5.1 is taken from that description.

5.5.6 Pass3 - Plane Fitting

The plane fit is accomplished by an amplitude-weighted fit. The fit performs a minimization of the following χ^2.

$$\chi^2 = \sum_i^N \frac{(\hat{n} \cdot \hat{n}_i) S_i}{\sigma_i^2} \tag{5.2}$$

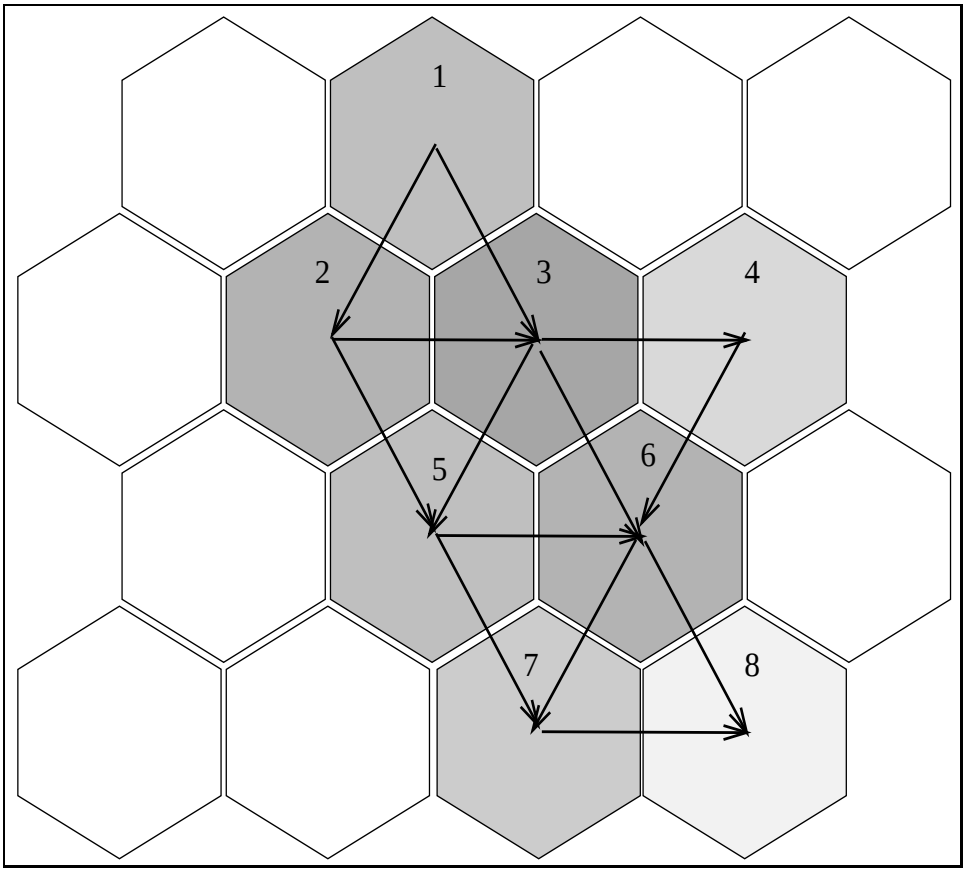

Figure 5.1. Schematic of the Rayleigh Filter[22]

The terms in equation 5.2 are the number of triggered tubes N, the plane normal being found $\hat{n}$, the pointing direction of each tube $\hat{n}_i$, the signal (pe) in each tube S_i and the error in each tubes signal σ_i, where

$$\sigma_i^2 = \frac{S_i + S_{noise}}{S_i}. \tag{5.3}$$

The resolution of the plane fit procedure can be found in Chapter 7.

5.5.7 Pass4 - Event Reconstruction - Geometry Reconstruction

The current method to determine the geometry is to find the intersection of the two shower detector planes ($\hat{n}_{HiRes-1} \times \hat{n}_{HiRes-2}$). More detailed geometric information is required for an anisotropy study, but the geometric resolution obtained in this manner is sufficient for energy resolution. A more detailed geometric fit which uses both geometry and timing information is being developed by Jose Bellido of Adelaide for his anisotropy studies[14].

5.5.8 Pass4 - Event Reconstruction - Binning

Once the geometry of the air shower is determined, the flux of light arriving at the detector as a function of angle is determined by the formula

$$\Phi_i = \frac{N_{pe_i}}{A_{eff}} = N_{pe_i} \times C_{aeff} \tag{5.4}$$

$$C_{aeff} = \frac{1}{A_{eff}} \tag{5.5}$$

where N_{pe_i} is the number of photo-electrons detected in the PMT, and E_{eff} is the effective area of the tube. The correction factor, C_{aeff} of the PMT is determined by the ray trace table which accounts for the obscuration of the PMT cluster, the optical spot size, the geometrical arrangement of PMTs, the tube response and the distance of the optical spots path from the center of the PMT. This procedure is

implemented via a ray-trace table that averages the result of millions of incoming photons. The ray-tracing table has all of the information of the photon-by-photon ray-trace used by the Monte Carlo. However, due to the averaging it lacks non-symmetric effects such as coma. These effects are averaged on a tube-by-tube basis.

The amount of light that enters a tube depends on two factors. First, the position of the tube in the cluster determines the amount of obscuration from the PMT cluster. Additionally, the optical spot size grows due to aberrations as the tube position gets further from the cluster center.

In addition to tube position, the distance of the track from the tube center must be accounted for. The PMT response is a function of the position on the tube face as shown in Figure 5.2. The amount of light lost in the cracks between phototubes also depends on this distance. Tubes that are quite far from the shower plane detect only a small portion of the light arriving at the detector and therefore have a larger correction in determining the light flux.

Iterative calculations also allow for additional width in the shower due to the lateral distribution of particles. The shower width depends on both the initial energy of the primary as well as the age of the shower being viewed according to equation 6.7. For each triggered tube that is within one degree of the shower track, a sample measurement of the incoming light flux is made.

5.5.9 Pass4 - Event Reconstruction - Profile Fitting

Once the flux of light arriving at the detector has been determined, an "inverse Monte Carlo" fit is done. This fit determines the parameters of an air shower that most likely could have produced the detected signal. This fit is accomplished by minimizing the following χ^2.

$$\chi^2 = \sum_i^N \frac{(\Phi_i - \Phi_i^{mc})^2}{\sigma_i^2} \tag{5.6}$$

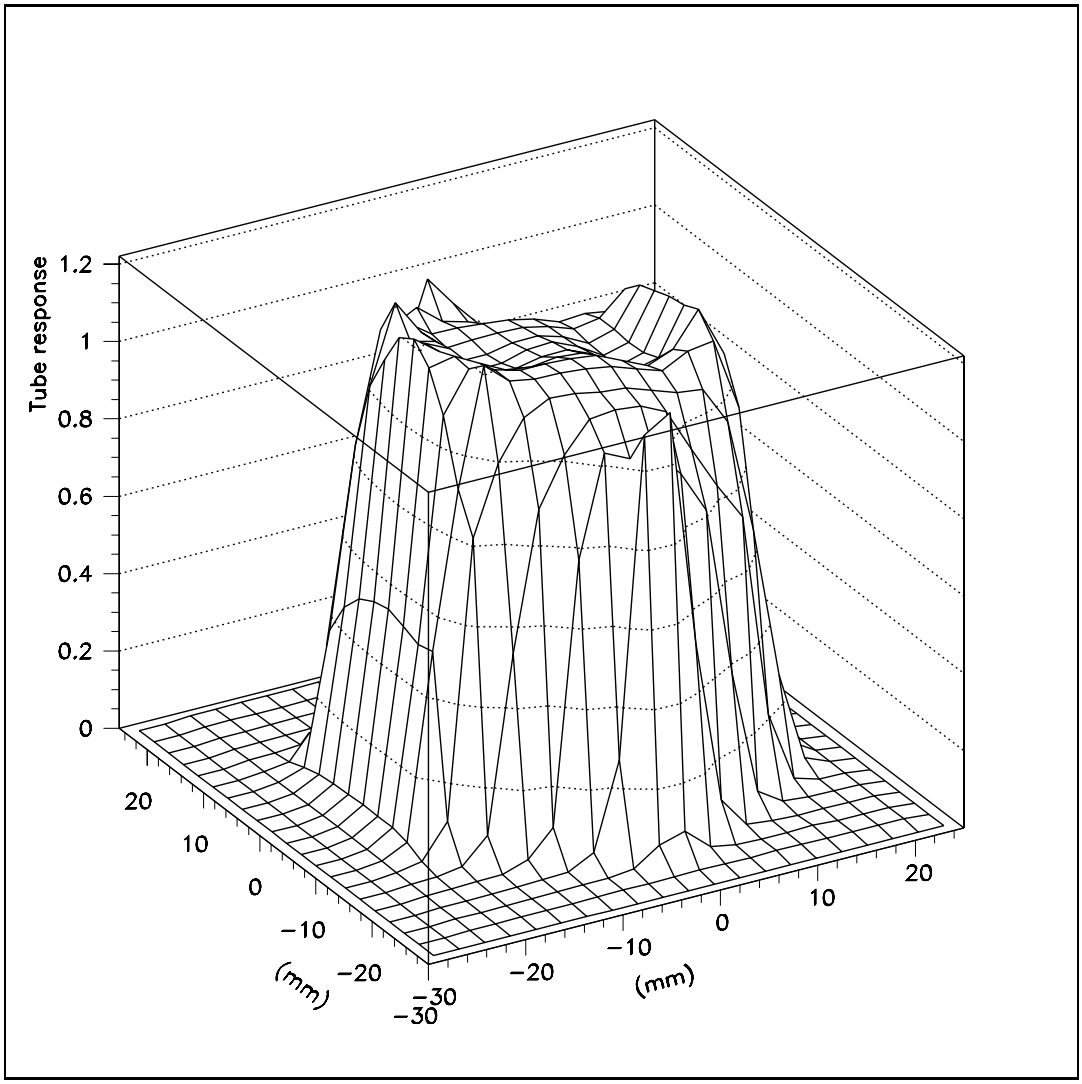

Figure 5.2. Response of a PMT as a Function of Position on the PMT Surface

where Φ_i is the measured flux from a given direction and Φ_i^{mc} is the Monte Carlo predicted signal for the same direction. The σ^2 term is the error in the measured flux and is found using

$$\sigma_i = \sqrt{N_{pe_i}^2 \sigma_{C_{aeff_i}}^2 + \sigma_{N_{pe_i}}^2 C_{aeff_i}^2} \tag{5.7}$$

with

$$\sigma_{N_{pe_i}} = \sqrt{N_{pe_i}^+ 40^2}. \tag{5.8}$$

40 is the measured sky noise. Most of the time, the sky noise and Poisson fluctuations dominate the error. However, when the signal becomes very large the first term in equation 5.7 dominates. The error in the correction factor, C_{aeff}, while small, is nonzero and is best determined by varying the geometry of the air shower slightly using the Monte Carlo and determining the fluctuations in the correction factor. However, the Monte Carlo does not simulate real errors in the locations of the PMTs, and an additional constant amount of uncertainty may be need to properly simulate real data.

The Monte Carlo predicted signal used in equation 5.6 is obtained by creating Gaisser-Hillas showers using the reconstructed geometry. The parameters which are varied are the energy and X_{max}. The details of the Gaisser-Hillas shower driver can be found in section 6.2.1.

Figures 5.3 to 5.10 depict two typical events. The first event has a reconstructed energy of 1.36 EeV and the second event 7.74 EeV. In Figure 5.3 the flux of light at HiRes-1 in units of $NPE/deg/m^2$ is shown with circles and the flux of light at HiRes-2 is shown with triangles. The fitted line shows the Monte Carlo predicted flux for an event with $E_{12} = 1.36$ EeV and $X_{max} = 600\ g/cm^2$. Figure 5.4 shows the same information but in this case the χ^2 fits were done independently for each site. In this case, $E_1 = 1.90$ EeV and $E_2 = 1.34$ EeV. Additionally, different X_{max}

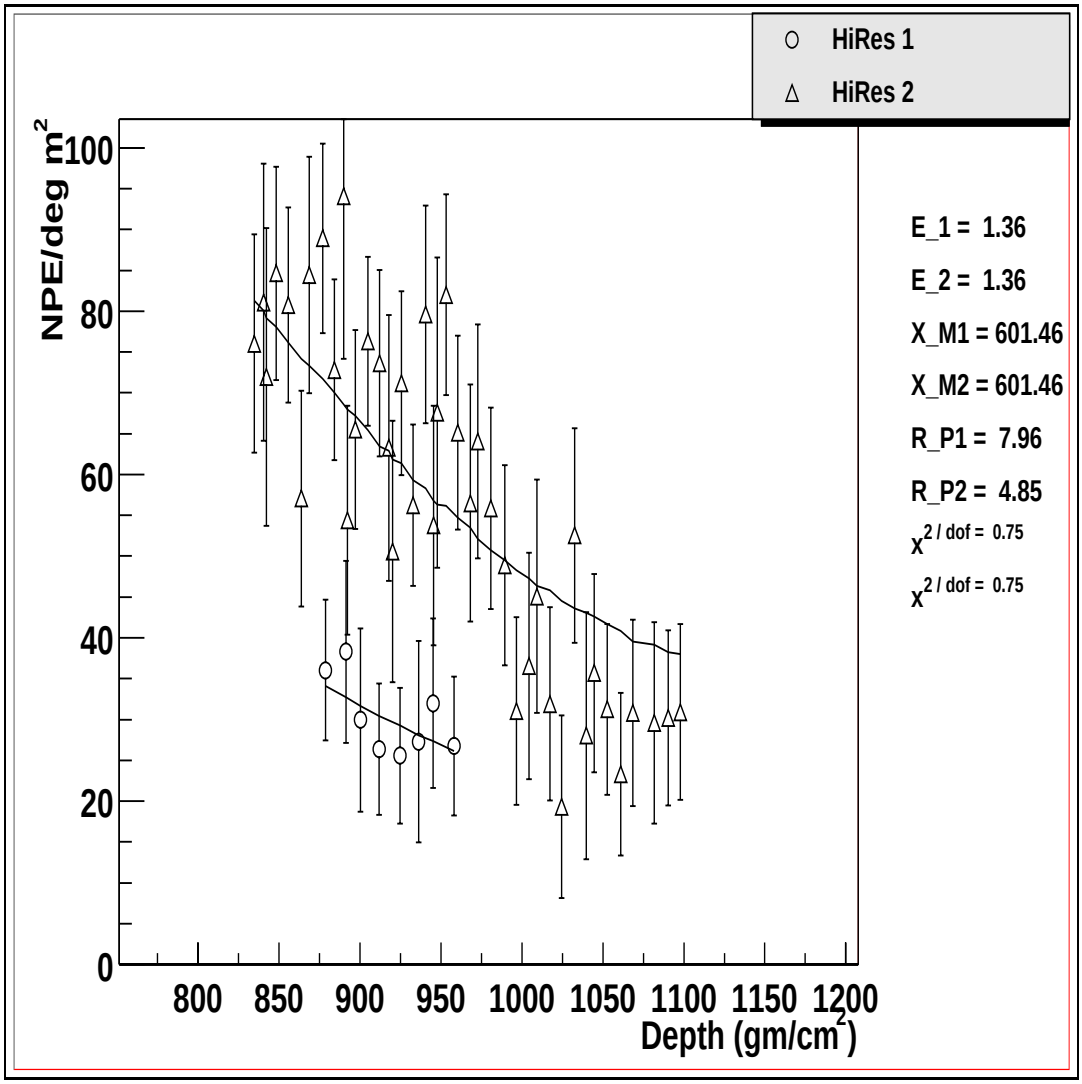

Figure 5.3. Typical HiRes Event #1 - Profile with Combined Site χ^2

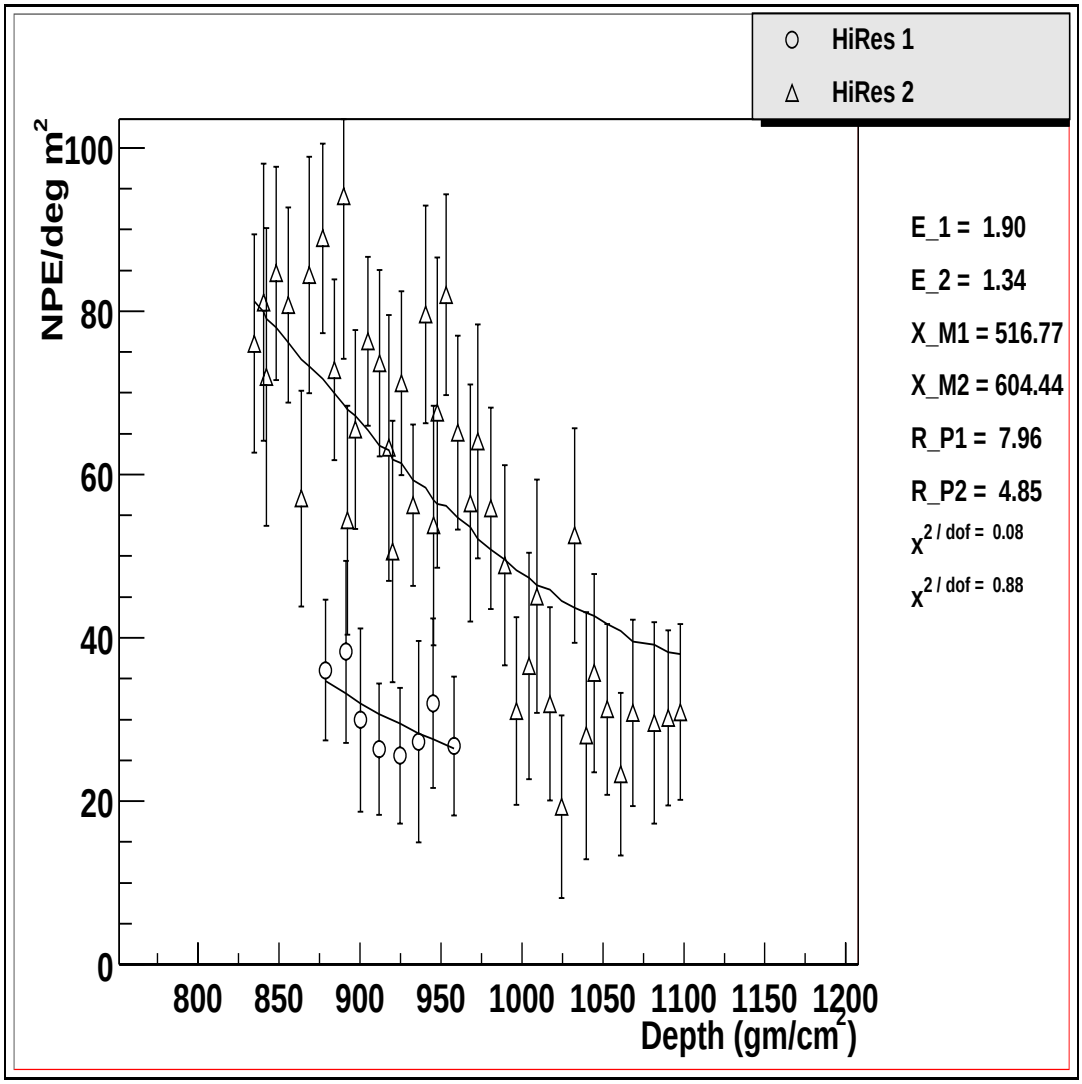

Figure 5.4. Typical HiRes Event #1 - Profile with Individual Site χ^2

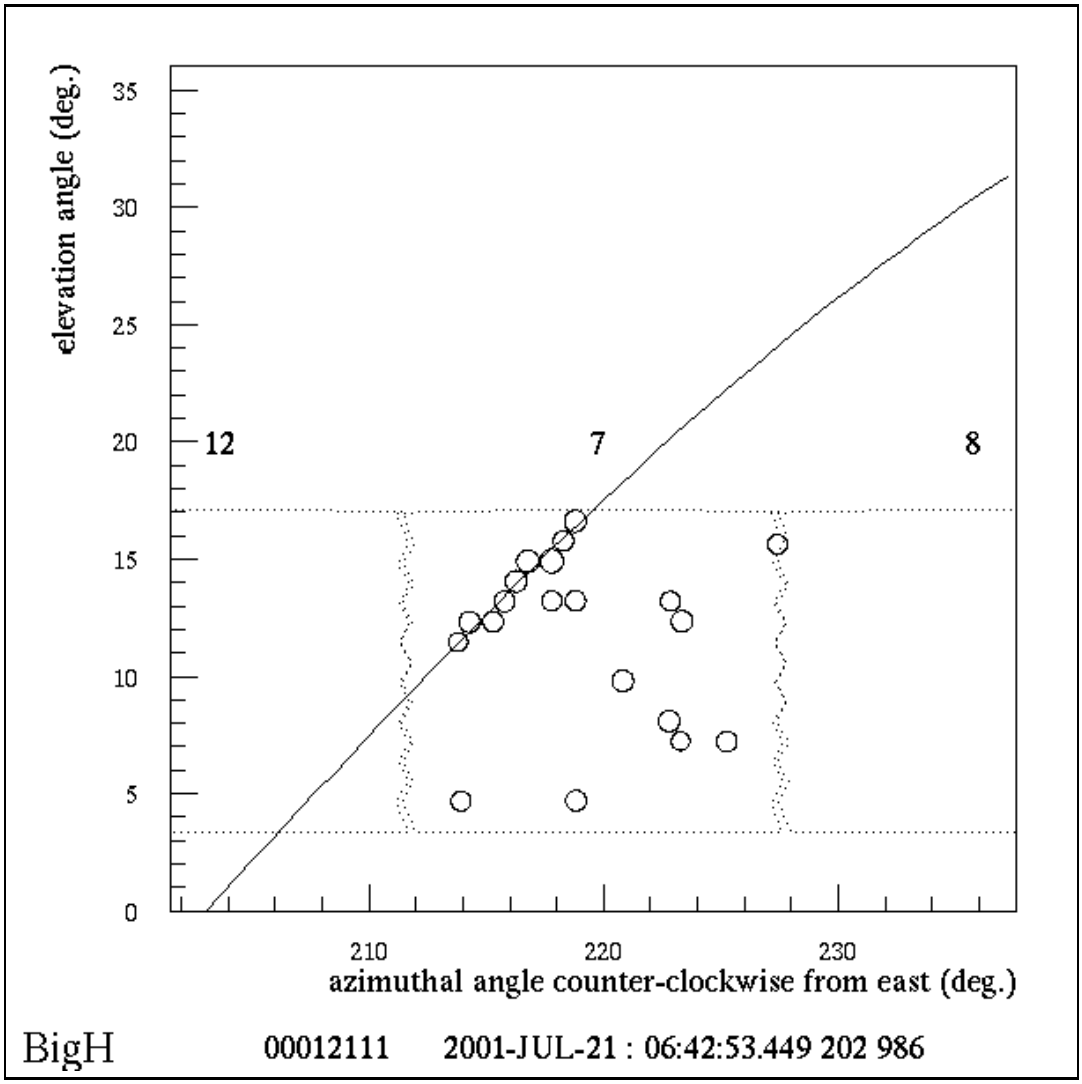

Figure 5.5. Typical HiRes Event #1 - HiRes-1 Event Display 2

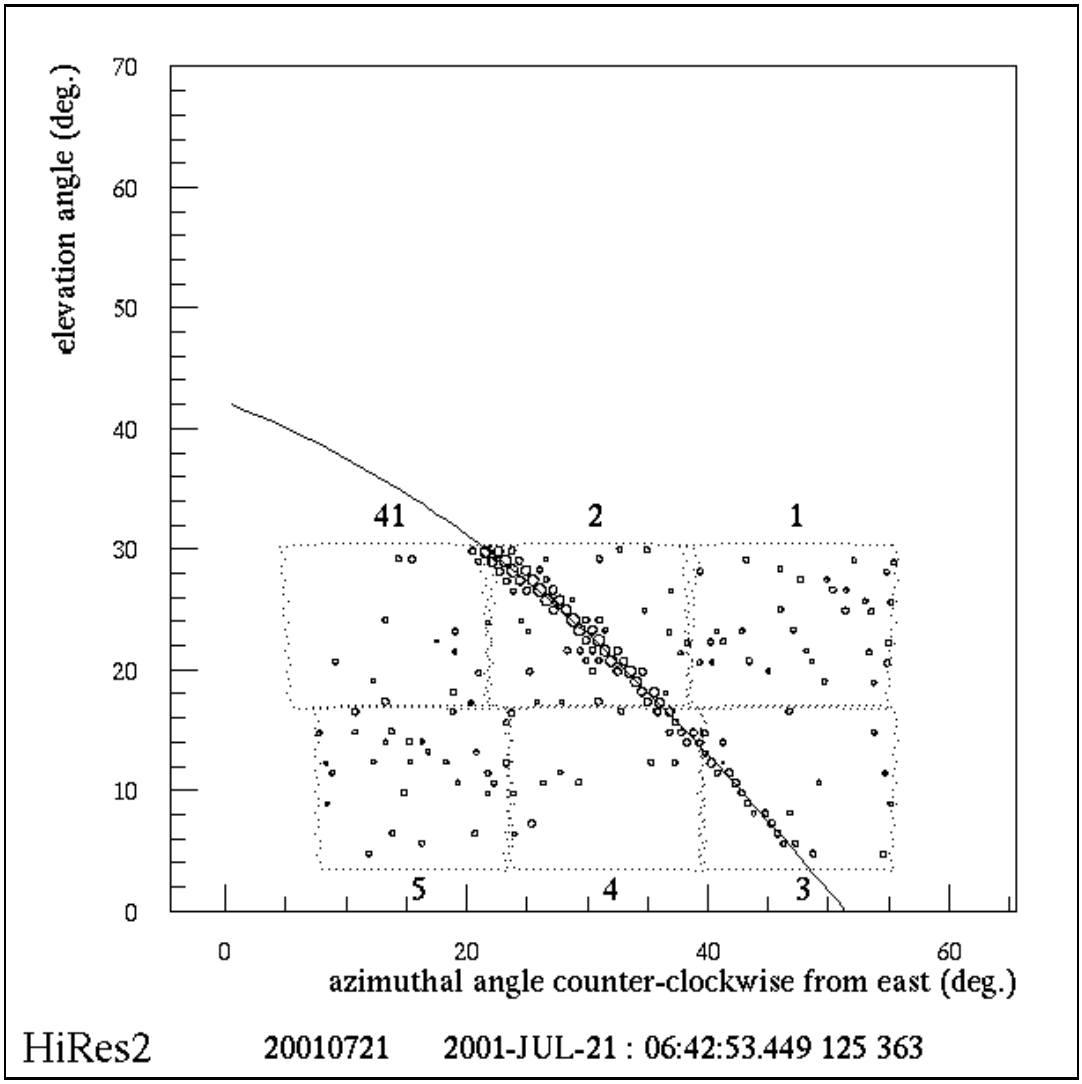

Figure 5.6. Typical HiRes Event #1 - HiRes-2 Event Display 2

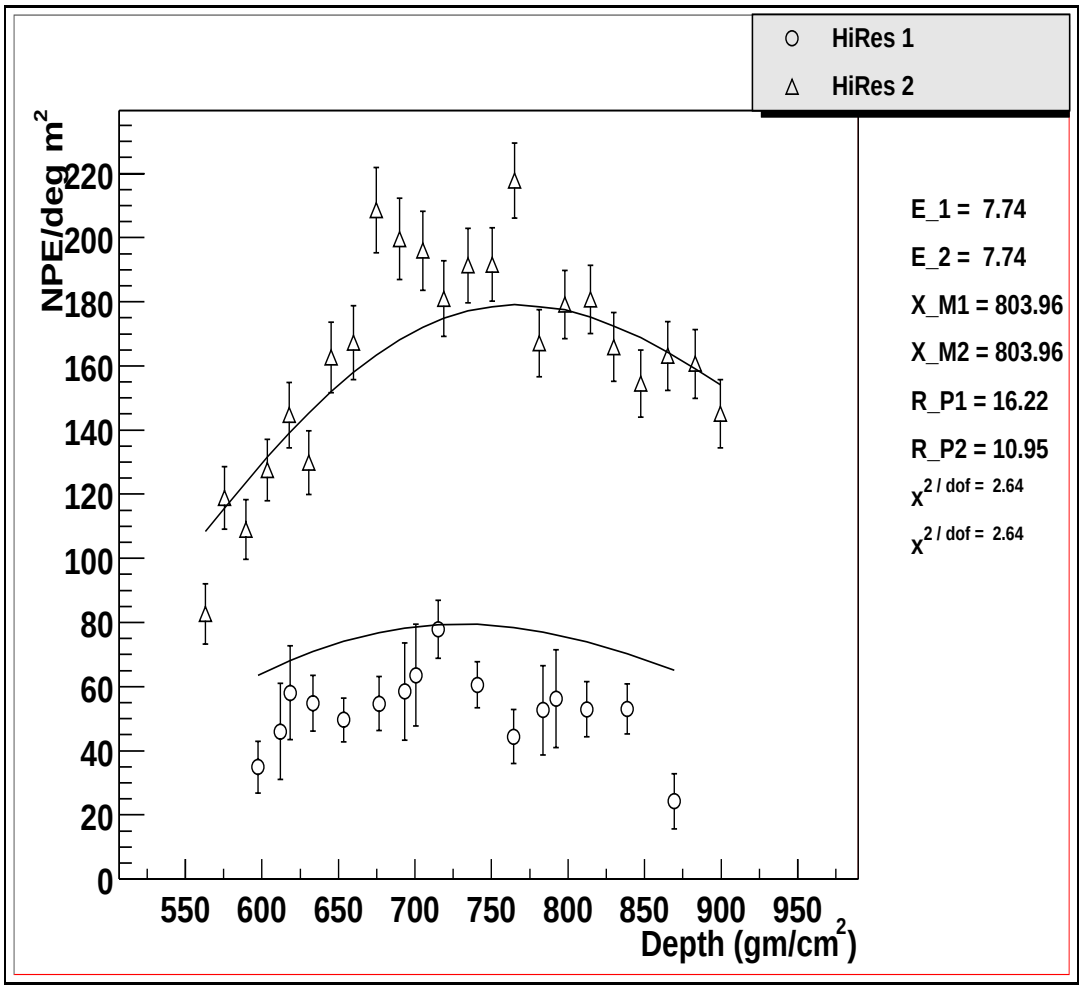

Figure 5.7. Typical HiRes Event #2 - Profile with Combined Site χ^2

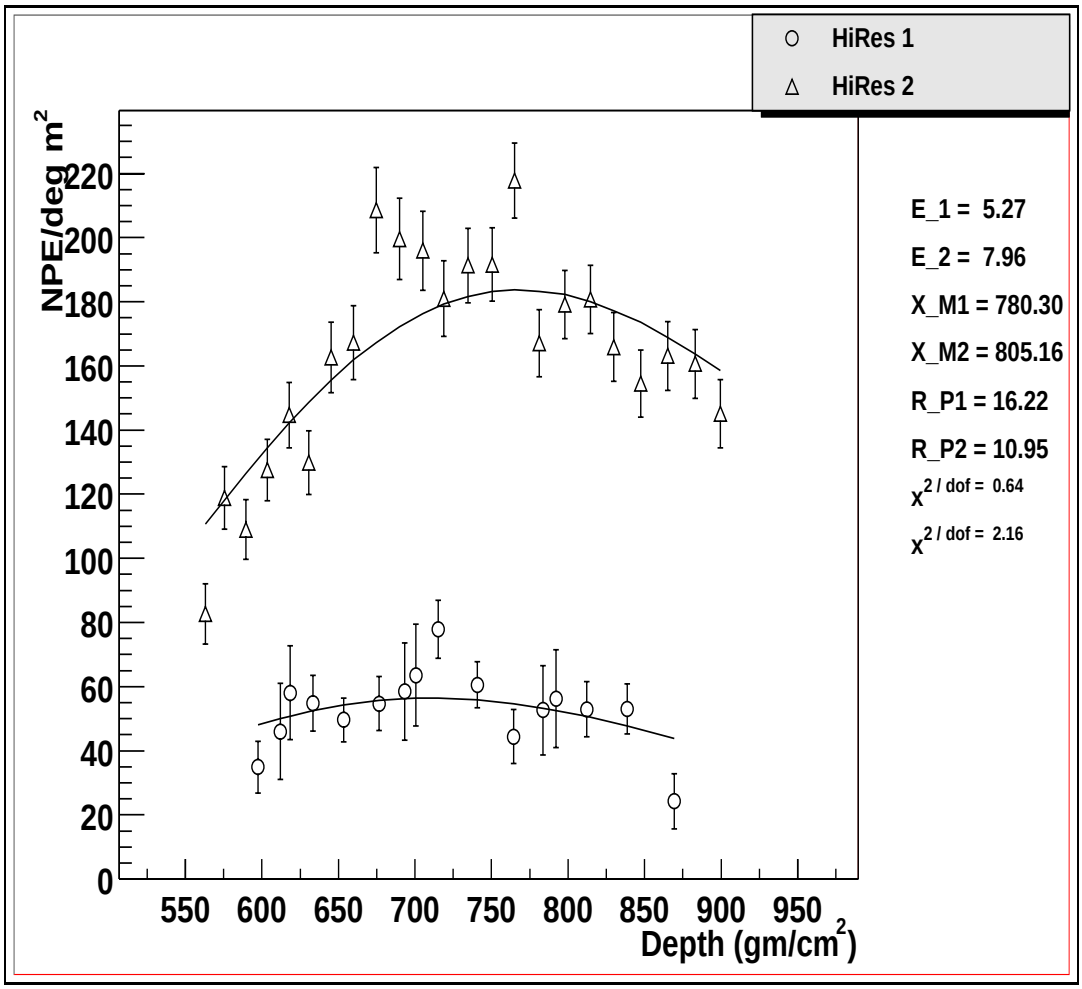

Figure 5.8. Typical HiRes Event #2 - Profile with Individual Site χ^2

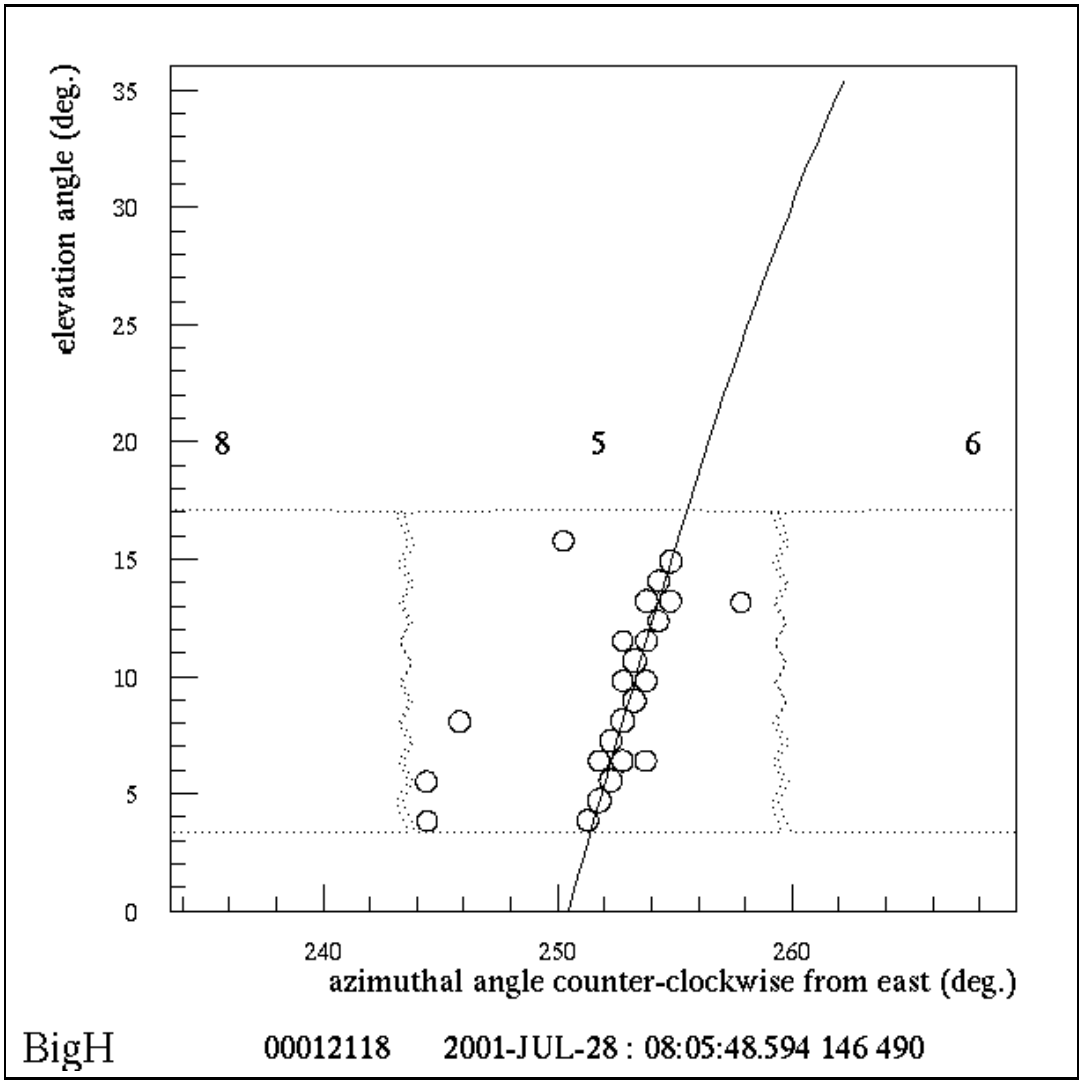

Figure 5.9. Typical HiRes Event #2 - HiRes-1 Event Display 2

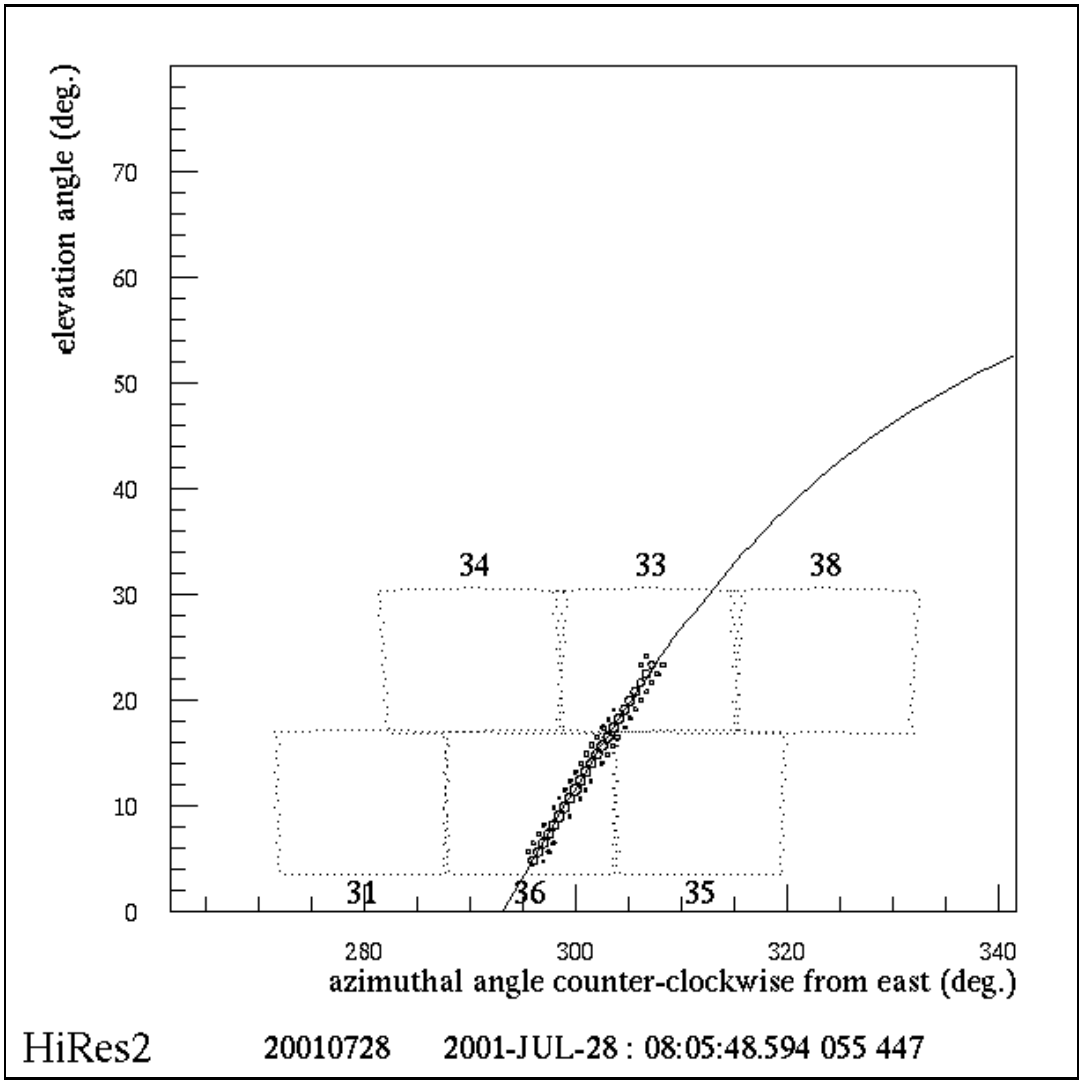

Figure 5.10. Typical HiRes Event #2 - HiRes-2 Event Display 2

values are determined for each site. Figures 5.5 and 5.6 are event displays of this event. Figures 5.7 to 5.10 repeat the same information for the second event.

5.6 Effects of Processing Cuts

Table 5.2 shows the number of events at each processing stage. Almost 10% of all triggers are identified as calibration light sources. 90% of the events in the data set are filtered as either not downward going or noise.

5.6.1 Steer-able Laser Systems

The GPS millisecond cuts provide a total of

$$T_{dead} = 3_{systems} \times 4_{offsets}/sec \times 1.2ms_{deadtime} = 14.4ms/sec \tag{5.9}$$

or 1.44 % dead time. Prior to the use of GPS times to exclude laser events, the noise and upward filter of pass2 is used to remove most of the HiRes-2 steer-able laser events. In stereo mode, the laser cannot produce a non-noise, downward going track in both sites. Finally, after the noise filter, any remaining lasers are removed using the laser systems recorded geometries and firing times as described in section 5.5.1. Prior to the autumn of 2001, the HiRes-1 and roving steer-able lasers were non existent and unused respectively during the stereo data period.

5.6.2 Vertical Flashers

The probability of real cosmic ray events being identified as flashers and removed from the data set can be determined using the Monte Carlo. Figure 5.11 shows that less than 2.5% of all real cosmic ray events will be tagged as flasher events and removed from the data set. The probability that a real cosmic ray event will be

Table 5.2. Number of Stereo Events at Each Processing Stage

Stage	N_{cut}	$N_{remaining}$	% Cut	% of Total
Calibrated	0	10,544,498	0%	0%
HiRes-2 SLS	411,787	10,132,711	3.9%	3.9%
HiRes-1 SLS	219,267	9,913,444	2.2%	2.1%
Roving SLS	21,312	9,892,132	0.2%	0.2%
Flashers	236,491	9,855,641	2.4%	2.2%
Noise Filter	9,638,223	17,418	97.8%	91.4%
Plane Fit/Geo	15,850	1,568	91.0%	$< 0.1\%$
$N_{flasher}$	111	1,457	15.2%	$< 0.1\%$
$E > 10^{18}$ eV	480	977	40.8%	$< 0.1\%$
χ^2	56	921	5.5%	$< 0.1\%$

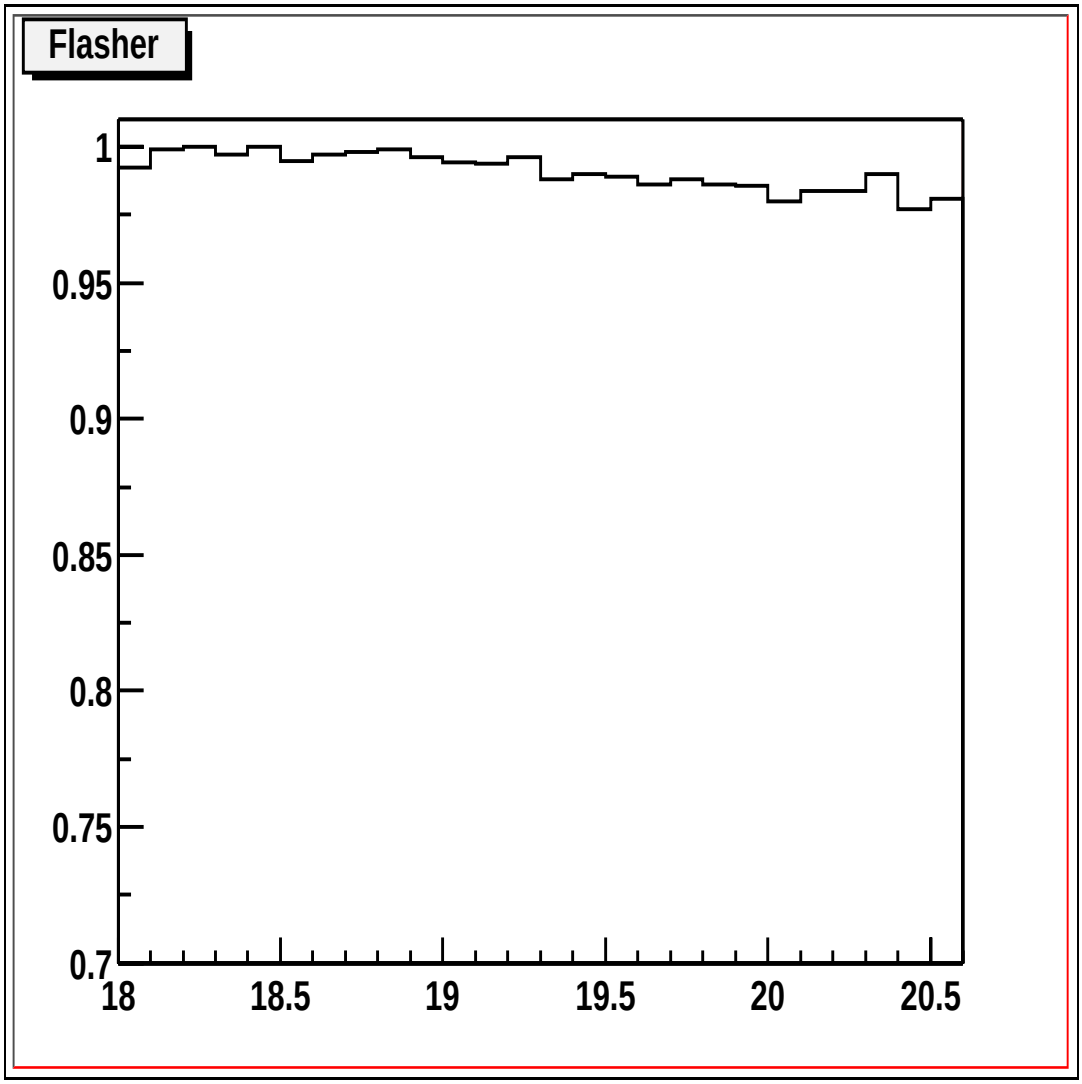

Figure 5.11. Percent of Monte Carlo Events Remaining after Flashers Removed.

misidentified increases slightly with energy. Visual confirmation that these sources are in fact extracted has been carried out.

5.6.3 Noise Filter: Pass2

The most effective noise filter in this analysis is the requirement that both detectors trigger. The rate of coincident random noise and random noise coincident with a cosmic ray or calibration trigger is significantly lower than the rate of random noise at the individual sites. The noise filter removes all events for which the signal at both sites cannot be confirmed to be non-noise.

There are three ways in which an event can be cut by the pass2 noise filter. First, if the triggered tubes at a site contain no set of adjacent tubes the random walk calculation cannot occur. In this case the sites signal is given an error code of -1 and the event will be removed from the data stream.

The second cut is the actual noise filter. If it is determined that there is greater than a 1% probability that a random walk could have produced the signal at either site, then the event is removed from the processing stream. The stored value for this cut is the absolute value of the logarithm of the probability. This value is given the name P_{log}. The requirement that the probability be less than 1% is equivalent to $P_{log} >= 2.0$ since $|log(0.01)| = 2$. A lower probability results in a higher P_{log} value.

The third case in which an event is removed by the noise filter is the orientation of its Rayleigh vector. As mentioned the events are categorized to be upward, horizontal or downward going. Any event that is determined to be horizontal or upward going at either site is removed. Events that are not cut by the noise filter are assumed to be downward going cosmic ray candidates.

Figures 5.12, 5.13, 5.14, and 5.15 show the distributions of the P_{log} values for all real data events that were subjected to the noise filter. In the latter two cases

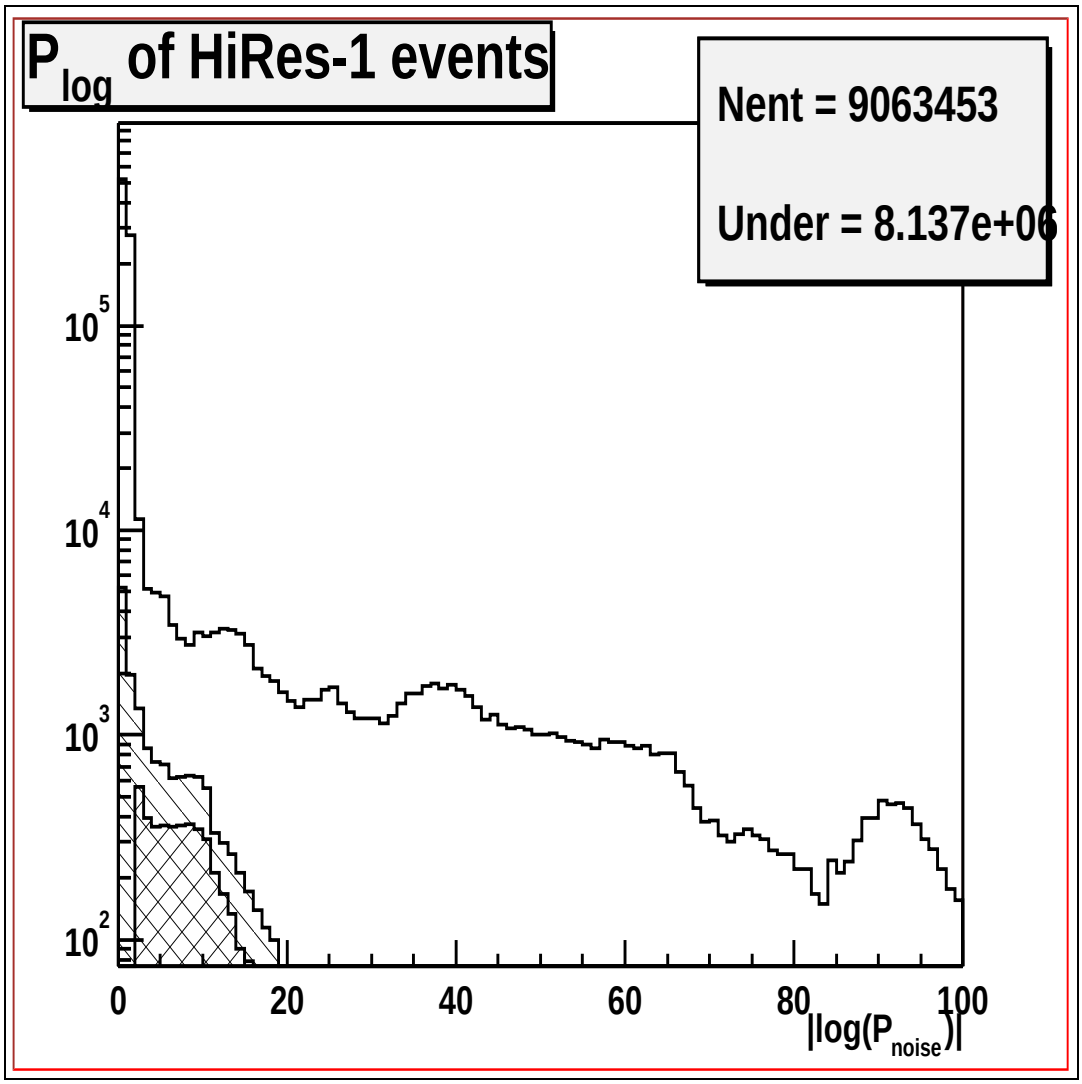

Figure 5.12. P_{log} Values at HiRes-1 in Real Data

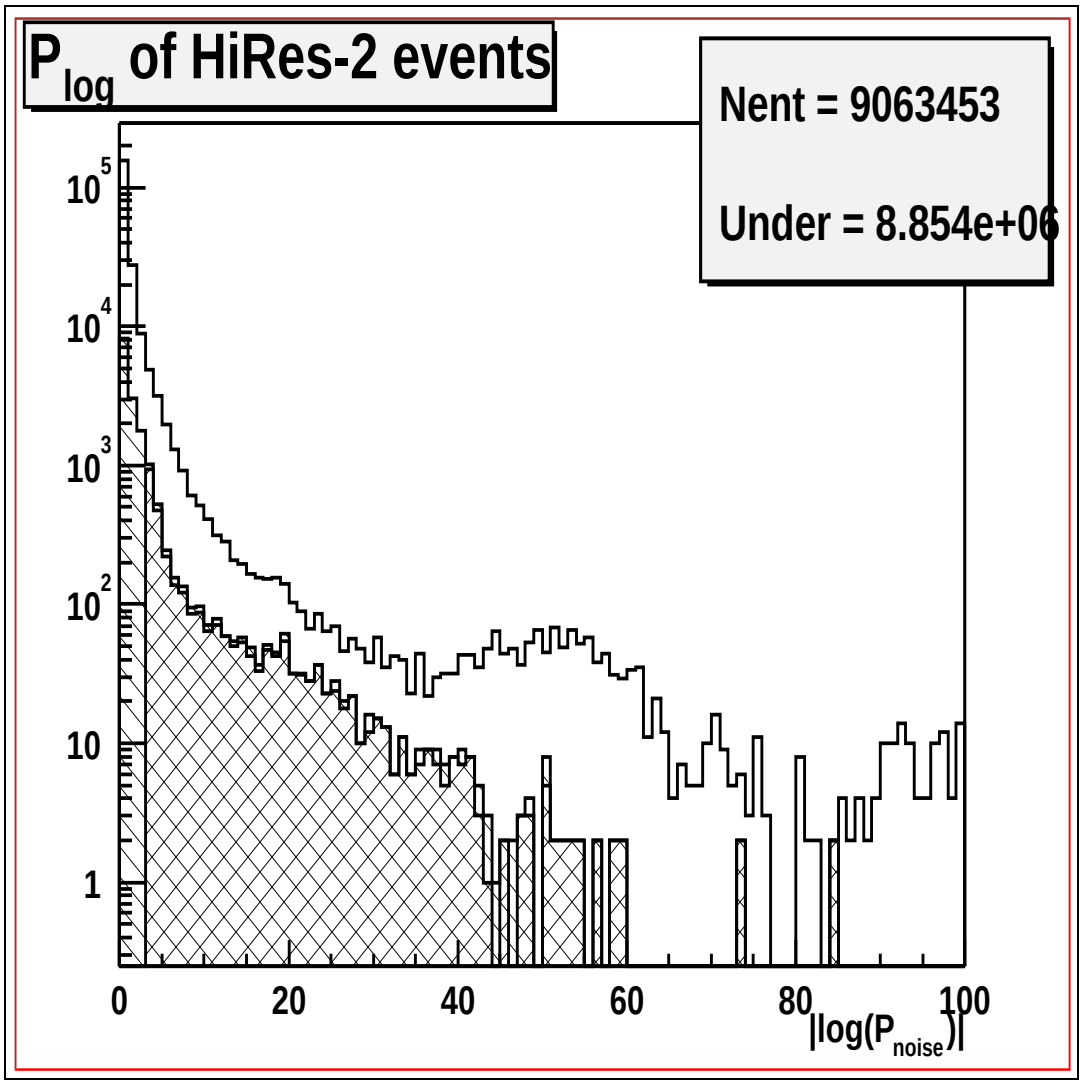

Figure 5.13. P_{log} Values at HiRes-2 in Real Data

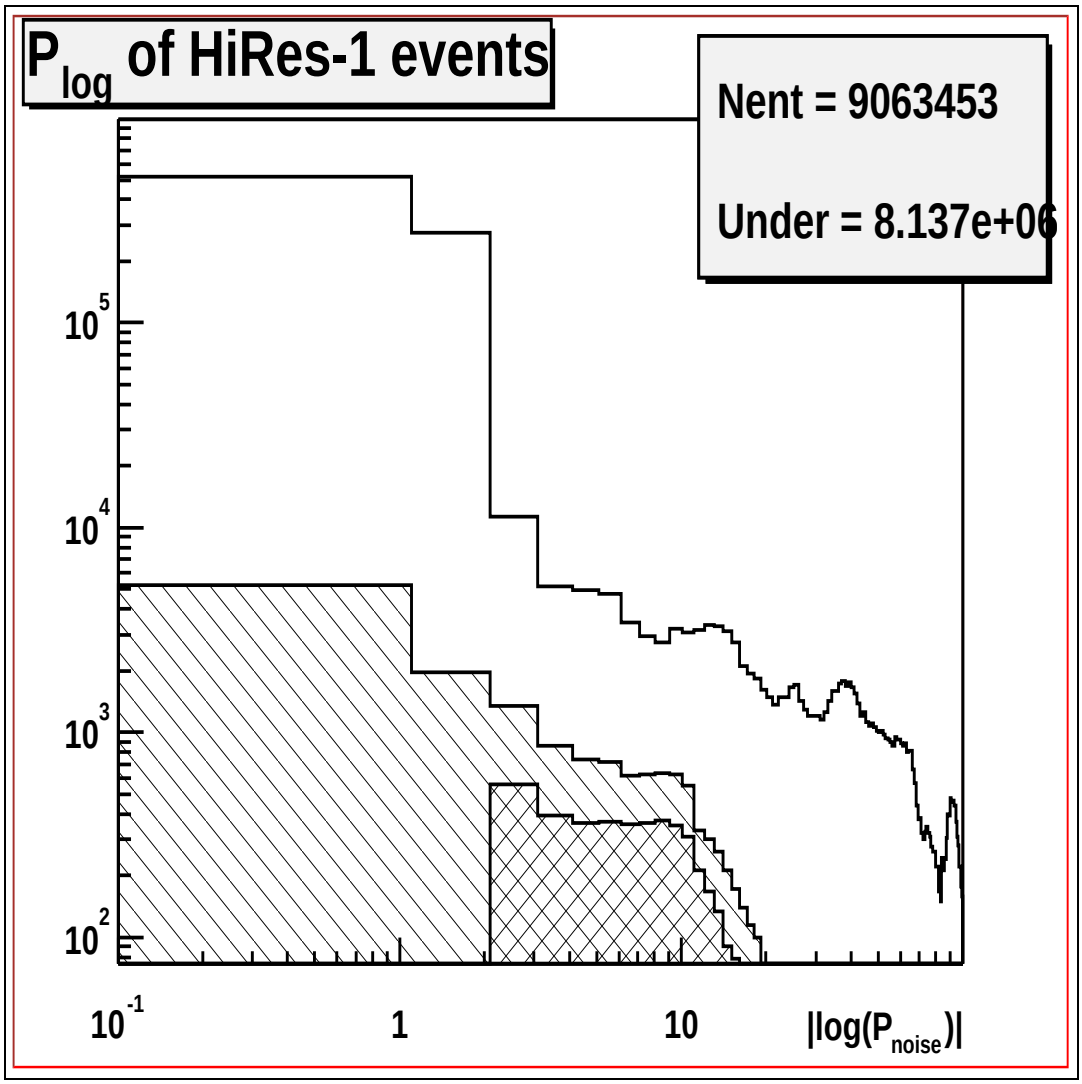

Figure 5.14. P_{log} Values at HiRes-1 in Real Data

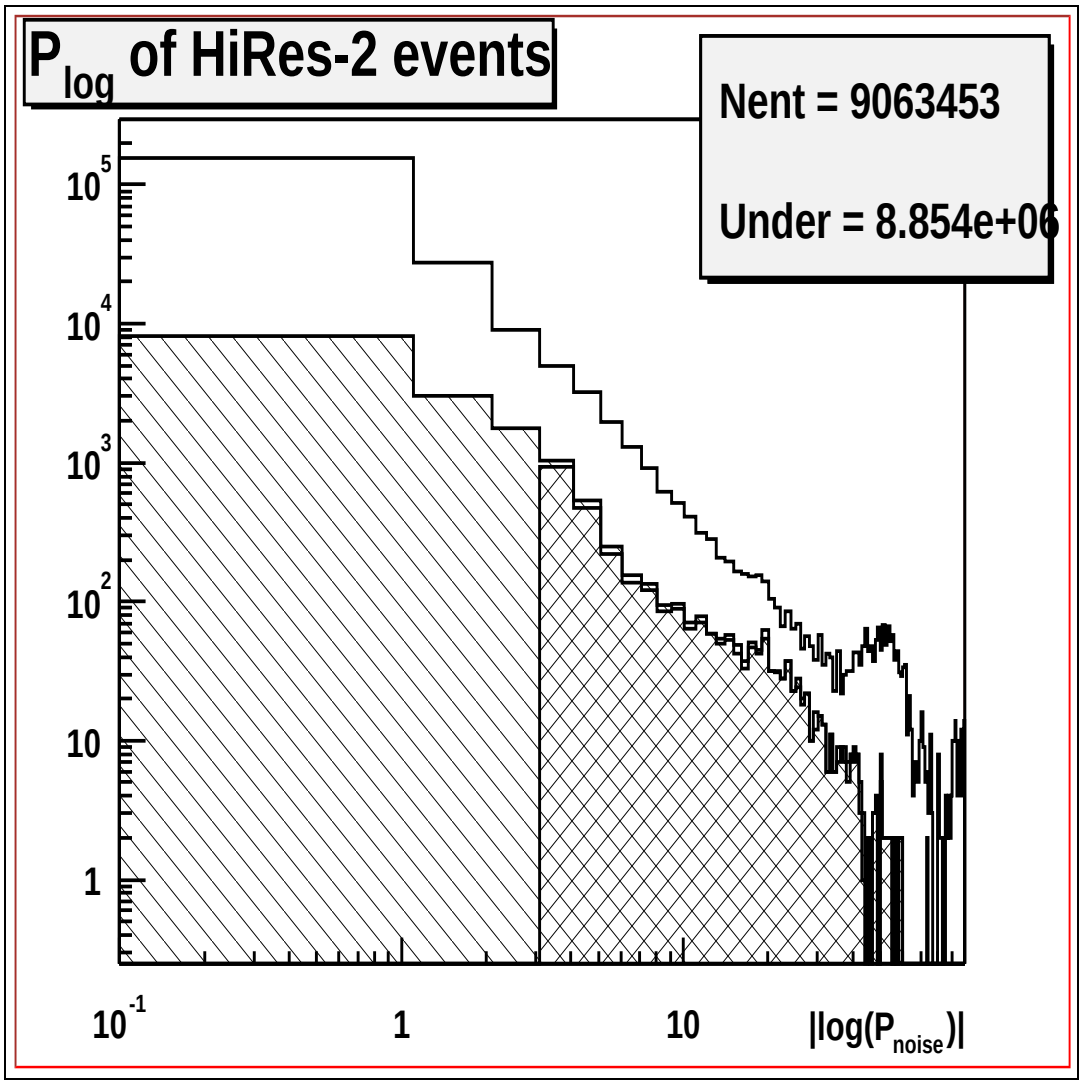

Figure 5.15. P_{log} Values at HiRes-2 in Real Data

the x-axis is set to log scale so that the very strong peak at low P_{log} values can be seen. All events at the far left of these figures have a high probability of being noise. The underflow bin contains the number of events that contained no pairs of adjacent triggered tubes. The middle histogram in each case shows the P_{log} values of all events that meet the requirement of being downward going at both sites. The lowest histogram shows the P_{log} distribution of all events which are not cut by the noise filter.

Moving from the upper to middle histograms in these figures a large number of events with very large P_{log} values are removed. These events are upward going and horizontal tracks created by our calibration systems. Especially in the case of horizontal laser tracks, which may extend over many mirrors, the probability that random noise could produce a calibration light sources signal is extremely low. This results in a very large P_{log} value. These events are cut at this stage since they are not candidates for a cosmic ray signal.

Figures 5.16, 5.17, 5.18, and 5.19 show the same distributions except only Monte Carlo generated cosmic ray events are included. Examination of the lowest histogram on Figures 5.14 and 5.18 shows that the P_{log} distribution for real events HiRes-1 is quite similar to the distribution one would expect for real cosmic rays. The P_{log} value in this case starts at the required value of 2 and slowly falls off extending to approximately 20. Figures 5.15 and 5.19 show the same agreement for HiRes-2 events. In this case, the P_{log} values extend to 50. HiRes-2 events can have much high P_{log} values because of the two ring configuration. A vertical air shower, for example, can produce a track approximately twice as long at HiRes-2 than at HiRes-1.

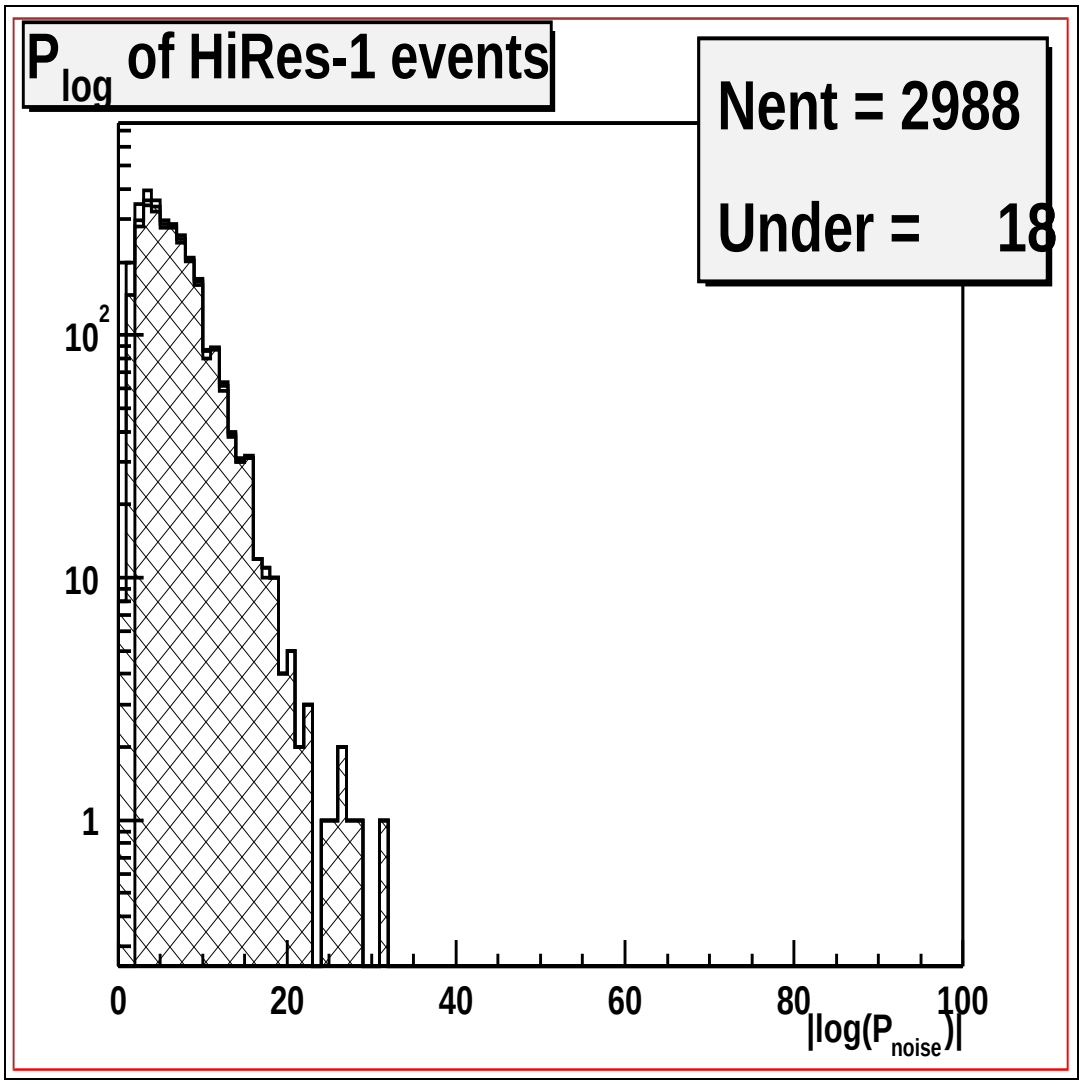

Figure 5.16. P_{log} Values at HiRes-1 for Monte Carlo Cosmic Ray Events

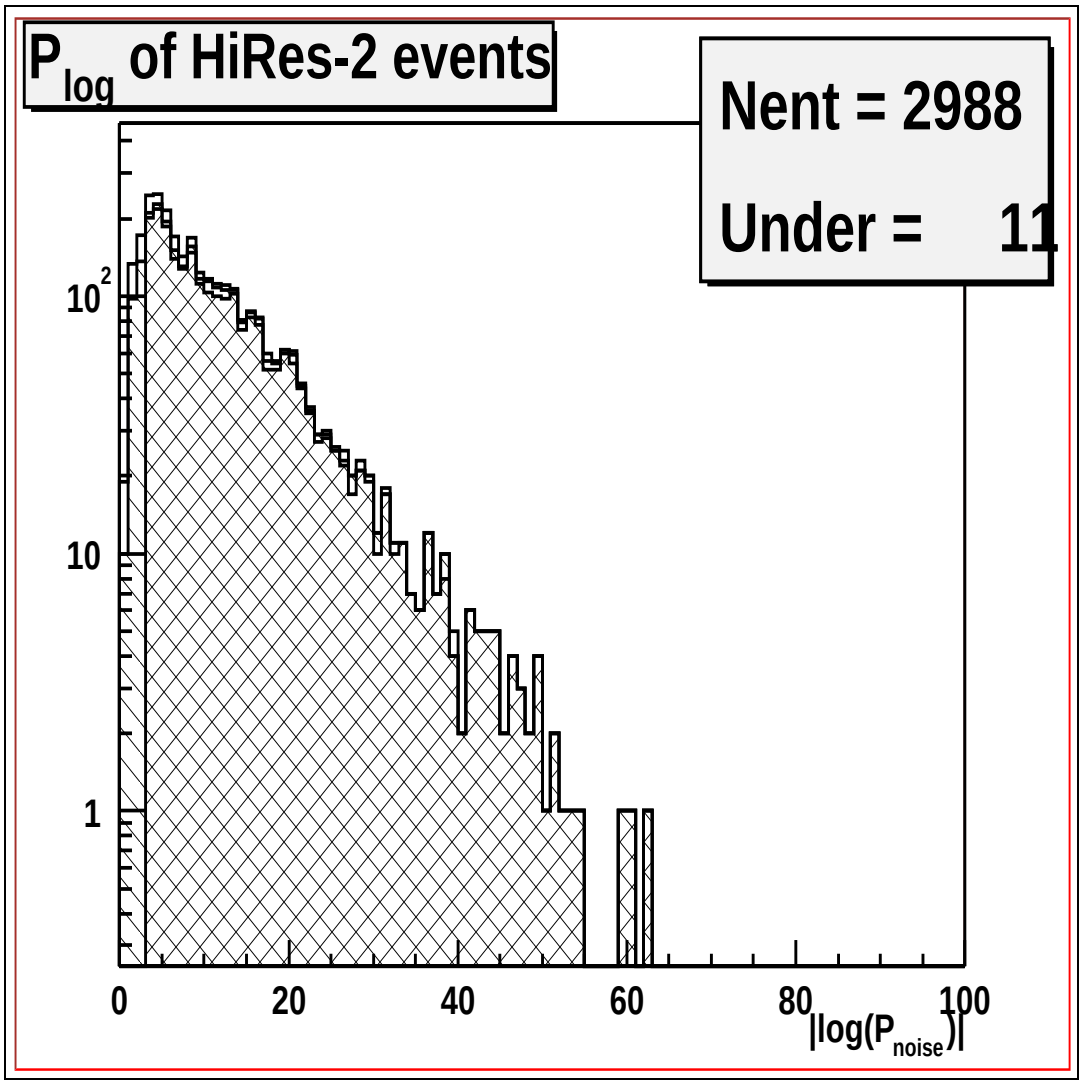

Figure 5.17. P_{log} Values at HiRes-2 for Monte Carlo Cosmic Ray Events

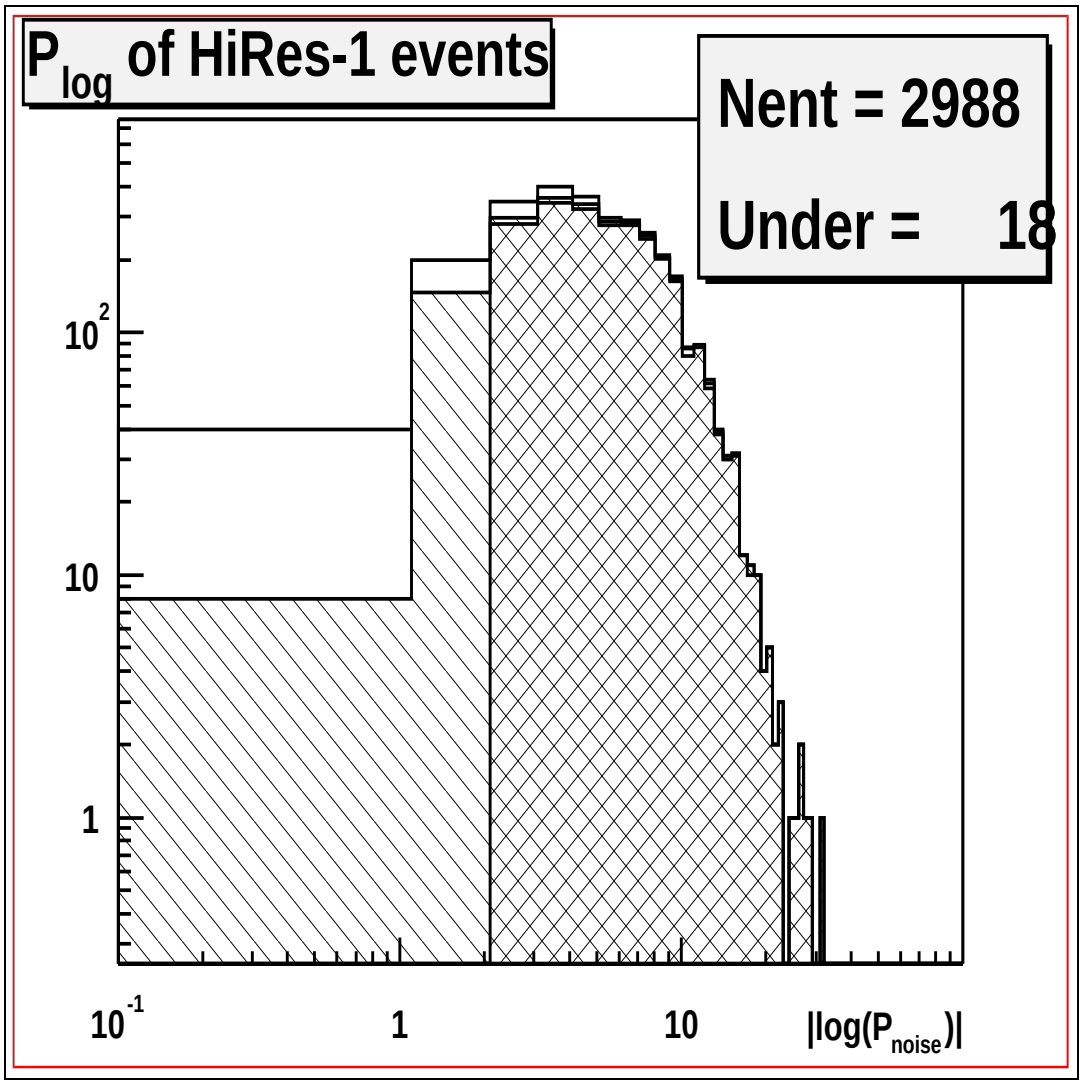

Figure 5.18. P_{log} Values at HiRes-1 for Monte Carlo Cosmic Ray Events

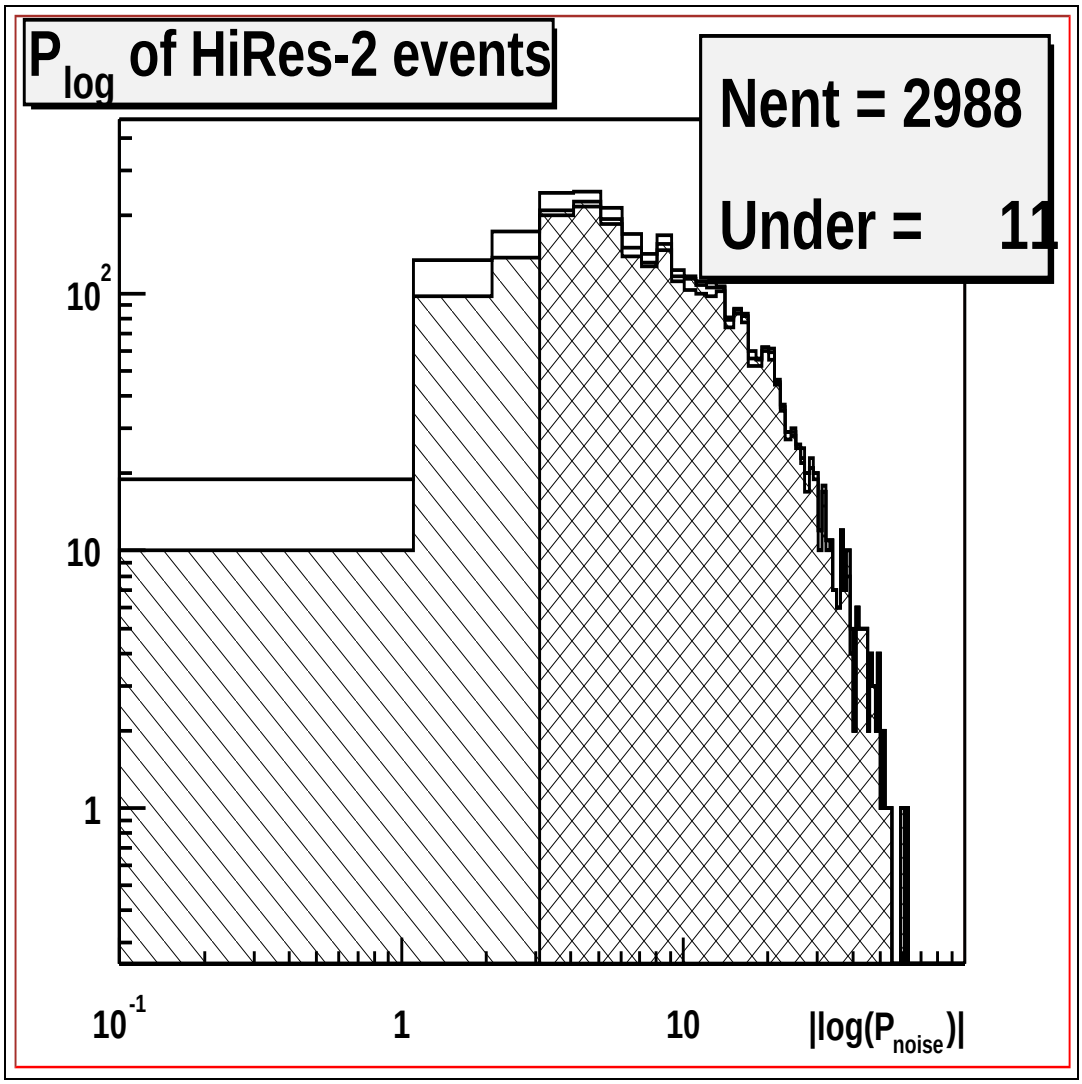

Figure 5.19. P_{log} Values at HiRes-2 for Monte Carlo Cosmic Ray Events

5.6.4 Plane Fit: Pass3

After fitting a plane to the PMT signals, tracks of less than 6^o are cut. Figures 5.20 and 5.21 show the distribution of track-lengths for events which remain after the noise filter both before and after the 6^o track-length cut. This requirement provides a minimum length of shower profile. Figures 5.22 and 5.23 show the distributions of track-lengths at HiRes-2 before and after the 6^o track-length cut. Further track-length comparison between the Monte Carlo and data will be shown in Chapter 7.

5.7 Postprocessing Cuts

Three cuts on the data occur after processing. These cuts are a profile fit quality cut, a number of flashers cut and a minimum energy cut of 10^{18} eV.

5.7.1 $N_{flasher}$ Cut

Our vertical flasher array has proved to be extremely useful in confirming the synchronization of our two detectors. Additionally, the flashers provide a very quick check that the detector is observing light.

In calculating exposure, very short data parts are of great concern. We must be able to confirm that the detectors were truly operational during the data taking time period. A few solutions have been proposed for this problem. The first and easiest is to simply ignore all part shorter than a certain minimum length, such as ten minutes minimum[36]. However, this does not ensure operation or synchronization. Additionally setting this cut at 10 minutes removes a very large portion of our exposure.

Rather, I have opted to confirm operation and synchronization by the counted number of vertical flashers seen. Figure 5.24 shows the cosmic ray event rate for

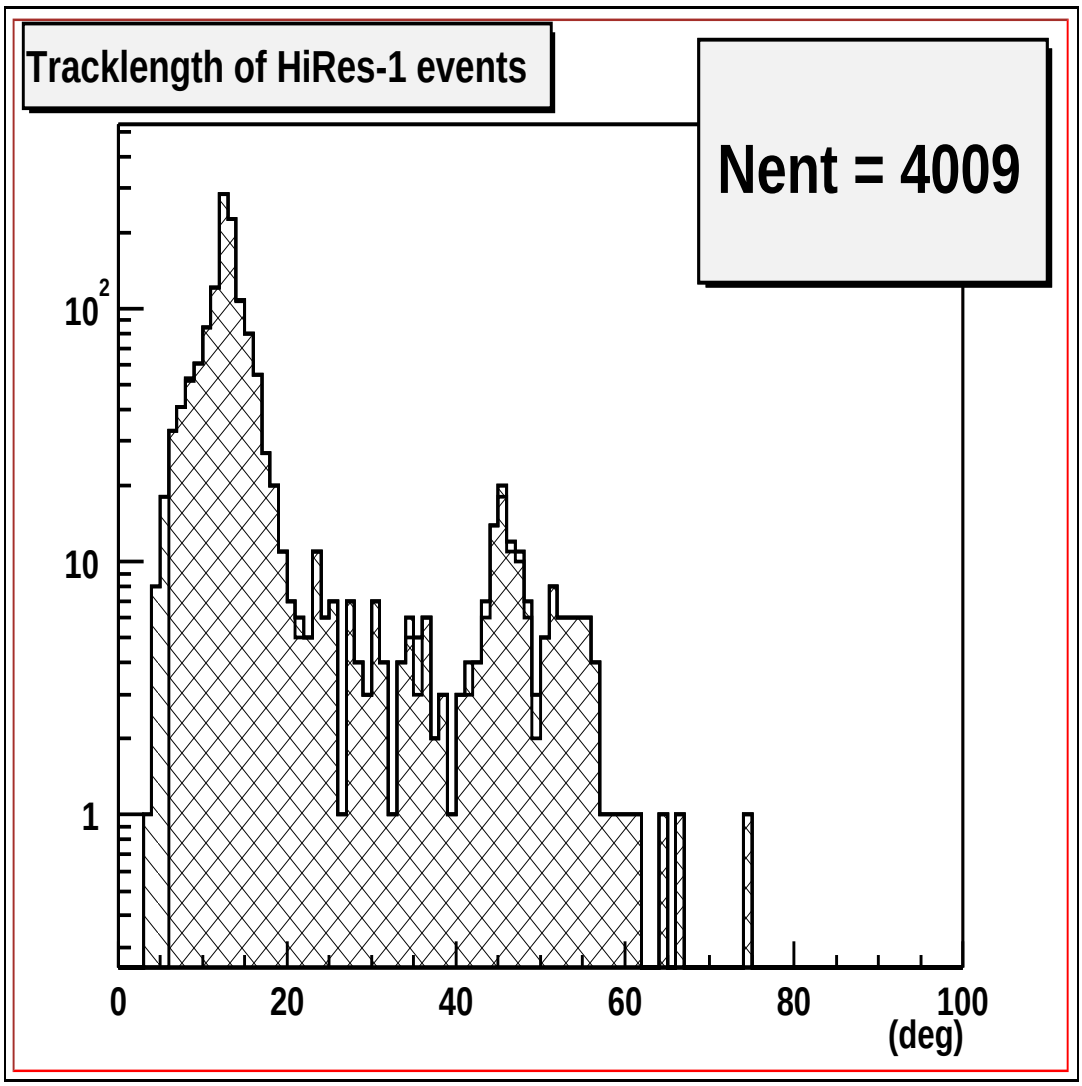

Figure 5.20. Pre- and Postcut HiRes-1 Track-Lengths

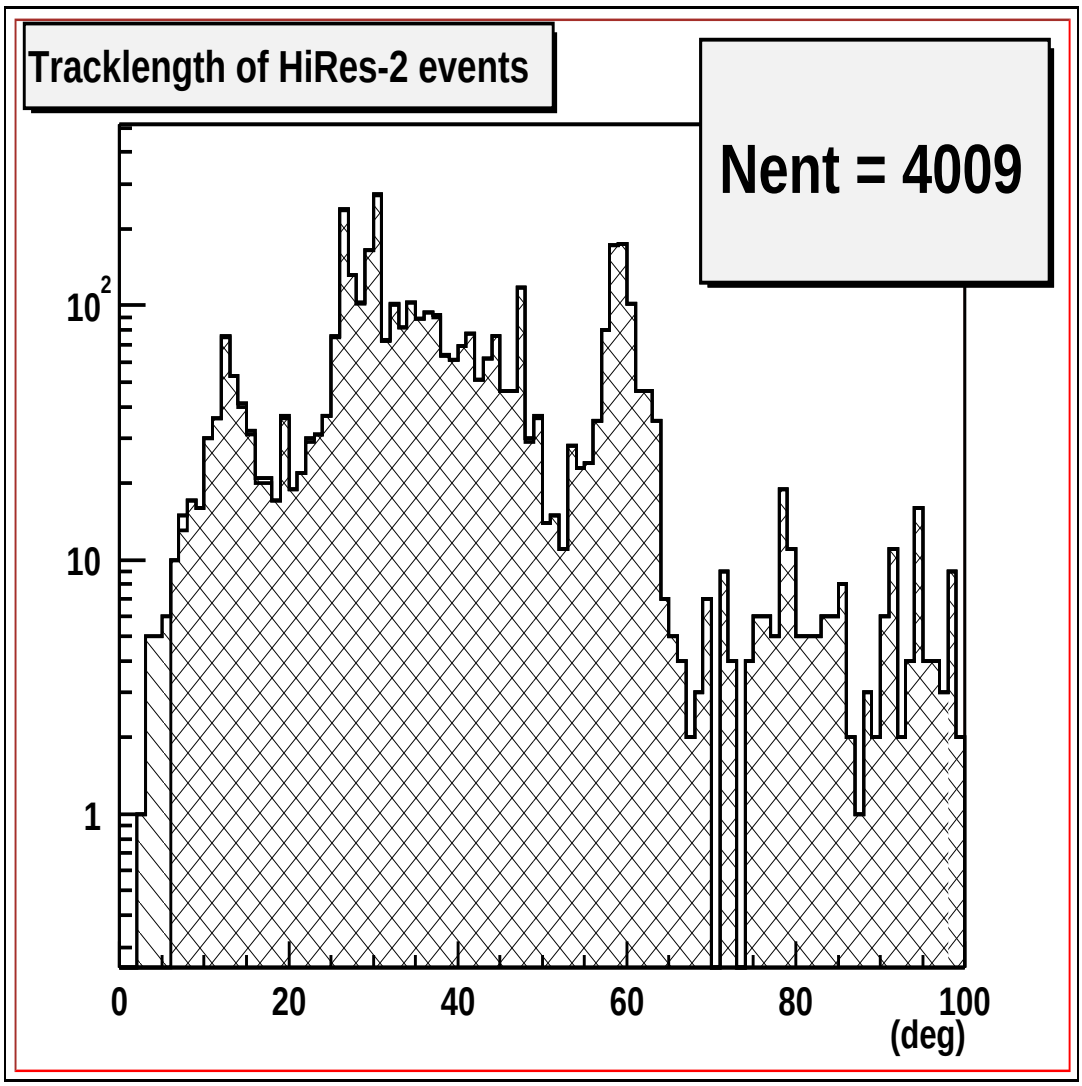

Figure 5.21. Pre- and Postcut HiRes-2 Track-Lengths

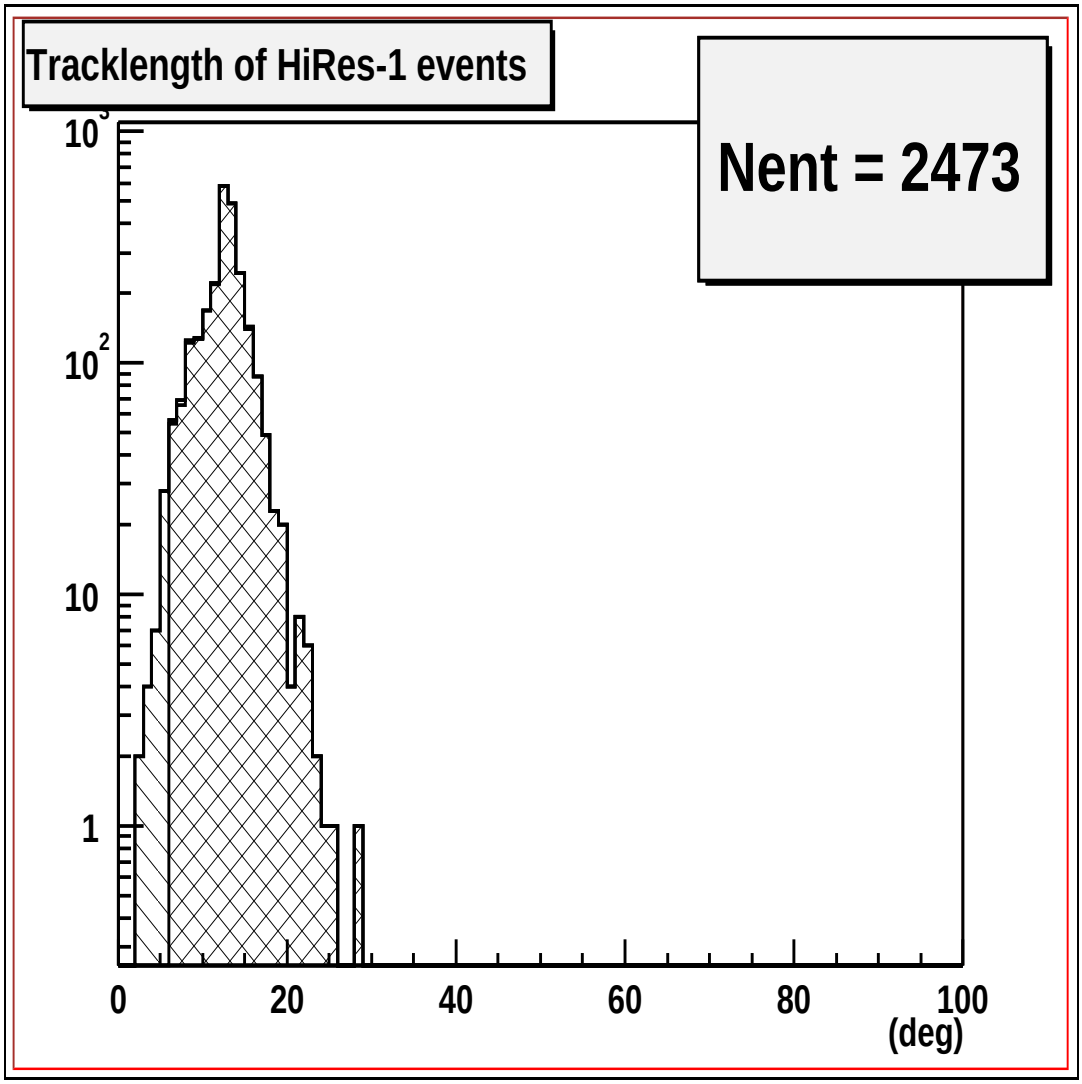

Figure 5.22. Pre- and Postcut HiRes-1 Track-Lengths for Monte Carlo Events

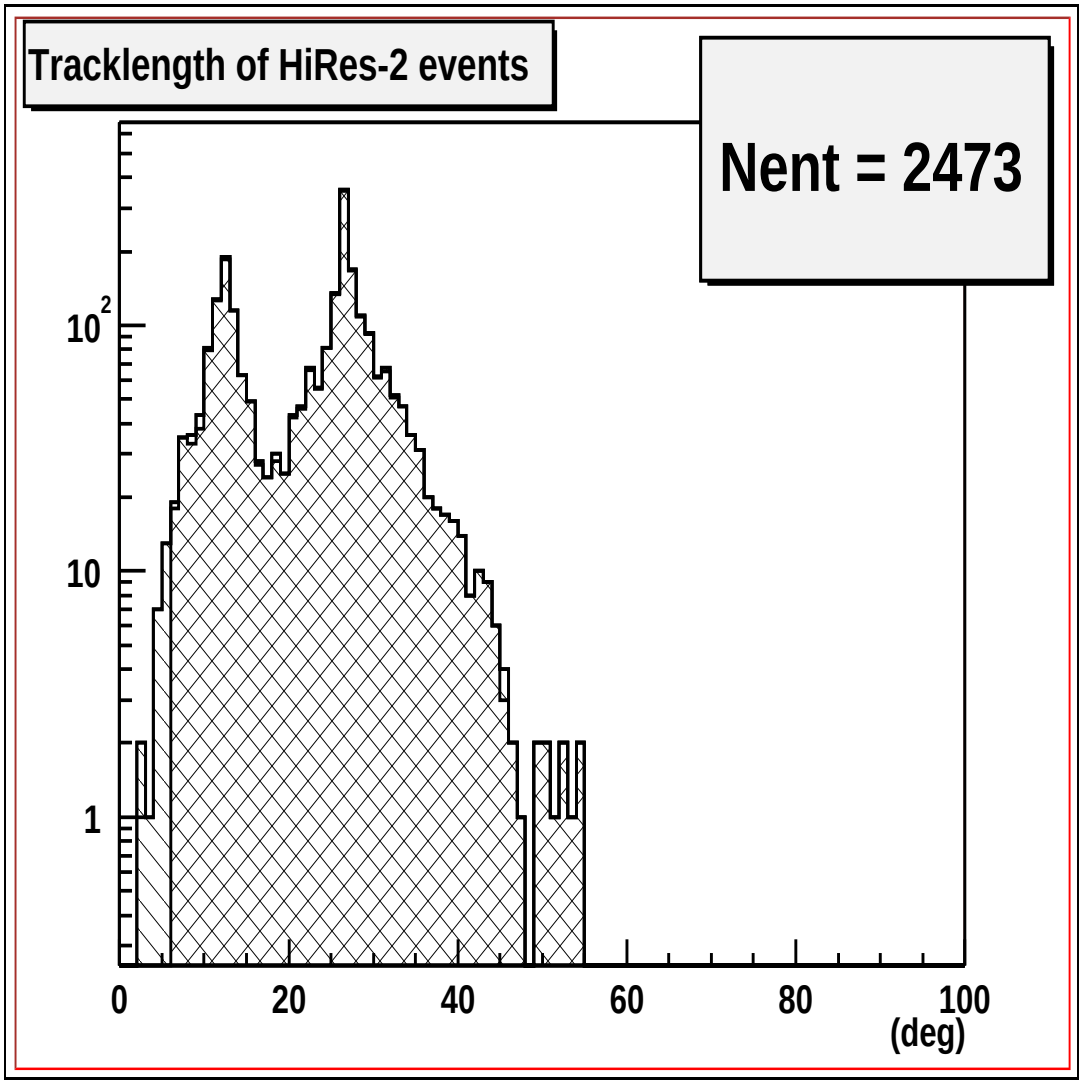

Figure 5.23. Pre- and Postcut HiRes-2 Track-Lengths for Monte Carlo Events

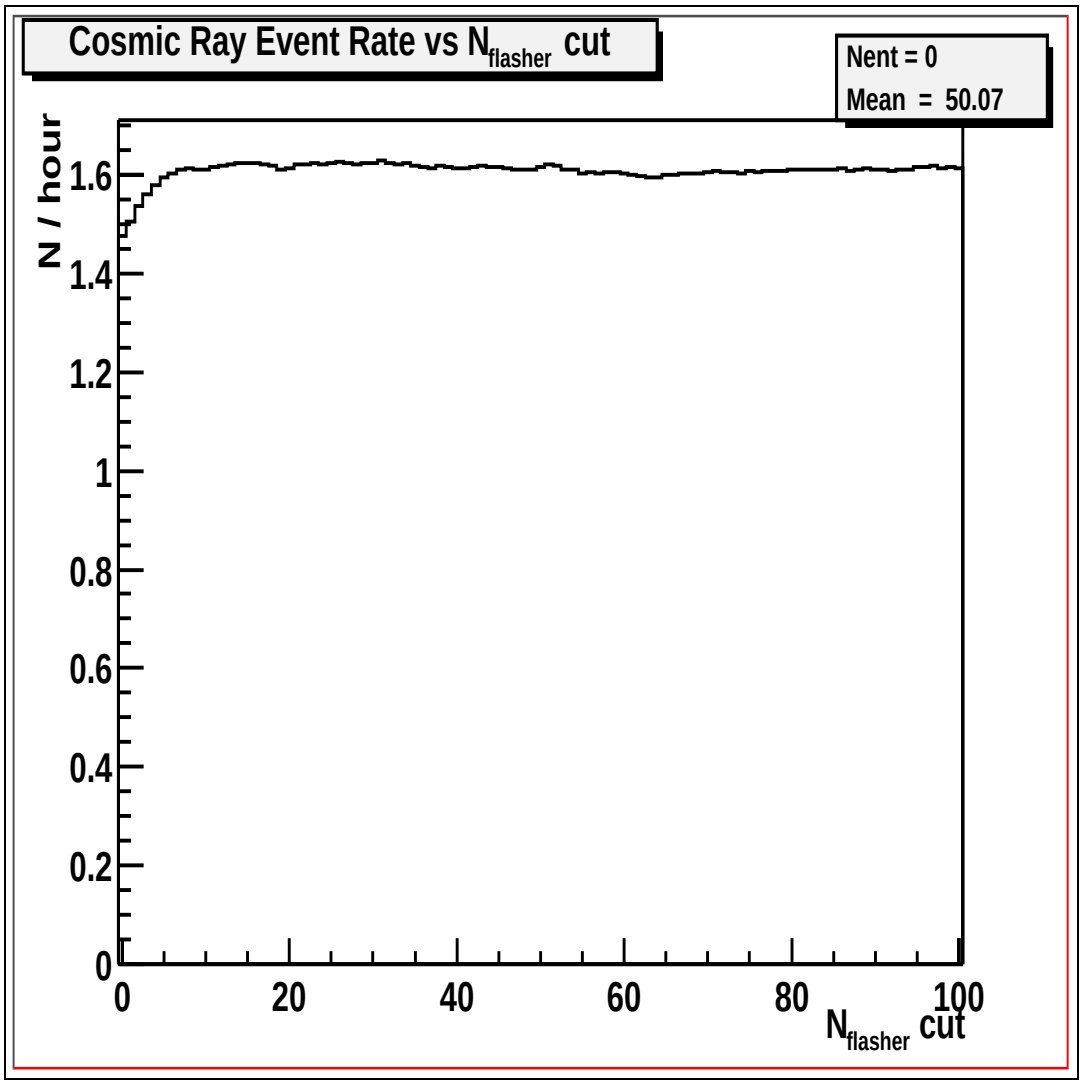

Figure 5.24. Cosmic Ray Event Rate vs. $N_{flasher}$ Minimum

energy above 1 EeV versus the value selected for the $N_{flasher}$ cut. At low values of $N_{flasher}$ the event rate is significantly lower than at higher values. This indicates that the detector was not taking data or was not synchronized. A value of $N_{flasher} > 20$ was selected based upon this figure. The effect of this cut on exposure is discussed in section 8.2.

5.7.2 $E_{recon} > 10^{18}$ eV Cut

It will be shown in chapter 9 that the aperture of our detector initially grows very quickly with energy. In determining the flux of cosmic rays, the number of events at a given energy is divided by the aperture at that energy. If the aperture is varying rapidly, a small error in energy determination will lead to a large error in flux. Events below 10^{18} eV are not used in this analysis. for this reason.

5.7.3 Reconstructed Energy Quality Cut

The value of the χ^2 from equation 5.6 divided by the number of degrees of freedom quantifies the quality of the fit. Figure 5.25 shows the distribution of the χ^2/dof from the data together with the quality cut of $\chi^2/dof < 10$. In addition to the χ^2/dof cut a second quality cut is used in this analysis. The cut is

$$\left\| \frac{E_1 - E_2}{(E_1 + E_2)/2} \right\| < 3\sigma. \tag{5.10}$$

The values E_1 and E_2 are the reconstructed energy using only the HiRes-1 and HiRes-2 signal respectively. In both cases, the stereo geometry is used. This cut removes events having divergent energy results and uses a measurable distribution.

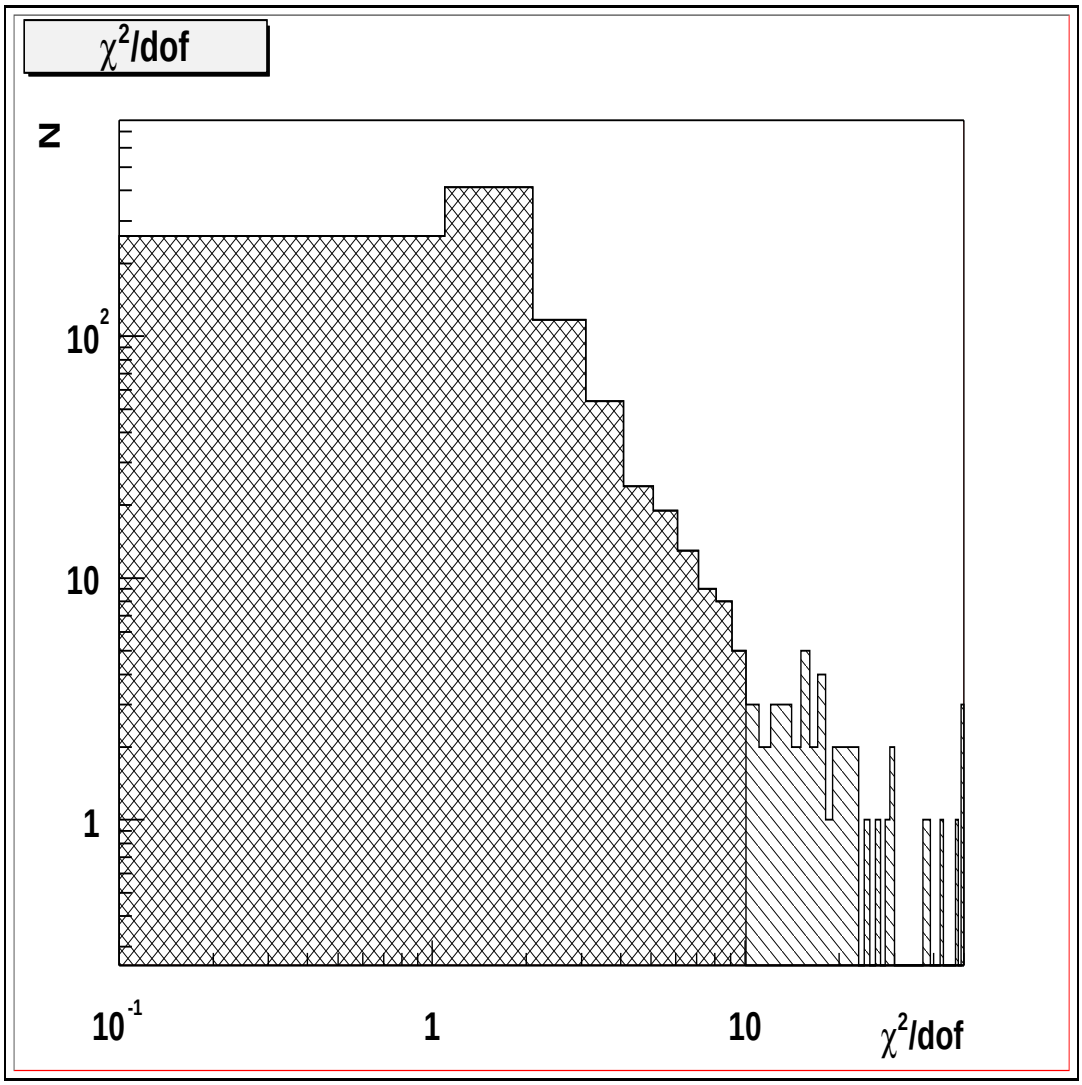

Figure 5.25. Profile Fit χ^2/dof for Data

CHAPTER 6

THE DETECTOR MONTE CARLO

This work is dependant on the accuracy of the Monte Carlo simulation, especially in the calculation of detector aperture. After first describing the details of the Monte Carlo, this chapter will provide evidence that the event reconstruction can properly determine shower properties. Additionally, it will be shown that the Monte Carlo produces data that reflect the true cosmic ray flux, EAS physics and detector response.

6.1 CORSIKA, QGSJET and SIBYLL

Simulating extensive air showers and tracking all of the shower products requires extremely careful programming and attention to physics details. The cosmic ray community, therefore, has produced a few standard Monte Carlo programs for this purpose. The extensive air shower Monte Carlo used in this analysis is CORSIKA[42].

Within CORSIKA the two hadronic interaction models QGSJet and SIBYLL are used in this analysis. These models describe interactions outside of the realm of accelerator studies. Additionally, CORSIKA simulates the electromagnetic (e^+, e^-, γ) portion of the air shower using the EGS4 Monte Carlo which was designed specifically for such interactions[43, 44].

After each interaction, CORSIKA tracks each product until it interacts again. The repeated interactions cause the number of particles to grow very rapidly. The

large number of particles traveling through the atmosphere is the extensive air shower. Due to the large number of particles involved, CORSIKA uses a procedure known as thinning for particles below a threshold energy. Thinning follows, for example, one out of 1000 particles and then claims that 1000 particles would produce that same result 1000 times. The defense of this assumption is that at the thinning level billions of particles exist and the statistics of thinned particles is still very high. Additionally, studies have shown that thinning produces no visible change in results[45].

Models exist for the interaction of ultra relativistic particles. Since no manmade accelerator can reach the energies of the magnitude discussed here, the models are based on extrapolations from accelerator data. The two interaction models used in this analysis are SIBYLL and QGSJet [46, 47]. The reader is referred to the Simpson and Archbold theses as well as the Heck paper for information[13, 48, 42].

It is my belief that a detailed Monte Carlo based on cross sections is the best method for study of air showers. However, the computation time required to track billions of particles makes this Monte Carlo inefficient in high statistics studies.

6.2 Monte Carlo Description

The detector Monte Carlo performs three separate tasks. First, it must produce the light that is to be detected. Second, the light must be propagated and attenuated as it passes through the atmosphere. Finally, the light must be sent through the HiRes optics and electronics. Once the Monte Carlo signal from the air shower has produced the electronic signal in the detector, it is stored in the same format as the real data recorded at the detectors.

6.2.1 Air Shower Production

In the production of an air shower, there are two major steps. First, a number of charged particles must be determined as a function of depth in the atmosphere. This is known as the longitudinal development.

Currently three methods exist for this purpose. First, there are two functional forms that can be used to simulate an air shower. The first function is the Gaisser-Hillas (GH) shower profile. This functional form is found in cascade theory and has been shown to fit air shower development empirically[49]. The GH shower profile functional form is

$$N_e(X) = N_{max}(\frac{X - X_0}{X_{max} - X_0})^{(X_{max}-X_0)/\lambda} e^{-(X-X_0)/\lambda} \tag{6.1}$$

The four parameters are X_0, X_{max}, N_{max}, and λ.

X, X_0 and X_{max} have units of $grams/cm^2$ and are related to the depth in the atmosphere. x_0 has historically been called the depth of initial interaction but more detailed studies have shown that it is merely a fitting parameter which has no physical meaning[48, 45]. Additionally, it has been shown that fixing this parameter to a reasonable value has little effect on the resolution of energy[48, 45]. In the studies shown here, X_0 has been fixed at a value of 0. X_{max} on the other hand is of vital importance in the fit. This parameter determines the depth in the atmosphere at which the maximum number of particles exists in the air shower. As mentioned before, this parameter is of interest in determination of the primary particle composition.

N_{max} determines the normalization of the profile. It is therefore directly related to the primary energy. Finally, λ is a characteristic length in air showers. In these studies it is fixed at 70 gm/cm^2[48].

In order to "create" a GH shower the energy of the primary particle is related to the amount of electromagnetic energy that will be deposited. This is accomplished using

$$E_{em}/E_0 = 0.9437 - 0.0963E_{em}^{-0.126}, \tag{6.2}$$

which comes from recent work of Zhen Cao using CORSIKA[50]. The units of energy in this equation are EeV. This formula represents the average amount of energy in the air shower that is not converted into electromagnetic products in the atmosphere. Additionally, particles that reach the surface of the earth cannot be detected. More details on equation 6.2 are provided in section 6.2.2.

The shower products that do not produce a calorimetric signal in the atmosphere are produced in higher abundance in hadronic interactions. This results in heavier nuclei depositing less energy into the atmosphere. Figure 6.1, produced by Zhen Cao in support of equation 6.2, shows the ratio of E_{em}/E_0 for both protons and iron. As expected, iron has a lower percentage of its shower energy converted into visible signal. The average between the two species is contained in equation 6.2. This figure also shows the change between two recent versions of CORSIKA. Figure 6.1 does not show the fluctuations from the mean values of E_{em}/E_0 which are on the order of 7%. This fluctuation will put a lower limit on energy resolution.

GH showers are created with the E_{em}/E_0 ratio determined by the average of protons and iron. This fit result is contained in equation 6.2. Since the GH shower driver also provides our Monte Carlo predicted signal for fitting in equation 6.2, an average composition is also used in reconstruction. This leads to approximately 5% uncertainty in reconstructed energy since we do not know the composition of the primary. When reconstructing Monte Carlo events of known composition this average composition assumption will produce a visible effect in the energy resolution. This will be shown in section 9.4.

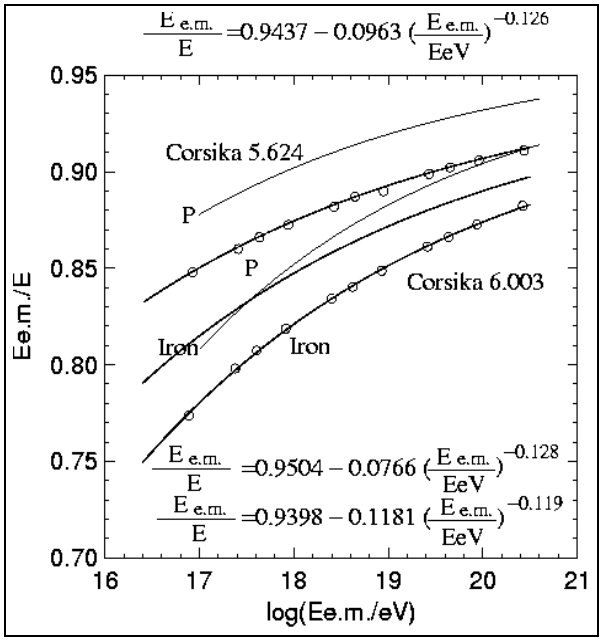

Figure 6.1. E_{em}/E_0 for Proton and Iron[50]

After determining the amount of energy that will be deposited into electromagnetic signal we must then convert E_{em} into a total number of charged particles. This is accomplished through

$$E_{em} = \frac{E_C}{X_0}\int_0^\infty N_e(x)dx \approx 2.379\frac{MeV}{gm/cm^2}\int_0^\infty N_e(x)dx. \tag{6.3}$$

Here E_C is the critical energy of an electron in air. E_C is found using

$$E_C = \frac{710MeV}{Z+0.92} = \frac{710MeV}{7.22+0.92} = 87.22MeV[51]. \tag{6.4}$$

The value of $Z = 7.22$ is a weighted average of 78% nitrogen and 22% oxygen. X_0 has been measured to be 36.66 m[51]. The parameters of the GH equation, X_{max} and N_{max}, must be selected so that the integrated nuber of charged particles maintains the relation of E_{em} to E_0.

It should be noted that most prior fluorescence measurements have been made using $E_C/X_0 \approx 2.18$[22]. This has caused a divergence between equation 6.3 and

detailed works such as CORSIKA. All alternate explanation for the divergence was offered by Song in his thesis but this author is skeptical about his conclusion resulting in a 10% shift in energy[22].

The second functional form for an air shower is known as Gaussian-in-Age. Shower age is defined as

$$s = \frac{3x}{x + 2x_{max}}. \tag{6.5}$$

The shower age is a useful parameter since $s = 0$ at initial interaction, $s = 1$ at X_{max} and $s \rightarrow 3$ as the shower goes deep in the atmosphere. This function is symmetric about X_{max}. It has been shown that the Gaussian in age function,

$$N_e(x) = N_{max} e^{\frac{(s-1)^2}{2\sigma^2}}, \tag{6.6}$$

also provides a good description of shower development. In this formulation we have only three parameters. N_{max} and X_{max} have the same meaning as before, while σ describes the width of the Gaussian function. This form has two advantages over the GH shower profile. The first advantage is that this form has only three parameters instead of four and all parameters contain useful information. The second advantage is that both X_{max} and σ contain information about the composition[52]. The reader is reminded that within this and many works only two of the GH parameters are varied.

Both functional forms describe air shower development very well. Within the Monte Carlo, the difference in application of the two functional forms is the fluctuation of X_{max}. The GH form uses a single average X_{max} value for a given energy based upon average experimental values. Additionally, it assumes an average E_{em}/E_0 value. When using the Gaussian-in-Age shower driver, the value of X_{max}, N_{max} and σ are sampled from distributions obtained from CORSIKA. The details of this driver are not yet published. Additionally, at the time of this writing, this

Gaussian-in-Age driver provides only QGSJet proton showers. For these reasons, this driver is not used in this study.

Instead, with the help of Greg Archbold, I recently added the ability to pass CORSIKA longitudinal development directly into the detector Monte Carlo, thereby removing the need to use any functional form for an air shower. CORSIKA provides $N_e(x)$ directly.

Since the production of UHE CORSIKA events is extremely time consuming it is not practical to run CORSIKA each time we wish to simulate an air shower in the detector Monte Carlo. Instead, a shower library has been created. This shower library consists of approximately 500 proton and 400 iron events for each 0.1 log(E) energy bin. These same statistics are produced for the SIBYLL and QGSjet hadronic models. The energy range included spans from $10^{17.5}$ to $10^{20.5}$. Each shower can then be inserted into the Monte Carlo in any geometric orientation allowing for an extremely large set of unique air shower events. In addition to the longitudinal development and energy of each shower, a fitted X_{max} and N_{max} for each shower is provided. This allows comparison of fits before and after all detector effects have been taken into account.

Since the shower library was created in discreet energy bins, the ability to scale events to any energy is needed. Figures 6.2 through 6.5 show the linear relation between $log_{10}(E)$ and $log_{10}(N_{max})$ for protons and iron for the two models. Since the relationship is so linear, these lines are used to scale the number of particles from the nearest energy bin.

In addition to longitudinal development, the particles in the shower are assumed to spread out radially according to the NKG function (6.7),

$$f_{NKG}\Big(\frac{r}{r_m}\Big) = N_e\Big(\frac{\Gamma(4.5-s)}{2\pi\Gamma(s)\Gamma(4.5-2s)}\Big)\Big(\frac{r}{r_m}\Big)^{(s-2)}\Big(1+\frac{r}{r_m}\Big)^{(s-4.5)} \tag{6.7}$$

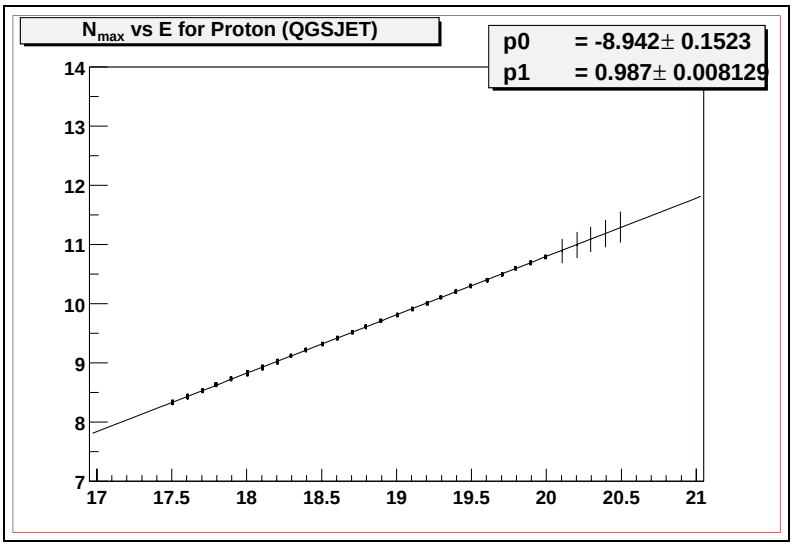

Figure 6.2. N_{max} vs. E for QGSJET Protons

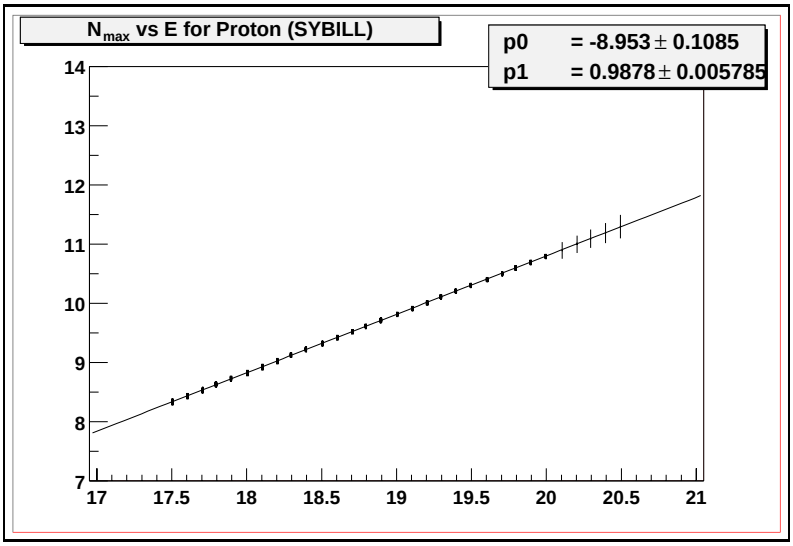

Figure 6.3. N_{max} vs. E for SIBYLL Protons

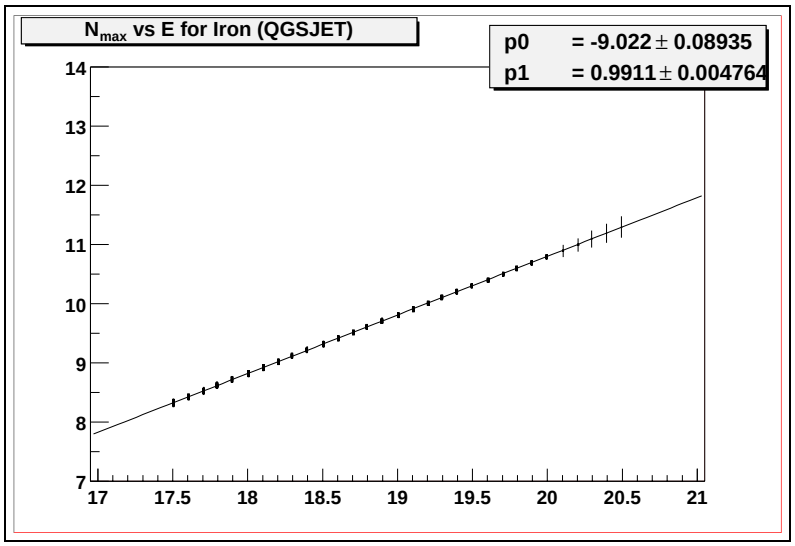

Figure 6.4. N_{max} vs. E for QGSJET Iron

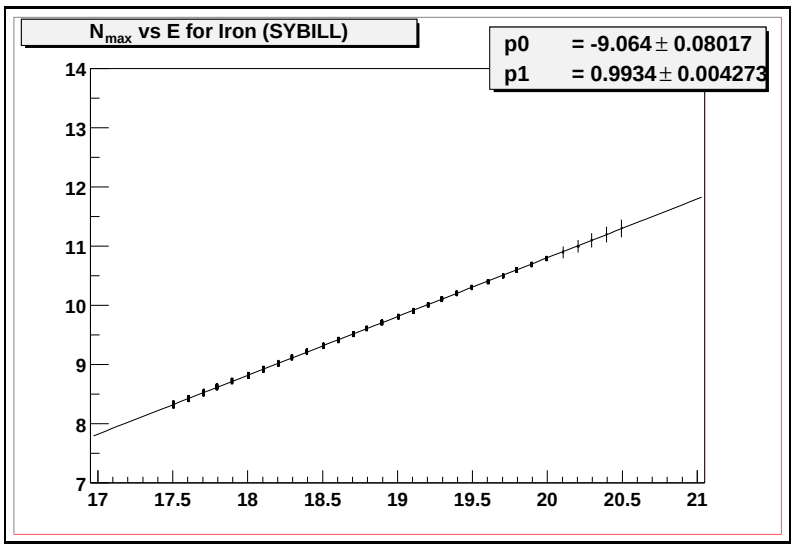

Figure 6.5. N_{max} vs. E for SIBYLL Iron

where r_m is the Moliere radius and s is the shower age (6.5). The density of charged particles versus distance from the shower core can then be found by (6.8),

$$\rho(N_e, r) = \frac{N_e}{r_m^2} \cdot f_{NKG}(\frac{r}{r_m}). \tag{6.8}$$

Four examples of the lateral distribution can be found in Figure 6.6 taken from the AbuZayyad thesis.

6.2.2 Missing Energy

Many products of the interactions, especially those created in hadronic interactions, do not produce fluorescence light. Instead, between 15% and 25% of the shower energy will reach the earth. Additionally, neutrinos produced in the air

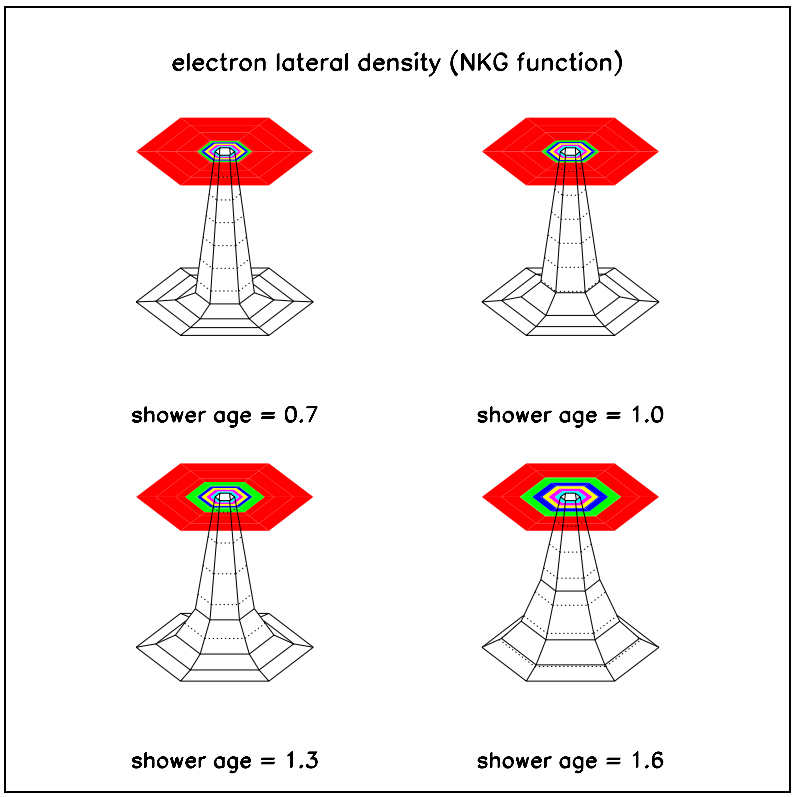

Figure 6.6. Electron Lateral Distribution for Four Shower Ages[20]

shower will carry away energy although this is typically less than 1%. Figure 6.1 shows the percent of the total shower energy which is deposited as electromagnetic energy. The is the ratio E_{em}/E_0.

Figure 6.1 shows that iron, which contains more hadrons, deposits as little as 75% of its total energy in the electromagnetic shower. Protons, which are represented by the upper line, deposit between 85 and 90% of their energy. The middle line, the average between protons and iron, is the assumed E_{em}/E_0 used by the GH driver and the event reconstruction.

6.2.3 Light Production

In an extensive air shower light is produced in two ways. First, Nitrogen atoms are excited by the electromagnetic components of the air shower. Second, particles that are traveling faster than the speed of light in air produce Čerenkov light.

As mentioned, scintillation is produced in the interaction of charged particles with the nitrogen in the atmosphere. This light is released from the air shower isotropically. The amount of scintillation light produced is based upon the nitrogen fluorescence yield. Two spectra are currently available for use. The first spectra is based on physical chemistry calculations and can be seen in Figure 6.7 [53]. The second spectra, which is used in this work, is based on experimental results and can be seen in Figure 6.8 [54]. The total yield is given in equation 6.9[54].

$$Y = \frac{(dE/dx)}{(dE/dx)_{1.4MeV}} \cdot \rho\left\{\frac{A_1}{1+\rho B_1\sqrt{t}} + \frac{A_2}{1+\rho B_2\sqrt{t}}\right\} \tag{6.9}$$

In equation 6.9, ρ is the density and t is the temperature in K. The constants A_1, A_2, B_1 and B_2 are 89 and 55 m^2/kg and 1.85 and 6.50 $m^2/kg\sqrt{K}$ respectively. The

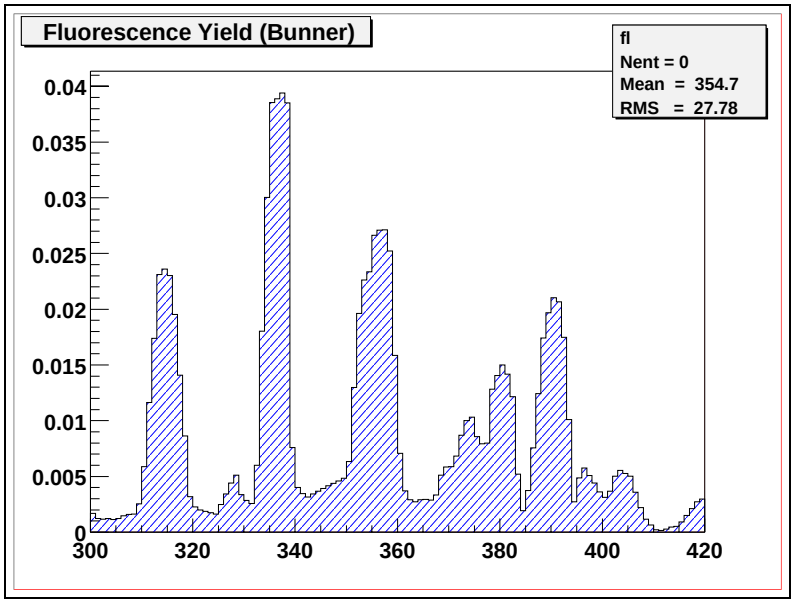

Figure 6.7. Normalized Fluorescence Spectrum: Adapted from Bunner[53]

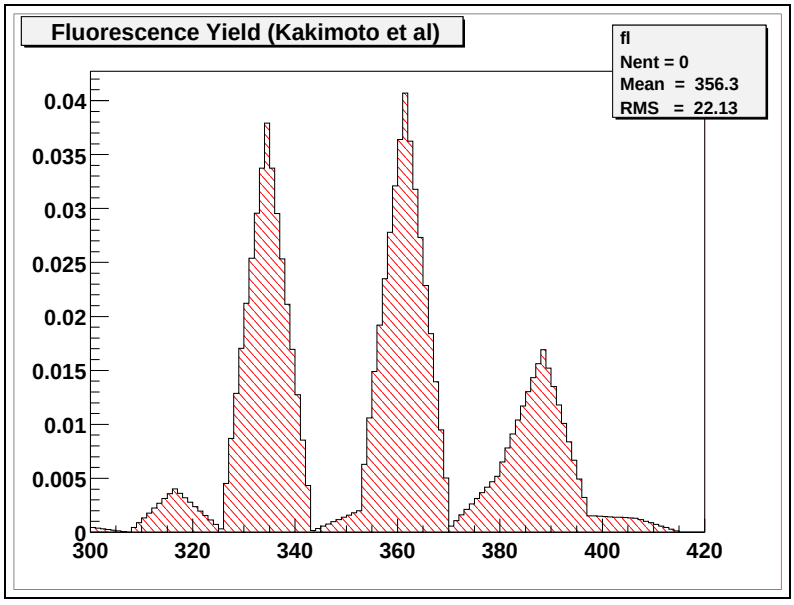

Figure 6.8. Normalized Fluorescence Spectrum: Adapted from Kakimoto et al.[54] This is the yield as used in this analysis

average dE/dx (energy loss of electrons in MeV/cm) as a function of age is used. This scintillation light is distributed isotropically according to

$$\frac{d^2N}{dld\Omega} = Y\frac{Ne}{4\pi}. \tag{6.10}$$

Čerenkov light is produced as the charged particles in the air shower traverse the atmosphere faster than the speed of light in air. As the air shower propagates, more and more Čerenkov photons are produced forming a Čerenkov beam. Light from the Čerenkov beam is then scattered from the air shower and adds to the signal of light from the air shower. Additionally, the geometry of the air shower may also allow direct Čerenkov light to enter the detector. Events which travel towards out detector may have very strong direct Cherekov signals, but since the light arrives together, the resulting signal has little time development and is filtered out as noise.

The energy requirement for Čerenkov light production is given by the formula

$$E_{min} = \frac{E_{min}(MeV)}{\sqrt{2\sigma}} \tag{6.11}$$

where $\sigma = n - 1$ and n is the index of refraction at the current atmospheric depth.

The number of Čerenkov photons produced per meter for a single charged particle of energy E is

$$\frac{dN_p(E)}{dl} = 4\pi\alpha\left[\left(\frac{E_{min}}{E}\right)^2\right]\int\frac{\sigma}{\lambda^2}d\lambda. \tag{6.12}$$

This leads to the total amount of light produced per meter at depth X to be

$$\frac{dN_{cv}(X)}{dl} = \int_{E_{min}}^{\infty} N_e(X)f(E,X)\frac{dN_p(E)}{dl}dE \tag{6.13}$$

where $N_e(X)$ is the number of charged particles at the given depth, $f(E,X)$ is the distribution of electron energies at the given depth and the final term is the Čerenkov light production per particle. $f(E,X0)$ is given by

$$f(E,X) = \int_E^\infty \left(\frac{0.89E_0 - 1.2}{E_0 + E}\right)^s (1 + 10^{-4}sE)^{-2} \tag{6.14}$$

where s is the shower age and $E_0 = 44 - 17(s-1.46)^2$. This relation has been found using Monte Carlo techniques[23].

Čerenkov light is forward directed and is approximately

$$\frac{d^2N_{cv}(X)}{dld\Omega} = \frac{dN_{cv}(X)e^(-\theta/\theta_0}{dl\sin\theta} \tag{6.15}$$

with $\theta_0 = 0.83E_{min}^{-0.67}$[23].

Since the Čerenkov beam remains contained around the air shower, it builds up as the shower traverses the atmosphere. Some light is lost over each unit distance due to Rayleigh and aerosol scattering. The total size of the Čerenkov bean at any depth can be found by

$$N_{cv}(X) = \int_0^X \frac{dN_{cv}(X')}{dl} T(X',X) dl(X') \tag{6.16}$$

which is essentially the sum of all produced Čerenkov light less the amount removed by scattering ($T(X',X)$).

In addition to light from the air shower there are also background sources of sky noise mostly star light. The sky noise at Dugway has been measured to be 40 photoelectron per $1.2\mu s$[22].

6.2.4 Atmosphere

The UV light that we detect consists of both nitrogen fluorescence light and Čerenkov light that has been scattered by the molecules and aerosols in the atmosphere. Both Rayleigh and aerosol scattering then attenuate the light that leaves the air shower. Additionally, absorption due to ozone must be accounted for.

The number of photons scattered by Rayleigh scattering follows

$$\frac{dN_R^\gamma}{dl} = -\frac{\rho}{(X_R = 2970gm/cm^2)}\left(\frac{400nm}{\lambda}\right)^4 N_R^\gamma \tag{6.17}$$

where N^γ is the number of photons, ρ is the atmospheric density and X_R is the mean scattering length at $\lambda = 400nm$.

The angular distribution of Rayleigh scattered light is

$$\frac{d^2N_R^{gamma}}{dld\Omega} = \frac{3}{16\pi}\left|\frac{dN_R^\gamma}{dl}\right|(1+\cos\theta^2) \tag{6.18}$$

The transmission coefficient for Rayleigh scattering is

$$T_R = e^{-\frac{dX}{X_R}\left(\frac{400}{\lambda}\right)^4} \tag{6.19}$$

In addition to Rayleigh (molecular) scattering, scattering from aerosols in the air also occurs. Aerosol scattering is a much more complicated phenomenon so a simplified model for aerosols is used instead[18]. In this model, the density of aerosols is assumed to fall off exponentially with a vertical scale height (H_s). Additionally a simple horizontal attenuation length (L_M) is used. This allows for the "net effect" of aerosols to be used. The transmission factor due to aerosols for light leaving height h_1 and arriving at height h_2 after traveling a distance dl is given as

$$T_M = exp[\frac{H_s dl}{(h2-h1)L_M}(e^{-h_1/H_s} - e^{-h2/H_s})] \tag{6.20}$$

As mentioned in Chapter 4, the average values used for this analysis are $H_s = 1km$ and $L_M = 25km$. Additionally, where possible, events have been processed with the measured parameters for the hour in which they occurred.

Finally, ozone in the upper atmosphere absorbs UV light. The absorption is given by

$$\frac{dN^\gamma}{dl} = -N\gamma A_{O_3}(\lambda)\rho_{O_3}(h) \tag{6.21}$$

where $A(\lambda)$ is the wavelength dependant absorption and ρ_{O_3} is the density at a given height. The USAF Handbook of Geophysics and Space Environment was

used to model O_3 and the information is shown in Figures 6.9 and 6.10. The ozone transmission coefficient is given by

$$T_{O_3} = e^{-dX_{O_3} A_{O_3} x} \tag{6.22}$$

where dX_{O_3} is the slant depth of ozone.

The total amount of light reaching the detector is given by the product of 6.19, 6.20 and 6.22

$$N_{\gamma\ detector} = N_{\gamma\ shower} T_R T_M T_{O_3}. \tag{6.23}$$

6.2.5 Optics and Electronics

After arriving at the detector, the light flux ($number of photons/degree/m^2 \times area$) must be distributed into the individual PMTs. A detailed ray tracing procedure calculates PMT signal from the flux. The procedure calculates obscuration from the PMT cluster, reflection and uneven mirror surfaces and attenuation from our UV-pass filter. The light lost in the cracks between phototubes is simulated. The reflection of our mirrors is assumed 80% which is degraded from the "clean" mirror reflectivity shown in Figure 3.3. The transmission of light through the UV-pass filter is shown in Figure 3.5.

Once the photon has arrived at the surface of a PMT the quantum efficiency of converting the photon into a photoelectron is taken into account as a function of the location on the PMT surface of shown in Figure 5.2. The average response is a quantum efficiency of 0.28 or 28%.

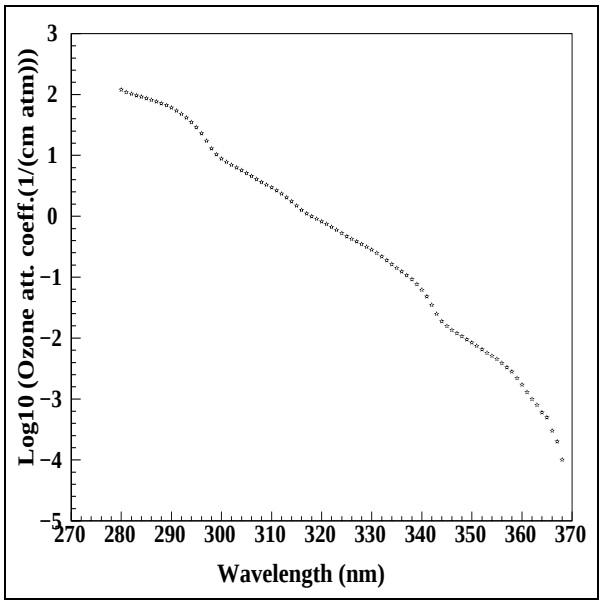

Figure 6.9. Ozone Absorbtion vs. Wavelength

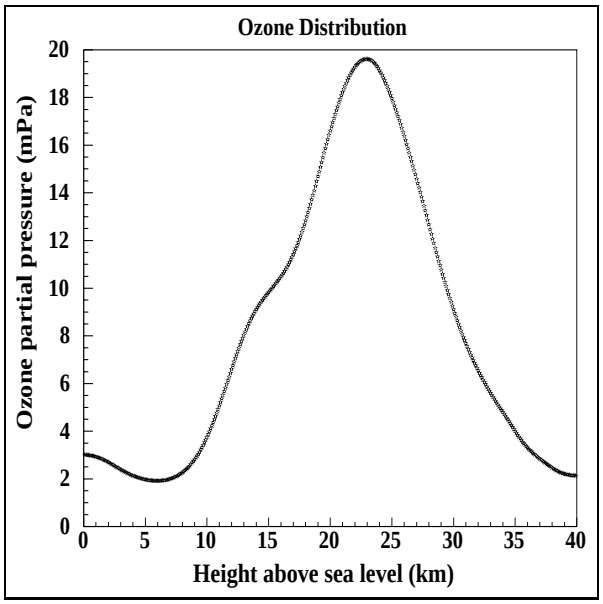

Figure 6.10. Ozone Density vs. Height

The electronic response and triggering conditions for the individual detectors is then simulated. The resulting information is now analogous to real detector data and is stored in the identical dst format. For HiRes-1 the total number of photoelectrons is stored. For HiRes-2 the number of photoelectrons in each 100ns time slice is stored. These time slices are then integrated to give the total number of photoelectrons.

The full timing information for each photon is tracked by the Monte Carlo from creation to arrival in the PMT. This tracking includes geometrical differences due to the lateral distribution. Since the primary method of geometric reconstruction is based on geometry alone, this information only affects the noise filter and plane fitting routines.

CHAPTER 7

MONTE CARLO STUDIES

7.1 Resolution Studies

Once an EAS has triggered our detector, it is essential to understand how well the geometric and physics quantities involved can be determined. In the geometric resolution studies, proton showers generated by CORSIKA using QGSJet following a stereo Fly's Eye spectrum were used. Geometric quantities are almost completely independent of composition. All geometric resolutions are presented for QGSJet protons. For the resolution of physics quantities data sets are created using a stereo Fly's Eye spectrum energy distribution. Individual resolutions are provided for 100% proton and 100% iron composition using both QGSJet and SIBYLL. The Monte Carlo events are processed using all of the cuts discussed in chapter 5 except for the steer-able laser systems filter. The study includes 2414 QGSJet protons, 2333 SIBYLL protons, 2418 QGSJet iron and 2207 SIBYLL iron primaries with an energy distribution sampled from the Fly's Eye stereo measurement.

7.1.1 Geometric Resolution

Due to the very large aperture involved, determination of the geometry of the air shower is essential. The resolution studies of the following geometric quantities are shown: R_p, θ, ϕ, Ψ, R_{core}. R_p is the impact parameter, θ and ϕ are the zenith and azimuthal angle of the shower at the earth's surface, Ψ is the in plane angle of the shower and R_{core} is the distance from the detector to the location of impact

of the air shower on the $z = 0$ plane. The distance to each segment of the air shower can be determined from these values. From this distance, the amount of light lost due to attenuation is determined. Additionally, the angle Ψ is essential in the calculation of direct Čherenkov light.

Figure 7.1 shows that the zenith angle of extended air showers is measured to within one or two degrees. Significantly less than 1% of all events have errors beyond 10 degrees. A good zenith angle resolution is required since the depth of the earth's atmosphere grows rapidly with increasing zenith angle. This figure, as will all resolution figures, shows the number of events using a logarithmic scale on the y-axis. The logarithmic scale is used to make the tails in all resolution visible.

Figure 7.2 shows the angular resolution of the azimuthal angle at impact of air showers. In azimuth, the rms is slightly larger due to the slightly larger tails in the resolution. The sigma of the resolution is approximately 1 degree. A slightly poorer azimuthal resolution is acceptable since this angle has almost no impact on physics quantities.

From Figures 7.3 and 7.4 we see that the distance to the shower (R_p is the impact parameter or distance of closest approach of shower trajectory) is determined very well. The RMS is dominated by tails but is still around 3%. This leads to distance uncertainty of only hundreds of meters over several kilometers. The resolution of R_P in kilometers is shown in Figure 7.5 and 7.6.

All geometrical resolutions shown are centered at zero indicating no systematic shifts in geometrical reconstruction. Some improvement can be made by utilizing timing information in the event, however, at this point, other systematic errors will be shown to dominate the errors in the energy calculation and the small gains in geometric resolution would not be visible. A software package called stfit1 is being developed by Jose Bellido to improve stereo geometric reconstruction utilizing the

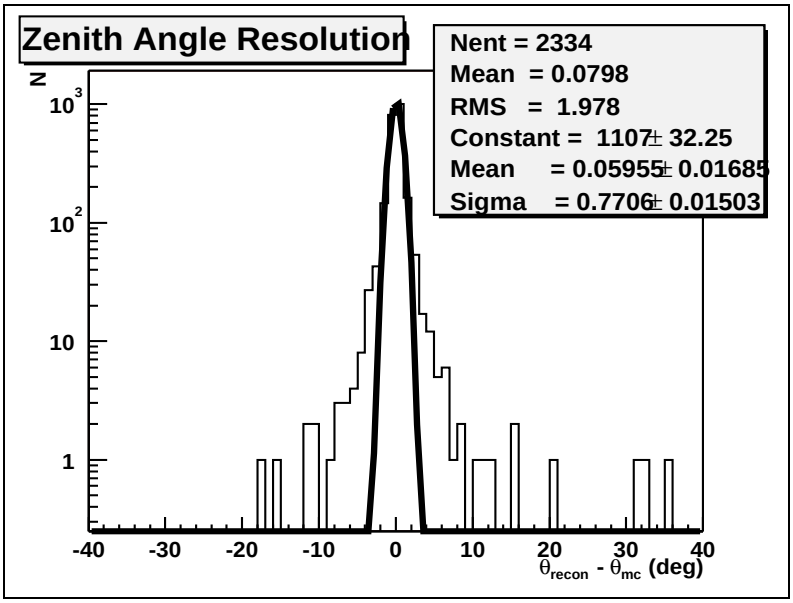

Figure 7.1. Resolution of Impact Zenith Angle θ

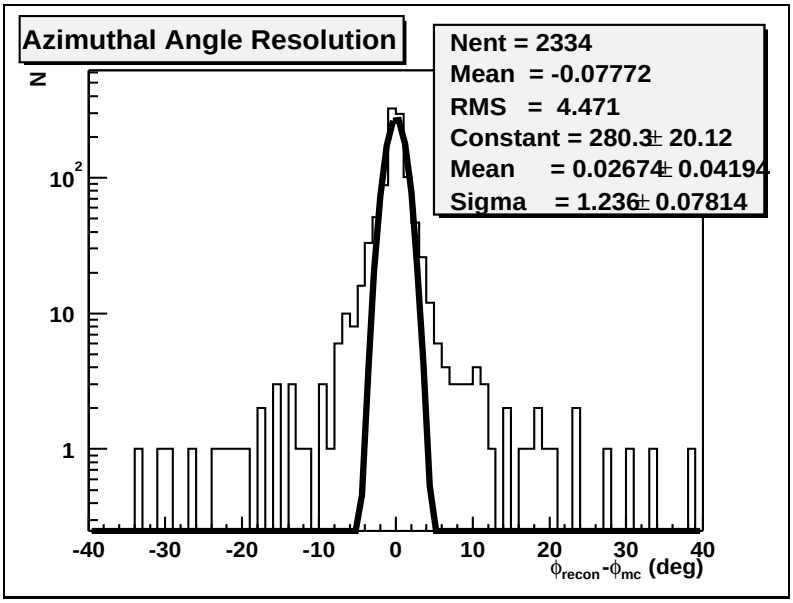

Figure 7.2. Resolution of Impact Azimuthal Angle ϕ

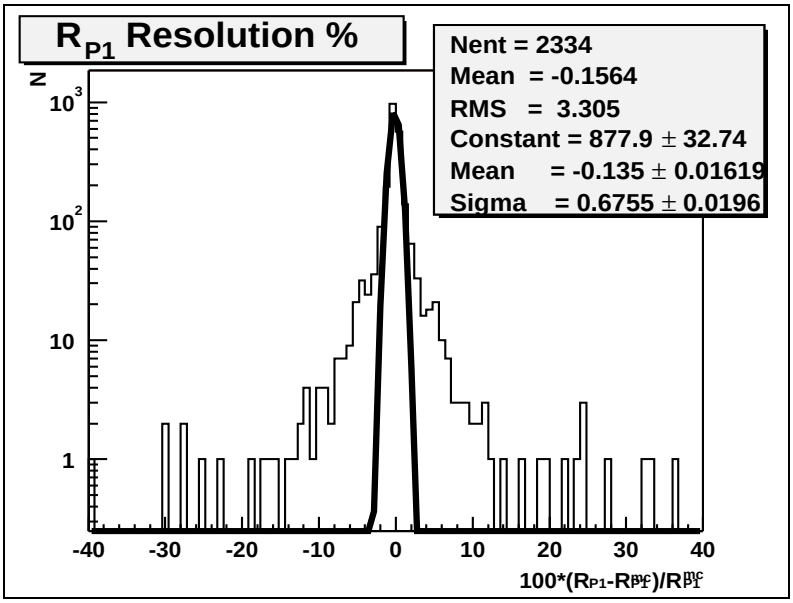

Figure 7.3. Resolution (%) of Impact Parameter for HiRes-1 (R_p) Created from Fly's Eye Spectral Distribution of GQSJet Protons

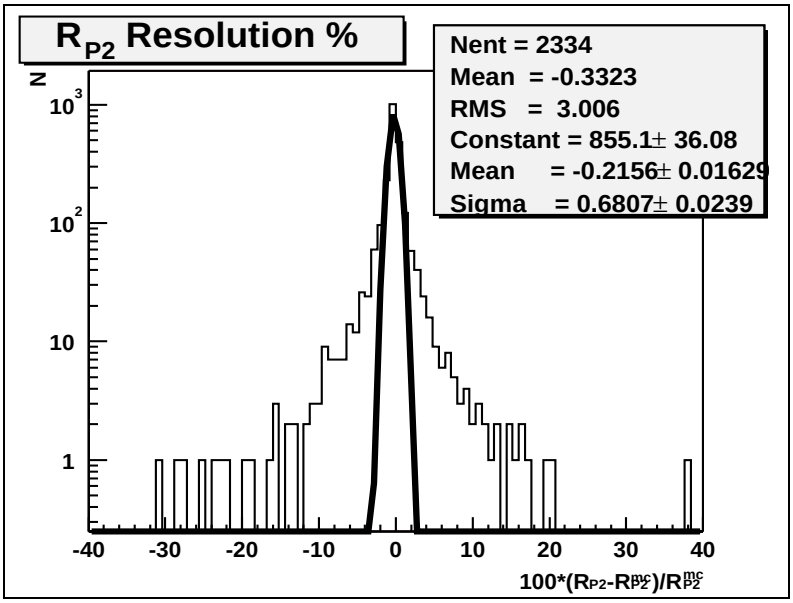

Figure 7.4. Resolution (%) of Impact Parameter for HiRes-1 (R_p) Created from Fly's Eye Spectral Distribution of GQSJet Protons

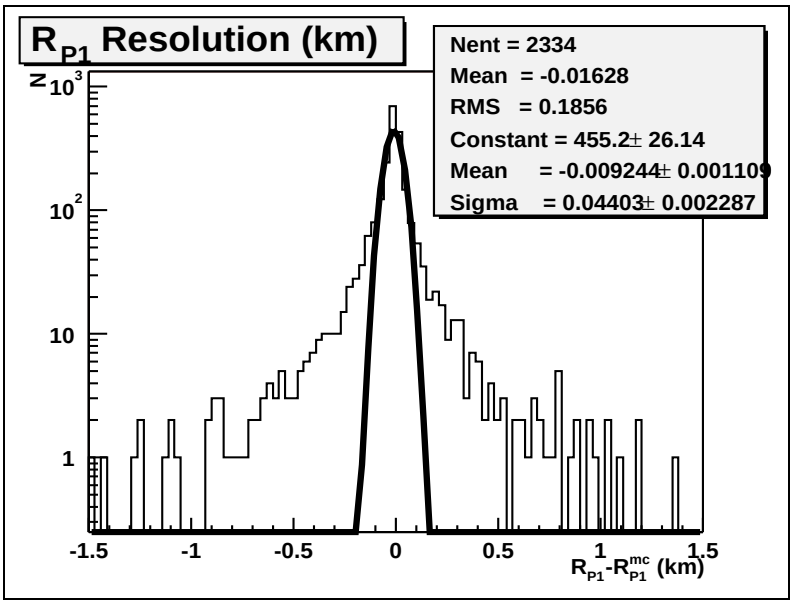

Figure 7.5. Resolution (km) of Impact Parameter for HiRes-1 (R_p) Created from Fly's Eye Spectral Distribution of GQSJet Protons

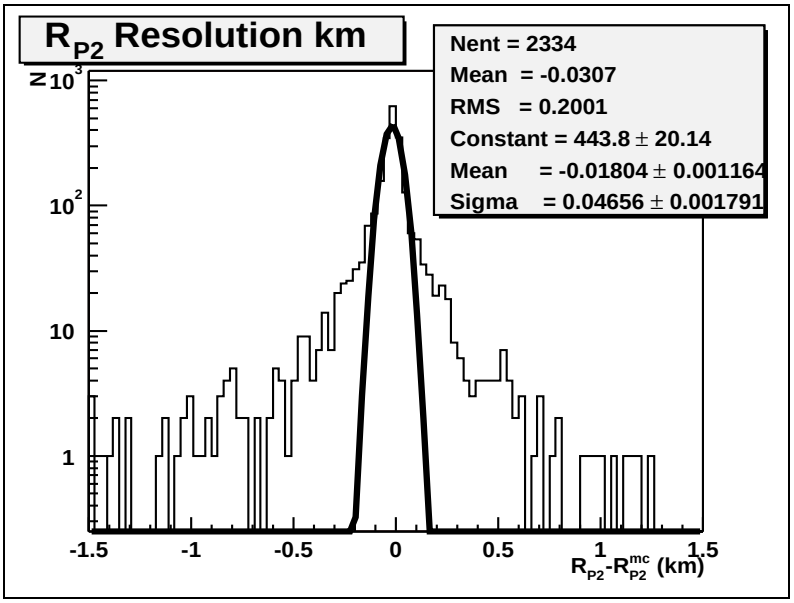

Figure 7.6. Resolution (km) of Impact Parameter for HiRes-2 (R_p) Created from Fly's Eye Spectral Distribution of GQSJet Protons

additional timing information[14]. The calculation of geometric error is done in great detail in his work as this is essential in anisotropy studies.

7.1.2 Physics Quantities

The two most important physics quantities to be determined are the energy of the primary particle and the depth of X_{max}. Figures 7.7, 7.8, 7.9 and 7.10 show the resolution of X_{max} in $grams/cm^2$ for the two species and the two models discussed. In all four cases, a resolution of less than $20g/cm^2$ is shown and all with a systematic shift of around $6g/cm^2$.

Figures 7.11, 7.12, 7.13 and 7.14 show the energy resolution for the two species and models respectively. In all four cases, the intrinsic energy resolution is shown to be better than 10%. For protons, the mean is approximately 5% higher than for iron as expected due to the average composition assumption made for missing energy. This assumption is discussed in section 6.2.2. Figure 7.15 shows one resolution without the quality cut discussed in section 5.7.3.

Figure 7.16 shows the energy resolution if showers are generated using the Gaisser-Hillas shower driver discussed in section 6.2.1. Again the parameters X_0 and λ are fixed at 0 and $70g/cm^2$ respectively. A very tight resolution of less than 5% is seen with no systematic offset. This shows that the Monte Carlo and reconstruction are very consistent when the same assumptions are made for both Monte Carlo generation and reconstruction. Additionally, the fluctuations in E_{em}/E_0 are lost since the average is used. at each energy.

7.2 Distributions

If the Monte Carlo truly simulates the physics of extensive air showers and our detector response, then it should be able to reproduce distributions of quantities

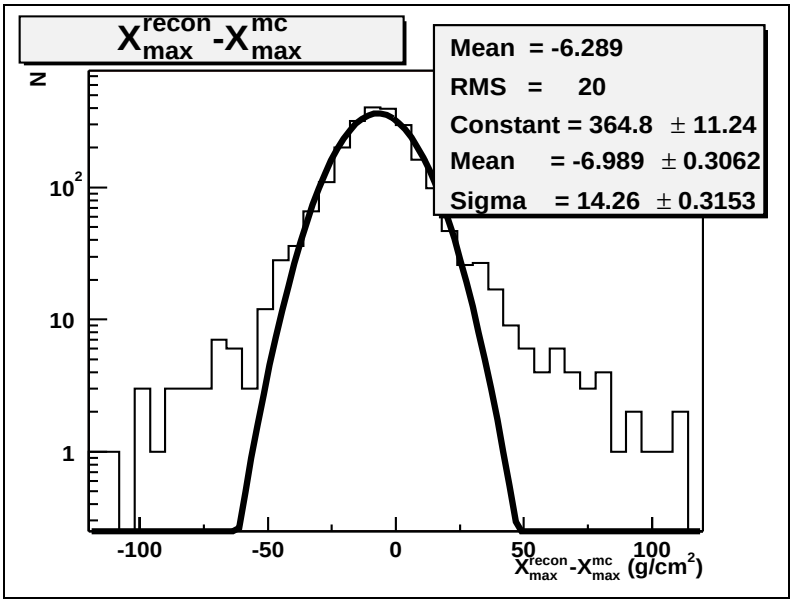

Figure 7.7. Spectral Resolution of X_{max} for QGSJet Protons

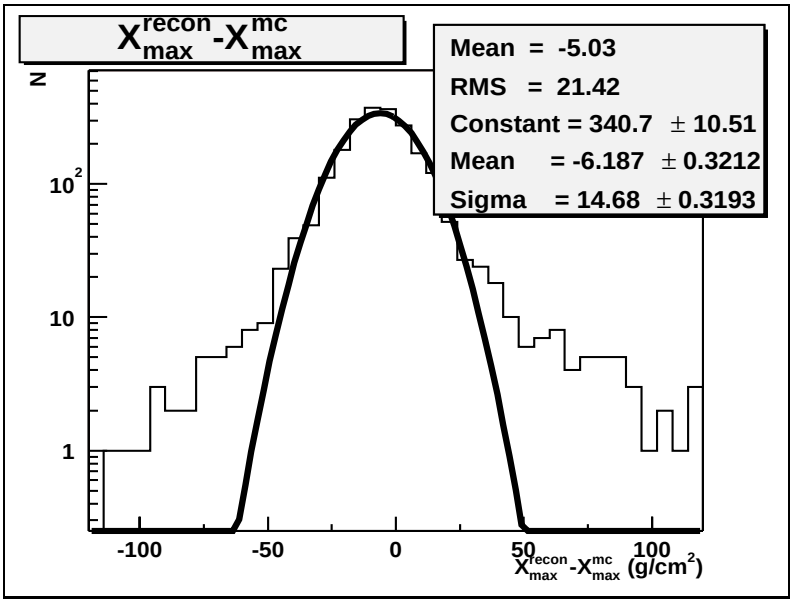

Figure 7.8. Spectral Resolution of X_{max} for SIBYLL Protons

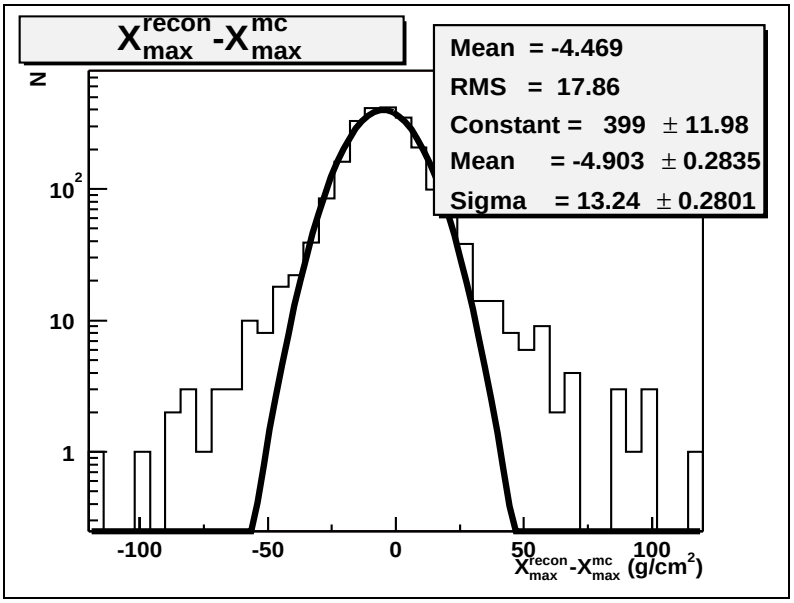

Figure 7.9. Spectral Resolution of X_{max} for QGSJet Iron

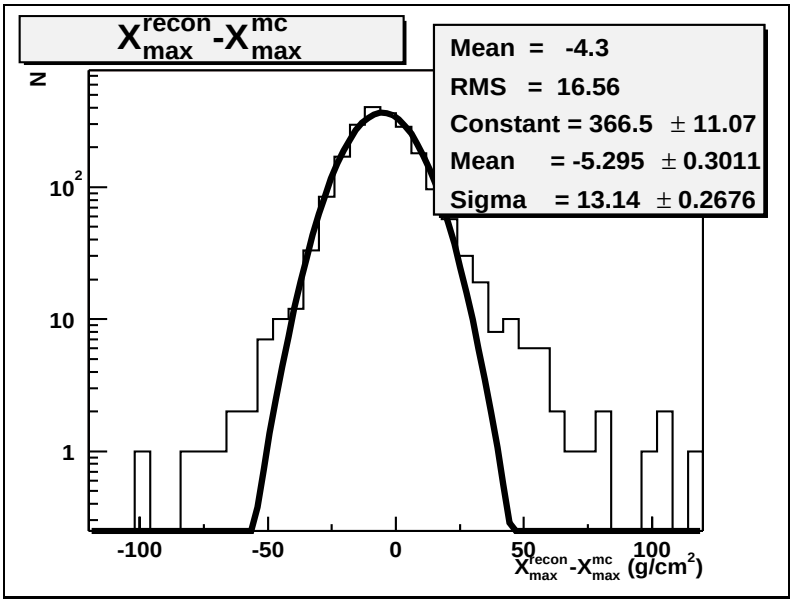

Figure 7.10. Spectral Resolution of X_{max} for SIBYLL Iron

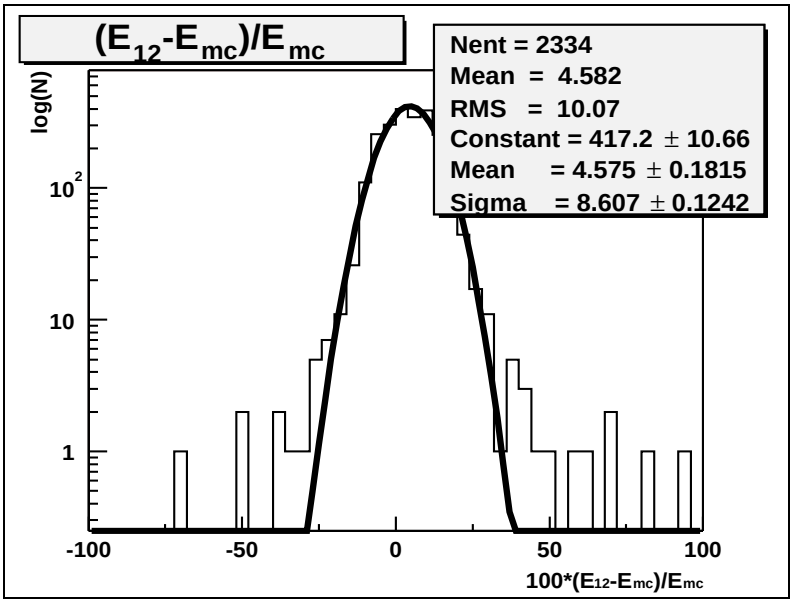

Figure 7.11. Spectral Energy Resolution for QGSJet Protons
The systematic overestimate in energy is expected because of the average composition assumption made.

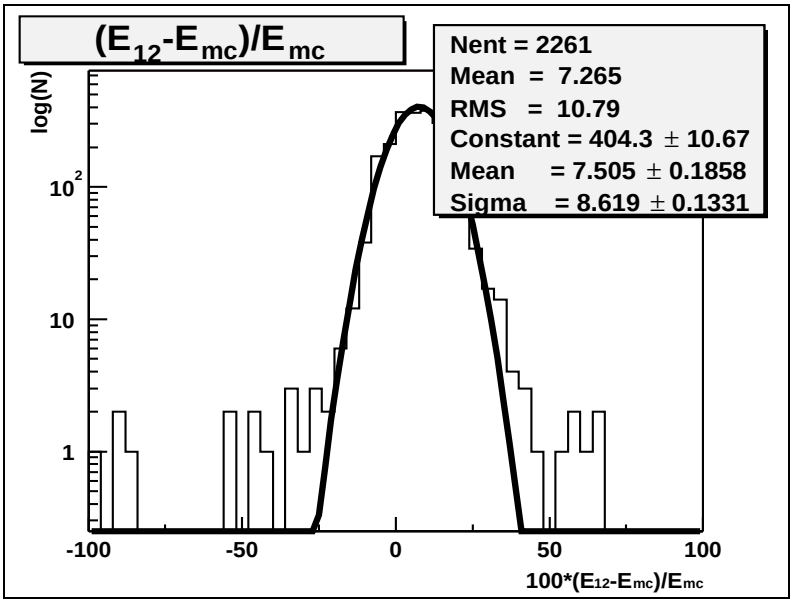

Figure 7.12. Spectral Energy Resolution for Sibyll Protons
The systematic overestimate in reconstructed energy is expected because of the average composition assumption made.

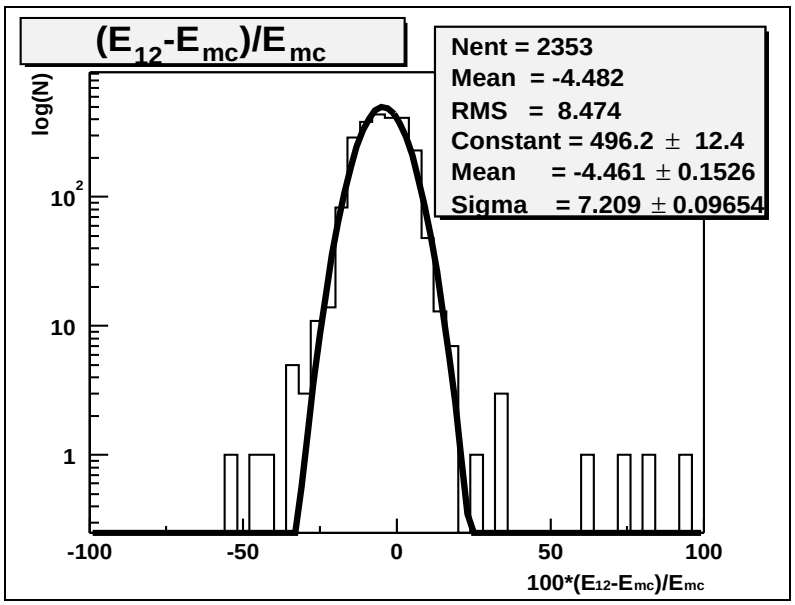

Figure 7.13. Spectral Energy Resolution for QGSJet Iron
The systematic underestimate in reconstructed energy is expected because of the average composition assumption made.

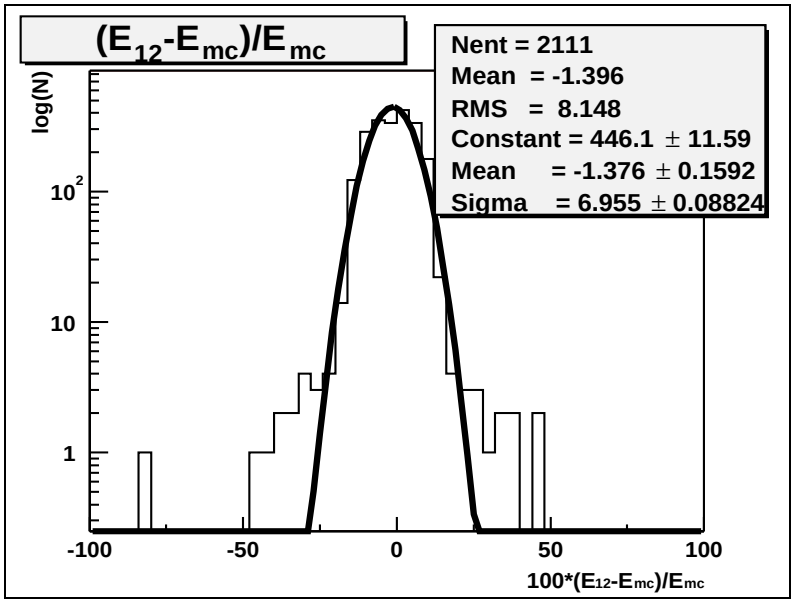

Figure 7.14. Spectral Energy Resolution for SIBYLL Iron
The systematic underestimate in reconstructed energy is expected because of the average composition assumption made.

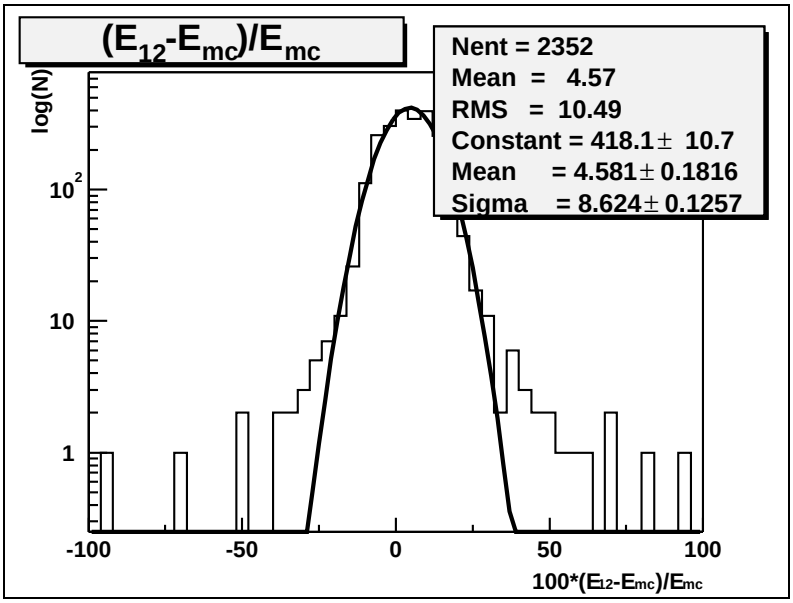

Figure 7.15. Spectral Energy Resolution for QGSJet Protons Without Quality Cut

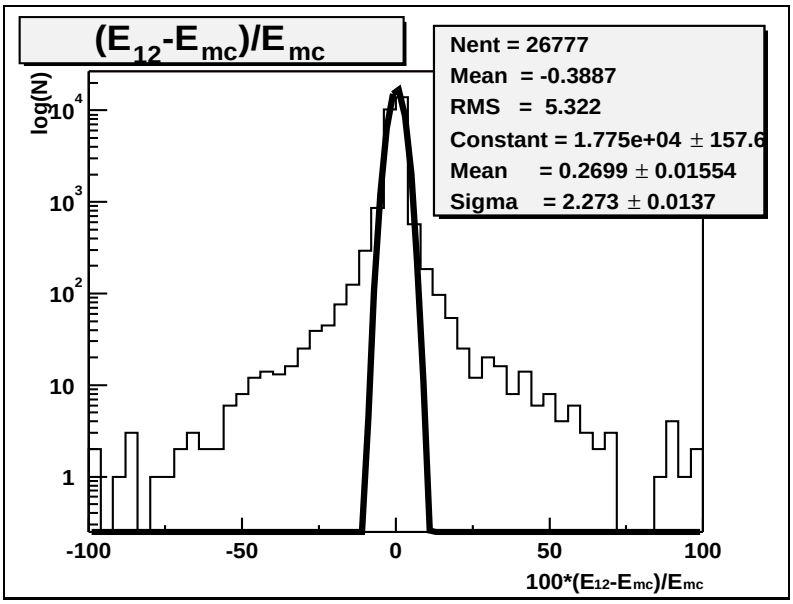

Figure 7.16. Spectral Energy Resolution for Gaisser-Hillas Showers

found in the data. The following comparisons of geometric and physics distributions give support to the veracity of our Monte Carlo simulation.

The following sections show the distributions found in the data of quantities such as distance to shower, zenith angle, X_{max} and energy. Monte Carlo data sets produced from a Fly's Eye stereo spectrum for various models and species are then compared to the data.

7.2.1 Geometric Distribution

Figure 7.17 shows the distribution of zenith angles for events found in the data. Figures 7.18, 7.19, 7.20, and 7.21 all show the distribution of distance to real events. In all cases the Monte Carlo predictions agree very well with the data. Figures 7.22 and 7.23 show the average distance to showers versus the reconstructed shower energy. At all energies, the Monte Carlo predictions agree very well with the data. This gives tremendous support to the calculation of our detector aperture.

Figures 7.24 and 7.25 show the track-length of events at HiRes-1 and HiRes-2. This geometric quantity also appears to be predicted well by the Monte Carlo.

7.2.2 Physics Quantities

Figures 7.26 shows that the distribution of X_{max} values can be correctly predicted for a proton dominated flux. Additionally, Figure 7.27 shows that the average X_{max} value versus energy is also correctly predicted by a flux dominated by protons. As mentioned in chapter 2 composition studies from prior experiments suggested that the composition of cosmic rays was moving towards a lighter composition between 10^{17} and $10^{18}eV$. This trend, ending with a lighter composition, seems supported by this preliminary result. Finally, the number of events seen in each energy bin is predicted very well by the Monte Carlo regardless of species or model. This is shown in Figure 7.28.

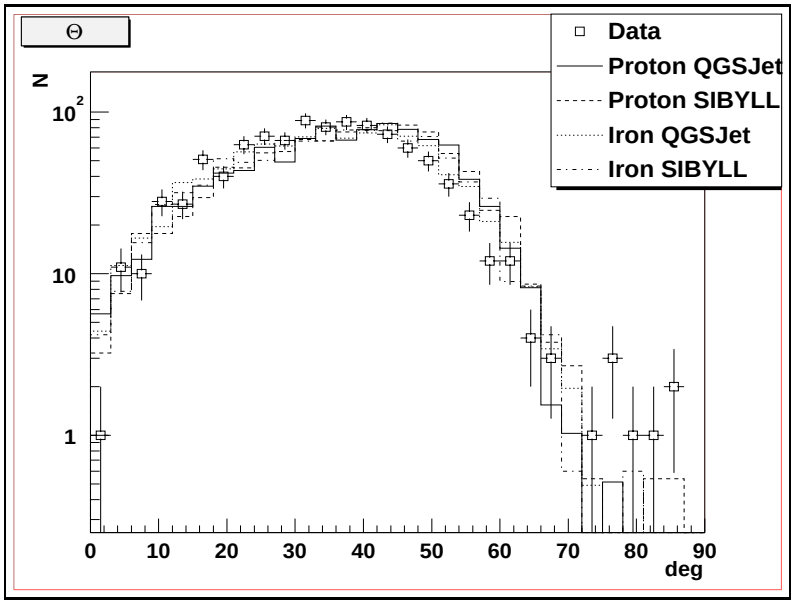

Figure 7.17. Zenith Angle Distibutions for Fly's Eye Spectrum

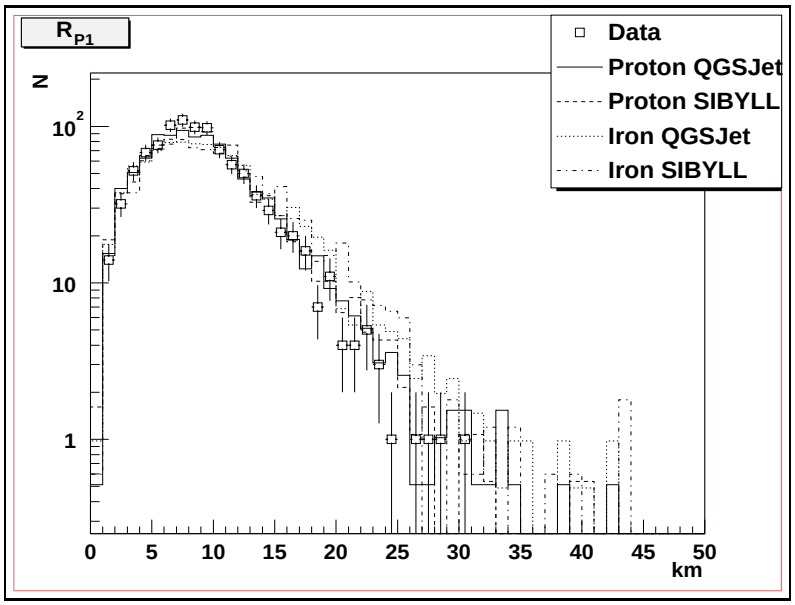

Figure 7.18. R_p Distributions for HiRes-1

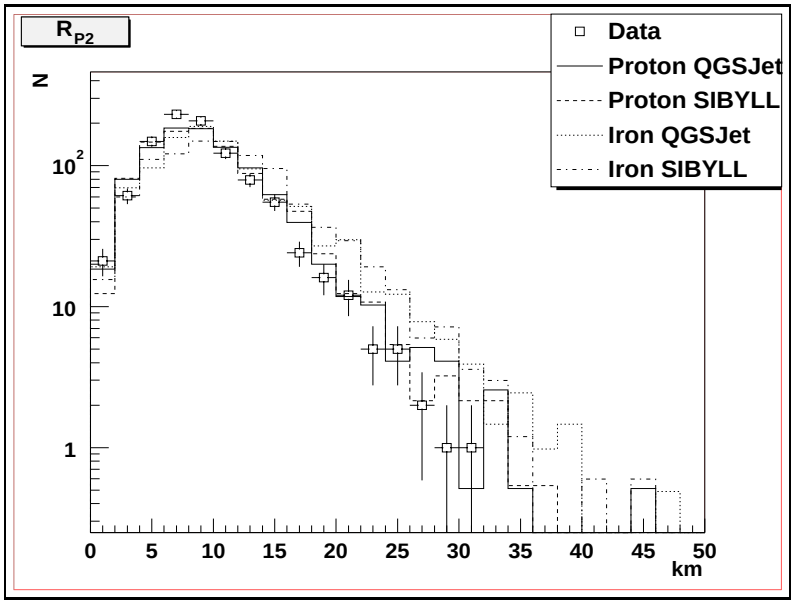

Figure 7.19. R_p Distributions for HiRes-2

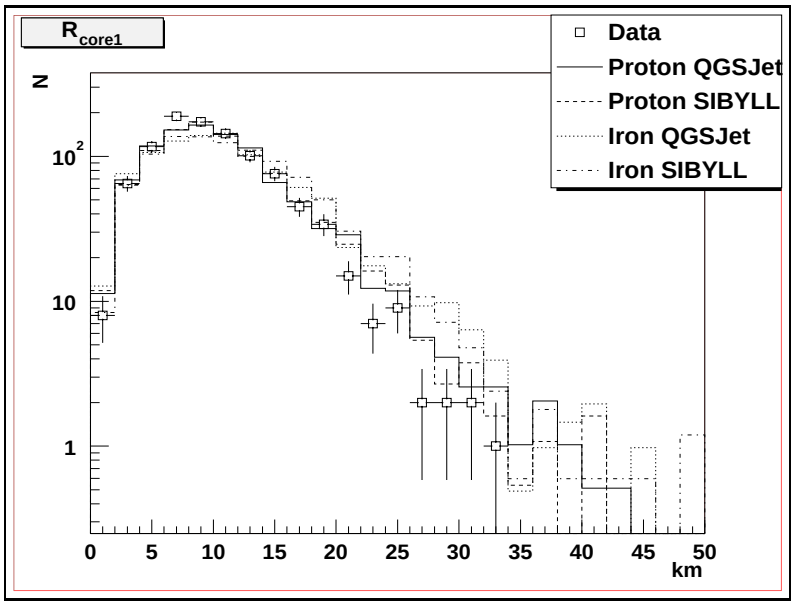

Figure 7.20. R_{core} Distributions for HiRes-1

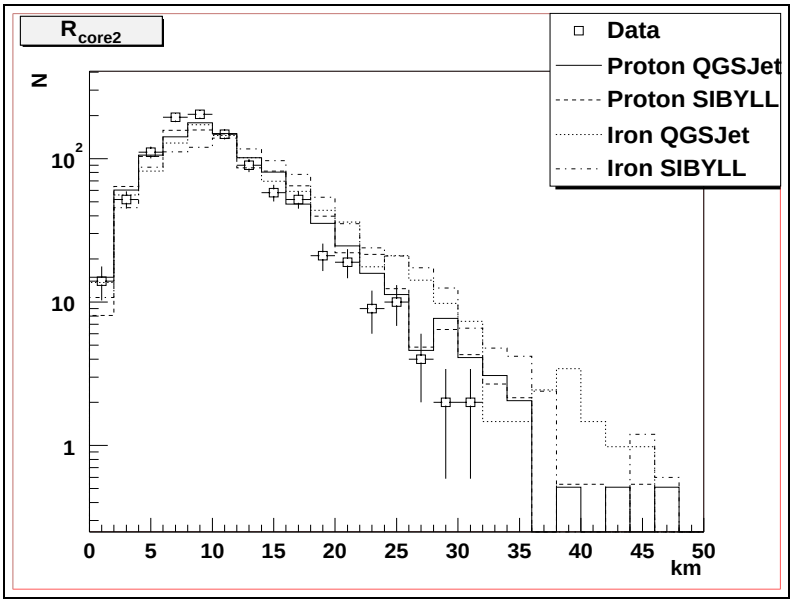

Figure 7.21. R_{core} Distributions for HiRes-2

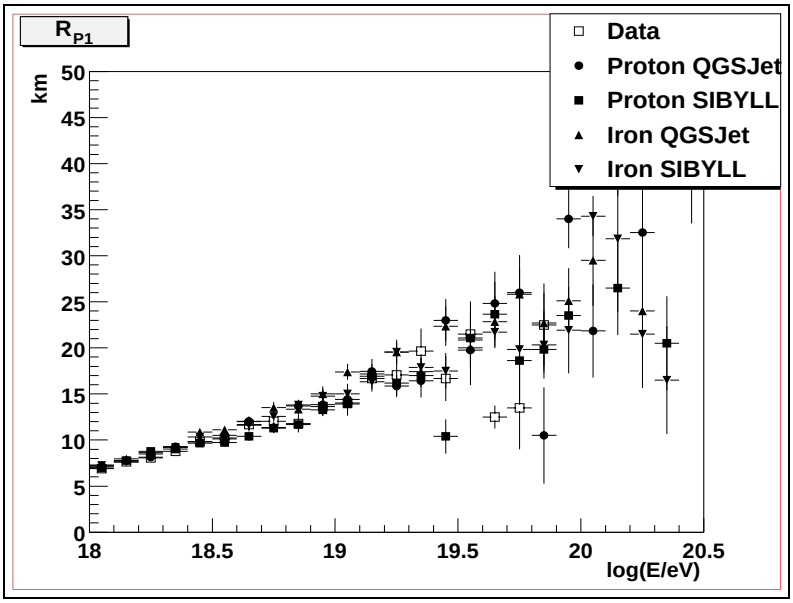

Figure 7.22. R_{P1} vs. log(E/ev)

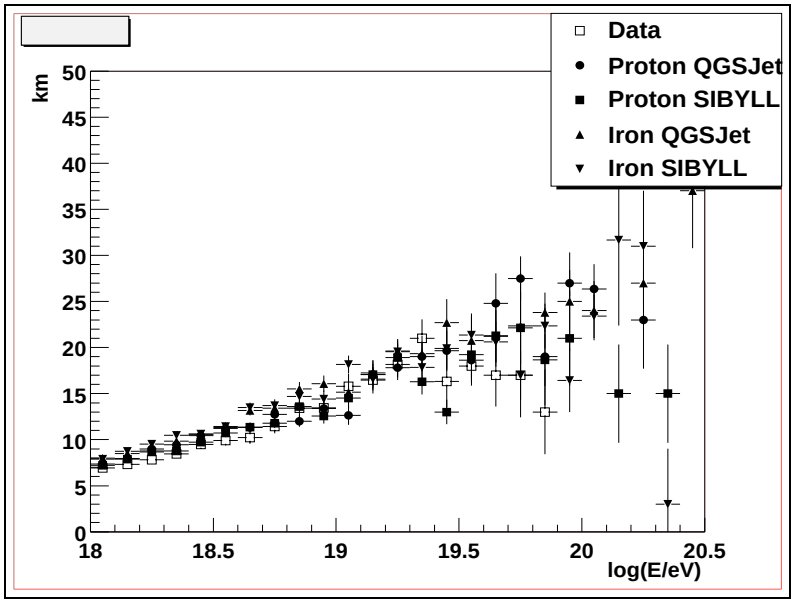

Figure 7.23. R_{P2} vs. log(E/ev)

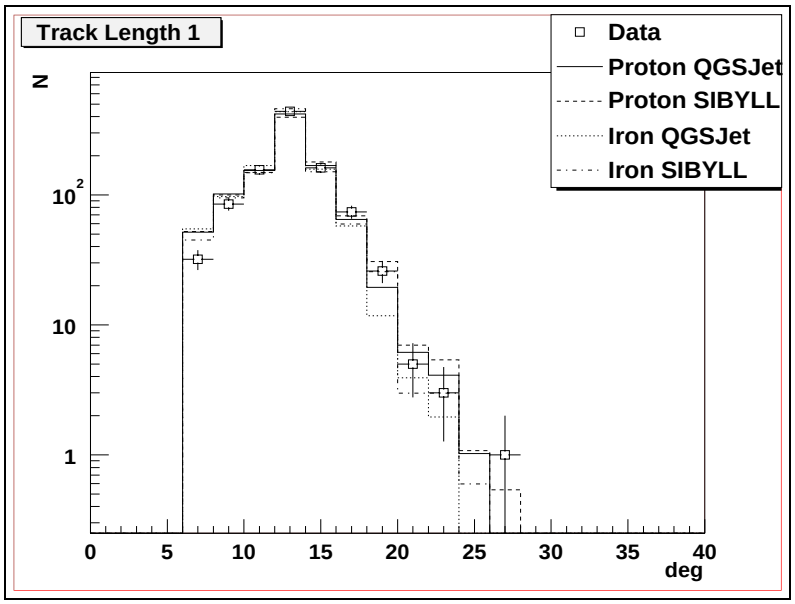

Figure 7.24. Tracklength Distributions at HiRes-1

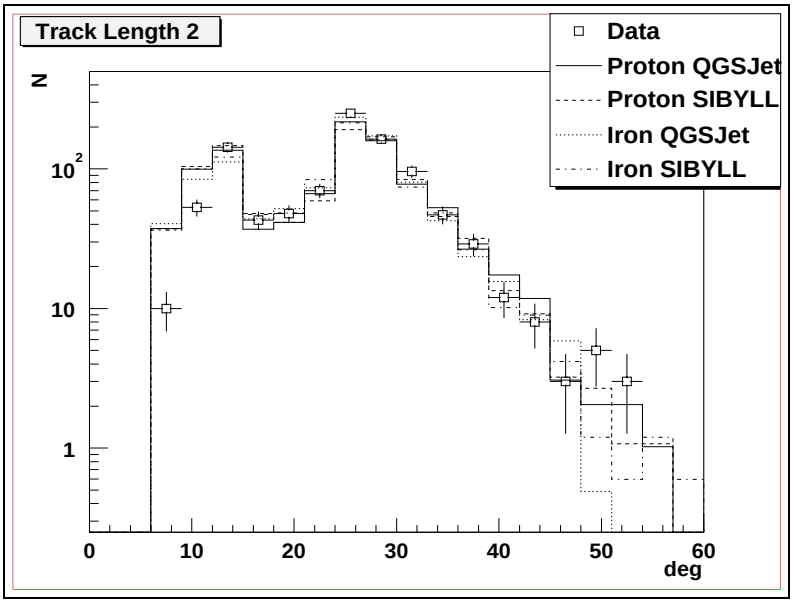

Figure 7.25. Tracklength Distributions at HiRes-2

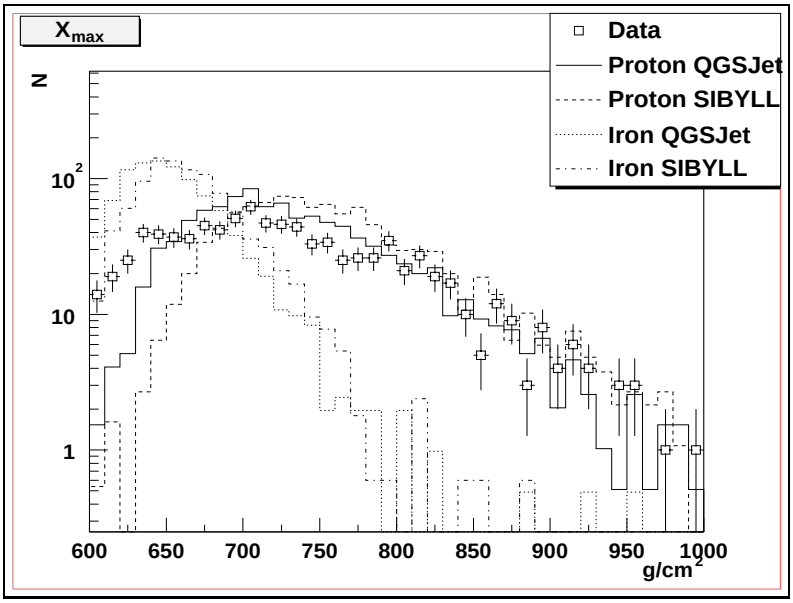

Figure 7.26. X_{max} Distributions

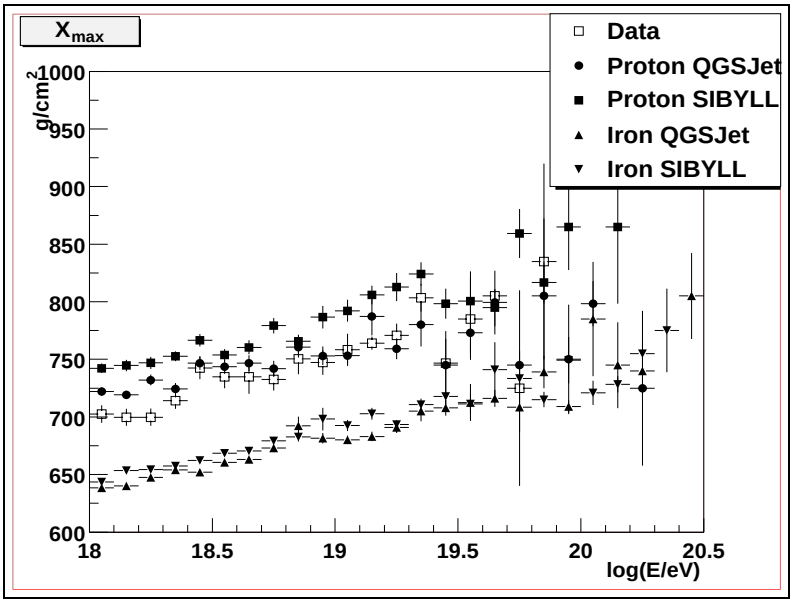

Figure 7.27. Average X_{max} vs. Energy

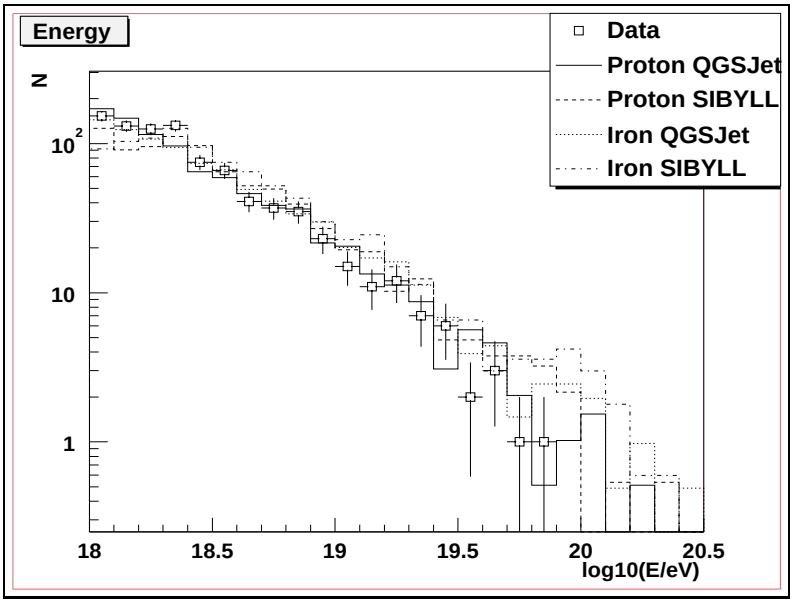

Figure 7.28. Distributions of Energy

CHAPTER 8

ENERGY SPECTRUM

The energy spectrum measurement is calculated using the formula

$$J(E) = \frac{dN/dE}{A\Omega(dE)\ \Delta t} \tag{8.1}$$

where dN/dE is the number of events in each energy bin, $A\Omega$ is the detector aperture and Δt is the exposure time. In practice, this equation becomes

$$J(E_i) = \frac{N(E_i)/\Delta E_i}{(A\Omega(E_i))\ \Delta t(E_i)}. \tag{8.2}$$

Calculations in this section are done using histograms and the E_i terms are the width of the energy bin being calculated.

8.1 Aperture

Calculating the aperture of our detector should be accomplished by the integral

$$A\Omega(E_i) = \int_{R_{min}}^{R_{max}} r\ dr \int_0^{2\pi} d\phi \int_0^{\pi/2} \sin\theta d\theta\ \eta(r,\theta,\phi,E). \tag{8.3}$$

However, $\eta(r,\theta,\phi,E)$ is not known. Instead, the aperture of our detector is determined using the Monte Carlo simulation with AΩ is determined according to

$$A\Omega(E_i) = A_{assumed} \times \Omega_{assumed} \times \eta_{calculated} \tag{8.4}$$

$$A\Omega(E_i) = \pi(R^2_{p_{max}}(E_i) - R^2_{p_{min}})\ 2\pi\ \eta_{trig}(E_i) \tag{8.5}$$

where $R_{p_{min}} = 0.5km$. To maximize the speed of this calculation the aperture is calculated separately for each 0.1 log(E) energy bin. For each bin a unique $R_{p_{max}}$

value is used. The value is selected to be large enough to fully enclose the true aperture but small enough to facilitate quick computation. $R_{p_{max}}$ is determined according to

$$R_{p_{max}}(E_i) = 20 + 20 * (X - 18) + 2 * Y \ km \tag{8.6}$$

where the energy of the current point is $Y * 10^X$. The reason for this formulas odd shape is the limitations of mathematics in the Korn shell scripts used to submit these Monte Carlo jobs. Using equation 8.6 the assumed $R_{p_{max}}$ starts at 22 km for 10^{18} eV showers and rises to 62 km for 10^{20} eV showers. Figure 8.1 shows both equation 8.6 and the distribution of R_p values which actually trigger our detector when R_p is set to a maximum of $70km$.

The efficiency at which events at the given energy trigger our detector within the overly large aperture is $\eta_{trig}(E_i)$. Events are "thrown" uniformly into all geometries covered by $(0.5km < R_p < R_{p_{max}})$, $(0 < \phi < 360)$ and $(0 < \theta < \pi/2)$ which covers our potential 2π solid angle. The trigger efficiency is then

$$\eta_{trig}(E_i) = \frac{N_{trig}(E_i)}{N_{thrown}(E_i)} \tag{8.7}$$

However, what we really need to know is not the trigger aperture of our detector, but rather the aperture in which events can be reconstructed. To determine our reconstructed aperture the events that trigger our detector are subjected to the same cuts which the data undergoes. These cuts are detailed in Chapter 5. After applying these cuts, η becomes

$$\eta_{reconstructed}(E_i) = \frac{N_{recon}(E_i)}{N_{thrown}(E_i)} \tag{8.8}$$

and our final aperture is

$$A(E_i)\Omega = \pi R^2_{p_{max}}(E_i)\ 2\pi\ \eta_{recon}(E_i). \tag{8.9}$$

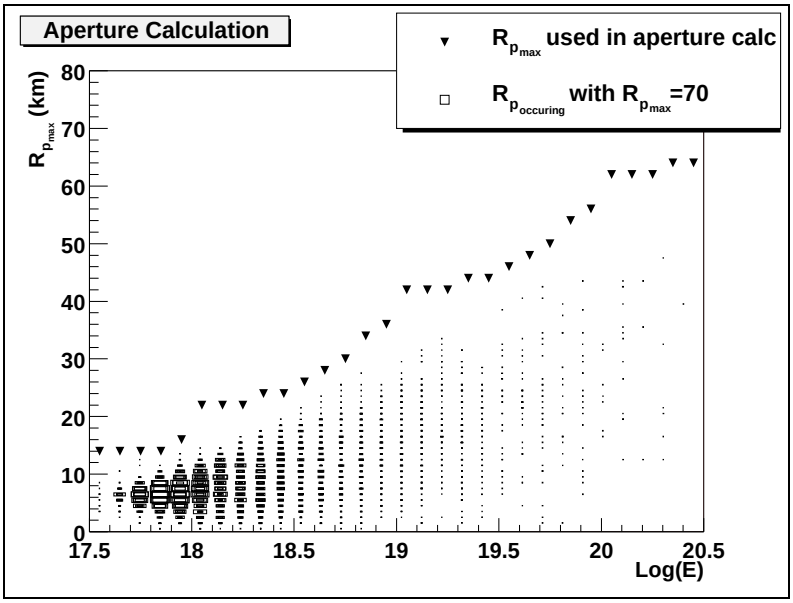

Figure 8.1. $R_{p_{max}}$ with overlay of $R_{p_{max}}$=70km
Triangles show the $R_{p_{max}}$ value used to calculate the aperture for each energy bin. Below the triangles are the distribution of R_P values which trigger our detector at the given energy when $R_{p_{max}}$ is set to 70km.

In addition to trigger and reconstruction efficiencies, the atmospheric assumptions that we make also affect the aperture. If more aerosols are present, then more light is lost between the air shower and our detector. This reduces the distance at which a given air shower can be seen and reconstructed. The detector aperture has been calculated for a full range of atmospheric conditions. Additionally, assuming a pure molecular atmosphere provides an upper bound on the aperture.

Figures 8.1, 8.2 and 8.3 illustrate the procedure to determine the aperture. Figure 8.2 shows the number of events that were thrown in each energy bin. Additionally it shows the number of those events that triggered our detector and the number that could be reconstructed. In calculating the aperture between 10,000 and 100,000 events were thrown in each energy bin with between 1,000 and 2,000 events triggering and being reconstructed. Figure 8.3 shows the η efficiency values

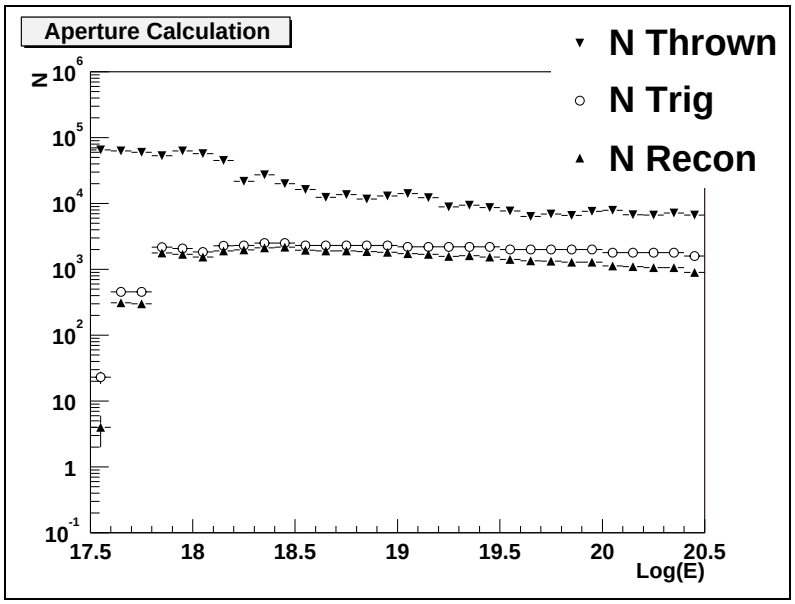

Figure 8.2. Number of Thrown, Triggerred and Reconstructed Events vs log(E)

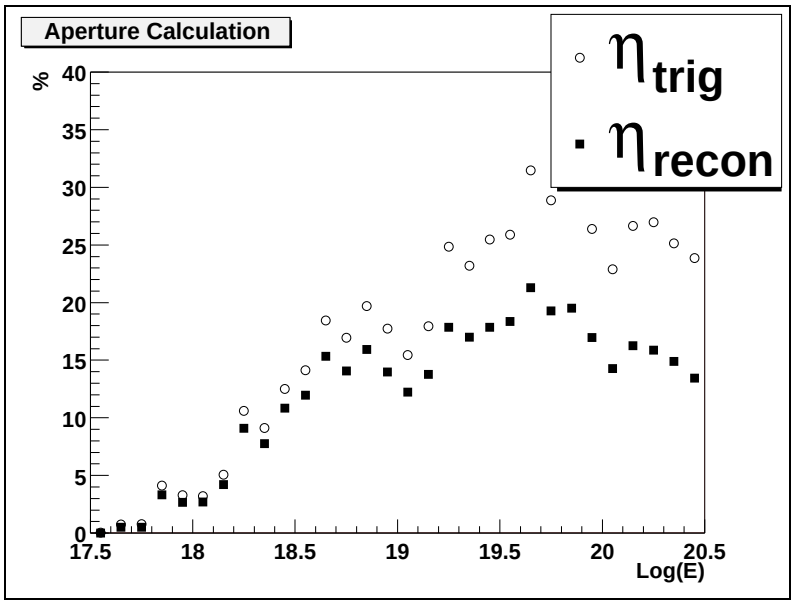

Figure 8.3. η Values for Aperture Calculation

for the aperture calculation. Figure 8.1 shows the $R_{p_{max}}$ values used in all aperture calculations and is overlayed with the distributions of R_ps which trigger our detector when $R_{p_{max}}$ is set to 70 km.

Finally, Figure 8.4 shows our calculated aperture using our average atmosphere and the one sigma variations in measured optical depth. Additionally, molecular and standard desert atmospheres are included for reference. The apertures are then fit to

$$A\Omega = 10^{A*(1-exp(\frac{B-log(E)}{C}))} \tag{8.10}$$

which fits the aperture very well. This fitting reduces any statistical fluctuations.

In Figure 8.4 it is difficult to see the variations between the different atmospheric assumptions because the aperture changes so quickly. Figure 8.5 shows each apertures ratio to the average atmospheric aperture. This figure shows that the aperture is changed by less than 20% above $10^{18}eV$ over a very large range of atmospheric parameters. These figures also show, however, that below $10^{18}eV$ the aperture falls two orders of magnitude very quickly and the calculated apertures for different atmospheric assumptions diverge very quickly. For these reasons, the spectrum measurement starts above $10^{18}eV$.

8.2 Exposure

The calculation of exposure (Δt) is relatively easy. First the overlap in time between the HiRes-1 and HiRes-2 data parts must be calculated. The stereo start time is the later of the two start times and the end time is the earlier of the two end times. The start and stop times are the second since midnight UT. Table 8.1 gives an illustration from the data.

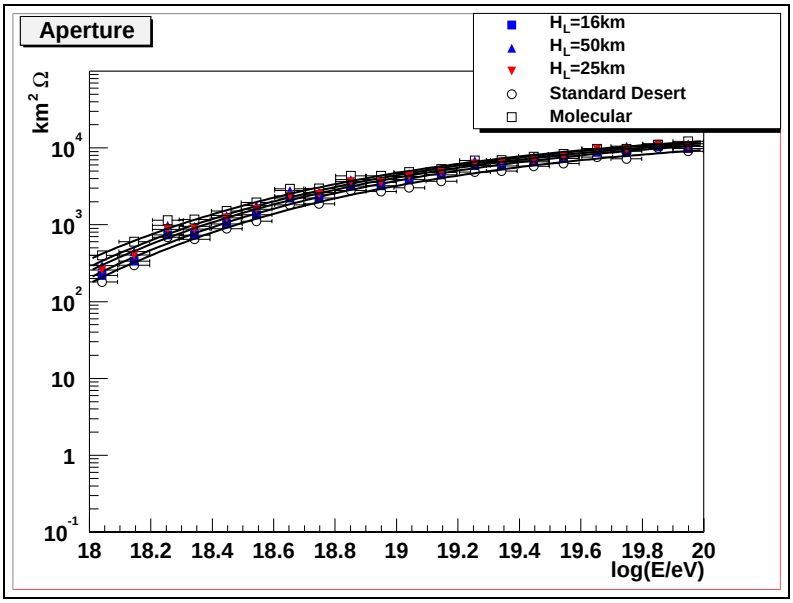

Figure 8.4. Calculated Apertures

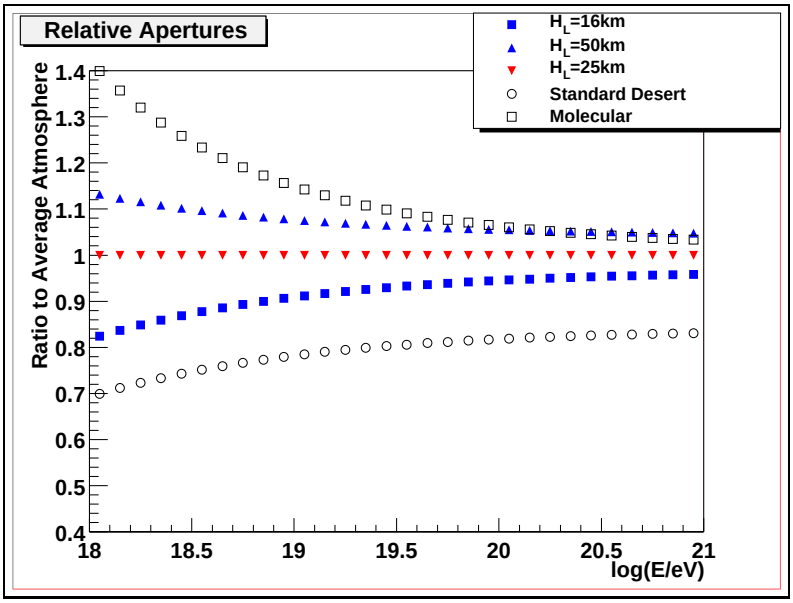

Figure 8.5. Apertures Relative to Average Atmosphere

Table 8.1. Stereo Overlap Calculation

Stereo Exposure / Date 20010115				
Site	Part	Start	Stop	Ontime
HiRes-1	p02	13829	16459	2630
HiRes-2	p024	14413	15974	1561
Stereo	p02p024	14413	15974	1561

8.2.1 Missing Mirrors

There are also time dependent aperture corrections that must be made. The most important correction is that of missing mirrors. For more than one half of our exposure time, we operated our detector with at least one mirror not operating. The full detector aperture is calculated assuming all mirrors are functional. The effect of a missing mirror is the percent of events that are lost in each energy bin if that mirror is removed. The correction is made by determining the percent of Monte Carlo events that are no longer reconstructable if a mirror is removed. An event is assumed to no longer be reconstructable if more than 60% of the tubes in the event are on the missing mirror(s). Additionally, if the track-length is reduced to less than 6^o it would not be reconstructed. Multiplying the total exposure of the part by the relative percentage of remaining events in each energy bin provides a time weighted, energy dependent aperture correction.

The correction that must be made to the aperture depends on which mirror is not functioning. Figures 8.6 through 8.12 display the effect of different mirrors being absent. This leads to the energy dependent exposure $\Delta t(E_i)$ which is really a time dependent aperture correction.

Some important features of our detector are also visible from these figures. For example, our low energy aperture is mostly contained between our two sites. Mirror

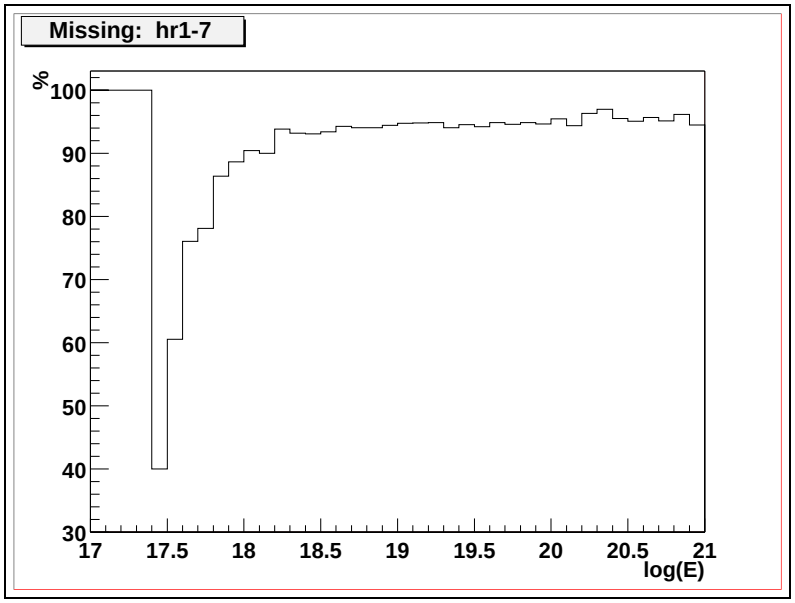

Figure 8.6. Aperture Correction with HiRes-1 Mirror 7 Missing

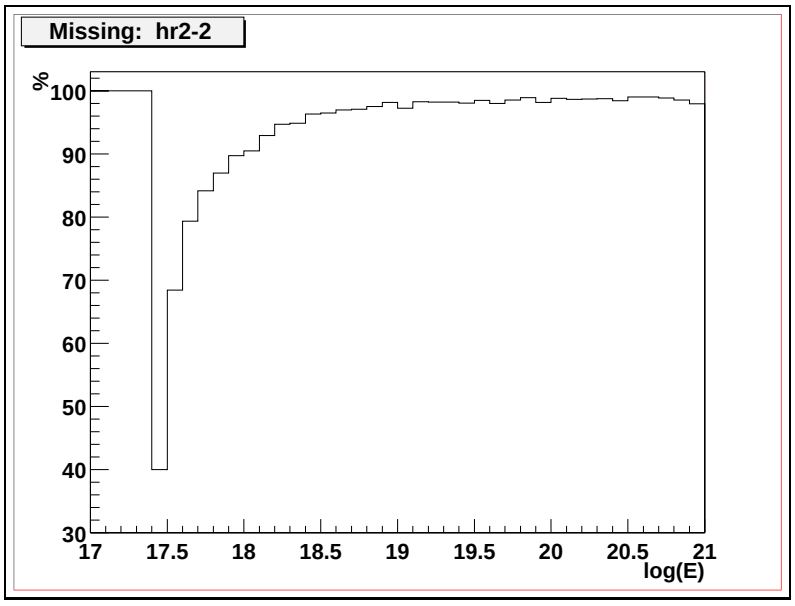

Figure 8.7. Aperture Correction with HiRes-2 Mirror 2 Missing

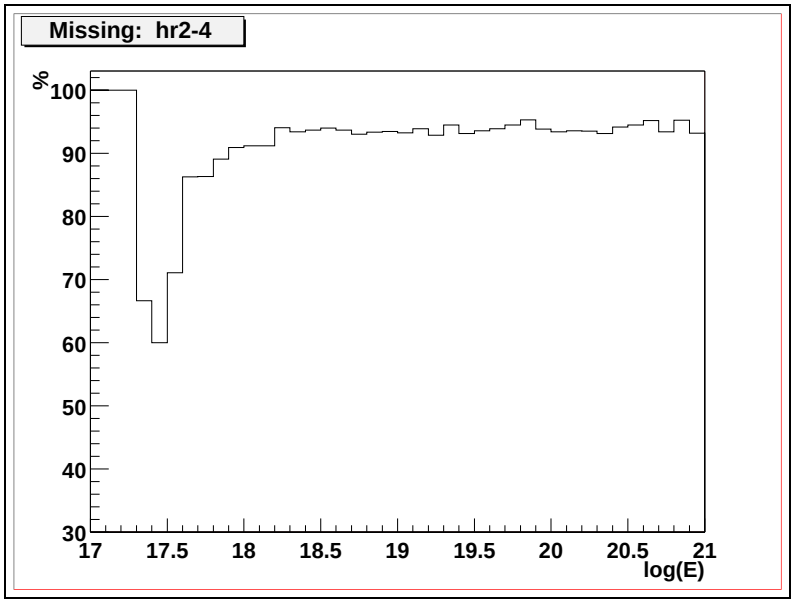

Figure 8.8. Aperture Correction with HiRes-2 Mirror 4 Missing

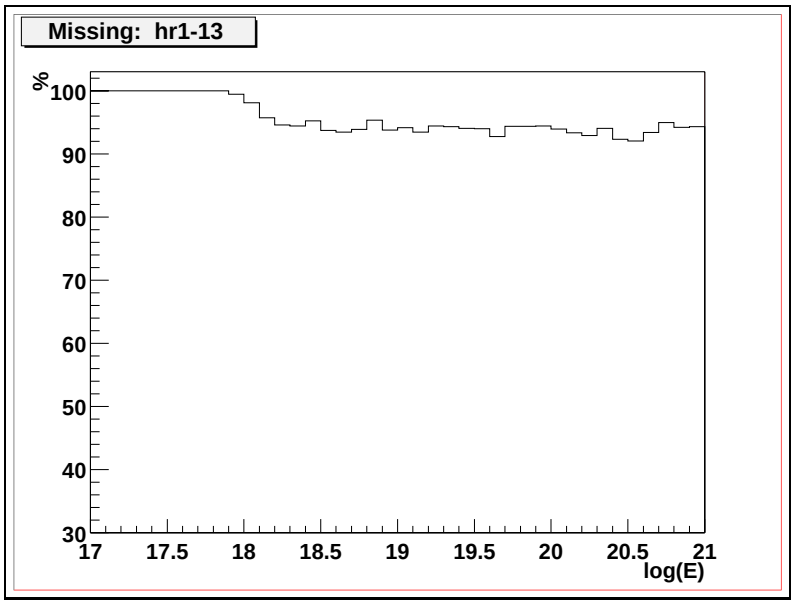

Figure 8.9. Aperture Correction with HiRes-1 Mirror 19 Missing

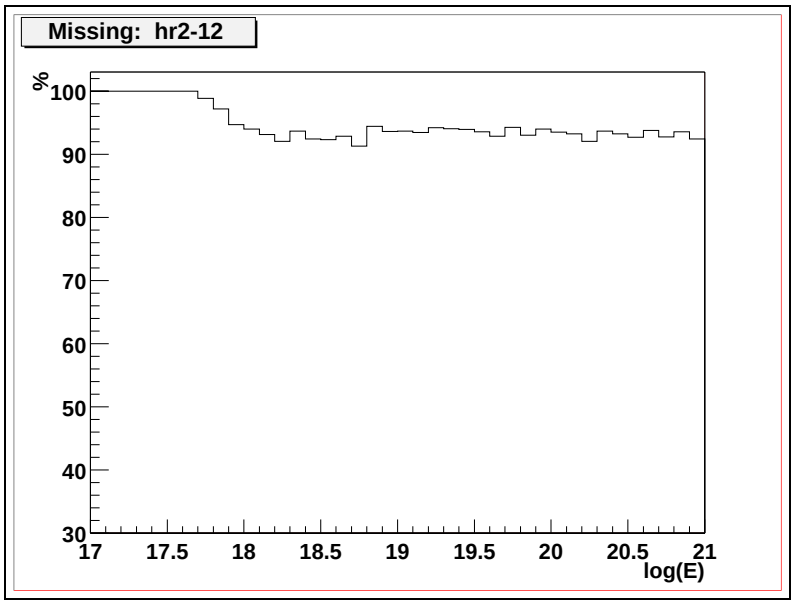

Figure 8.10. Aperture Correction with HiRes-2 Mirror 12 Missing

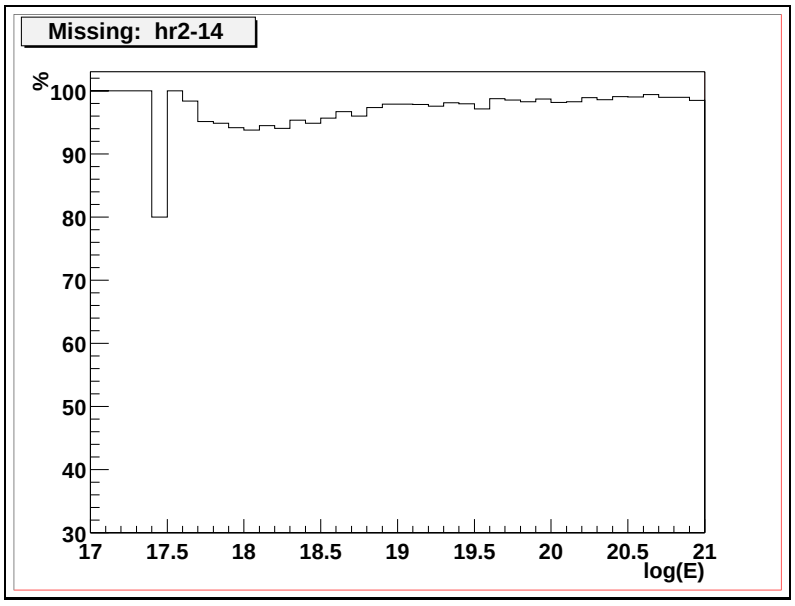

Figure 8.11. Aperture Correction with HiRes-2 Mirror 14 Missing

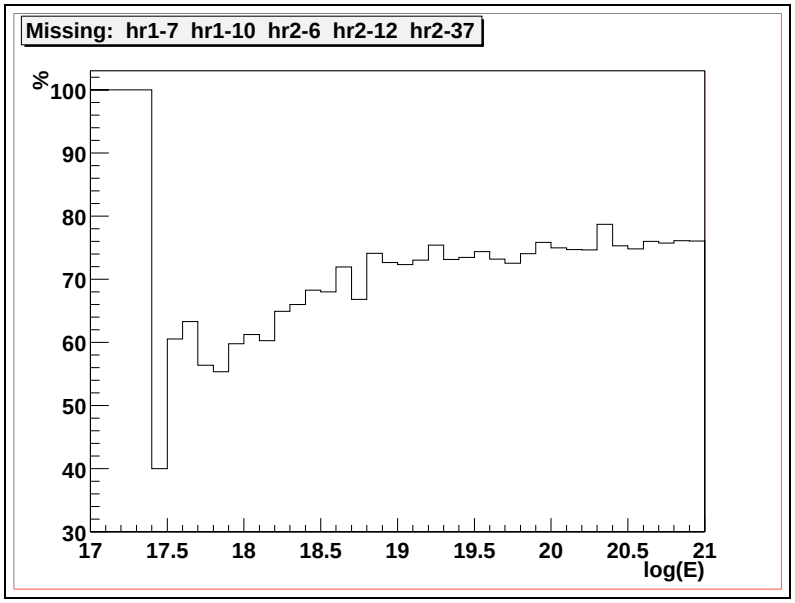

Figure 8.12. Aperture Correction with Several Mirrors Missing

7 at HiRes-1 looks almost directly at HiRes-2. Therefore, its absence removes a great deal of our 10^{18} aperture as shown in Figure 8.6. Additionally mirrors 2 and 4 are ring 1 and 2 mirrors looking towards HiRes-1. Figures 8.7 and 8.8 show not only the low energy effect but also that very little high energy aperture is located within the upper ring of HiRes-2. This is expected since at 10^{20} eV events are on average so far away that they do not develop until they are below this upper ring's view. A much smaller high energy effect is seen in Figure 8.7 than 8.8 for this reason.

If the mirror in question is not looking toward the opposing site, the low energy effect is almost removed. Figures 8.9 and 8.10 show little effect on apertures at low energy. These figures indicate the effect increasing to almost 5% at higher energy. This 5% effect is expected as each mirror views $16^o/360^o$ or about 5% of the field of view. Figure 8.11 shows a relatively small effect at all energies. The small low energy aperture correction is a result of its north facing orientation. The small

correction at high energy is the result of mirror 14's upper ring location. Finally, Figure 8.12 shows the effect of removing many mirrors. This happens rarely in the data.

To continue the example from the data in Table 8.2, Figure 8.13 shows the missing mirrors on-time correction for that stereo part. The total on time from the part is 1561 seconds or 0.433 hours. Since we have no aperture below $10^{17.5}$ these columns are never corrected and allow tracking of the full on time. Mirror 18 at HiRes-1 was missing in this part. A small correction at higher energies must be made as shown.

By adding together the histograms (like Figure 8.13) for all stereo data parts, we produce our total stereo on time histogram containing $\Delta t(E_i)$ (Figure 8.14). This shows that the total stereo on time is just over 600 hours. Figure 8.15 shows the exposure histogram used in this analysis. This figure is made after applying the $N_{flasher} >= 20$ cut (see section 5.7.1). The flasher cut removes less than 5% of our exposure but provides assurance that our detectors were synchronized. If our detectors are not synchronized then we will overestimate our exposure.

8.2.2 HiRes-2 Deadtime

The data rates at HiRes-2 are significantly higher than at HiRes-1. At times, so much information needs to be read out that the detector must disable triggers in order to prevent memory from filling. This causes a dead time in which the detector is not actually taking data. This time is, however, included in the exposure necessitating a correction. Figure 8.16 shows the time weighted dead time for all data parts in this analysis. The net reduction in exposure is 4.3%. This information is calculated in the "pass1" processing and stored in as part of a summary created for each data part.

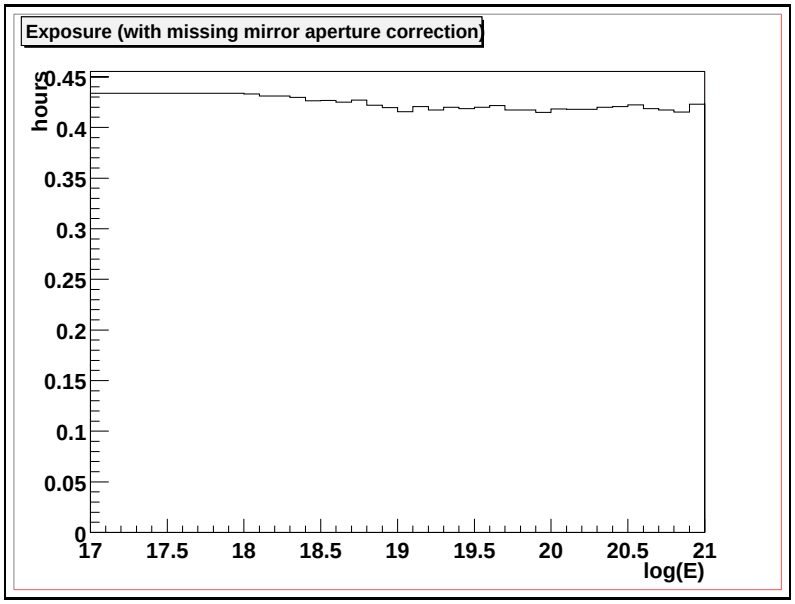

Figure 8.13. Missing Mirror Correction For y2001m01d15p02p024

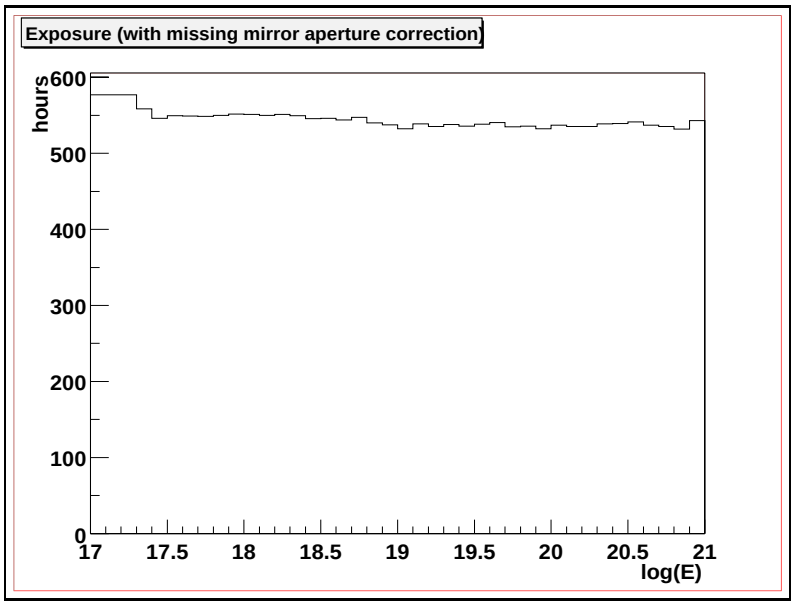

Figure 8.14. Total Stereo Exposure: Prior to $N_{flasher} >= 20$ Cut

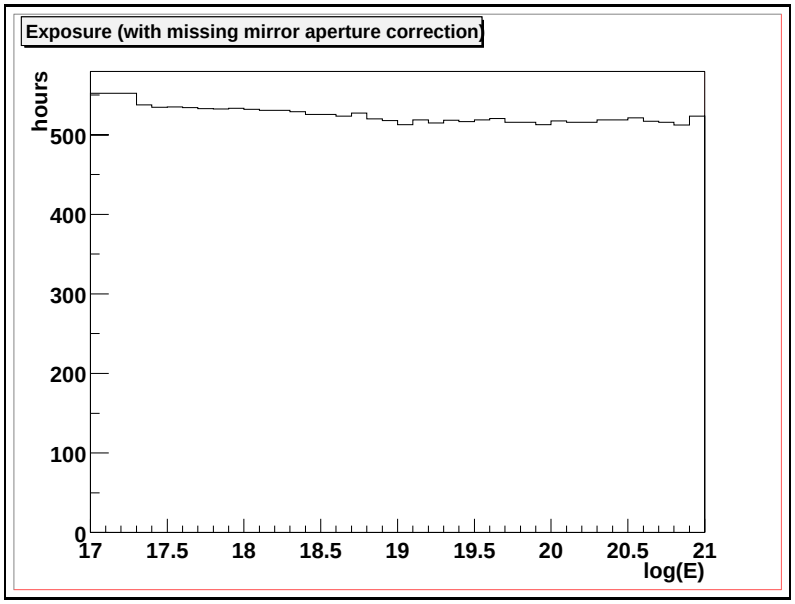

Figure 8.15. Total Stereo Exposure: After $N_{flasher} >= 20$ Cut

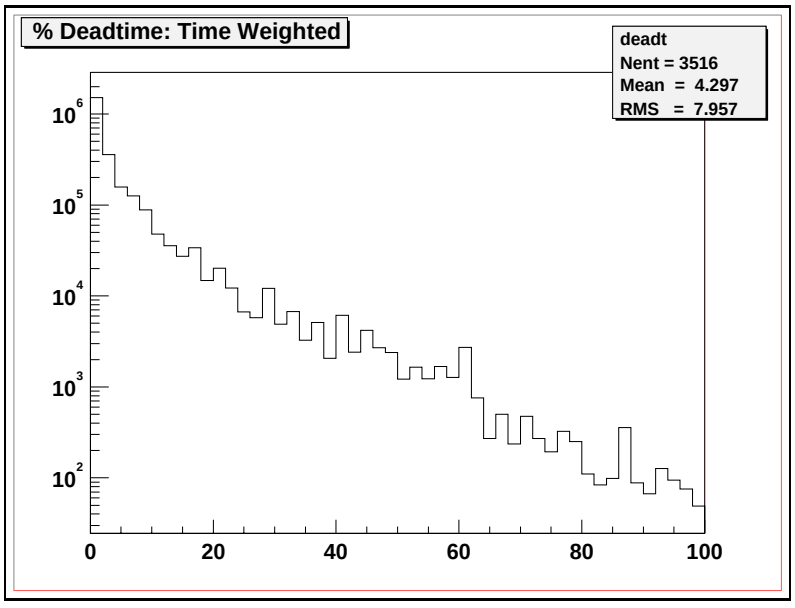

Figure 8.16. Time Weighted HiRes-2 Deadtime

8.3 ΔN/ΔE

The energy distribution of events found in the data using the average atmosphere is shown in Figure 8.17. The reconstructed energy is found by simulataneously minimizing the χ^2 value for both site using equation 5.6. Figure 8.18 shows the energy distribution after hourly corrections have been made. The effects of the hourly corrections will be discussed in the next chapter. The reader is reminded that only 50% of the events had an atmospheric correction available when this document was created. Figure 8.19 shows the percent change in energy for events that were corrected. The mean of this figure is centered at zero showing that our average atmospheric assumption is correct. The rms of this distribution is 6% adding an additional 6% uncertainty in our energy determination when using the average atmosphere.

8.4 Flux (J(E))

Combining Figures 8.17, 8.4, and 8.15 using

$$J(E_i) = \frac{N(E_i)/\Delta E_i}{(A(E_i)\Omega)\ \Delta t(E_i)} \tag{8.11}$$

calculates the flux of cosmic rays. It must be noted that Figure 8.17 shows $\Delta N/\Delta log(E_i)$. However, dN/dE_i is wanted so either the linear bin width ΔE_i must be calculated for each bin or one may use

$$\frac{dN}{dE_i} = \frac{log(e)}{E_i}\frac{dN}{dlog(E_i)}. \tag{8.12}$$

The following example for the energy bin covering $10^{18.0}$ to $10^{18.1}$ shows the equivalence of these two methods.

$$\frac{\Delta N}{\Delta E_i} = \frac{\Delta N}{10^{18.1} - 10^{18.0}} = \frac{\Delta N}{2.589 \times 10^{17}} \tag{8.13}$$

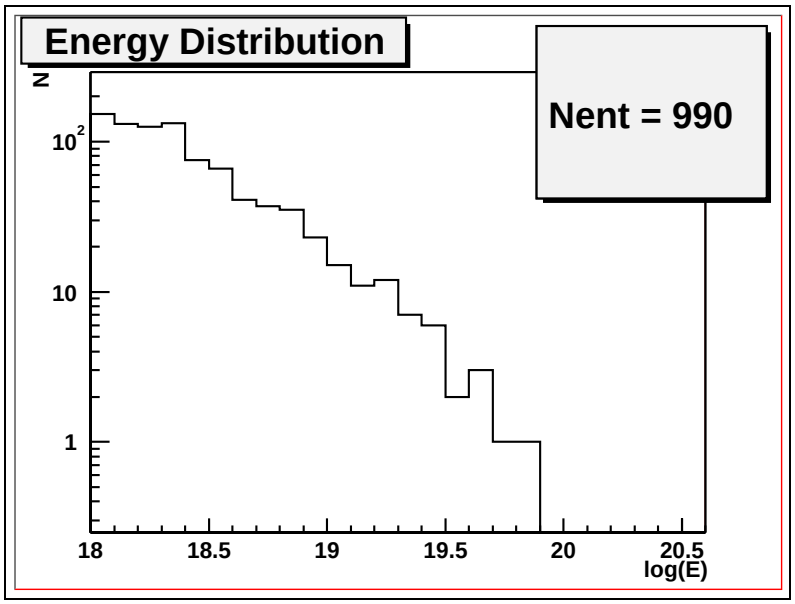

Figure 8.17. Energy Distribution of Events using Average Atmosphere

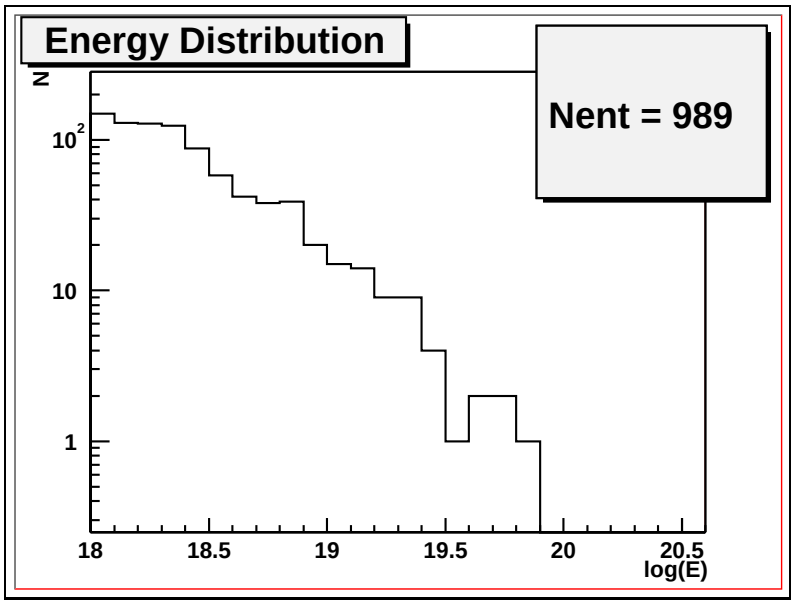

Figure 8.18. Energy Distribution of Events using Hourly Corrections

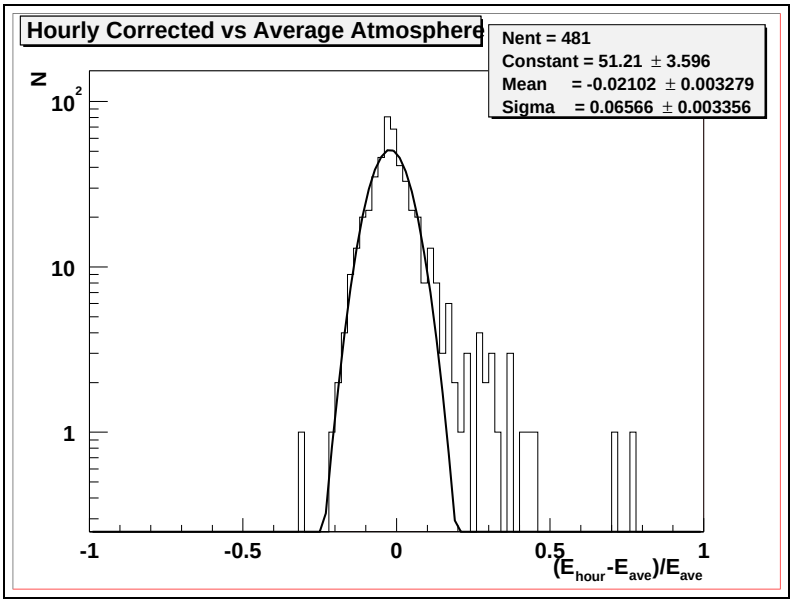

Figure 8.19. Percent Correction for Events with Hourly Atmospheric Correction

$$\frac{\Delta N}{\Delta E_i} = \frac{log(e)}{E_i}\frac{\Delta N}{(\Delta log(E_i))} = \frac{0.4343}{10^{18.05}}\frac{\Delta N}{(18.1-18.0)} = \frac{\Delta N}{2.589\times 10^{17}} \tag{8.14}$$

Using the first method the flux is calculated for an average atmosphere and the result is shown in Figure 8.20.

When hourly atmospheric corrections are made to the energy calculation, a time weighted aperture correction could also be made. This would be accomplished by applying the relative correction to the $\Delta t(E_i)$ term as was done with the missing mirrors. The correction value would be obtained by interpolation between the aperture results shown in Figure 8.5. However, this calculation has not been done and the average aperture has been used.

The flux calculation for the hourly corrected data is shown in Figure 8.21. For all energy bins, including those with no events, the Feldman Cousins 68% confidence limits are shown for the error in the flux [55].

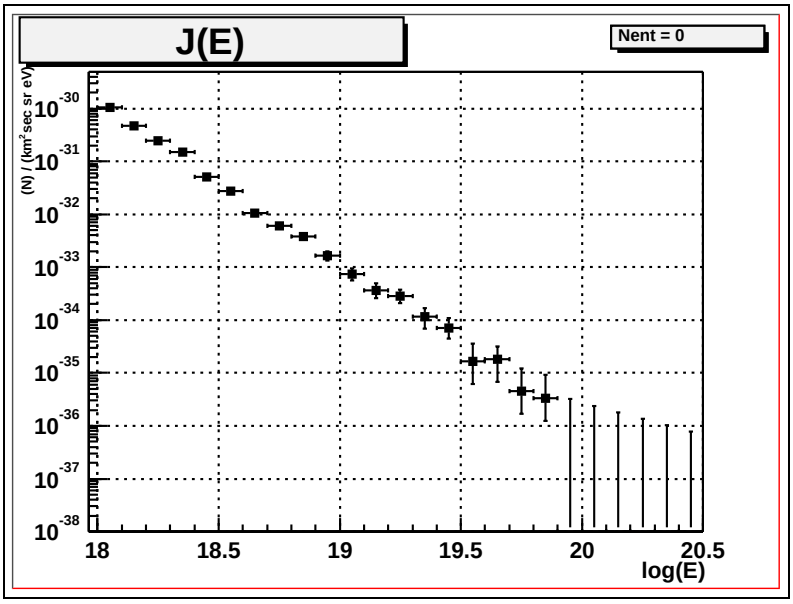

Figure 8.20. Cosmic Ray Flux ($J(E)$) using Average Atmosphere

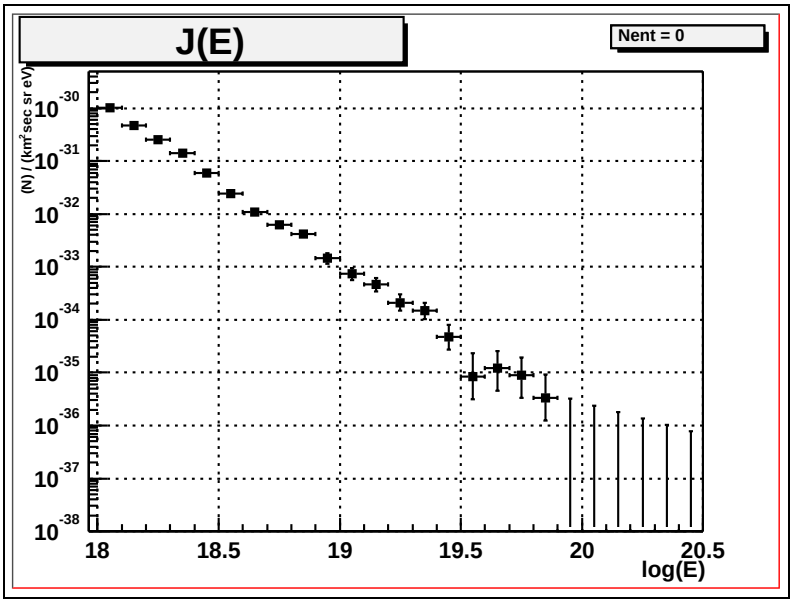

Figure 8.21. $J(E)$ using Hourly Corrections

8.5 $E^3\ J(E)$

As mentioned previously, the common method of displaying the cosmic ray flux is to multiply each bin by a factor of E^3 which will flatten out an E^{-3} spectrum. However, even small systematic shifts in energy will drastically affect the normalization of an $E^3J(E)$ pot. Table 8.2 shows several normalization corrections. For a systematic shift in energy of even 20% the normalization of $E^3J(E)$ shifts by almost a factor of two.

Figures 8.22 and 8.23 show the resulting $E^3J(E)$ plots. Again, the Feldman Cousins 68% confidence limits are shown.

Table 8.2. Effect of Energy Shift on $E^3J(E)$

$E^3J(E)$ correction factors		
Systematic Offset	E_{true}/E_{recon}	$(E^3J(E))_{true}/(E^3J(E))_{recon}$
10%	1.1	1.33
20%	1.2	1.73
30%	1.3	2.20
40%	1.4	2.74

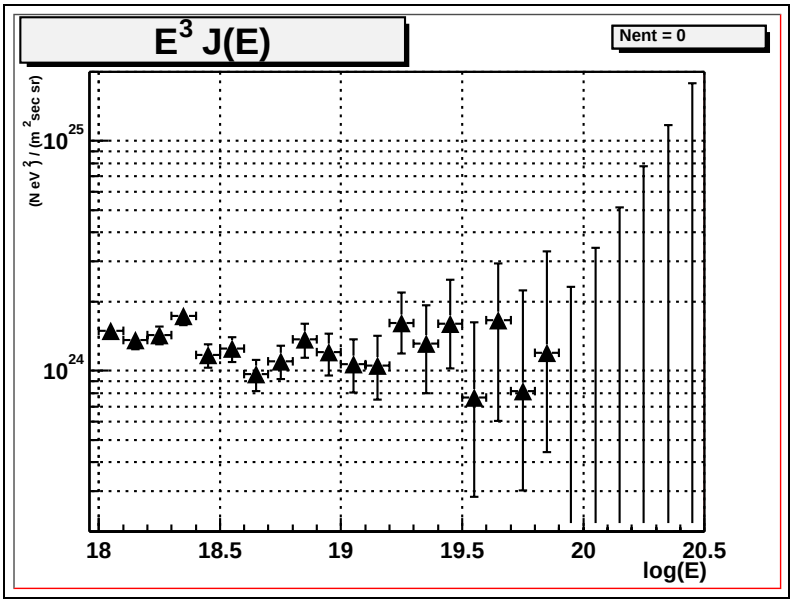

Figure 8.22. $E^3J(E)$ using Average Atmosphere

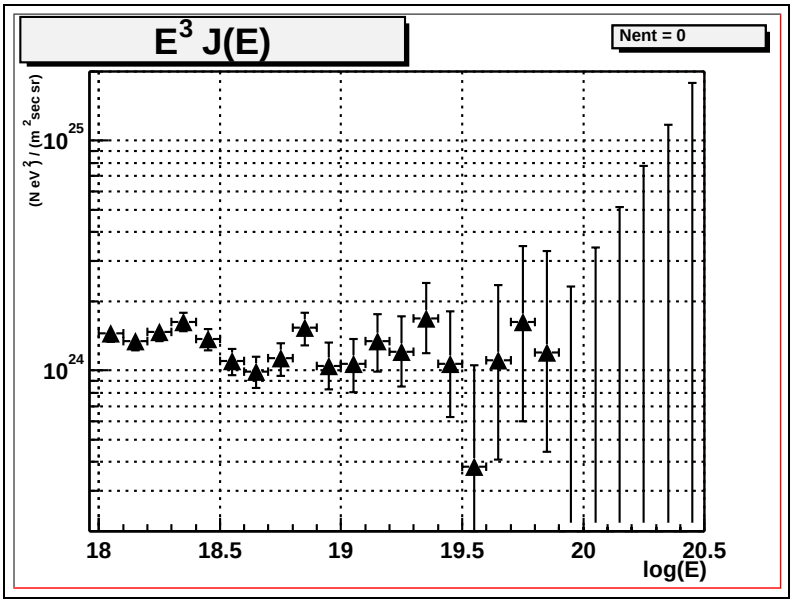

Figure 8.23. $E^3J(E)$ using Hourly Corrections

CHAPTER 9

SYSTEMATICS AND RESULTS

The assumptions made in the previous chapters are twofold. First, it is assumed that our atmospheric and detector calibration is correct and complete. Second, the Monte Carlo has assumed perfect detector alignment and perfect atmospheric parameterization. Neither of these assumptions can be assumed to be correct. In this chapter I will discuss some of the studies I have done trying to understand the weaknesses in the assumptions made. I will then apply these studies to the final spectrum calculation. Unless noted otherwise, the data presented in this chapter were reconstructed using the average atmosphere.

9.1 Energy Resolution from the Data

As mentioned previously, our energy is determined by minimizing the χ^2 for both detector signals simultaneously. However, using the same stereo geometry, a χ^2 minimization can be run for the HiRes-1 and HiRes-2 signals separately. In this case E_{12} is replaced with E_1 and E_2. By comparing the HiRes-1 and HiRes-2 reconstructed energies, we can get a feel for our true energy resolution. Restricting $\chi^2/dof < 5$ ensures a high quality fit at each site.

Figure 9.1 shows that the true energy resolution of our detector must be better than 30%. Using the individual χ^2 minima must reduce the energy resolution from its true value. It also shows that on average, HiRes-1 reconstructs events at 5% higher energy than HiRes-2. This may be an indication of a discrepancy in the

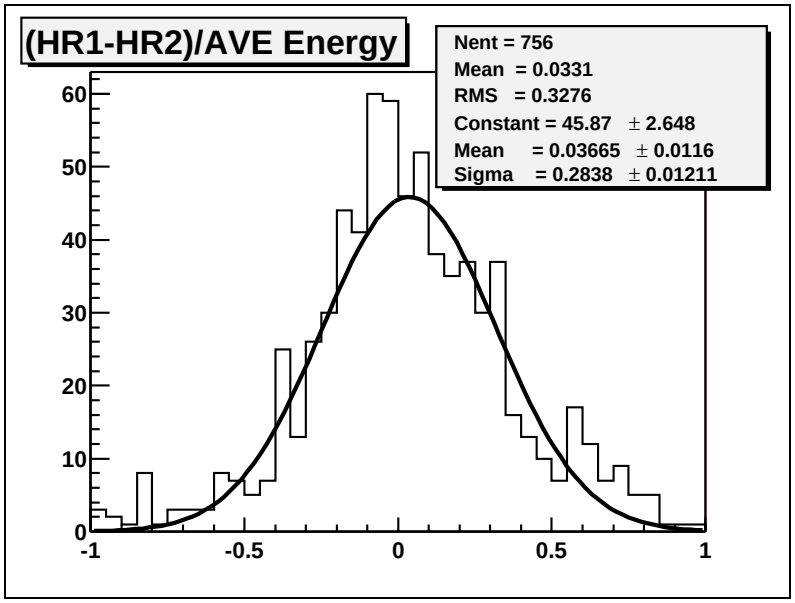

Figure 9.1. HiRes-1 vs HiRes-2 Reconstructed Energy

calibration methods used at the individual sites. No real improvement in this value is seen when using the hourly corrected data, as shown in Figure 9.2. The reason for this is the dominance of low energy events located between our detectors that have only a small aerosol correction.

The level of agreement between the HiRes-1 and HiRes-2 reconstructed energy provides us with an opportunity to use a measured property of detector performance to perform a quality cut on energy reconstruction. Figure 9.3 shows the same distribution for QGSJet protons. In this case a σ of only 3% is seen. This indicates the influence of systematic uncertainty that is not simulated in the Monte Carlo. A full list of systematic uncertainties will be discussed in section 9.8.

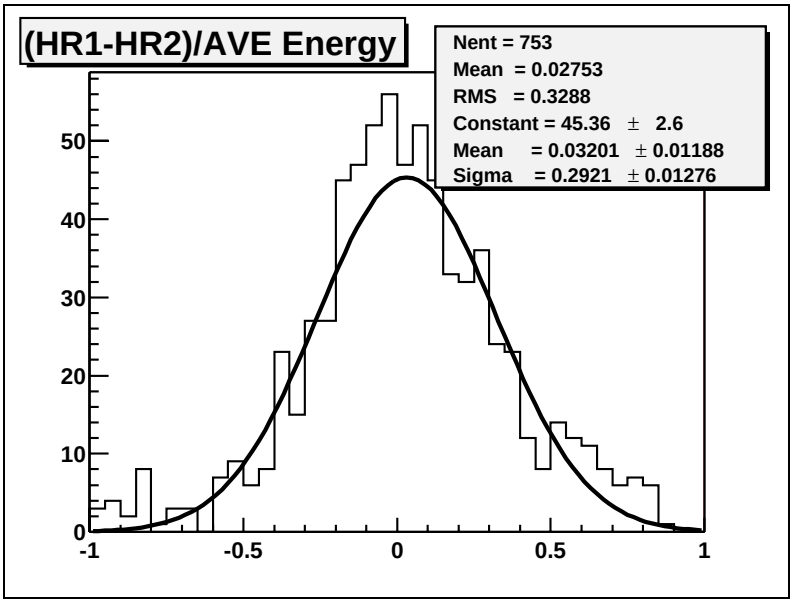

Figure 9.2. HiRes-1 vs HiRes-2 Reconstructed Energy with Hourly Corrections

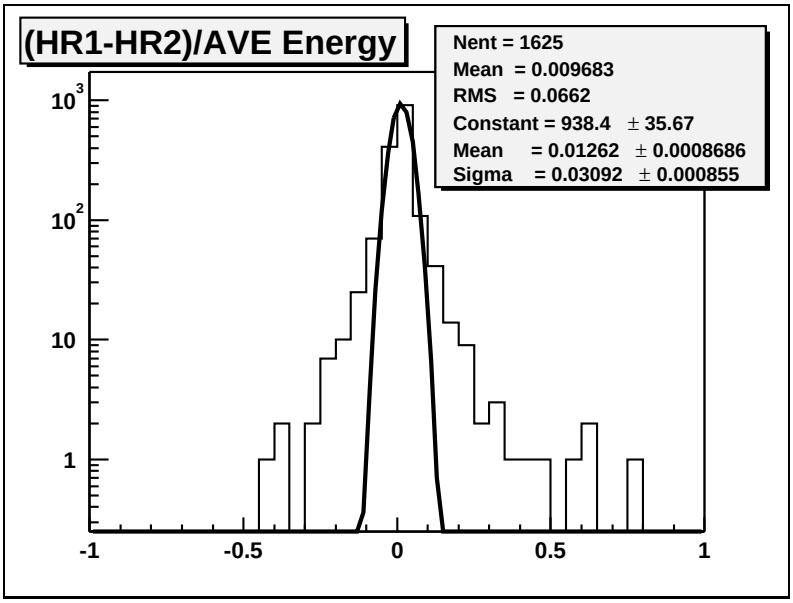

Figure 9.3. HiRes-1 vs HiRes-2 Reconstructed Energy for GQSJet Protons

9.2 Reconstructed Energy Quality Cut

The first measure of the quality of the profile fit is χ^2/dof. If in addition to the χ^2/dof cut a second quality cut is used. This cut is defined by the formula

$$\left\| \frac{E_1 - E_2}{(E_1 + E_2)/2} \right\| < 3\sigma. \tag{9.1}$$

This quality cut removes events that have divergent energy reconstructions at the two sites. With $\sigma = 30\%$ this cut requires E_1 and E_2 to agree within a factor of 2.

9.3 Trigger Thresholds

The initial attempts at calculating a spectrum contained clear evidence of a trigger threshold dependence. The trigger thresholds are the required amount of light that must hit a tube before that tube will trigger. At HiRes-1 the Monte Carlo contained a nominal value of $500mV$. However, a quick check of the actual threshold values in the data produced Figure 9.4. In further discussion with Charlie Jui, who developed the Monte Carlo electronics for HiRes-1 it was agreed that an average value of $700mV$ was much more appropriate and is therefore used.[56].

A similar study was also done for HiRes-2 trigger thresholds. At HiRes-2 the thresholds are controlled by trigger gain values. These values are set by digital to analog electronics (DACS). The nominal Monte Carlo trigger DAC settings had to be adjusted only slightly to the time weighted mean values. The nominal values were 1300 for ring 1 and 1100 for ring 2. Figures 9.5 and 9.6 show the time weighted distributions for these two values. The time-weighted values of 1280 and 1189 for rings 1 and 2 respectively were used. The effect of the changes in the trigger threshold values was a decreased aperture at all energies. However, the low energy aperture was the most affected.

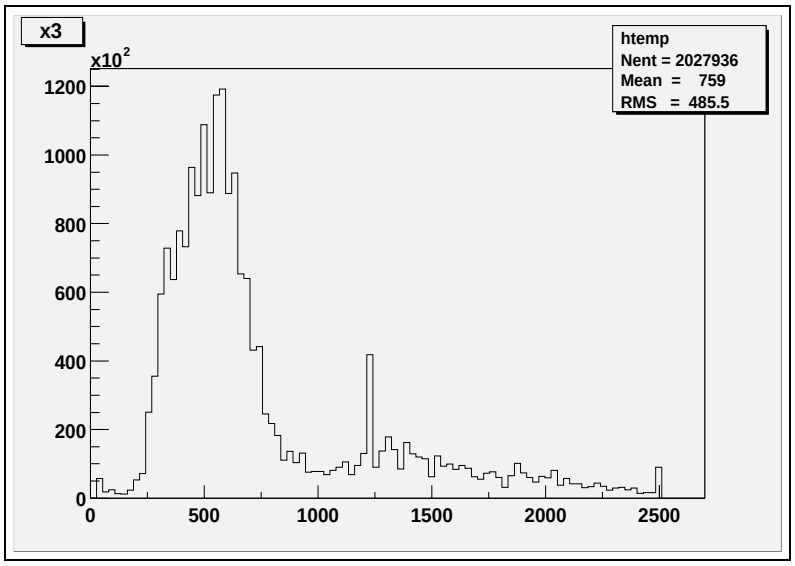

Figure 9.4. Actual HiRes-1 Trigger Thresholds from 10 Days Data Selected at Random

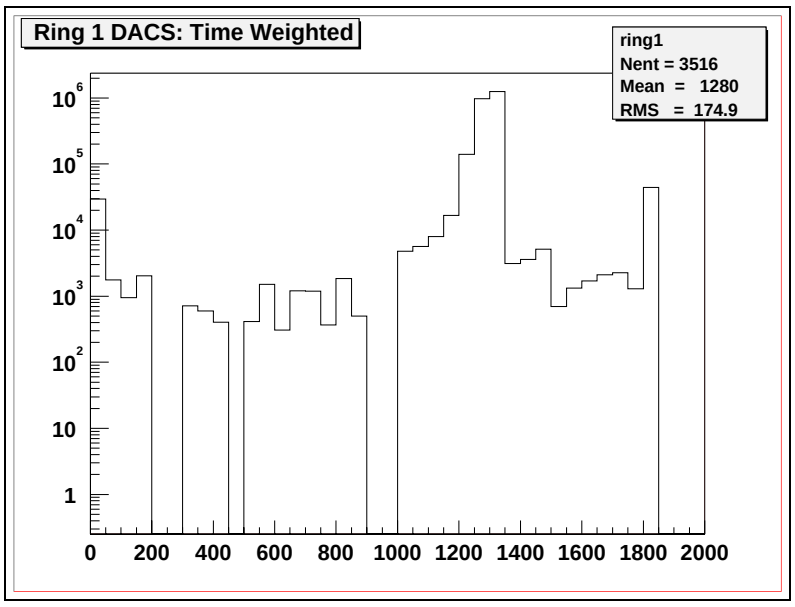

Figure 9.5. Time Weighted DAC values for HiRes-2: Ring1

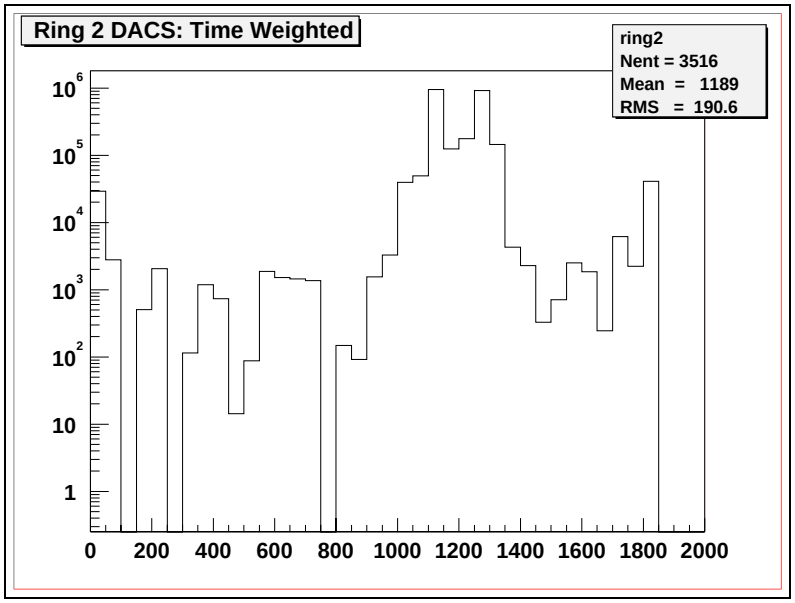

Figure 9.6. Time Weighted DAC values for HiRes-2: Ring2

9.4 Systematic Effects on Energy Resolution from Composition Assumptions

Figure 6.1 shows that by assuming an average composition a systematic shift of around 5% in the reconstructed energy should be expected. For protons, this shift should be 5% high and for iron 5% low. The mean values shown in Figures 7.11 to 7.14 show this systematic shift.

In addition to this 5% uncertainty in energy due to composition, it is also important to check if there are any energy dependent effects. For example, does our resolution improve or degrade with energy. Since most figures in this thesis are produced using approximately an E^{-3} spectral energy distribution, events at the lowest energies, here $10^{18}eV$, dominate the resolution.

Figures 9.7 to 9.10 show the energy resolution for events with energies in different energy ranges. These figures show that our energy resolution is constant over the

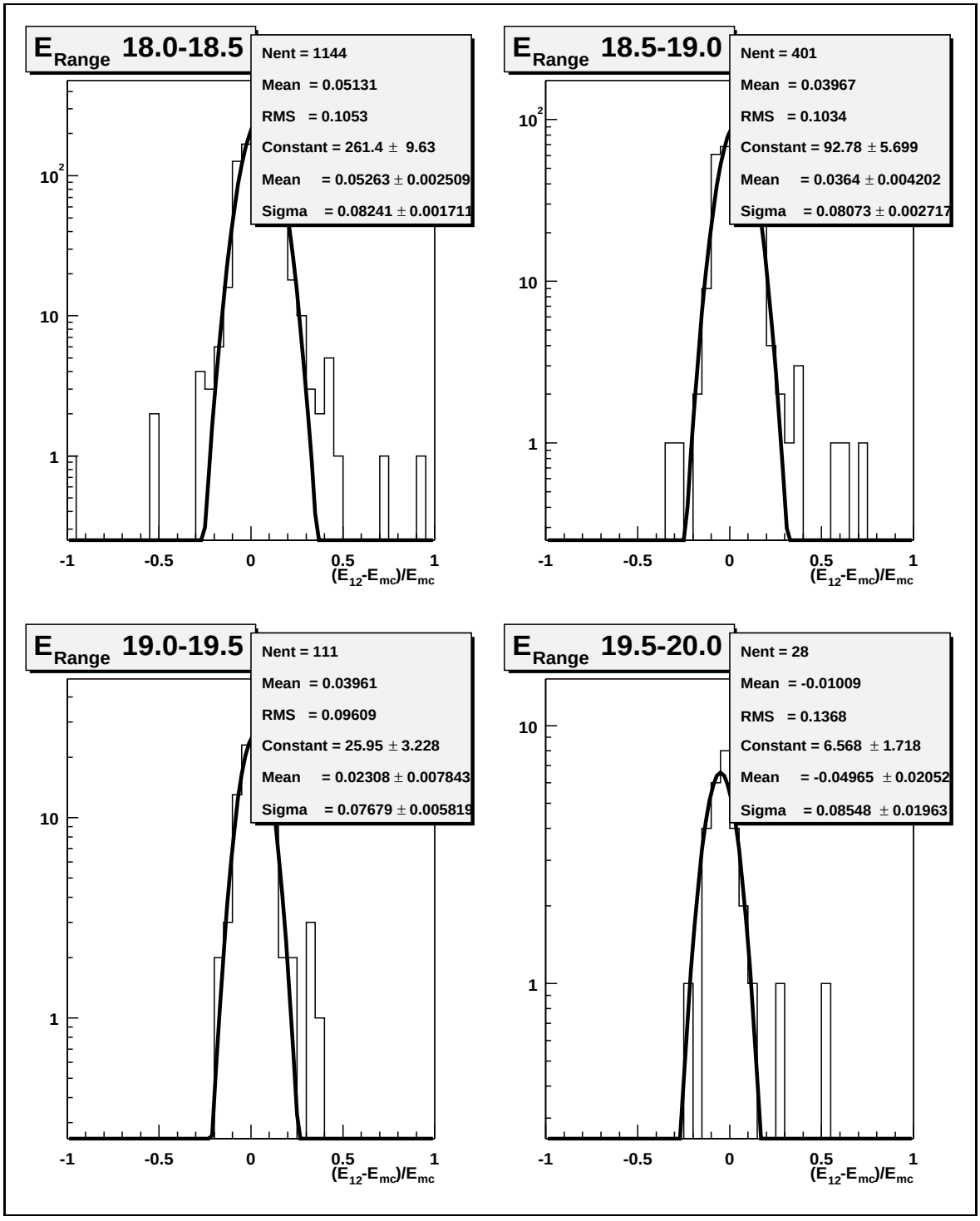

Figure 9.7. Energy Resolution in Four Energy Ranges for QGSJET Protons

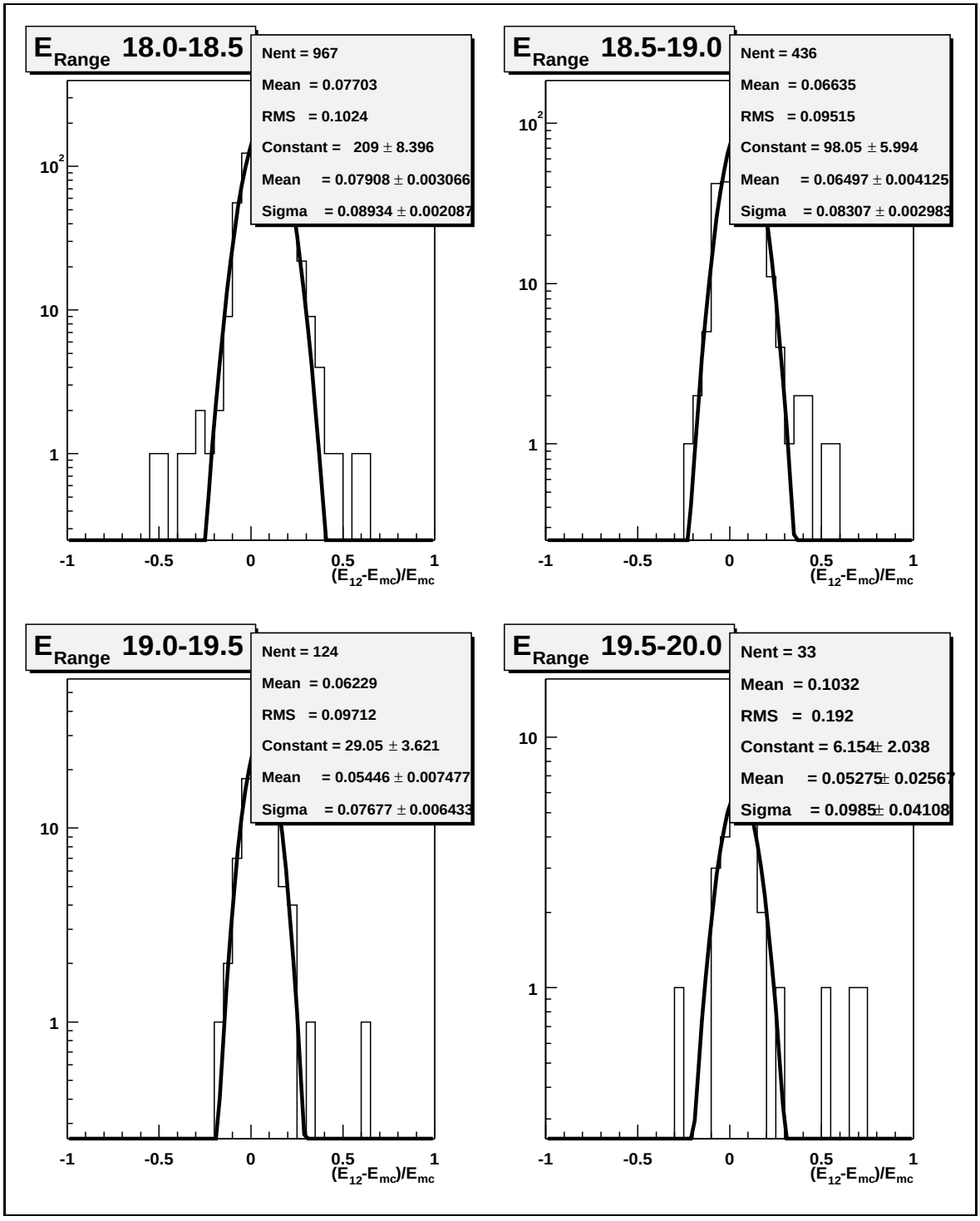

Figure 9.8. Energy Resolution in Four Energy Ranges for SIBYLL Protons

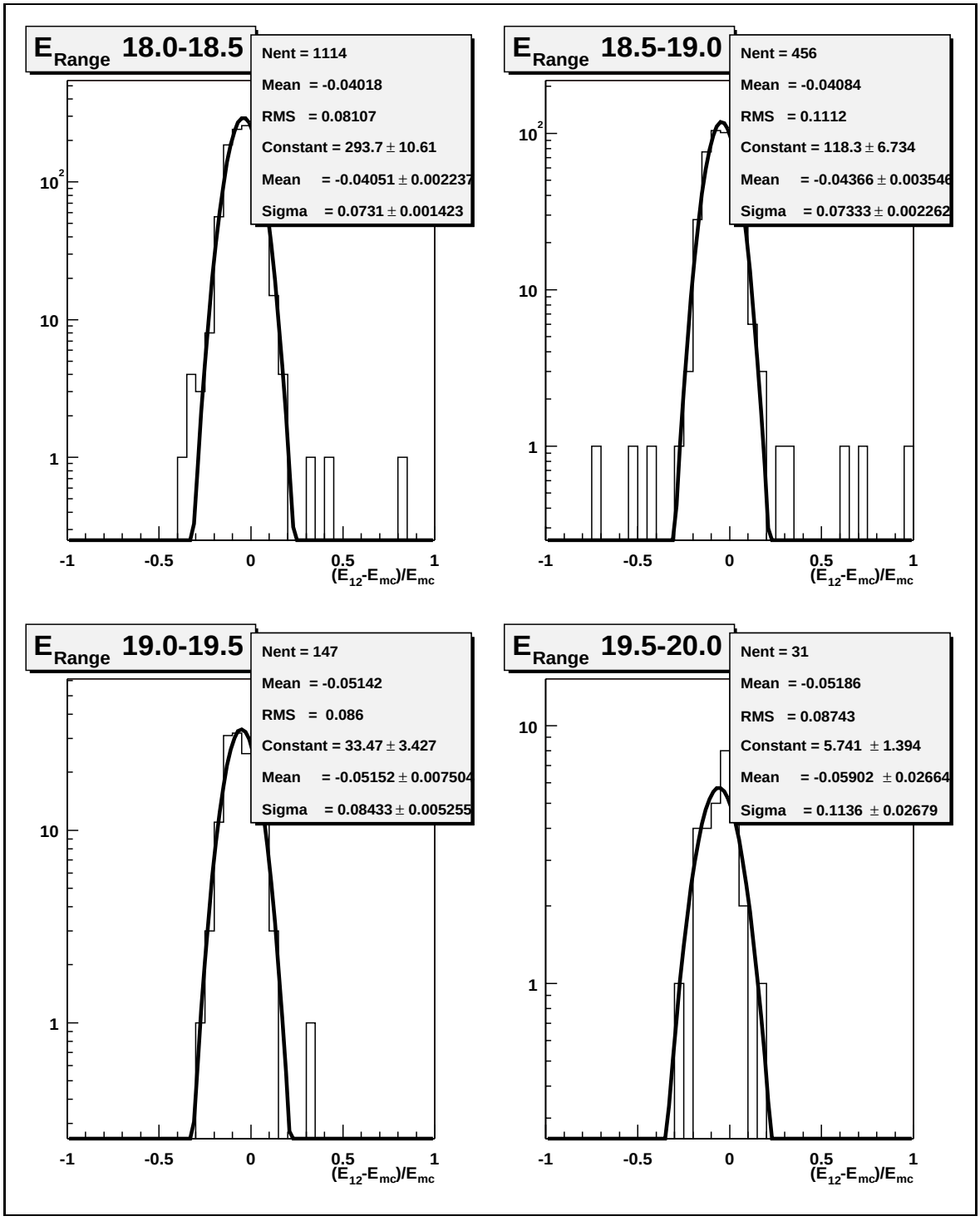

Figure 9.9. Energy Resolution in Four Energy Ranges for QGSJET Iron

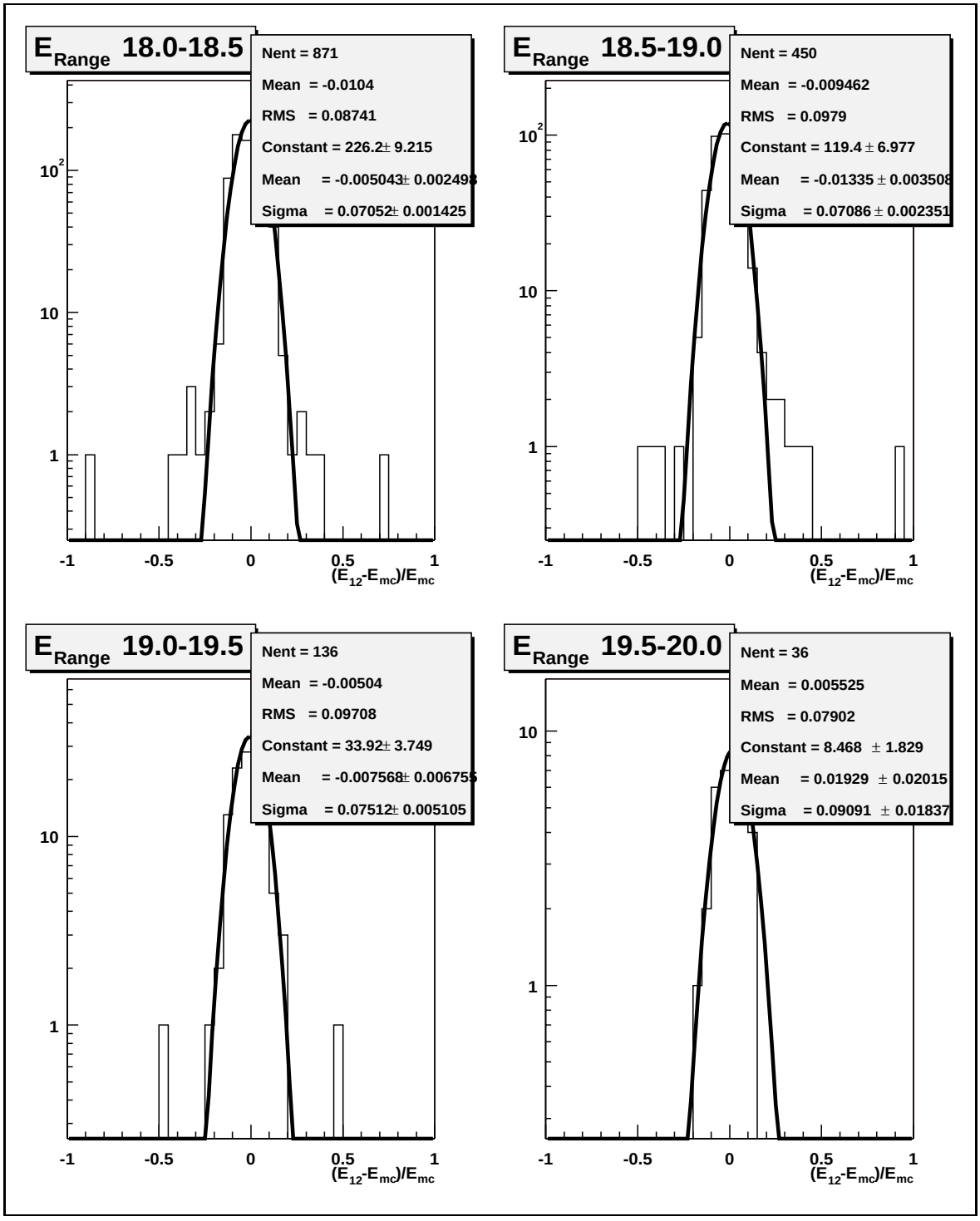

Figure 9.10. Energy Resolution in Four Energy Ranges for SIBYLL Iron

energy range in question. Additionally, the 4% shift in the mean value for protons and iron is seen in each model. For SIBYLL, an additional systematic shift of around 3% in the reconstructed energy is seen. The differing models cause this systematic shift.

9.5 Atmospheric Effects on Aperture

The calculation of detector aperture was discussed in the previous chapter. The aperture of our detector grows with atmospheric clarity and decreases with increasing aerosol content. Our detector aperture has been calculated with five sets of atmospheric parameters. These parameters range from a very clean atmosphere (molecular) to a very dirty atmosphere (standard desert model). Table 9.1 shows the relative atmospheric parameters. Figure 8.5 shows the ratio of the aperture calculated for each atmosphere relative to the average atmosphere.

Table 9.1. Atmospheric Parameters for Five Atmospheres

Atmosphere	Horizontal Aerosol Attenuation Length L_M (km)	Vertical Aerosol Scale Height H_S (km)	Aerosol Optical Depth $\frac{H_S}{L_M}$
Molecular	99	0.1	0.001
1σ	50	1.0	0.02
Average	25	1.0	0.04
1σ	16	1.0	0.06
St. Desert	12	1.2	0.1

9.6 Super-GZK Events

The measured spectrum in this analysis has only a few events above the GZK cutoff. However, it must be pointed out that the confidence limits provide a better feel for our ability to measure the flux at this high energy. Additionally, there are a few additional events that failed the final selection criteria that have a reconstructed energy well above the cutoff. Figures 9.11 to 9.22 show the profile and event displays for three "super-GZK" events. All three events have large χ^2/dof values for profile fits and would have been cut by the $\chi^2/dof < 10$ cut. The first event shown has a $P_{log} = 1.3$ at HiRes-1 and was cut by the noise filter. In all of these cases, it seems clear that the term $N^2_{pe_i}\sigma_{C_{aeff}}$ in equation 5.7 is the dominant term and the error in the correction factor is not being sufficiently simulated. Further studies are currently under way by the HiRes collaboration.

9.7 One Sigma Uncertainty in Atmosphere

The dominant systematic uncertainty in the measurement of the flux is the uncertainty in the aerosol content of the atmosphere. Since atmospheric clarity affects both the reconstructed energy and the aperture small changes lead to large effects. Recall that the stated systematic uncertainty on the atmospheric calibration is $AOD = 0.04 + / - 0.02$ *systematic*.

Figure 9.23 shows the calculated flux for the case of $AOD = 0.04 + 0.02$. $H_S = 1.0km$ and $L_M = 16km$ is used in this case. By assuming a "dirtier" atmosphere two things occur. First, the reconstructed energy is increased since more light is assumed to have produced in the air shower but then lost due to increased scattering. Second, the calculated aperture is decreased since the atmosphere is less clear. Both of these effects cause the flux to be increased. Increasing energy increases the numerator and the decreased aperture creates a smaller denominator

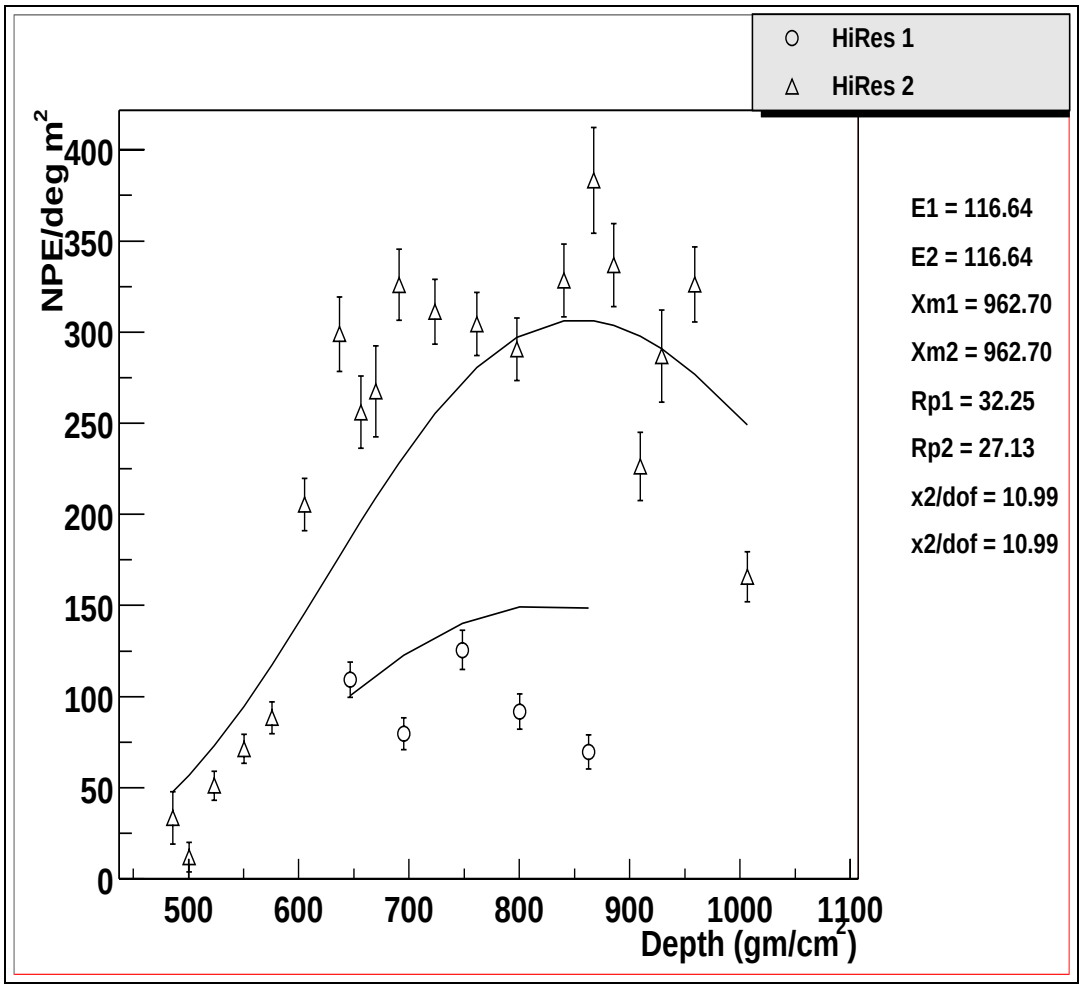

Figure 9.11. Atypical HiRes Event #1 - Profile with Combined Site χ^2
Time and date of each event is shown on Event Display #2 on following pages.

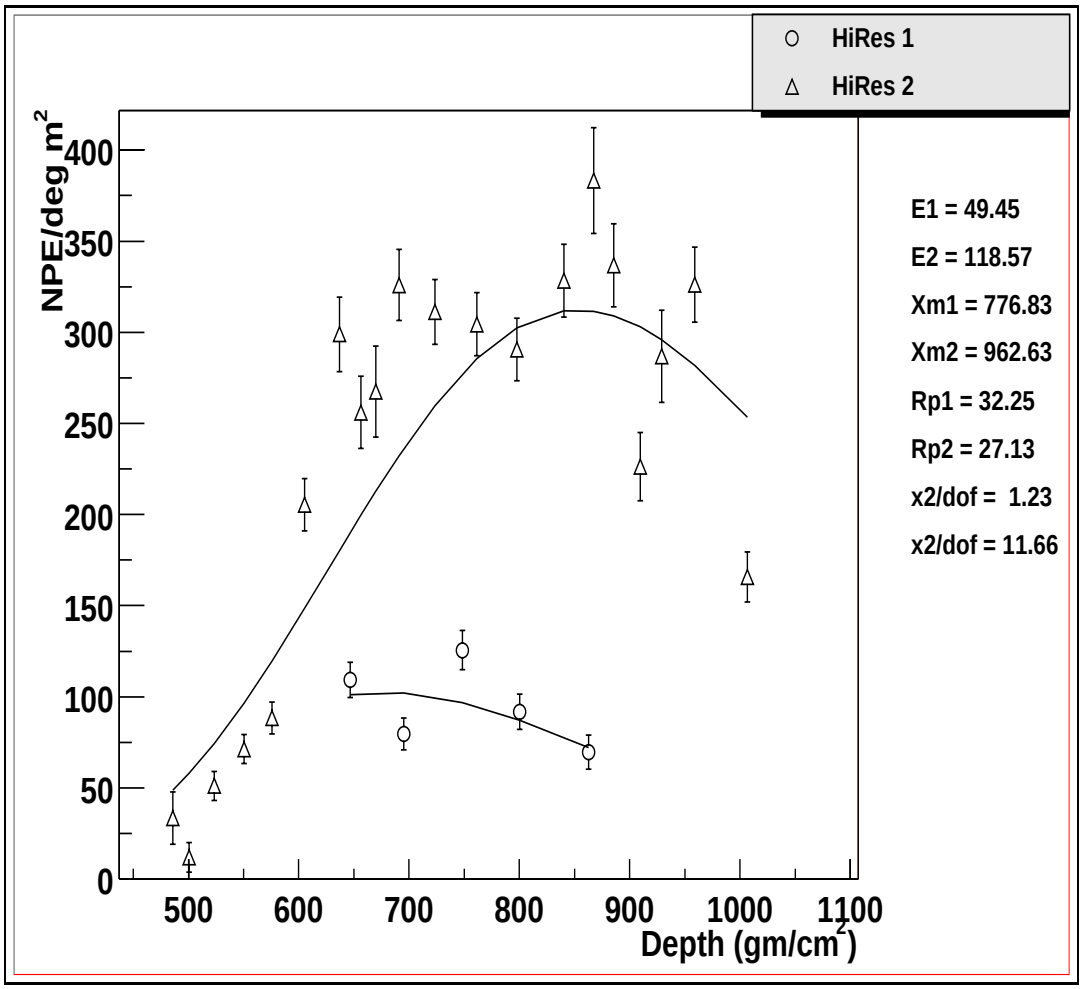

Figure 9.12. Atypical HiRes Event #1 - Profile with Individual Site χ^2

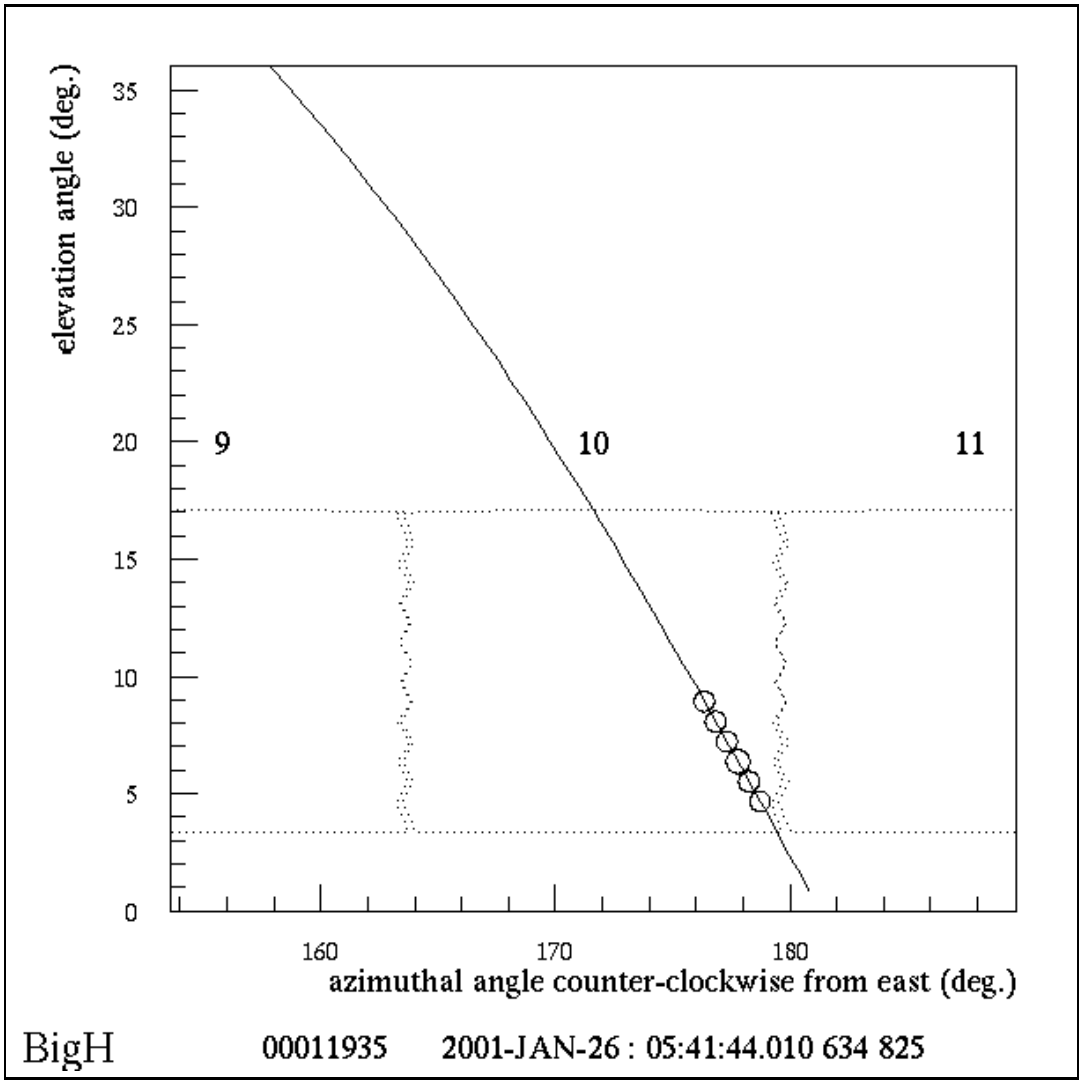

Figure 9.13. Atypical HiRes Event #1 - HiRes-1 Event Display 2

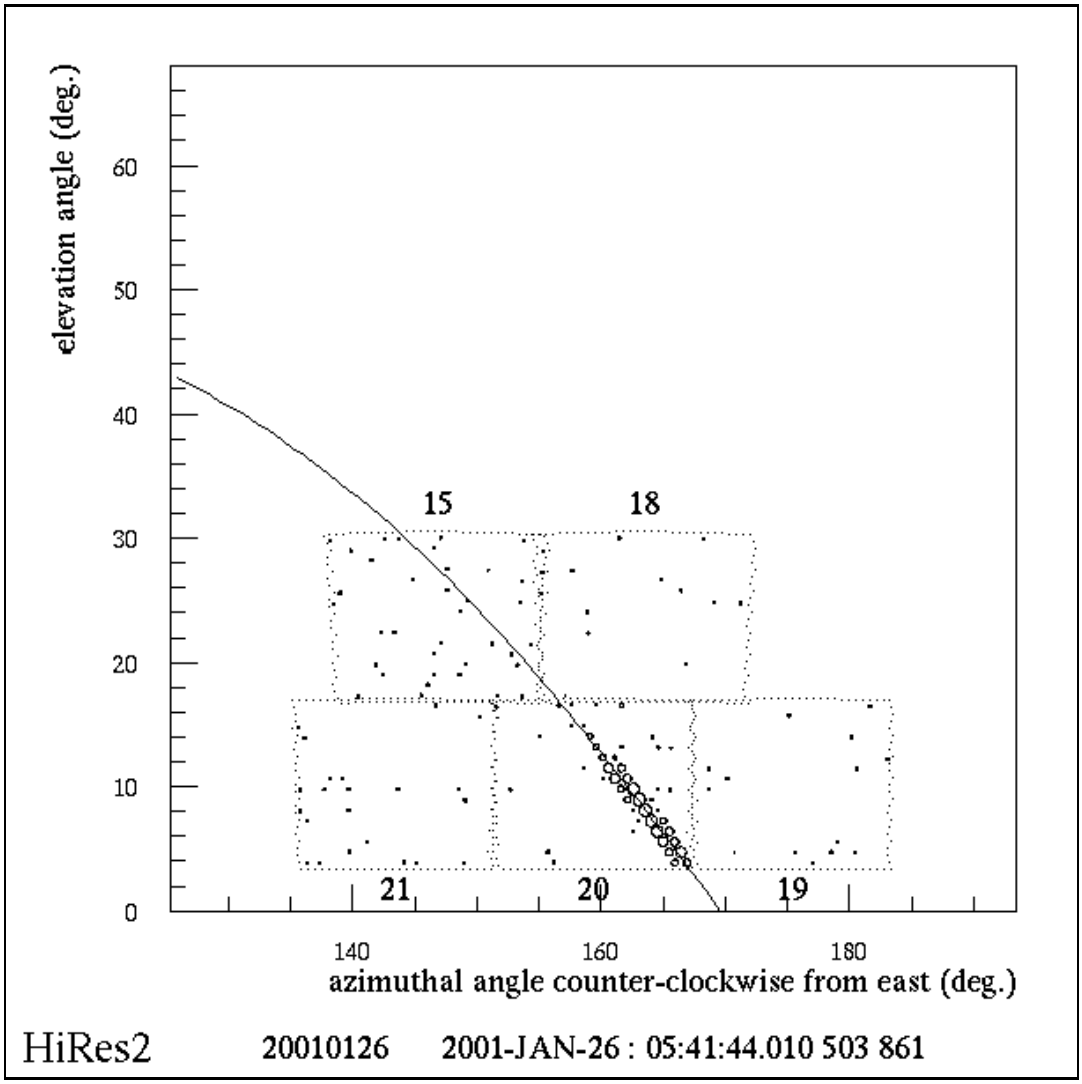

Figure 9.14. Atypical HiRes Event #1 - HiRes-2 Event Display 2

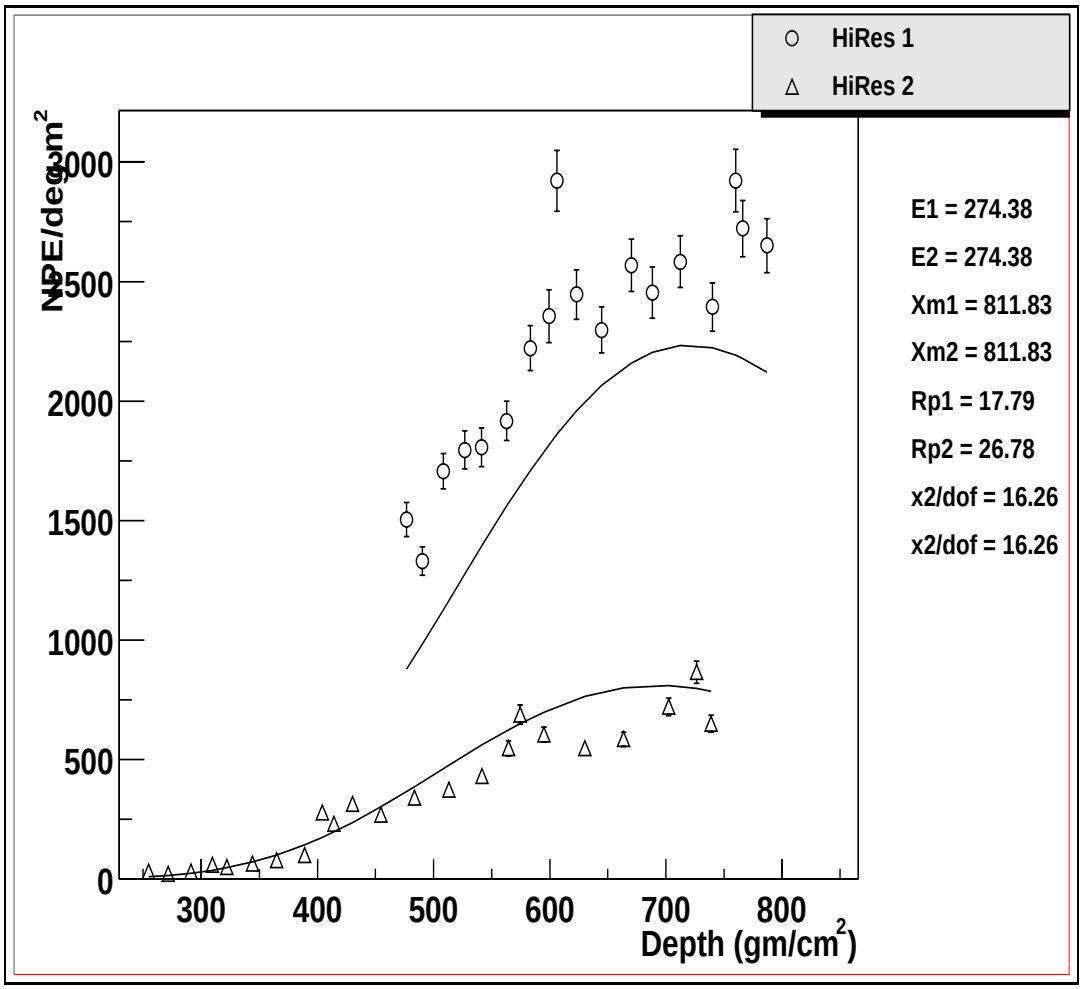

Figure 9.15. Atypical HiRes Event #2 - Profile with Combined Site χ^2

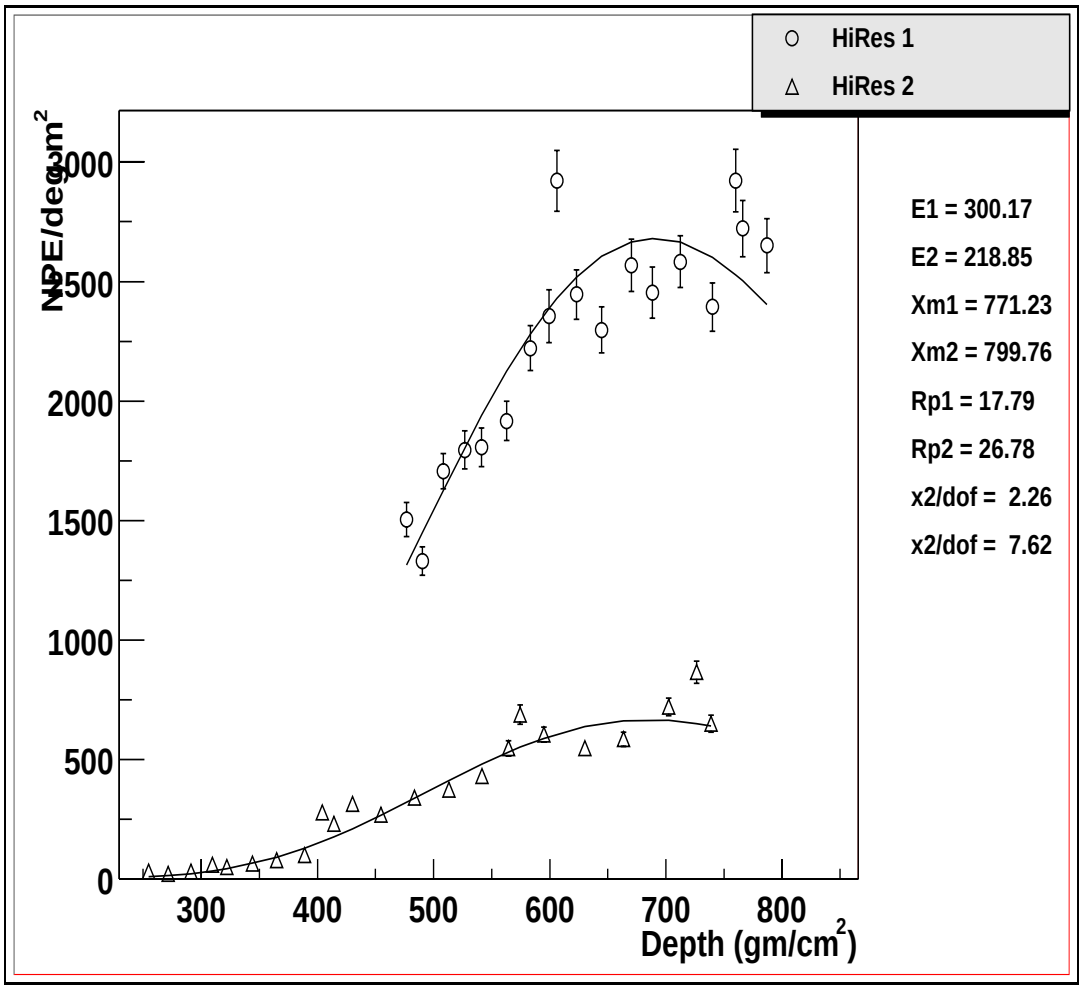

Figure 9.16. Atypical HiRes Event #2 - Profile with Individual Site χ^2

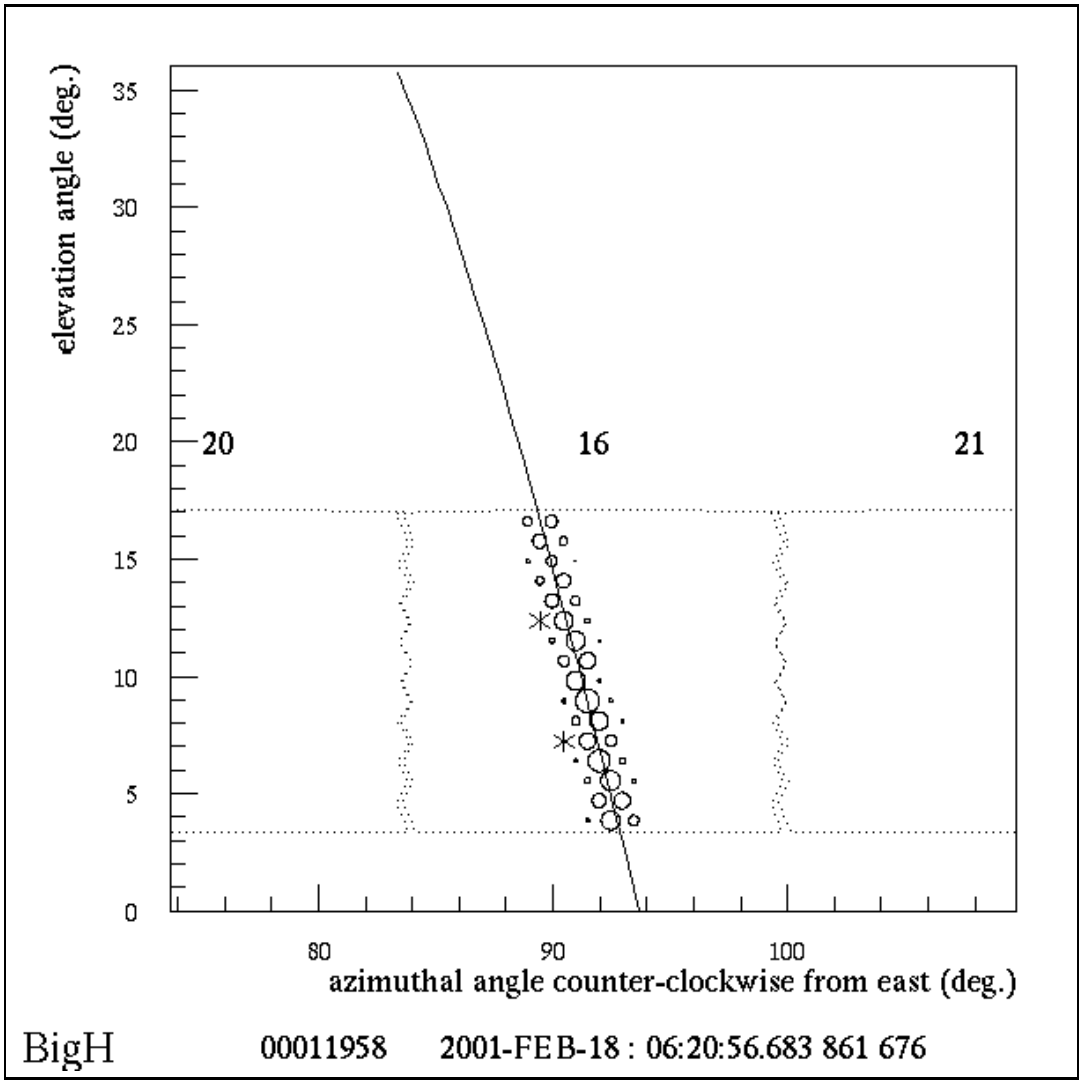

Figure 9.17. Atypical HiRes Event #2 - HiRes-1 Event Display 2

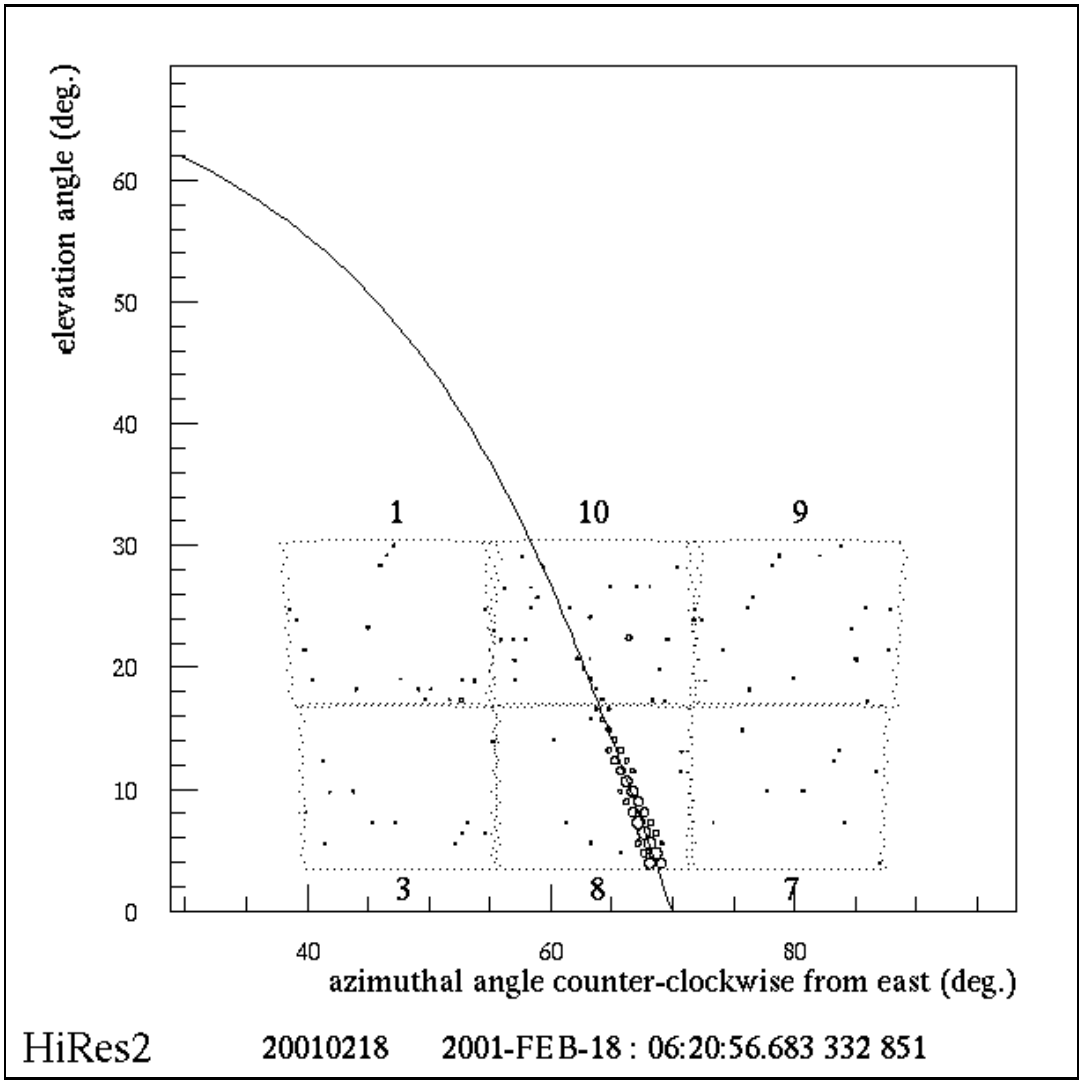

Figure 9.18. Atypical HiRes Event #2 - HiRes-2 Event Display 2

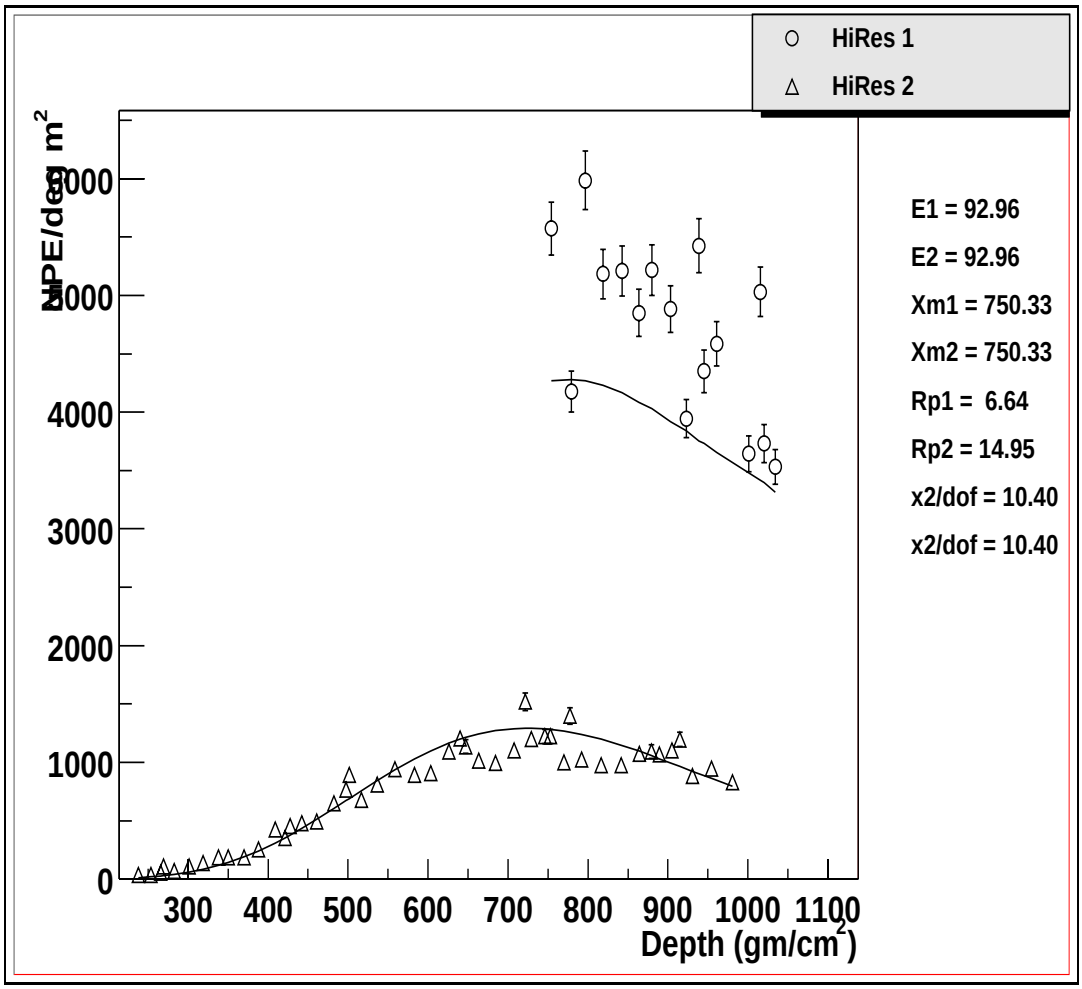

Figure 9.19. Atypical HiRes Event #3 - Profile with Combined Site χ^2

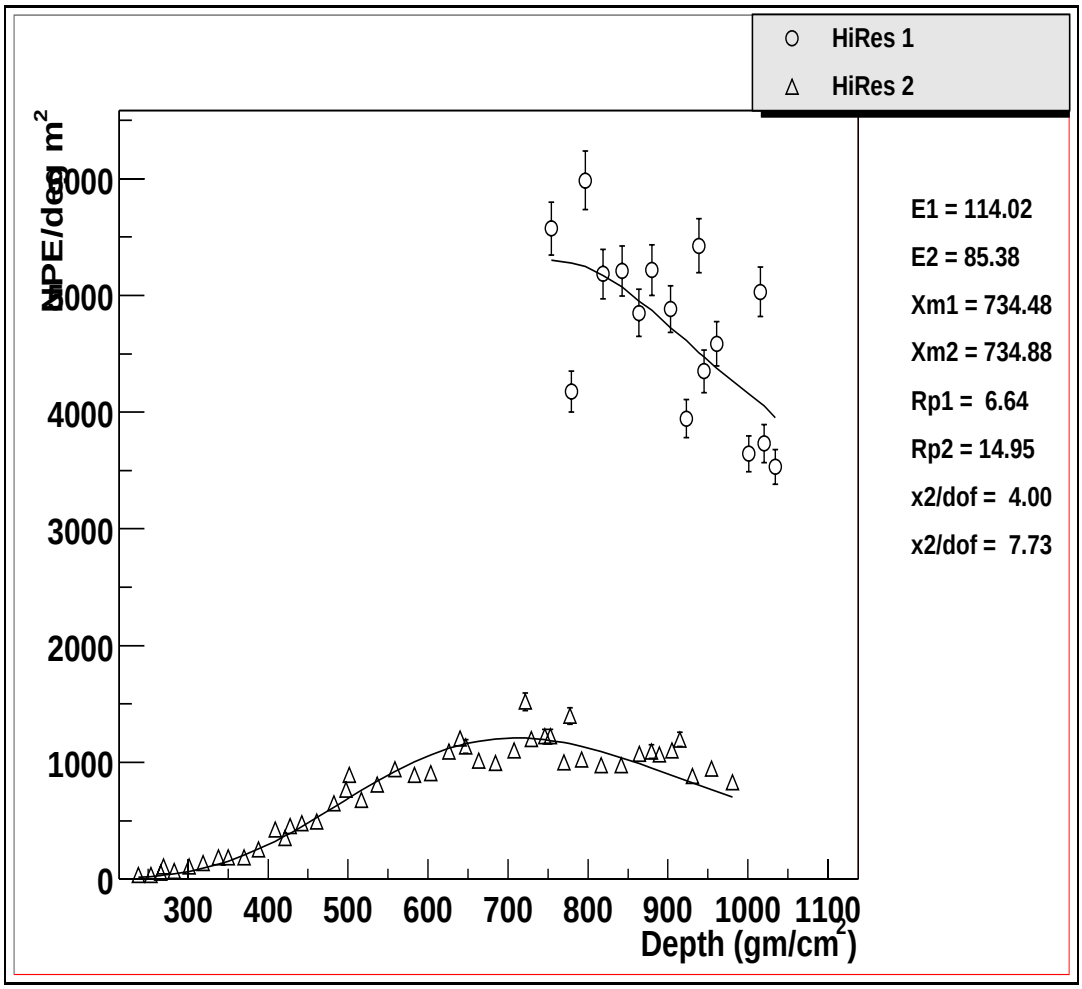

Figure 9.20. Atypical HiRes Event #3 - Profile with Individual Site χ^2

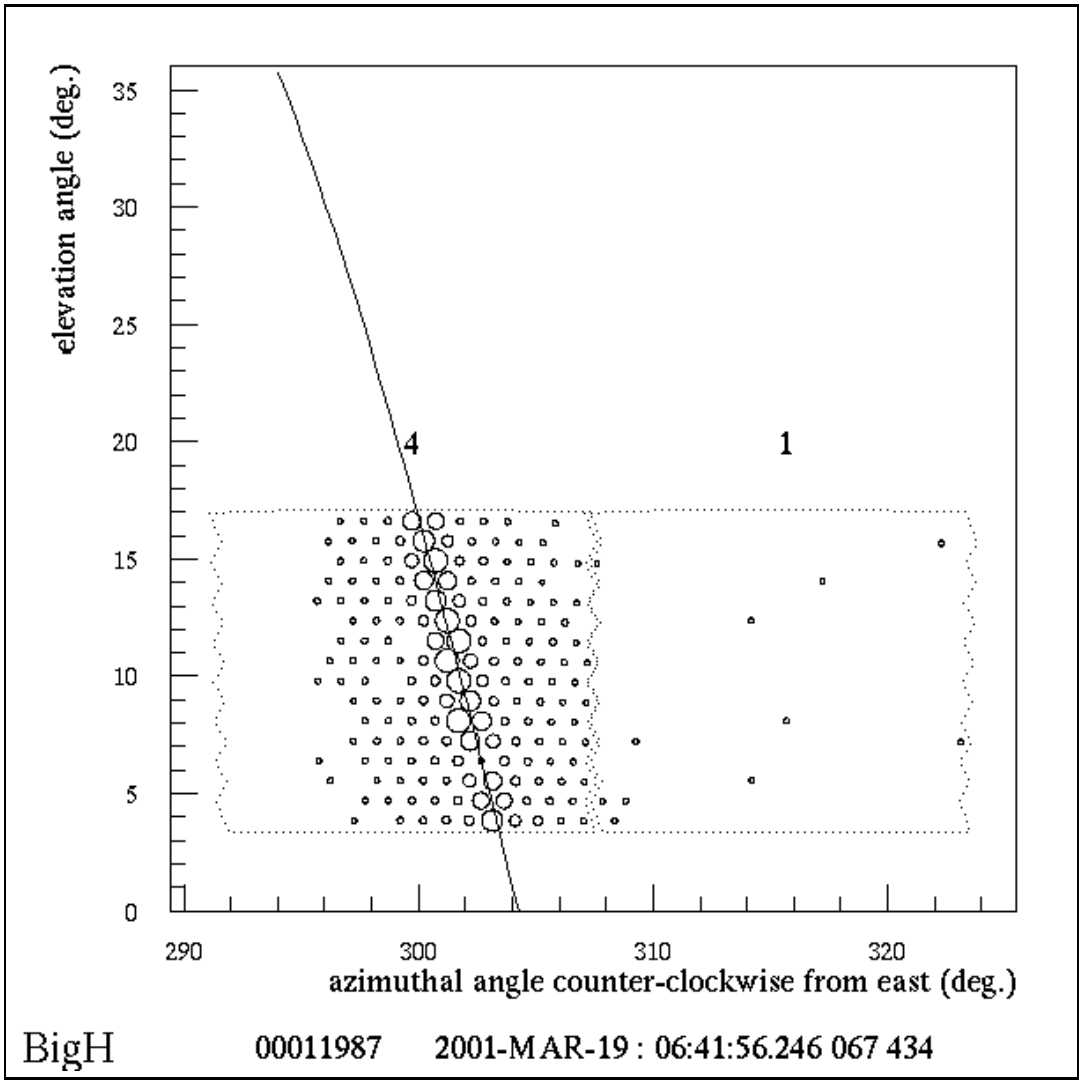

Figure 9.21. Atypical HiRes Event #3 - HiRes-1 Event Display 2

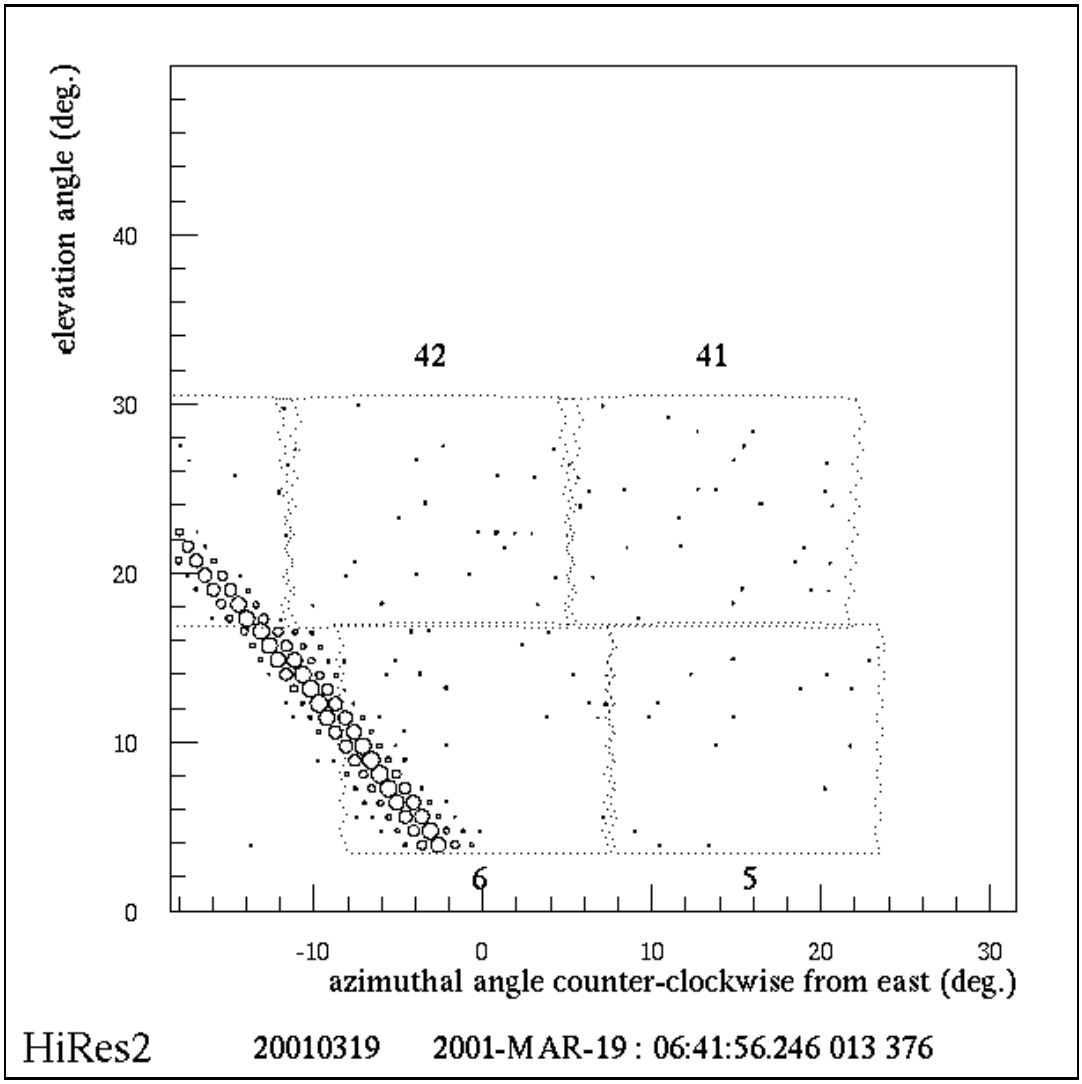

Figure 9.22. Atypical HiRes Event #3 - HiRes-2 Event Display 2

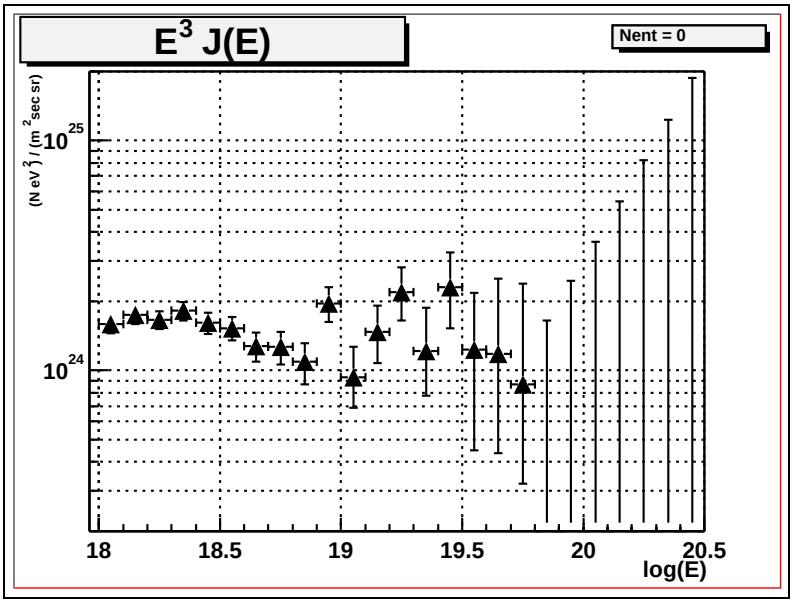

Figure 9.23. $E^3J(E)$ using $AOD = 0.06$

in E^3 times equation 8.2. Figure 9.24 shows the effect on the reconstructed energy from that found using the average atmosphere. The average effect is approximately an 8% increase in reconstructed energy.

Figure 9.25 shows the calculated flux for the case of $AOD = 0.04 - 0.02$. $H_S = 1.0km$ and $L_M = 50km$ is used in this case. By assuming a "cleaner" atmosphere the effect is opposite from before. In this case, the reconstructed energy is decreased since less light is assumed to have been produced in the air shower. Second, the calculated aperture is increased since the atmosphere is clearer. Both of these effects cause the flux to be decreased but the effect is less dramatic. Figure 9.26 shows the effect on the reconstructed energy from that found using the average atmosphere. The average effect is approximately a 7% decrease in reconstructed energy.

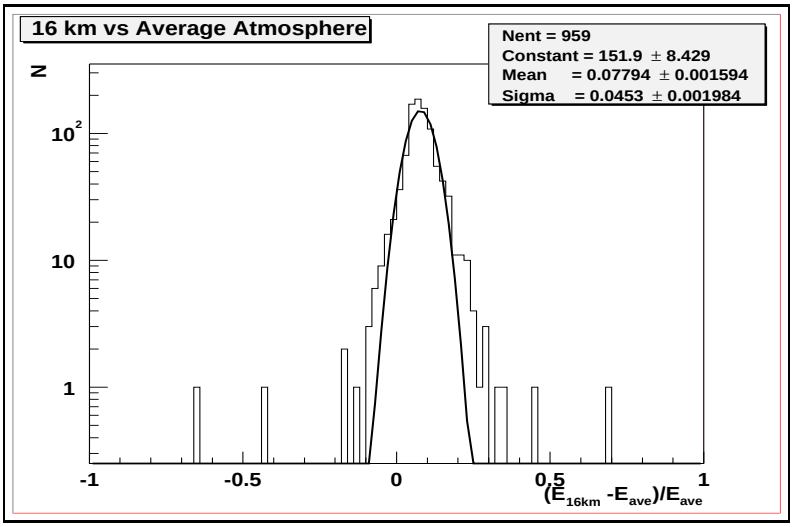

Figure 9.24. Effect of Using $AOD = 0.06$ on E_{recon} Compared to Average Atmosphere

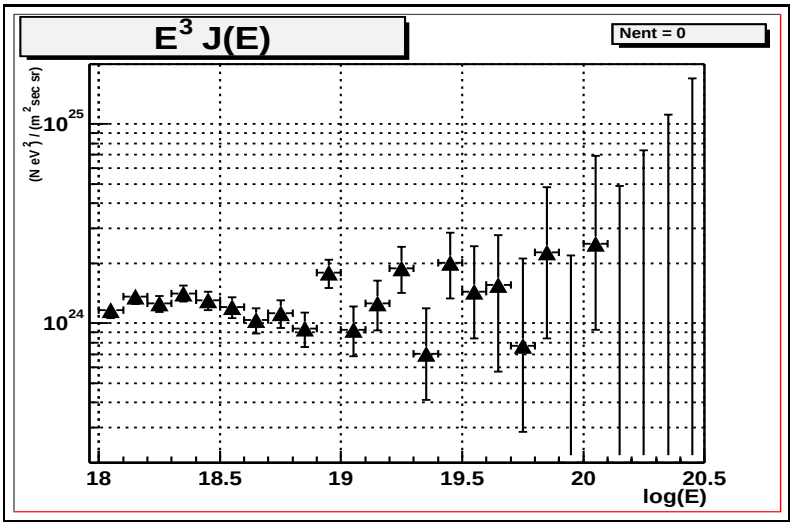

Figure 9.25. $E^3J(E)$ using $AOD = 0.02$

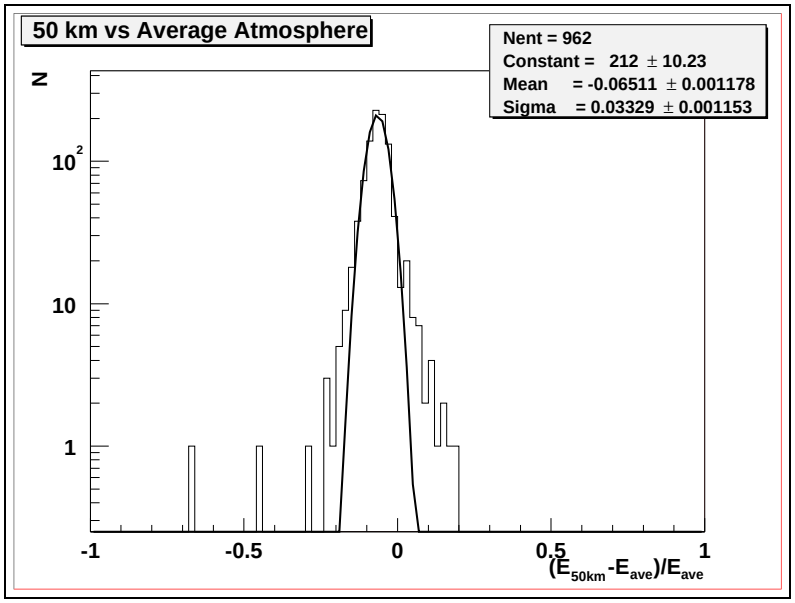

Figure 9.26. Effect of using $AOD = 0.02$ on E_{recon} Compared to Average Atmosphere

9.8 Sytematics

As indicated before a small systematic shift in energy scale can cause a large change in normalization on an $E^3J(E)$ plot. Table 9.2 summarizes the systematic errors in energy determination. The total systematic uncertainty in reconstructed energy is found by summing these errors in quadrature.

9.9 Measurement of the Flux of Ultra High Energy Cosmic Rays

Figure 9.27 shows the measured spectrum using hourly atmospheric corrections when available. Included are the statistical and statistical plus systematic error bars using the one sigma variations in the atmosphere.

Table 9.2. Systematic Errors in Energy Determination. †Also affects aperture in nonlinear manner. ‡Systems exist or are being developed to reduce this systematic.

Systematic	%	Figure(s)	Page(s)	Notes
E_{em}/E_0	8%	6.1	87,139	5% ave. composition + + 3% difference between SIBYLL & QGSJET
E_C/X_0	10%		82	Change in ratio from previous works
Fluorescence Yield Yield	10%	6.8 6.7	6.2.3	Quoted systematic in reference[54]
Amosphere	8% †	9.24, 9.26	145	Calculated in this paper
Mirror Reflectivity	10% ‡	3.3	18	Estimated
PMT Calib/Gain	15% ‡	4.7, 4.6	32	Estimated
Total	61%			If all systematics have same directional effect on energy
Quadrature	27%			$\sigma_E = \sqrt{\sigma_1^2 + \sigma_2^2 + \ldots}$

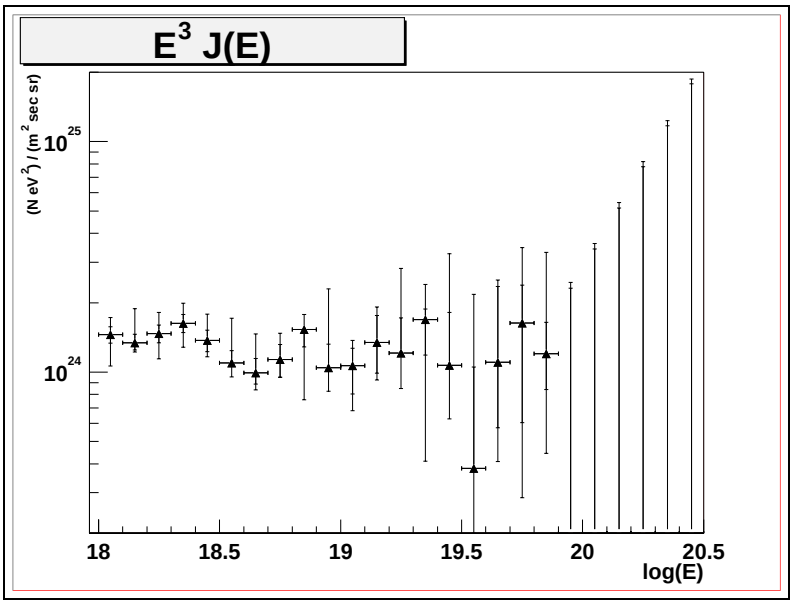

Figure 9.27. Hourly Corrected $E^3J(E)$ Spectrum. Statistical plus Atmospheric Systematic Error Bars

9.10 Comparison to Prior Results

Figure 9.28 shows this measurement with the original Flys Eye stereo result[1]. Figure 9.29 shown the comparison of the AGASA result[2]. Figure 9.30 shows the comparison with the results from the HiRes-1 and HiRes-2 monocular studies[57, 36].

The stereo Fly's Eye experiment measured the spectral index at the ankle. They measured a change from $\gamma = 3.27$ to $\gamma = 2.7$ at $10^{18.5} eV$. Figures 9.31 and 9.32 show a fit for γ for this data. With the current error, no stable fit to a change in spectral index can be found. However, fitting for a single spectral index in the region for the $J(E)$ and $E^3 J(E)$ results gives $\gamma = 3.27 + / - 0.16$ or $\gamma = 3.21 + / - 0.13$ respectively.

The normalization of this measurement is lower than both the Fly's Eye stereo and AGASA measurements. The difference is much more significant when compared to the AGASA measurement. However, as was outlined in table 8.5 a small systematic offset in energy scale has a large effect on this normalization. In order to match the Fly's Eye stereo normalization, an unreasonable error of almost 50% in exposure or aperture would be required. However, a 20% shift in energy scale would also bring the measurements into very good agreement. Figure 9.33 shows the comparison if the energy scale of this work is shifted 20% higher. In order to match the normalization of the AGASA measurement a shift in energy scale of 40% is required. This is shown in Figure 9.34. Agreement with the stereo Fly's Eye result is within the estimated systematic errors of this measurement. Agreement with AGASA cannot be obtained within the errors.

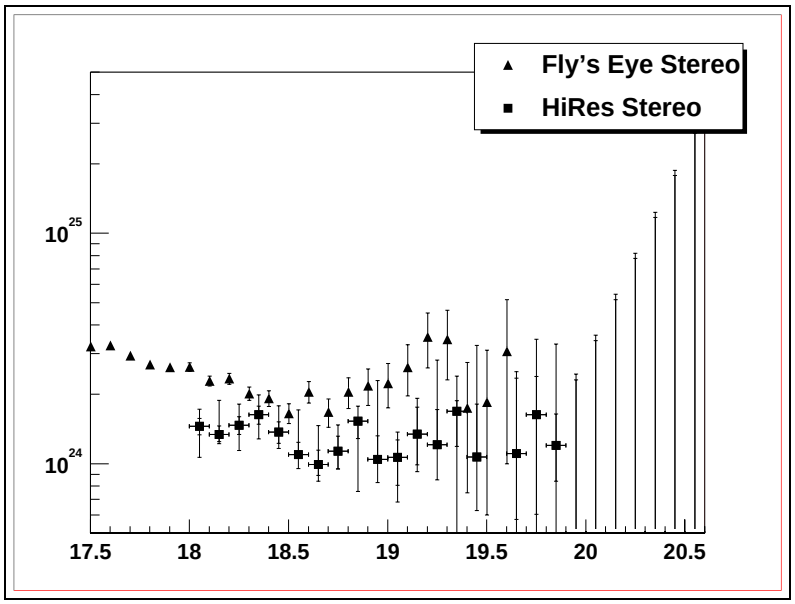

Figure 9.28. Comparison of E^3J from Original Fly's Eye Stereo

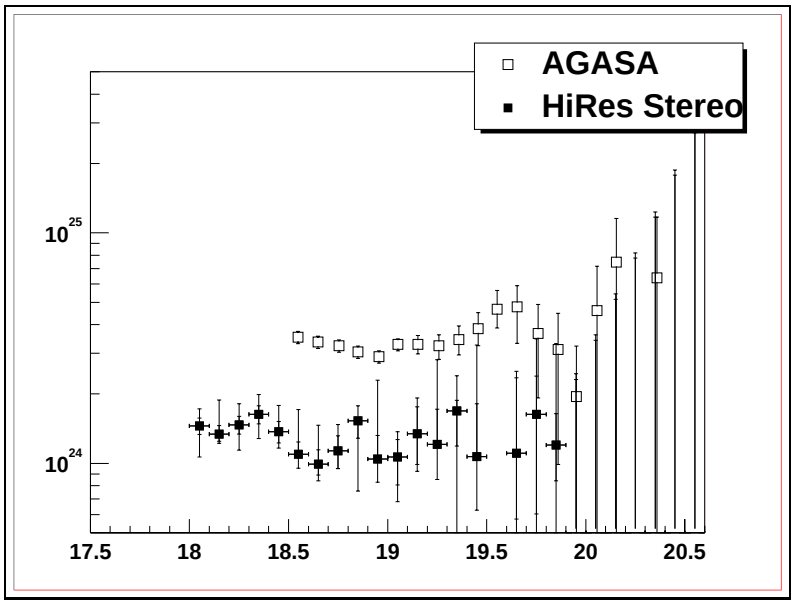

Figure 9.29. Comparison of E^3J from AGASA

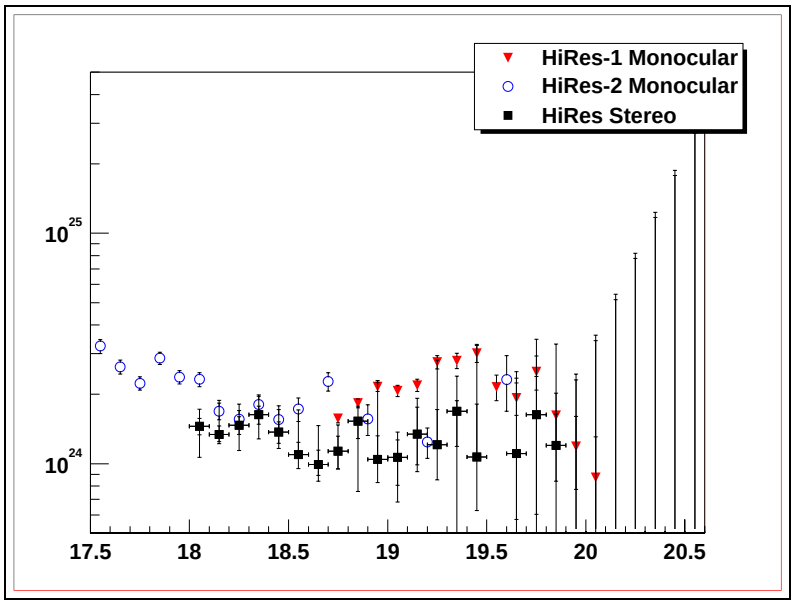

Figure 9.30. Comparison of E^3J from HiRes-1 and HiRes-2 Monocular Studies

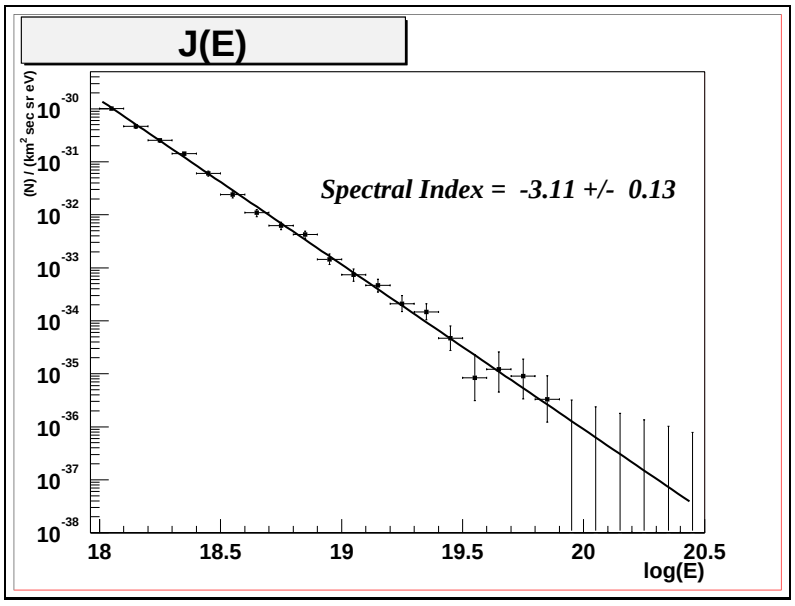

Figure 9.31. Fit for Spectral Index

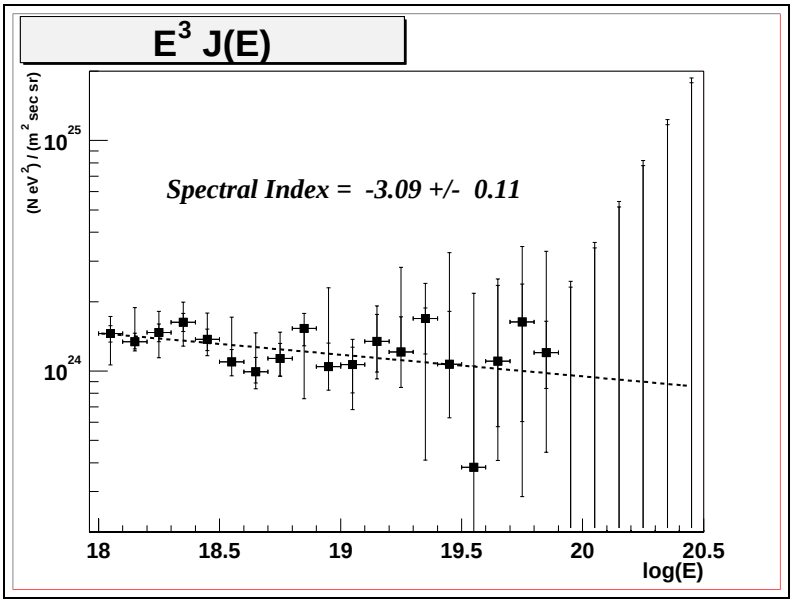

Figure 9.32. Fit for Spectral Index using $E^3J(E)$

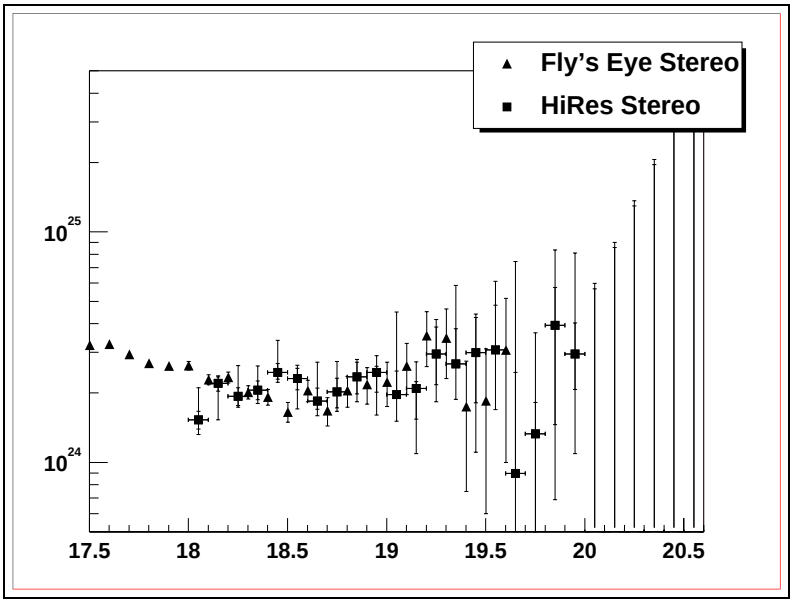

Figure 9.33. Comparison of $E^3J(E)$ to Fly's Eye Stereo with $E_{true} = 1.2E_{recon}$

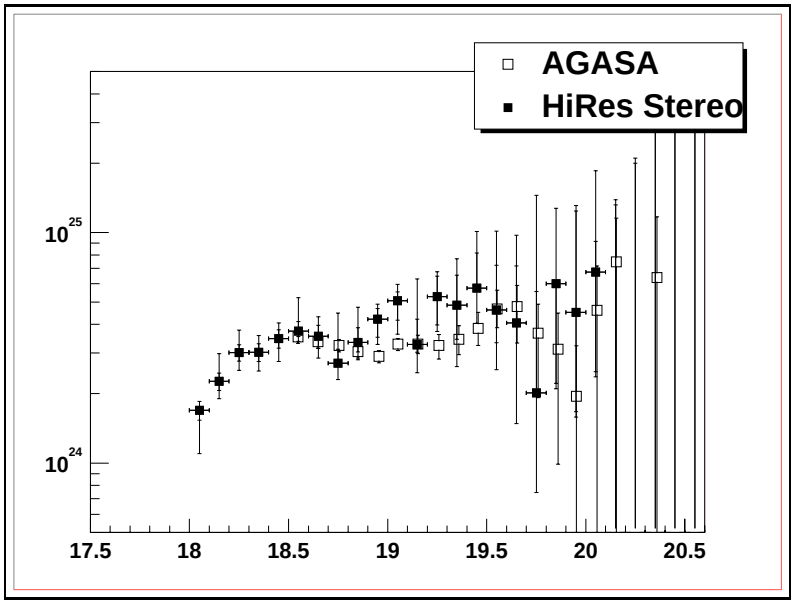

Figure 9.34. Comparison of $E^3J(E)$ to AGASA with $E_{true} = 1.4E_{recon}$

CHAPTER 10

CONCLUSION

It has been shown that if we fully understand the atmosphere and our detector response that we have an intrinsic energy resolution better than 10%. However, looking at the data itself as in Figure 9.1 it is clear that this lower limit is not truly achieved. Rather an energy resolution of closer to 30% is a better estimate. In addition to energy resolution Table 9.9 shows the systematic uncertainty in energy determination to be around 20%.

Preliminary results on composition are visible in Figures 7.26 and 7.27. In the first figure the distribution of X_{max} values found in the data can be best explained by a purely protonic composition. In the second figure the average X_{max} values for each energy bin in this study follow closely with the expected values for protons.

In determining the flux of ultra high energy cosmic rays, the uncertainty in the measurement is dominated by the systematic uncertainty in the atmospheric calibration at low energy. At high energy, statistics limit the measurement.

The measured flux is shown to be lower than both the Fly's Eye stereo and AGASA measurements (Figures 9.28 and 9.29). Within the systematic uncertainties of this measurement agreement with the Fly's Eye stereo result can easilty be obtained (Figure 9.33). Agreement with the AGASA measurement cannot be obtained.

10.1 Future

The most essential future projects are the collection of more data and better determination of the properties of the atmosphere at Dugway. Additional projects should include the full use of the FADC information at HiRes-2 and completion of the hourly atmospheric calibration database. More detailed studies to improve systematic errors in energy scale and shower profiles are needed. Also a better understanding of true air shower fluorescence yields and E_C/X_0 ratio. Finally, the systems that exist to reduce systematic uncertainties should be more fully incorporated into the analysis.

APPENDIX

PROCESSING STEP DETAILS

HiRes1 Pass0

Software: */hires_soft/dst2k/src/hma/bin/hma.c*

Script: *ãcme/scripts/process/steps/hr1pass0.ksh*

Input: *.pkt.hal*

Output: *.ps0-1.dst*

Banks: *HPKT1*

HiRes2 Pass0

Software: */hires_soft/dst2k/src/fadcanal/bin/pass0.c*

Script: *ãcme/scripts/process/steps/hr2pass0.ksh*

Input: *.fpkt1.raw*

Output: *.fpkt1.dst*

Banks: *FPKT1 FTRG1 FMSG1*

HiRes1 Pass1

Software: */hires_soft/dst2k/src/hps1/bin/hps1.c*

Script: *ãcme/scripts/process/steps/hr1pass1.ksh*

Input: *.ps0-1.dst*

Output: *.ps1-1.dst*

Banks: *HRAW1 HBAR*

HiRes2 Pass1

Software: */hires_soft/dst2k/src/fadcanal/bin/pass1.f*

Script: *ãcme/scripts/process/steps/hr2pass1.ksh*

Input: *.fpkt1.dst*

Output: *.pass1.dst*

Banks: *FRAW1 FPHO1*

Software: */hires_soft/dst2k/src/fadcanal/bin/pass1.f*

Script: *ãcme/scripts/process/steps/hr2pass1fma.ksh *.pass1.dst*

Input: *.pass1.dst*

Output: *.ps1-2.dst*

Banks: *FPHO1 FRAW1 made multi mirror*

Stereo Pass1

Software: */hires_soft/dst2k/src/sma/bin/sma.c*

Script: *ãcme/scripts/process/steps/st_sma.ksh*

Input: *.ps1-1.dst .ps1-2.dst*

Output: *.ps1-s.dst*

Banks: *HRAW1 HBAR FRAW1 FPHO1 merged*

Step 1 hr_process (remove HiRes2 steerable laser events)

Software: */hires_soft/dst2k/src/hr_extract/lib/extract_hr2sls_lib.cpp*

Input: *.ps1-1.dst .ps1-2.dst .ps1-s.dst*

Output: *.hr2sls-1.dst .hr2sls-2.dst .hr2sls-s.dst*

Banks: *None: ksid future*

Step 2 hr_process (remove HiRes1 steerable laser events)

Software: */hires_soft/dst2k/src/hr_extract/lib/extract_hr1sls_lib.cpp*

Input: *.ps1-1.dst .ps1-2.dst .ps1-s.dst*

Output: *.hr1sls-1.dst .hr1sls-2.dst .hr1sls-s.dst*

Banks: *None: ksid future*

Step 3 hr_process (remove roving steerable laser events)

Software: */hires_soft/dst2k/src/hr_extract/lib/extract_rsls_lib.cpp*

Input: *.ps1-1.dst .ps1-2.dst .ps1-s.dst*

Output: *.rsls-1.dst .rsls-2.dst .rsls-s.dst*

Banks: *None: ksid future*

Step 4 hr_process (remove intersite and vertical flasher events)

Software: */hires_soft/dst2k/src/hr_extract/lib/extract_flasher_lib.cpp*

Input: *.ps1-1.dst .ps1-2.dst .ps1-s.dst*

Output: *.flsh-1.dst .flsh-2.dst .flsh-s.dst*

Banks: *None: ksid future*

Step 5 hr_process (pass2 noise filter)

Software: */hires_soft/dst2k/src/hr_pass2/lib/hr_pass2_lib.cpp*

Input: *.ps1-1.dst .ps1-2.dst .ps1-s.dst*

Output: *.ps2cut-1.dst .ps2cut-2.dst .ps2cut-s.dst*

Banks: *None if cut. FPASS2 PASS2*

Step 6 hr_process (pass3 plane fit)

Software: */hires_soft/dst2k/src/hr_pass3/lib/hr_pass3_lib.cpp*

Input: *.ps1-1.dst .ps1-2.dst .ps1-s.dst*

Output: *.ps3cut-1.dst .ps3cut-2.dst .ps3cut-s.dst*

Banks: *None if cut. HPLN1 FPLN1 PASS3 FPASS3*

Step 7 hr_process (geometry fit)

Software: */hires_soft/dst2k/src/hr_pass4/lib/hr_geo.c*

Input: *.ps1-1.dst .ps1-2.dst .ps1-s.dst*

Output: *.geocut-1.dst .geocut-2.dst .geocut-s.dst*

Banks: *None if cut. HCTIM*

Step 8 hr_process (Light flux / binning)

Software: */hires_soft/dst2k/src/hr_pass4/lib/hr_bin.c*

Input: *.ps1-1.dst .ps1-2.dst .ps1-s.dst*

Output: *.bincut-1.dst .bincut-2.dst .bincut-s.dst*

Banks: *None if cut. HCBIN*

Step 9 hr_process (Profile Fit)

Software: */hires_soft/dst2k/src/hr_pass4/lib/hr_pfl.c*

Input: *.ps1-1.dst .ps1-2.dst .ps1-s.dst*

Output(cut): *.pflcut-1.dst .pflcut-2.dst .pflcut-s.dst*

Output: *.ps4-1.dst .ps4-2.dst .ps4-s.dst*

Banks: *None if cut. PRFC. Future PRFA*

hr_process is run by the following command line:

hr_process [-nostep X] [-nowrite X] [-v N] fname.ps1-X.dst

You may choose which steps not to perform and which forms of output not to write out.

REFERENCES

[1] D. J. Bird *et al.*, *Ap. J.*, **441**, 144 (1995).

[2] M. Takeda *et al.*, Phys. Rev. Lett. **81**, 1163 (1998).

[3] , R Clay and B. Dawson, *Cosmic Bullets - High Energy Particles in Astrophysics*, (Addison Wesley, 1997).

[4] J. Cronin, T.K. Gaisser, and S.P. Swordy, Sci. Amer., **276**, 44 (1997).

[5] E. Fermi, Phys. Rev., **75**, 1169 (1949).

[6] J. N. Bahcall and E. Waxman, Astrophys. J., **542**, 543-547 (2000).

[7] G. R. Farrar and T. Piran, Phys. Rev. Lett., **84**, 3527 (2000).

[8] S. Yoshida and H. Dai, J. Phys. G: Nucl. Part. Phys., **24**, 905 (1998).

[9] V. A. Kuzmin and V. A. Rubakov, Phys. Atom. Nucl., **61**, 1028 (1998).

[10] P. Bhattacharjee and G. Sigl, Phys. Rev. D, **51**, 4079 (1995).

[11] A. J. Gill and T. W. B. Kibble, Phys. Rev. D, **50**, 3660 (1994).

[12] C. T. Hill, D. N. Schramm and T. P. Walker, Phys. Rev. D, **36**, 1007 (1987).

[13] G.C. Archbold, *A Study of the Composition of Ultra High Energy Cosmic Rays Using The High Resolution Fly's Eye*, Ph.D thesis, (University of Utah, Salt Lake City, 2002).

[14] J. Bellido, private communication (2002).

[15] J. Boyer, B. Knapp, E. Mannel and M. Seman, in Proceedings of the 26_{th} International Cosmic Ray Conference (ICRC), Salt Lake City, 1999, (University of Utah, Salt Lake City, 1999) **5**, 441.

[16] B. Jones *et al.*, in Proceedings of 26_{th} ICRC (Ref. [15]), **5**, 429.

[17] B. Jones *et al.*, in Proceedings of 27_{th} ICRC, Hamburg, 2001, (Copernicus Gesellshaft, Hamburg, 2001), **1**, 641.

[18] L. Wiencke *et al.*, in Proceedings of the 27_{th} ICRC, (Ref. [17]), **1**, 631.

[19] L. Wiencke *et al.*, in Proceedings of the 27_{th} ICRC, (Ref. [17]), **1**, 635.

[20] T. Abu-Zayad, *The Energy Spectrum of Ultra High Energy Cosmic Rays*, Ph.D. thesis, (University of Utah, Salt Lake City, 2000).

[21] X. Z. Zhang, *The Energy Spectru m of Cosmic Rays with Energy Above 1 EeV*, Ph.D. thesis, (Columbia University, New York, 2001).

[22] C. Song. Ph.D. thesis, (Columbia University, New York, 2001)

[23] P. Sokolsky, *Introduction to Ultrahigh Energy Cosmic Ray Physics* (Addison Wesley, New York, 1989).

[24] M. S. Longair, *High Energy Astrophysics, Vol. 1*, (Cambridge University Press, Cambridge, 1994).

[25] M. S. Longair, *High Energy Astrophysics, Vol. 2* (Cambridge University Press, Cambridge, 1994).

[26] S. I. Nikolsky, Nucl. Phys. B, Proc. Suppl., **39A**, 228 (1995).

[27] A. M. Hillas, in Proceedings of the 16_{th} ICRC, Kyoto, 1979, (University of Tokyo, Tokyo, 1979), **8**, 7.

[28] P. L. Biermann, in Proceedings of the 23_{th} ICRC, Calgary, Canada, (Department of Physics and Astronomy, The University of Calgary, Calgary, 1993), *Rapporteur*, 45.

[29] K. Greisen, Phys. Rev. Lett., **16**, 748 (1966).

[30] G.T. Zatsepin and V. A. Kuzmin, Sov. Phys. JETP Lett., **4**, 78 (1966).

[31] M. S. Longair, *High Energy Astrophysics, Vol. 2, 2nd Ed. with corrections* (Cambridge University Press, Cambridge, 1994).

[32] Jeffery Bennett, Megan Donahue, Nicholas Schneider, and Mark Voit, *The Cosmic Perspective, 2nd Edition*, (Addison Wesley, 2002).

[33] B. Stokes, private communication (2002).

[34] T.C. Weekes, Phys. Rept., **160**, 1 (1988).

[35] T. Abu-Zayyad *et al.*, Nucl. Inst. Meth., **A 450**, 253 (2000).

[36] R. Abassi *et al.*, "Measurement of the Spectrum of UHE Cosmic Rays by the FADC Detector of the HiRes Experiment", Astropart. Phys. (to be published).

[37] C. R. Wilkinson, *The Application of High Precision Timing in the Hihg Resolution Flys Eye Cosmic Ray Detector*, Ph.D. thesis, (University of Adelaide, Adelaide, 1998).

[38] L. R. Wiencke, *et al.*, Nucl. Inst. Meth., Sect. A **428**, 593 (1999).

[39] NASA (National Aero Space Administration), NOAA (National Oceanic and Atmospheric Administration) and US Air Force, "US Standard Atmosphere", *NASA technical report* **NASA-TM-X-74335** (1976).

[40] G. Archbold *et al.*, in Proceedings of the 27_{th} ICRC (Ref. [17]), **1**, 623 (2001).

[41] J. H. V. Girard *et al.*, Nucl. Inst. Meth., **A 460**, 278 (2000).

[42] D. Heck *et al.*, University of Kalsruhe Report No. **FZKA-6019**, (1998).

[43] W. R. Nelson, H. Hirayama, and D. W. O. Rogers, "The EGS4 Code System", SLAC-Report-265 (December 1985).

[44] A. F. Bielajew, H. Hirayama, W. R. Nelson, and D. W. O. Rogers, *Report* **PIRS-0436**, National Research Council of Canada (1994).

[45] C. L. Pryke, Astropart. Phys., **14**, 319 (2001).

[46] R. S. Fletcher, T. K. Gaisser, P. Lipari and T. Stanev, Phys. Rev. D, **50**, 5710 (1994).

[47] N. N. Kalmykov, S. S. Ostapchenko and A. I. Pavlov, Nucl. Phys. B, Proc. Suppl. **52**, 17 (1997).

[48] K. M. Simpson, *Studies of Cosmic Ray Composition Using a Hybrid Fluorescence Detector*, Ph.D. Thesis, (University of Adelaide, Adelaide, 2001).

[49] T. Gaisser and A. M. Hillas, in Proceedings of the 15^{th} ICRC, Plovdiv, Bulgaria, (Institute for Nuclear Research, Bulgarian Academy of Sciences, Sofia, Bulgaria, 1977), **8**, 353.

[50] Z. Cao, private communication (2002).

[51] D. E. Groom *et al.*, The Euro. Phys. J. **C15**, 1 (2000).

[52] T. Abu-Zayad, *et al.*, Phys. Rev. Lett., **84**, 4276 (2000).

[53] A. N. Bunner, *Cosmic Ray Detection by Atmospheric Fluorescence*, Ph.D. thesis, (Cornell University, Cornell, 1967).

[54] F. Kakimoto *et al.*, NIM **A372**, 527 (1996).

[55] G. J. Feldman and R. D. Cousins, Phys. Rev. D **57**, 3873 (1998).

[56] C. Jui, private communication (2002).

[57] T. Abu-Zayad *et al.*, "Measurement of the Flux of Ultrahigh Energy Cosmic Rays from Monocular Observations by the High Resolution Fly's Eye Experiment", Astro. Ph. **0208243**.